TU Delft

Delft University of Technology

Quantum Networks with Diamond Color Centers
Local Control and Multi-Node Entanglement

Beukers, H.K.C.

DOI
10.4233/uuid:23b7e27a-fc12-449b-aa2a-4d1827aa4b6b

Publication date
2025

Document Version
Final published version

Citation (APA)
Beukers, H. K. C. (2025). *Quantum Networks with Diamond Color Centers: Local Control and Multi-Node Entanglement*. [Dissertation (TU Delft), Delft University of Technology].
https://doi.org/10.4233/uuid:23b7e27a-fc12-449b-aa2a-4d1827aa4b6b

Important note
To cite this publication, please use the final published version (if applicable).
Please check the document version above.

Copyright
Other than for strictly personal use, it is not permitted to download, forward or distribute the text or part of it, without the consent of the author(s) and/or copyright holder(s), unless the work is under an open content license such as Creative Commons.

Takedown policy
Please contact us and provide details if you believe this document breaches copyrights.
We will remove access to the work immediately and investigate your claim.

This work is downloaded from Delft University of Technology.
For technical reasons the number of authors shown on this cover page is limited to a maximum of 10.

Quantum Networks with Diamond Color Centers

Local Control and Multi-Node Entanglement

Hans Beukers

QUANTUM NETWORKS WITH DIAMOND COLOR CENTERS

LOCAL CONTROL AND MULTI-NODE ENTANGLEMENT

Dissertation

for the purpose of obtaining the degree of doctor
at Delft University of Technology,
by the authority of the Rector Magnificus, Prof.dr.ir. T.H.J.J. van der Hagen,
Chair of the Board for Doctorates,
to be defended publicly on
Monday May 26th 2025 at 15:00 o'clock

by

Hans Karel Clemens BEUKERS

Master of Science in Physics and Master of Science in Medicine,
University of Groningen, The Netherlands,
born in Apeldoorn, The Netherlands.

This dissertation has been approved by the promotors.

Composition of the doctoral committee:

Rector Magnificus	chairperson
Prof.dr.ir. R. Hanson	Delft University of Technology, promotor
Dr.ir. T.H. Taminiau	Delft University of Technology, copromotor
Independent members:	
Prof.dr. L. DiCarlo	Delft University of Technology
Prof.dr.ir. C.H. van der Wal	University of Groningen
Prof.dr. F. Jelezko	Ulm University, Germany
Prof.dr. T.E. Northup	University of Innsbruck, Austria
Prof.dr.ir. L.P. Kouwenhoven	Delft University of Technology, reserve member

Copyright © 2025 Hans Beukers

Cover design: Eveline Beukers and Hans Beukers

ISBN 978-94-6384-794-0

Printed by: Gildeprint

An electronic version of this dissertation is available at
`http://repository.tudelft.nl/`.

CONTENTS

SUMMARY

The ability to send quantum information over long distances can enable fundamentally new applications, such as intrinsically secure communication, enhanced metrology, and distributed quantum computation. Entangled links serve as powerful resources for sending quantum information between nodes in a quantum network. However, generating entanglement in sufficient quantity and quality across a network, such that they can be used for applications, remains an open challenge.

In this thesis, we explore the use of color centers in diamond as network nodes. Their electron spin serves as a matter qubit with an optical interface, enabling the entanglement of two distant color centers, mediated by photons. The surrounding nuclear spins are used as memory qubits for local computation and entanglement storage. In this thesis, we investigate both the well-established nitrogen-vacancy (NV) center in diamond and the recently discovered tin-vacancy (SnV) center in diamond. The physics and control methods for both types of color centers are discussed in Chapter 2.

Remote entanglement between matter qubits can be achieved with many different entanglement protocols. In Chapter 3, we present a framework that explains and categorizes different protocols and quantum network hardware components. This framework is then used to compare the performance of various protocols while using similar hardware.

There have been many realisations of rudimentary network links between two network nodes using various quantum hardware. In Chapters 4 and 5 , we realize the first entanglement-based three-node quantum network employing NV centers in diamond. In this network, we demonstrate fundamental network capabilities such as the creation of a remote three-party Greenberger–Horne–Zeilinger (GHZ) state and entanglement swapping to connect non-neighboring network nodes, as detailed in Chapter 4. These advancements are facilitated by storing an entangled state in a network node while generating a second entangled link. In Chapter 5 we demonstrate quantum teleportation between two non-neighboring network nodes by adding a fifth qubit to the network and utilizing the entangled link generated through the entanglement swapping.

The three-node network experiments were enabled by the nuclear spin memory, emphasizing the importance of nuclear spin control for quantum networks based on color centers. In Chapter 6, we explore nuclear spin control with the SnV center in diamond. This recently discovered color center promises enhanced entanglement rates compared to the NV center due to its superior optical interface. We control single nuclear spins and show entanglement between the electron and nuclear spin. These experiments provide insights into the challenges and opportunities of controlling nuclear spins using an electron spin-1/2.

SAMENVATTING

Het vermogen om kwantuminformatie over grote afstanden te versturen kan fundamenteel nieuwe toepassingen mogelijk maken, zoals intrinsiek veilige communicatie, verbeterde metrologie en gedistribueerde kwantumberekeningen. Verstrengelde verbindingen dienen als krachtige middelen om kwantuminformatie te versturen tussen knooppunten in een kwantuminternet. Het genereren van verstrengeling in voldoende hoeveelheid en kwaliteit in een netwerk, zodat deze voor toepassingen kan worden gebruikt, blijft een open uitdaging.

In dit proefschrift verkennen we het gebruik van kleurcentra in diamant als netwerkknooppunt. Hun elektronspin fungeert als een materiequbit met een optische interface, waardoor het mogelijk wordt om twee ververwijderde kleurcentra te verstrengelen, gefaciliteerd door fotonen. De omringende kernspins worden gebruikt als geheugenqubits voor lokale berekeningen en de opslag van verstrengeling. In dit proefschrift onderzoeken we zowel het goed bestudeerde stikstof-holtecentrum (NV-centrum) in diamant als het recent ontdekte tin-holtecentrum (SnV-centrum) in diamant. De fysica en controlemethoden voor beide typen kleurcentra worden besproken in Hoofdstuk 2.

Verstrengeling op afstand tussen materiequbits kan worden bereikt met verschillende verstrengelingsprotocollen. In Hoofdstuk 3 presenteren we een raamwerk dat verschillende protocollen en kwantumnetwerkcomponenten uitlegt en categoriseert. Dit raamwerk wordt vervolgens gebruikt om de prestaties van verschillende protocollen te vergelijken bij gebruik van vergelijkbare hardware.

Er zijn veel successvolle experimenten geweest die rudimentaire netwerkverbindingen tussen twee netwerkknooppunten hebben laten zien met een verscheidenheid aan kwantumhardware. In hoofdstukken 4 en 5 realiseren we het eerste op verstrengeling gebaseerde kwantumnetwerk met drie knooppunten, gebruikmakend van stikstof-holtecentrums in diamant. In dit netwerk demonstreren we fundamentele netwerkmogelijkheden, zoals het creëren van een afgelegen Greenberger-Horne-Zeilinger (GHZ)-toestand met drie partijen en verstrengelingsuitwisseling om niet-aangrenzende netwerkknooppunten te verbinden, zoals beschreven in hoofdstuk 4. Deze vooruitgang worden mogelijk gemaakt door een verstrengelde toestand op te slaan in een netwerkknooppunt terwijl een tweede verstrengelde verbinding wordt gegenereerd. In hoofdstuk 5 realiseren we kwantumteleportatie tussen twee niet-aangrenzende netwerkknooppunten door een vijfde qubit aan het netwerk toe te voegen en de verstrengelde verbinding te gebruiken die is gegenereerd door de verstrengelingswisseling.

De experimenten met het drieknooppuntenneterk werden mogelijk gemaakt door het gebruik van het kernspingeheugen, wat het belang benadrukt van controle over kernspins voor kwantumnetwerken gebaseerd op kleurcentra. In Hoofdstuk 6 onderzoeken we de controle van kernspins met het tin-holtecentrum in diamant. Dit recent ontdekte kleurcentrum belooft hogere verstrengelingssnelheden in vergelijking met het stikstof-holtecentrum dankzij een superieure optische interface. We controleren indi-

viduele kernspins en tonen verstrengeling tussen de elektron- en kernspin. Deze experimenten geven inzicht in de uitdagingen en mogelijkheden van het controleren van kernspins met behulp van een elektronspin-1/2.

1

INTRODUCTION

At the beginning of the twentieth century, there were multiple observations that were inconsistent with classical physics - or just physics at that time - including the photo-electric effect and the light spectrum of atoms. The description of the photo-electric effect by Albert Einstein had to assume that light was built up from small packets of energy: quanta. To explain the light spectrum from atoms, Niels Bohr needed to assume that electrons could only be in specific - quantized - orbits around the atom. It took the work of Heisenberg and Schrödinger to unify these assumptions in a single theory of quantum physics [1].

This new scientific theory had profound implications for our understanding of the world. In optically active materials, it meant that there could be a phenomenon known as population inversion. This insight, together with a lot of experimentation, led to the invention of the laser [2]. The understanding of the electronic band structure in solid-state materials fueled to the development of the transistor, which powers our contemporary computers [3]. These inventions based on exploiting quantum mechanical effects of many particles are considered Quantum 1.0 technology.

However powerful the developed technologies were, both in scientific progress and societal impact, they did not directly use the core characteristics of quantum mechanics: superposition and entanglement. In the second half of the twentieth century, the experimental capabilities to control individual quantum systems were realized. The control of atoms or photons allowed the exploration of these concepts. During this period, theoretical ideas around using quantum mechanics to process information also started to develop. Information was now stored in two-level quantum systems: qubits and processing achieved by controlling the exact evolution of the quantum system [4]. The marriage of the quantum information theory with unprecedented control over individual quantum systems resulted in the field that we now know as Quantum 2.0 technologies: quantum computing, quantum networking, and quantum sensing [5].

The promise of quantum computing stems from the richer structure of qubits and quantum operations compared to their classical counterparts. This insight was used by Shor to show that a quantum computer can outperform a classical computer in breaking widespread encryption [6]. Furthermore, quantum computers are naturally well suited for simulating quantum mechanical systems, which is hard to do for classical computers [7]. In quantum communication, quantum information is sent, which can be used to connect quantum computers and transmit information safely, fully encrypted in the laws

of quantum mechanics[8]. Finally, quantum sensors use quantum properties to measure an external physical parameter and are thereby able to give more precise readings than their classical cousins[9].

These three fields have different objectives but are united by the required hardware capabilities. In this thesis, we will focus on the development of quantum networks. However, all three fields are required to reach that goal. We use local computations in the quantum network nodes, photons to send quantum information in the network, and sensing techniques to search for nuclear spins that can be used as qubits.

Quantum networks will be made from individual nodes that can be linked by entanglement[8]. Quantum information can be sent between the nodes by using the entanglement. The nodes themselves can locally process quantum information. To link the nodes, we need to employ flying qubits to carry this quantum information over the large distances between the nodes. Optical photons are ideal candidates for this as they preserve their quantum properties at room temperature and can be easily transmitted. Therefore, it is important that the qubits in the network nodes interact with photons. Many systems have such a photon-qubit interface, such as trapped ions, cold atoms, quantum dots, and rare-earth ions. In this thesis, we will use color centers in diamond as our photon-qubit interface in the network nodes.

Diamond is host to a very rich variety of color centers. The wide bandgap gives these centers ion-like properties. The nitrogen-vacancy (NV) center in diamond has become the archetypical color center for the last two decades because of its rich combination of properties[10]. These include electron spin coherence and optical readout at room temperature, coherent spin-photon interface at cryogenic temperatures, and the ability to use surrounding carbon nuclear spins as additional memory qubits. Its great electron spin properties, in combination with the decent spin-photon interface, have made it into one of the forerunners of the quantum network field, with experiments like a loophole-free Bell test[11] and deterministic entanglement delivery[12]. The availability of the nuclear spin memory qubits made it possible to show entanglement distillation[13]. In this thesis, we build on top of these results and realize a multi-node quantum network in which three network nodes are connected through entanglement.

Network nodes in a future quantum internet will require many qubits per node[14]. Color centers can be integrated into nanophotonics[15], which allows many color centers to be combined on a single chip[16]. The NV center has been a great platform for proof-of-principle quantum network experiments. However, it cannot be combined with nanophotonic integration because their optical transitions are not stable so close to the electric field noise on the surface[17]. This is where the tin-vacancy (SnV) center in diamond enters the second act of this thesis. It is a color center that is resilient against this noise and, therefore, compatible with nanophotonics[18–20]. In this thesis, we show control over the electron spin qubit of the SnV center and use that to control nuclear spins surrounding the SnV center. With this, we establish the required control for a quantum network node.

The thesis has the following structure:

In **Chapter 2**, I describe the theoretical background and experimental techniques required for understanding the experiments performed in this thesis.

In **Chapter 3**, we develop a framework for understanding and characterizing the entanglement protocols. This can be used to understand the entanglement protocol used in the NV experiments and to design appropriate entanglement protocols for the SnV center.

In **Chapter 4**, we use the NV center to build a multi-node network consisting of three nodes. In this network we are able to generate entanglement while storing a first link. We can consume these two links and generate three-node entanglement with a GHZ state. Furthermore, these links can be used for entanglement swapping, in which the entanglement is distributed between two non-neighboring nodes.

In **Chapter 5**, we use the distributed entanglement in the multi-node network to show teleportation between two non-neighboring nodes. This showcases the basic functionality of routing and sending quantum information in a real network.

In **Chapter 6**, we show control over an electron and nuclear spin qubit register based on the SnV center. The control of the nuclear spin is different for the SnV center compared to the NV center, as it has an electron spin-1/2. This research provides insight in the challenges and opportunities for nuclear spin control with electron spin-1/2 systems in general.

In **Chapter 7**, I summarize the findings in this thesis and give an outlook on the near-term opportunities and long-term prospects of quantum networks with color centers.

1

REFERENCES

[1] C. Rovelli, *Helgoland: The Strange and Beautiful Story of Quantum Physics* (Penguin Books Limited, 2021).

[2] J. L. Bromberg, *The Birth of the Laser,* Physics Today **41**, 26 (1988).

[3] W. Brinkman, D. Haggan and W. Troutman, *A history of the invention of the transistor and where it will lead us,* IEEE Journal of Solid-State Circuits **32**, 1858 (1997).

[4] M. A. Nielsen and I. L. Chuang, *Quantum Computation and Quantum Information*, 10th ed. (Cambridge University Press, Cambridge ; New York, 2010).

[5] J. P. Dowling and G. J. Milburn, *Quantum technology: The second quantum revolution,* Philosophical Transactions of the Royal Society of London. Series A: Mathematical, Physical and Engineering Sciences **361**, 1655 (2003).

[6] P. Shor, *Algorithms for quantum computation: Discrete logarithms and factoring,* in *Proceedings 35th Annual Symposium on Foundations of Computer Science* (1994) pp. 124–134.

[7] I. M. Georgescu, S. Ashhab and F. Nori, *Quantum simulation,* Reviews of Modern Physics **86**, 153 (2014).

[8] S. Wehner, D. Elkouss and R. Hanson, *Quantum internet: A vision for the road ahead,* Science **362**, eaam9288 (2018).

[9] C. L. Degen, F. Reinhard and P. Cappellaro, *Quantum sensing,* Reviews of Modern Physics **89**, 035002 (2017).

[10] M. W. Doherty *et al.*, *The nitrogen-vacancy colour centre in diamond,* Physics Reports The Nitrogen-Vacancy Colour Centre in Diamond, **528**, 1 (2013).

[11] B. Hensen *et al.*, *Loophole-free Bell inequality violation using electron spins separated by 1.3 kilometres,* Nature **526**, 682 (2015).

[12] P. C. Humphreys *et al.*, *Deterministic delivery of remote entanglement on a quantum network,* Nature **558**, 268 (2018).

[13] N. Kalb, P. C. Humphreys, J. J. Slim and R. Hanson, *Dephasing mechanisms of diamond-based nuclear-spin memories for quantum networks,* Physical Review A **97**, 062330 (2018).

[14] F. F. da Silva, G. Avis, J. A. Slater and S. Wehner, *Requirements for upgrading trusted nodes to a repeater chain over 900 km of optical fiber,* Quantum Science and Technology **9**, 045041 (2024).

[15] A. Sipahigil *et al.*, *An integrated diamond nanophotonics platform for quantum-optical networks,* Science **354**, 847 (2016).

[16] N. H. Wan *et al.*, *Large-scale integration of artificial atoms in hybrid photonic circuits,* Nature **583**, 226 (2020).

[17] A. Faraon, C. Santori, Z. Huang, V. M. Acosta and R. G. Beausoleil, *Coupling of Nitrogen-Vacancy Centers to Photonic Crystal Cavities in Monocrystalline Diamond,* Physical Review Letters **109**, 033604 (2012).

[18] A. E. Rugar *et al.*, *Narrow-Linewidth Tin-Vacancy Centers in a Diamond Waveguide,* ACS Photonics **7**, 2356 (2020).

[19] A. E. Rugar *et al.*, *Quantum Photonic Interface for Tin-Vacancy Centers in Diamond,* Physical Review X **11**, 031021 (2021).

[20] M. Pasini *et al.*, *Nonlinear Quantum Photonics with a Tin-Vacancy Center Coupled to a One-Dimensional Diamond Waveguide,* Physical Review Letters **133**, 023603 (2024).

2

METHODS

In this chapter I describe the theoretical background and experimental techniques that are used in this thesis. I describe the properties of the nitrogen-vacancy and tin-vacancy center and techniques to control their electron spins and optical interfaces. They share many details but stand apart in a few key differences. Furthermore, the control techniques for surrounding nuclear spins are discussed, as well as the protocol to generate entanglement. Lastly, I discuss the device fabrication and the experimental setups used to control them.

2.1. NITROGEN-VACANCY CENTER IN DIAMOND

The nitrogen-vacancy (NV) center is a point defect in the diamond lattice and contains a substitutional nitrogen atom, directly replacing a carbon atom in the lattice, and a neighboring vacancy, a missing carbon atom, see Fig. 2.1(a). In this thesis, we work with the negatively charged NV center, where an extra electron is captured from the environment, for example, a close-by charge trap. Together with three electrons from the dangling sp^3 carbon bonds and two electrons from the nitrogen atom, this gives six electrons available to fill the molecular orbitals. Fig. 2.1(b) shows these molecular orbitals, of which the (partially) free ones reside in the bandgap for the ground and first excited state, giving the NV center ion-like properties. The electrons form a spin-1 system, resulting in singlet and triplet spin states [1].

2.1.1. ELECTRONIC STRUCTURE

The ground state is a spin-triplet orbital-singlet state and couples optically to the spin-triplet orbital-doublet excited state [1]. The NV center can decay from the excited state directly to the ground state with the emission of a zero-phonon line (ZPL) photon at a wavelength of 637 nm, see Fig. 2.2(a-b). Additionally, the emission can be accompanied by a phonon, giving rise to phonon sideband (PSB) decay. Lastly, the decay can happen via the intermediate singlet levels. Lateral strain or perpendicular electric fields split the orbital part of the electronic wavefunction of the excited state levels [1], as shown in Fig. 2.2(c). The spin part can be split by a magnetic field. The effect of the electric field on the excited state is later used to tune the frequency of the optical transitions [4].

The ground state has a zero-field splitting $D = 2.88\,\text{GHz}$ caused by electronic spin-

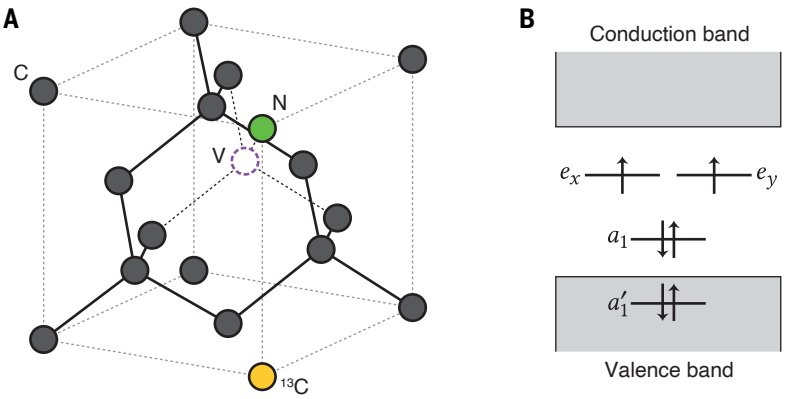

Figure 2.1: **Nitrogen-vacancy center in diamond.** (a) The NV center consists of a nitrogen atom (green sphere) and a vacancy (purple dashed circle), replacing two carbon atoms (gray spheres) in the lattice of diamond. Naturally abundant carbon consists of 1.1 % ^{13}C (yellow sphere). (b) Electron spin configuration in the ground state of the NV center. The molecular orbitals are labeled by their irreducible representation in the symmetry group C_{3v}: e_x, e_y, a_1, and a_1'. The two unpaired electrons form a spin triplet in the ground state. Adapted from Pfaff and Bernien [2,3].

spin interaction. On top of this, the spin state is split by a magnetic field through the Zeeman interaction, as depicted in Fig. 2.2(d). The Hamiltonian of the ground state is therefore

$$\hat{H} = D\hat{S}_z^2 + \gamma_e \vec{B} \cdot \vec{S}, \tag{2.1}$$

where $\vec{S} = (\hat{S}_x, \hat{S}_y, \hat{S}_z)$ is the spin-1 operator, $\vec{B}$ is the magnetic field and $\gamma_e = 28.025\,\text{GHz/T}$ is the gyromagnetic ratio of the electron spin.

We define a qubit in the ground state spin triplet with $|0\rangle = |m_S = 0\rangle$ and $|1\rangle = |m_S = \pm 1\rangle$. The sign for the latter is chosen depending on what gives the highest control fidelity in spin-photon entanglement, optical readout and microwave control.

In this thesis, we align the external magnetic field to the symmetry axis of the nitrogen-vacancy center. This will align the quantization axis of the spin in the ground and the excited state and make the spin-flipping transition mostly forbidden. This allows for the best readout and spin-photon entanglement fidelity.

2.2. TIN-VACANCY CENTER IN DIAMOND

The tin-vacancy center in diamond is an interstitial defect, where a tin atom resides between two vacancies in the carbon lattice, as depicted in Fig. 2.3(a-b). It is a member of the group-IV* vacancy centers in diamond, which include the silicon, germanium, tin, and lead vacancy centers. The group-IV vacancy centers have been mostly studied in the negatively charged state and that is also the case in this thesis. This group shares the same crystallographic structure and is governed by a Hamiltonian with the same terms, the main difference is in the strengths of the interaction in the Hamiltonian.

The interest in this group of color centers stems from the symmetry of the defect. The symmetry group of this point defect in the lattice is D_{3d} and includes the inversion symmetry. Because of this, there cannot be any permanent electric dipole, which renders the defect first-order insensitive to electric fields. The symmetry of the defect has been derived in ab initio simulations [6] and confirmed experimentally [7]. This is an important characteristic as defects in nanophotonic structures experience electric field noise caused by the charges on the surfaces, which can be as close as tens of nanometers [8]. The excited state of the nitrogen-vacancy center is susceptible to electric fields, which shows up as unstable optical transitions in nanophotonic devices [9]. The members from the group-IV vacancy group have shown to be stable in these same structures [8,10,11].

The silicon-vacancy (SiV) center was the first group-IV vacancy center of which single centers were investigated [12], which led to an efficient optical interface based on a SiV in a nanophotonic cavity [10] and a coherent electron spin qubit [13]. However, keeping the electron spin coherent required cooling the diamond to temperatures of 100 mK in a dilution refrigerator. As will be discussed in section 2.2.2, there were theoretical reasons to expect that heavier elements from the group-IV would have a coherent electron spin also at higher temperatures. The tin-vacancy (SnV) center was experimentally observed [14,15] and it was verified that the optical transitions could be coherent [16]. Additionally, experiments at 1.7 K showed that the prediction about a higher operation temperature for the tin-vacancy center was correct [17]. This positioned the tin-vacancy center as a promising

*In modern IUPAC notation, this is called group 14. However, it is known as group IV in the field of semiconductor physics.

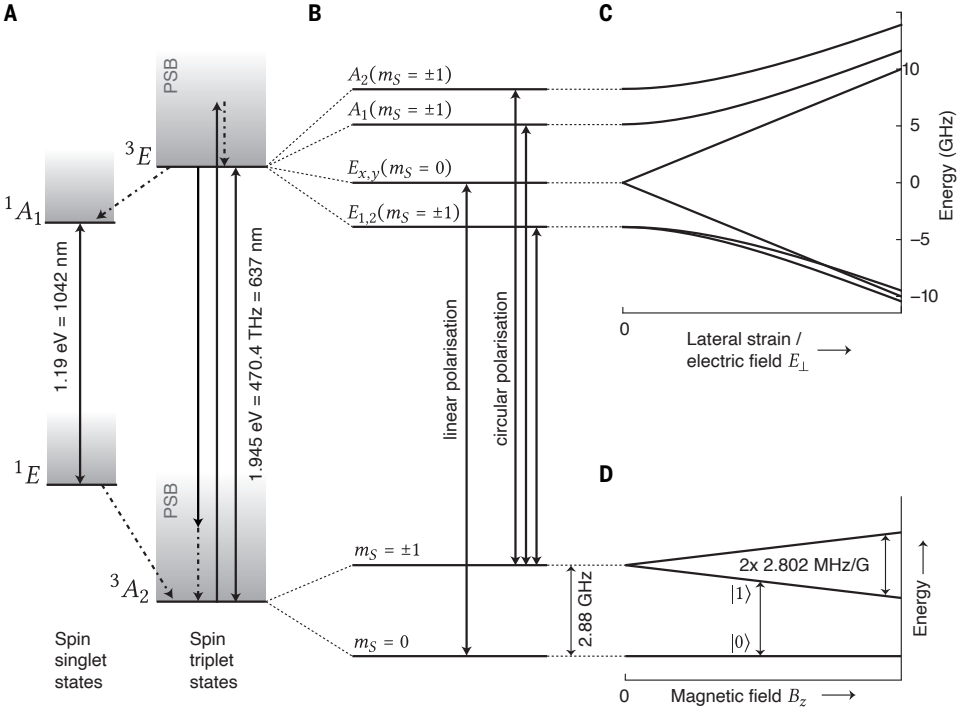

Figure 2.2: **Electronic structure of the NV center.** (a) The ground state $^3A_2$ and the excited state ^3E have a spin triplet and are optically connected by the zero-phonon line (ZPL) transition. Absorption with a higher energy or emission with a lower energy occurs with the additional emission of a phonon in the phonon sideband (PSB). Decay can also happen via the intermediate singlet states. (b) The ground state is split by the zero-field splitting. The excited states are labeled with the character of their symmetry, where the A levels are orbital singlets and the levels with an E are doublets. Spin-conserving optical transitions are allowed. (c) Lateral strain and perpendicular electric field split the orbital part of the wavefunction in two groups. Different emitters can have varying strain environments, which influences their optical spectrum. (d) A magnetic field aligned along the symmetry axis of the NV will split the $|m_S = \pm1\rangle$ levels. The qubit is defined as $|0\rangle = |m_S = 0\rangle$ and $|1\rangle = |m_S = \pm1\rangle$. Adapted from Pfaff and Bernien[2,3,5].

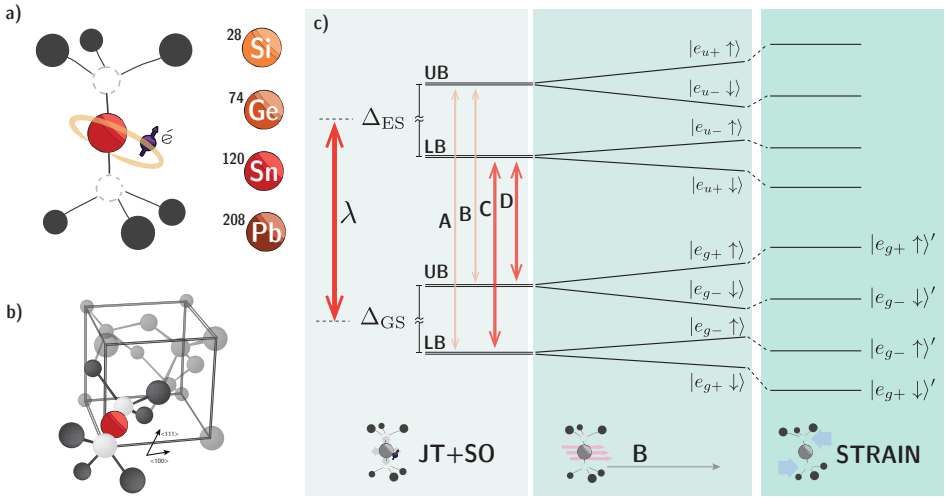

Figure 2.3: **Group-IV vacancy centers in diamond.** (a) A group-IV atom resides between two vacant lattice sites in the diamond. By capturing an extra electron from the surrounding it forms the desired negatively charged group-IV vacancy centers. (b) The placement of the center in the unit cell. (c) The four-fold degeneracy of the ground and excited state is lifted by the Jahn-Teller effect (JT) and the spin-orbit interaction (SO), splitting the four levels into a lower branch (LB) and an upper branch (UB). The degeneracy of these branches can be further lifted by a magnetic field (B) acting on the spin part of the electronic wavefunction. Transversal strain can further split the branches. Adapted from Pasini [18].

candidate for quantum network experiments with integrated photonics at temperatures above 1 K.

2.2.1. ELECTRONIC STRUCTURE

The electronic ground and excited state of the group-IV vacancy centers have a similar level structure. They are both a spin-doublet orbital-doublet state and have the same interaction, although with different strengths. The intrinsic Hamiltonian of the SnV center is formed by the spin-orbit interaction and the Jahn-Teller effect. These effects lift the degeneracy of the four levels of the ground and the excited state into an upper branch (UB) and a lower branch (LB), as illustrated in Fig. 2.3. Additionally, magnetic fields induce the Zeeman interaction and strain couples to the two orbital states within the ground and excited state [6,19]. We will indicate the electron spin-1/2 states with $|\uparrow\rangle$ and $|\downarrow\rangle$ to indicate the $|m_S = 1/2\rangle$ and $|m_S = -1/2\rangle$ spin projections, respectively. The orbital states can be described in the bases $|e_+\rangle$ and $|e_-\rangle$, in which the spin-orbit interaction Hamiltonian is diagonal [19].

The spin-orbit interaction is a relativistic effect, which couples the electron spin with its orbital angular momentum. The spin-orbit interaction is stronger for electrons around heavier nuclei, which can be seen in Table 2.1 in the ground (excited) state splitting Δ_{GS} (Δ_{ES}) of the group-IV vacancy centers. The Hamiltonian of the spin-orbit inter-

action is

$$\hat{H}_{\text{SOC}} = -\lambda \vec{L} \cdot \vec{S} = -\frac{\lambda}{2} \hat{\sigma}_z^{\text{orbit}} \hat{\sigma}_z^{\text{spin}}, \tag{2.2}$$

where λ is the strength of the spin-orbit interaction, $\vec{S} = (\hat{S}_x, \hat{S}_y, \hat{S}_z)$ is the spin-1/2 and $\vec{L} = (\hat{L}_x, \hat{L}_y, \hat{L}_z)$ is the orbital angular momentum, where $\hat{L}_z$ is the only non-zero orbital momentum operator on the $|e_\pm\rangle$ basis[19]. The minus sign comes from the fact that the SnV center actually houses an electron hole[6].

The Jahn-Teller effect arises from spontaneous symmetry breaking of the electronic wavefunction and causes two effects on the Hamiltonian[6]. First, it quenches the orbital angular momentum, which is captured in our treatment of the Hamiltonian as a lower value for λ. Second, it gives rise to a linear displacement of the nuclei, which has the same effect on the Hamiltonian as static strain in the lattice, which is discussed next.

Strain in the diamond couples to the electronic orbitals[20]. Strain can be decomposed into two representations of the symmetry group, each having its own distinct effect on the Hamiltonian. Longitudinal strain adds a common energy shift to all the levels in the ground or excited state. However, as this shift is different for the ground and excited state, this gives rise to a change in the optical transition frequency. Transversal strain splits the lower and upper branches by adding an off-diagonal term to the spin-orbit Hamiltonian:

$$\hat{H}_{\text{strain}} = \epsilon \hat{\sigma}_x^{\text{orbit}}, \tag{2.3}$$

where ϵ is the strength of the transversal strain and the coordinate system is rotated such that the strain can be described with a single parameter[21].

The final contribution to the Hamiltonian we discuss is the Zeeman effect. The Zeeman effect for the electron spin is isotropic

$$\hat{H}_{\text{B, S}} = \gamma_e \vec{S} \cdot \vec{B}, \tag{2.4}$$

where $\vec{B}$ is the magnetic field and γ_e is the same electronic gyromagnetic ratio as for the NV center. The orbital angular momentum also experiences the Zeeman effect

$$\hat{H}_{\text{B, L}} = \gamma_L \vec{L} \cdot \vec{B} = f \mu_B \hat{L}_z B_z, \tag{2.5}$$

where the orbital gyromagnetic ratio γ_L is the Bohr magneton μ_B quenched with a factor $f \approx 0.25$[22], and the $\hat{L}_z$ is the only non-zero angular momentum operator, like for the spin-orbit interaction.

Adding these effects together gives the total Hamiltonian of the SnV center

$$\hat{H} = \hat{H}_{\text{SOC}} + \hat{H}_{\text{strain}} + \hat{H}_{\text{B, S}} + \hat{H}_{\text{B, L}}. \tag{2.6}$$

The splitting between the lower and upper branches will play an important role in the coherence properties of the group-IV vacancy centers, as discussed in the next section. The splitting between the branches is

$$\Delta_{\text{GS/ES}} = \sqrt{\lambda^2 + 4\epsilon^2}. \tag{2.7}$$

In this thesis, we define the qubit in the two levels of the lower branch of the ground state, as this is the level with the longest coherence times in the SnV center: $|0\rangle = |{\downarrow}\, e_-\rangle$ and $|1\rangle = |{\uparrow}\, e_+\rangle$.

Center	λ_{ZPL} [nm]	τ [ns]	Δ_{GS} [GHz]	Δ_{ES} [GHz]
SiV	737[23]	1.8[24]	50[19]	260[19]
GeV	602[25]	6[11]	170[26]	1120[27]
SnV	619[16]	4.5-8[28]	822[22]	3030[28]
PbV	550[29]	4.4[29]	3870[29]	6920[6]*
NV	637[30]	12.3[31]	-	-

Table 2.1: Properties group-IV vacancy centers and the NV center. The NV has no ground and excited state splitting. * The values with a star are based on ab initio calculations.

2.2.2. COHERENCE OF GROUP-IV VANCANCY CENTERS

For spin-photon interfaces in quantum networks, it is important that the optical transition and the qubit subspace remain coherent. Both spin and optical coherence of the group-IV vacancy centers are discussed in detail in this section, as this discussion is closely related to their electronic structure. The higher operation temperature of the SnV compared to the SiV is also one of the main motivations for the interest in the tin-vacancy center. The coherence of the electron spin is further discussed in the context of the electron spin qubit and compared with the NV center in section 2.3.5.

The coherence of both the qubit and the optical transition of the group-IV vacancy centers has a strong temperature dependence as the decoherence is caused by phonons in the diamond. The phonon process that dominates the decoherence mechanism is a direct single-phonon process. In this process, a phonon brings the electron from the lower branch to the upper branch with a rate γ_+, after which it can decay back to the lower branch by emission of a phonon γ_- [32].

$$\gamma_+ = 2\pi\chi\rho\Delta_{GS}^3 n(\Delta_{GS}, T), \tag{2.8}$$

$$\gamma_- = 2\pi\chi\rho\Delta_{GS}^3 [n(\Delta_{GS}, T) + 1], \tag{2.9}$$

where χ and ρ are, respectively, the phonon-electron interaction frequency and the phononic densities of state. The Bose-Einstein distribution $n(\Delta_{GS}, T)$ for a temperature T and energy splitting Δ_{GS} is

$$n(\Delta_{GS}, T) = \frac{1}{e^{\Delta_{GS}/k_B T} - 1}, \tag{2.10}$$

where k_B is there Boltzmann constant.

To understand how the temperature influences the coherence time, we are interested in how fast an eigenstate decays to another, which we characterize with a depolarizing time T_1. Furthermore, we are interested in how fast the phase of a superposition gets lost, which we describe by a dephasing time T_2^*. These names are concepts carried over from the NMR (nuclear magnetic resonance) community.

At low temperatures, $k_B T \ll \Delta_{GS}$ we will have $\gamma_+ \ll \gamma_-$. This means that the upward rate will limit the overall rate of the two-phonon process. Therefore, the orbital decay time is

$$T_1^{\text{orbit}} = 1/\gamma_+. \tag{2.11}$$

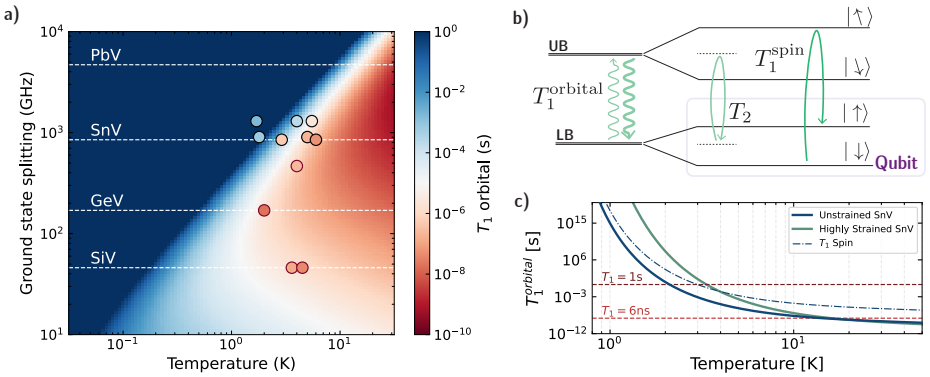

Figure 2.4: **Coherence of group-IV vacancy centers in diamond.** (a) The orbital coherence time T_1^{orbit} depending on ground state splitting and temperature. The colormap gives the simulated values using $\chi\rho = 4.6 \times 10^{-9}\,\text{GHz}^{-2}$, which was measured in our lab [34]. The circles indicate measured values of silicon-vacancy (SiV) [35–37], germanium-vacancy (GeV) [26] and tin-vacancy (SnV) [16,33,38] centers. The T_1^{spin} and $T_2^{*,\text{spin}}$ values have been converted to the corresponding T_1^{orbit}. The experimental values can be lower than the simulations as the coherence can be limited by other sources. (b) Phonons can couple the lower branch (LB) and the upper branch (UB), which sets the T_1^{orbital} time. A qubit defined in the lower branch will experience a complete dephasing for each phonon interesting, thereby limiting T_2. The T_1^{spin} is only affected if the cycle was not spin conserving. (c) Simulations similar to (a) for an unstrained ($\Delta_{\text{GS}} = 850\,\text{GHz}$) and a highly strained ($\Delta_{\text{GS}} = 1300\,\text{GHz}$) SnV center. For the simulation of T_1^{spin} a cyclicity of 1200 was assumend [33]. Lines of 6 ns and 1 s indicate the timescales relevant for optical and spin coherence, respectively. Adapted from Pasini [18].

This T_1^{orbit} determines all the other decoherence rates, which is depicted in Fig. 2.4(b). The dephasing rate of the spin qubit $T_2^{*,\text{spin}} = T_1^{\text{orbit}}$, as every phonon interaction completely mixes the phase of the spin. The depolarization rate of the qubit T_1^{spin} is slower than the dephasing as not every phonon interaction will cause a spin-flip. This probability depends on the overlap between the spin state in the lower and upper branches, which can be characterized by the spin cyclicity η^{spin}. This indicates how often the spin cycles on average before a spin-flip occurs. This results in $T_1^{\text{spin}} = \eta^{\text{spin}} T_1^{\text{orbit}}$. The cyclicity in an aligned field has been measured to be ≈ 1200 [33].

The optical transition has to be coherent longer than the lifetime of the excited state to be useful as a spin-photon interface for entanglement protocols. The coherence of the optical transition is determined by both the ground and excited state. At low temperatures, the ground state has the fastest dephasing as it has a smaller Δ. This results in $T_2^{*,\text{optical}} = T_1^{\text{orbit, GS}}$.

As long as the coherence is limited by the phonon processes, we can improve the coherence by reducing the number of phonons that are resonant with the transition between the two branches. By using Eq. 2.8 and 2.11 we can simulate the expected T_1^{orbit} for different temperatures in Fig.2.4(c). The T_1^{orbit} starts to exceed the lifetime of 6 ns at temperatures below 10 K, which means that those temperatures are required for a coherent optical interface. Temperatures below 2 K are required to mitigate the effect of phonons on the coherence of the spin state and bring the phonon-related coherence time to a

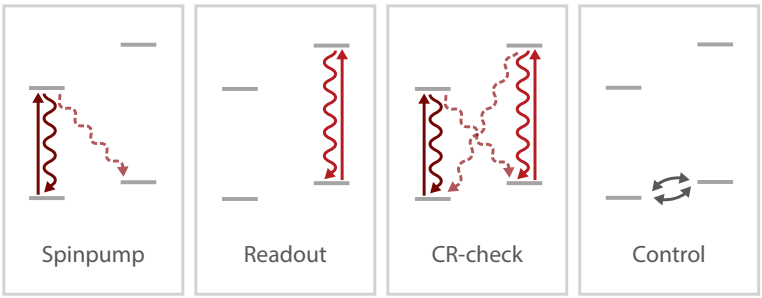

Figure 2.5: **Electron spin control.** Two ground and excited states are coupled through optical transitions. The two ground state levels are the used qubit levels. Initialization of the qubit is done by spin pumping, in which one level is excited with a laser until it decays to a level in which it will be initialized. Readout is performed by selectively exciting one of the ground states to the excited state. Detecting the fluorescence will tell that the qubit is in that state. A charge-resonance (CR) check is performed to ensure that the color center is in the right charge state and that the lasers are on resonance with the optical transitions. Both the spin pump and readout laser are used to prevent spin pumping to one of the two ground state levels. If the number of detected fluorescence photons surpasses a chosen threshold, the emitter is known to be on resonance. Control of the qubit is performed with microwave radiation, resonant with the splitting of the qubit states. Adapted from van de Stolpe [40].

second. This discussion only takes into account the direct single-phonon process. Other factors, such as electric or magnetic field noise, reduce the coherence as well.

Another approach of reducing the phonon occupation number is to increase the energy splitting Δ. Table 2.1 shows that the heavier elements from group-IV give rise to a bigger ground state splitting Δ_{GS}. The effect of this can be seen in Fig.2.4(a), where the $\Delta_{GS} = 50\,\text{GHz}$ of the SiV center demands dilution refrigerator temperatures of around 100 mK for a coherent electron spin, whereas the PbV center with $\Delta_{GS} = 3800\,\text{GHz}$ has the same spin coherence at around 10 K. Strain can also increase the ground state splitting as Eq.2.7 indicates, which has been used to increase the operation temperature of the SnV center [33]. Fig. 2.4(c) shows that a highly strained SnV center has longer coherence times at the same temperature as an unstrained one.

The last approach is to reduce the density of states of the phonons. This can be done by reducing the size of nanodiamonds to the point where the resonant phonons are not allowed anymore. The wavelength of the phonons is inversely proportional to the frequency, rendering this approach only feasible for the silicon-vacancy centers [39].

2.3. ELECTRON SPIN QUBIT

The electron spin of the NV and SnV center plays a central role in the experiments in this thesis. In this section we discuss the required single-qubit control and the optical interface required for remote entanglement protocols. We discuss the common properties of these the two centers and highlight their differences.

2.3.1. INITIALIZATION

The first step in our experiments is the initialization of the electron spin in a known state. We achieve this by spin pumping, in which a ground state is continuously excited until there is spontaneous decay to a different ground state, see Fig. 2.5. This is continued until the addressed ground state is emptied. The speed of the initialization depends on the decay probabilities from the excited state. This is characterized by the cyclicity, which is the average number of times the electron can be excited before it decays to a different state. If the used transition has a high cyclicity the spin pumping process will take longer than if the cyclicty is low.

For the NV center, we spin pump by exciting the ground states $|m_S = \pm 1\rangle$ until the electron spin is initialized into $|m_S = 0\rangle$. The optical transitions that couple the $m_S = \pm 1$ ground and excited states have a lower cyclicity[31] of ≈ 3 than the $m_S = 0$ transitions with ≈ 250[30,41]. This makes initializing in $|m_S = 0\rangle$ faster than in $|m_S = \pm 1\rangle$. We can initialize the electron spin within 1.5µs when using a laser power well above saturation power.

In the SnV center the situation is symmetric, so there is no preferred initial state. The $m_S = \pm 1/2$ transition can be used to initialize in the $m_S = \mp 1/2$ ground state. This requires more time as the transitions can have a cyclicity of 1200 in an aligned field, as was measured in Chapter 6.

2.3.2. READOUT

The readout of the electronic spin qubit can be achieved by exciting one of the ground states and detecting the fluorescence, as depicted in Fig. 2.5. In this thesis, we assign the qubit state $|0\rangle$ to the state that emits photons during readout. When we detect a single fluorescent PSB photon during readout, we assign the qubit to be in the $|0\rangle$ state. The $|1\rangle$ state is assigned to a dark state. For the readout we use the PSB photons as they are easy to separate from the resonant excitation light and give a higher signal-to-noise ratio.

In the NV center, the most cycling transition is the $|m_S = 0\rangle \leftrightarrow |E_x\rangle / |E_y\rangle$ and is therefore used as the readout transition. The average number of photons collected from the bright state is the cyclicity multiplied by the collection efficiency, which determines the readout fidelity in combination with the amount of noise counts[30].

In the SnV, there is no difference in reading out on the spin-up or down transition as they have a symmetric behavior. The high cyclicity in an aligned field is beneficial for a high readout fidelity[42].

2.3.3. CHARGE-RESONANCE CHECK

For the initialization, readout and the spin-photon interface, it is important that our emitter is in the right charge state and that the lasers are on resonance with the optical transitions. To achieve this we do a charge-resonance (CR) check, where we use both the readout and spinpump laser and check the amount of fluorescent photons n. If the number of detected fluorescence photons is high ($n_{\text{resonance}} \leq n$), we infer that the emitter is on resonance and continue to the experiment. For an intermediate number of photons ($n_{\text{charge}} \leq n < n_{\text{resonance}}$), we label it as the correct charge state but not on resonance, and we redo the CR check. This reshuffles the local charge environment and can probabilistically shift the emitter on resonance. For a low number of detected photons

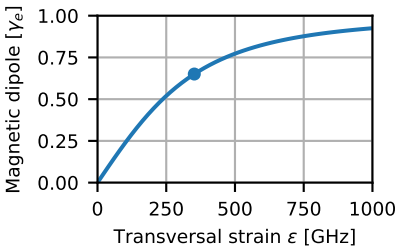

Figure 2.6: **MW driving efficiency of the SnV center.** Transversal strain ϵ in the diamond mixes the orbitals in the ground state lower branch. This creates overlap in the orbitals of the qubit subspace and makes MW driving more efficient. The effective magnetic moment is shown as a fraction of the magnetic moment of a free electron μ_e. For the simulation, Eq. 2.12 and 2.7 is used with $\lambda = 822\,\text{GHz}$[22]. The point at 352 GHz is the strain of the SnV center used in chapter 6.

($n < n_{\text{charge}}$), we apply a reset laser pulse in an attempt to reset the color center in its desired charge state, which we check by repeating the CR check.

For the NV center, the reset can be done resonantly by addressing the NV^0 optical transitions with a yellow 575 nm laser and off-resonantly, where we use a green 515 nm laser. When we use electric field tuning of the NV optical lines to get two emitters in resonance with each other, we can use the CR check to lock the emitter to the readout laser. We do this by modulating the DC voltage of the gates during a CR check, the generated error signal is then used to alter the DC voltages. During the electric field tuning, the reset has to be done resonantly as it requires much less power than the off-resonant approach. A high power would free up many electric charges that can shield the color center from the electric fields. The yellow laser is locked to the frequency of the emitter using the error signal generated during modulation of the yellow frequency during the resonant reset.

For the SnV center, the unwanted charge state is SnV^{2-}, which can be converted to the wanted charge state SnV^- by capturing an electron hole from the surroundings. This hole can be freed from di-vacancies using light from 400-600 nm[43]. For legacy reasons, we use the same 515 nm green laser as for the NV center experiments. The CR check is implemented in a similar way as for the NV experiments and works well to stabilize the charge state and emitter frequency[44].

2.3.4. CONTROL

The coherent control of the electron spin qubit is done using microwave (MW) driving of the spin[33,38]. The magnetic field of the MW radiation induces Rabi oscillations between the qubit states. By fitting a sine to these oscillations, we can calibrate π and $\pi/2$ pulses and the α pulse, which is required for the entanglement protocols, see Section 2.5.

In the NV center, the $|m_S = 0\rangle \leftrightarrow |m_S = \pm 1\rangle$ transition is used, where the sign depends on the chosen qubit subspace. The microwave radiation is applied through a golden stripline on the sample. The magnetic dipole has a magnitude of $\mu = \gamma_e$.

In the SnV center we drive the $|m_S = -1/2, e_-\rangle \leftrightarrow |m_S = 1/2, e_+\rangle$ with the MW radia-

tion. The MW pulses are delivered through a wire spanned over the diamond. We made earlier attempts to deliver the microwaves by golden striplines on the sample, but these gave considerable heating of the diamond. By physically separating the MW path from the diamond, the heating will only warm up the PCB, avoiding the detrimental effects of the direct heating[34].

In the SnV, there is a non-perfect overlap between the orbital parts of the qubit subspace, which are $|e_+\rangle$ and $|e_-\rangle$ for an unstrained emitter. Strain mixes these orbital parts as can be seen from Eq.2.3. The effective magnitude of the magnetic dipole is reduced compared to a free electron[21] to

$$\mu = \gamma_e \cdot 2\epsilon / \Delta_{\mathrm{GS}}, \tag{2.12}$$

as shown in Fig. 2.6. Therefore MW control of the SnV center requires strain in the diamond. Unstrained SnV centers can still be controlled by optical Raman schemes[45] but this method usually has lower control fidelities.

2.3.5. COHERENCE

During the experiments, it is important that the qubit state is preserved while no operations are performed. The timescale at which the eigenstates of the qubit, $|0\rangle$ and $|1\rangle$, are preserved is referred to as T_1, whereas a superposition is preserved for a time T_2^*. The coherence time of preserving the superposition can be extended with a Hahn echo, where quasi-static noise is canceled out, resulting in a T_2^{Echo}. This coherence time can usually be extended even more by applying more echo pulses in a method called dynamical decoupling (DD), resulting in the coherence time T_2^{DD}. In both the NV and the SnV center, the T_1 is much longer than T_2^{DD}, which makes the latter the relevant coherence time for storage of quantum information.

The T_1 time of the NV center can be longer than an hour. In our samples with naturally abundant carbon isotopes, we observe a typical $T_2^* \approx 2\,\mu\mathrm{s}$, which can be extended to over a second using dynamical decoupling[46].

In the SnV center, the coherence times are strongly correlated with temperature as described in section 2.2.2. Dynamical decoupling has been able to extend T_2^{DD} to 10 ms[22], but has so far been limited by control fidelity and heating of the MW pulses.

2.3.6. SPIN-PHOTON INTERFACE

Remote entanglement protocols require a coherent optical interface. For this, it is important that there are no decoherence processes on the timescale of the excited state lifetime, as discussed in section 2.2.2. Furthermore, we rely on the excited state to emit a single photon in the emission, see for further discussion Chapter 3.

The factors that determine how efficient the emitter is as a coherent single photon source are the quantum efficiency (η_{QE}), the Debye-Waller factor (η_{DW}) and the branching ratio (η_{BR}). The quantum efficiency is the ratio of the radiative decay paths compared to all the decay paths. The Debye-Waller factor is the ratio between the decay in the ZPL compared to all radiative decay. The lower branch of the excited state of the SnV center has two ZPL transitions to decay back to the ground state (C and D, see Fig. 2.3). Only the C transition is used for entanglement generation as this decays back directly into the

Center	η_{QE}	η_{DW}	η_{BR}	$\eta_{coherent}$
SiV	0.1-0.3 [10,24]	0.65 [49]	2/3 [19]	0.04-0.13
GeV	0.2 [50]	0.6 [51]	$\approx 2/3^{\dagger}$	0.08
SnV	0.8 [14]	0.57 [28]	0.8 [47]	0.36
PbV	-	0.34 [6]*	-	-
NV	>0.8 [52]	0.026 [53]	1	0.021-0.026

Table 2.2: Efficiency of the optical interface of the group-IV vacancy centers and the NV center. * The values with a star are based on ab initio calculations. † The branching ratio for the GeV has been estimated to be similar to the SiV and the SnV.

qubit subspace. The branching ratio describes the ratio of the preferred ZPL (C) transition to the decay into all the ZPL transitions (C and D). For the group-IV vacancy centers, this factor is around 2/3 [19,47]. The efficiency of the coherent transition can be calculated by the product of the factors

$$\eta_{coherent} = \eta_{QE}\,\eta_{DW}\,\eta_{BR} \tag{2.13}$$

The intrinsic factors of the NV and all group-IV vacancy centers are summarized in table 2.2, which shows that the SnV has a high $\eta_{coherent}$, especially compared to the NV center.

The reason we can still make entanglement even in the presence of these factors is that we use heralded entanglement schemes, which require the detection of a ZPL photon. In this way, only the rate, and not the fidelity, is affected by these incoherent processes. Usually, literature predominantly focuses on the Debye-Waller factor to compare color centers as it is the easiest factor to measure. However, the other factors are just as important for the rate of an entanglement protocol.

By filtering out the PSB and other ZPL photons, we are left with an effective two-level system. However, noise can couple to the defects and result in small perturbation of the optical transitions. These photons are not filtered out and will cause a reduced entangled state fidelity. Slow fluctuations show up as spectral diffusion and are mitigated by the CR check. Fast noise causes dephasing of the optical transition and reduces the indistinguishability of the photons, thereby impacting the fidelity of the entanglement [48]. This fast dephasing can't be mitigated by experimental methods and needs to be tackled during the fabrication of the samples.

2.3.7. OPTICAL TUNING

Entanglement protocols using spin-photon interfaces require the optical transitions to have the same frequency or a way to compensate for a known offset [54].

In the NV center, we use the electric field tuning to shift the optical transitions. We can usually achieve around 10 GHz of tuning, compared to a inhomogeneous linewidth of 100 GHz. Therefore, we preselect NV centers that are within the tuning range for the entanglement experiments in this thesis.

For future entanglement experiments with the SnV center a different approach needs to be taken for optical tuning. The SnV is first-order insensitive for electric fields, reducing the tuning to a few GHz at the expense of increased sensitivity to electric field

noise[55,56]. The SnV can be tuned by straining the diamond in a similar way as the electric field tuning in the NV center[57]. The photons can also be shifted in frequency after they are emitted by using an electric optic modulated[58] or during quantum frequency conversion[59]. A last approach would be to use very precise time detection of the photons to feedback on the acquired phase induced by the offset between the emitters[54].

2.4. NUCLEAR SPIN QUBIT

The diamond samples in this thesis are grown with naturally abundant carbon atoms, where 1.1 % is ^{13}C which has a nuclear spin-1/2, the rest is the spinless ^{12}C. These nuclear spins cause magnetic field noise, reducing the coherence times of the electron spin. However, they are also a very useful resource as they can be used as a quantum memory register.

The nuclear spins are coupled through the hyperfine interaction caused by the dipole-dipole interaction and the Fermi contact interaction. The hyperfine couplings in this thesis range from 30-300 kHz, which is lower than the inverse of the electron spin $1/T_2^* \approx 1$ MHz. Therefore, the electron spin coherence needs to be extended using dynamical decoupling to allow sensing and control of these weakly nuclear spins[60–62]. The two methods used for this are the dynamical decoupling (DD) method[60] and the dynamically decoupled radio frequency (DDRF) method[63], these methods are discussed in section 6.3 and 6.4.

In chapters 4 and 5, the DD method is used for the quantum memories of the quantum network. In chapter 6, the control over these ^{13}C-atoms is investigated using the electron spin-1/2 of the SnV center.

2.5. ENTANGLEMENT

In chapters 4 and 5 of this thesis, we use a single photon protocol to generate the entanglement between the two NV centers, which was proposed by Cabrillo et al.[64] and Bose et al.[65]. Chapter 3 of this thesis is a tutorial on remote-entanglement protocols. In this chapter, the basic principles are introduced, as well as the specifics of different implementations are discussed. In the nomenclature of Chapter 3, the protocol used in the three-node quantum network to generate the entangled links has a midpoint-detection topology with spin-photon emission logical building blocks. The photonic qubits are Fock-state encoded and use single photons. The spin-photon emission logical building blocks are implemented using the spontaneous emission physical building block.

To make it more concrete, we will go through the steps here to show how entanglement is generated between two NV centers in this thesis.

First, we initialize the electron spins of Alice (A) and Bob (B) in $|0\rangle$. With a MW control pulse, we generate a superposition

$$|\psi\rangle_{\mathrm{A/B}} = \sqrt{\alpha}\,|0\rangle + \sqrt{1-\alpha}\,|1\rangle\,, \tag{2.14}$$

for both Alice and Bob. The bright state population α can be used for a trade-off between the rate and fidelity of the entanglement generation, as we will see later. We can then entangle the spin state with a photon by selectively exciting the $|0\rangle$ to the excited

state with a short optical pulse, which performs a π pulse on the optical transition. After spontaneous decay, the emitted photon is entangled with the spin state:

$$|\psi\rangle_{A/B} = \sqrt{\alpha}\,|0\rangle\,|1\rangle_{ph} + \sqrt{1-\alpha}\,|1\rangle\,|0\rangle_{ph}\,. \tag{2.15}$$

The $|1\rangle_{ph}$ ($|0\rangle_{ph}$) indicates the presence (absence) of an emitted photon. The photons from both parties are sent to a beamsplitter, where the photons of Alice are routed to the input ports a and those of Bob to b. The beamsplitter then splits the photons to the output ports c and d[54]

$$|1\rangle_{ph,\,A,\,a} \rightarrow \frac{1}{\sqrt{2}}\left(|1\rangle_{ph,\,c} + |1\rangle_{ph,\,d}\right) \tag{2.16}$$

$$|1\rangle_{ph,\,B,\,b} \rightarrow \frac{1}{\sqrt{2}}\left(|1\rangle_{ph,\,c} - |1\rangle_{ph,\,d}\right) \tag{2.17}$$

The state of the complete system after the beamsplitter is

$$\begin{aligned}
&(1-\alpha)\ |1\rangle_A\,|1\rangle_B\ |0\rangle_{ph,\,c}\,|0\rangle_{ph,\,d}\\
&+\sqrt{(\alpha-\alpha^2)/2}\ (|0\rangle_A\,|1\rangle_B + |1\rangle_A\,|0\rangle_B)\ |1\rangle_{ph,\,c}\,|0\rangle_{ph,\,d}\\
&+\sqrt{(\alpha-\alpha^2)/2}\ (|1\rangle_A\,|0\rangle_B - |0\rangle_A\,|1\rangle_B)\ |0\rangle_{ph,\,c}\,|1\rangle_{ph,\,d}\\
&\frac{\alpha}{\sqrt{2}}\ |0\rangle_A\,|0\rangle_B\ (|2\rangle_{ph,\,c}\,|0\rangle_{ph,\,d} - |0\rangle_{ph,\,c}\,|2\rangle_{ph,\,d}).
\end{aligned} \tag{2.18}$$

At port c and d we detect the photons with non-number resolving detectors, which means that we cannot discriminate between $|1\rangle_{ph}$ and $|2\rangle_{ph}$. Moreover, we are in the high loss regime with only a 4×10^{-4} probability of detecting a photon. By heralding the detection of a photon on the c or d detector, we project the density matrix in

$$\rho = (1-\alpha)\,|\Psi^{\pm}\rangle\,\langle\Psi^{\pm}| + \alpha\,|00\rangle\,\langle 00|\,, \tag{2.19}$$

where $|\Psi^{\pm}\rangle = \frac{1}{\sqrt{2}}\left(|01\rangle \pm e^{i\theta}\,|10\rangle\right)$ are the desired Bell states. The sign depends on whether detector c or d detected a photon. The phase θ depends on the phase of the excitation lasers and the optical path length difference between the emitter and the detectors[66]. We keep the phase constant by stabilizing the path length and using the same laser for excitation, ensuring that the phase is constant. This is an important requirement; without knowing or stabilizing the phase θ, we would end up with a mixed state[67]. There is a probability α that we project both our emitters in the bright $|0\rangle$ state, which limits the fidelity of the single click protocol to $F = 1-\alpha$. The success probability $2\alpha p_{det}$ is proportional to α and the detection probability p_{det}. The linear dependence on the detection probability is the big advantage of using the single click protocol compared to double click protocols where the rate scales quadratically with the detection probability[68].

2.6. DEVICES

All experiments in this thesis are performed on color centers in chemical-vapor-deposition (CVD) grown high-purity IIa diamonds, which are grown along the $\langle 100\rangle$ crystal orientation, grown by Element Six.

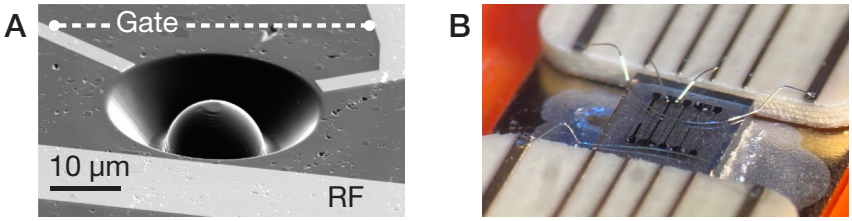

Figure 2.7: (a) Diamond sample with a solid immersion lens (SIL). Similar samples are used in the experiments of chapters 4 and 5. The SIL is fabricated around a pre-characterized NV center. A golden stripline is utilized for the delivery of radiofrequency pulses. Golden gates are used for electric field tuning of the optical transitions of the NV center. Adapted from Pfaff and Bernien [2,3]. (b) The diamond sample used in chapter 6 is surrounded by two printed circuit boards (PCB) for MW delivery. Golden straplines were fabricated for MW control of the SnV centers but caused too much heating to be used. Bondwires were hand-bent to get the MW field close to the diamond without bringing the wire in contact with the diamond sample. This thermal isolation reduced the heating of the diamond considerably and facilitated the MW control of the electron spin.

The NV centers occur naturally in these diamonds. The diamond has been cut along the ⟨111⟩ crystal orientation to align the optical dipole of the NV center properly with the crystal surface. The NV centers were pre-characterized at room temperature in search of NV centers that are aligned with the ⟨111⟩ direction. NV centers with a strongly coupled ^{13}C nuclear spin (>1 MHz) are excluded as this can reduce the control fidelities. A solid immersion lens (SIL) is milled by a focussed ion beam around the selected NV centers. The SIL improves the collection of photons emitted by the NV center by reducing total internal reflection in the diamond. An Al_2O_3 anti-reflection coating is added to reduce laser reflections. A golden stripline and golden electronic electrodes are patterned by electron beam lithography. The stripline is used to deliver the MW control pulses and the electrodes are used for electric field tuning of the optical transitions. Figure 2.7(a) is a scanning electron microscope image of a sample. The stripline and the gates are then wirebonded to a printed circuit board (PCB) to connect the electronic cables in the cryostat to it. More details on the NV center sample preparation can be found in these references [5,69].

SnV centers do not occur naturally in the high-purity diamond. Therefore, tin atoms are implanted with ion implantation. The implantation creates considerable crystal damage, including vacancies in the lattice. By annealing the diamond at 1100 °C in vacuum, the vacancies become mobile and can migrate through the crystal. A vacancy and a tin atom can then form a tin-vacancy center. A detailed description of the SnV sample fabrication process can be found in reference [18]. For the sample used in chapter Chapter 6, golden striplines were fabricated for MW control of the electron spin. However, the MW pulses heated the diamond so much that the SnV centers lost their coherence during MW control. By using a bondwire that was not in contact with the diamond we were able to thermally isolate the MW delivery from the SnV center, which drastically reduced the heating and allowed for electron spin coherence above a millisecond, as will be discussed in chapter 6.

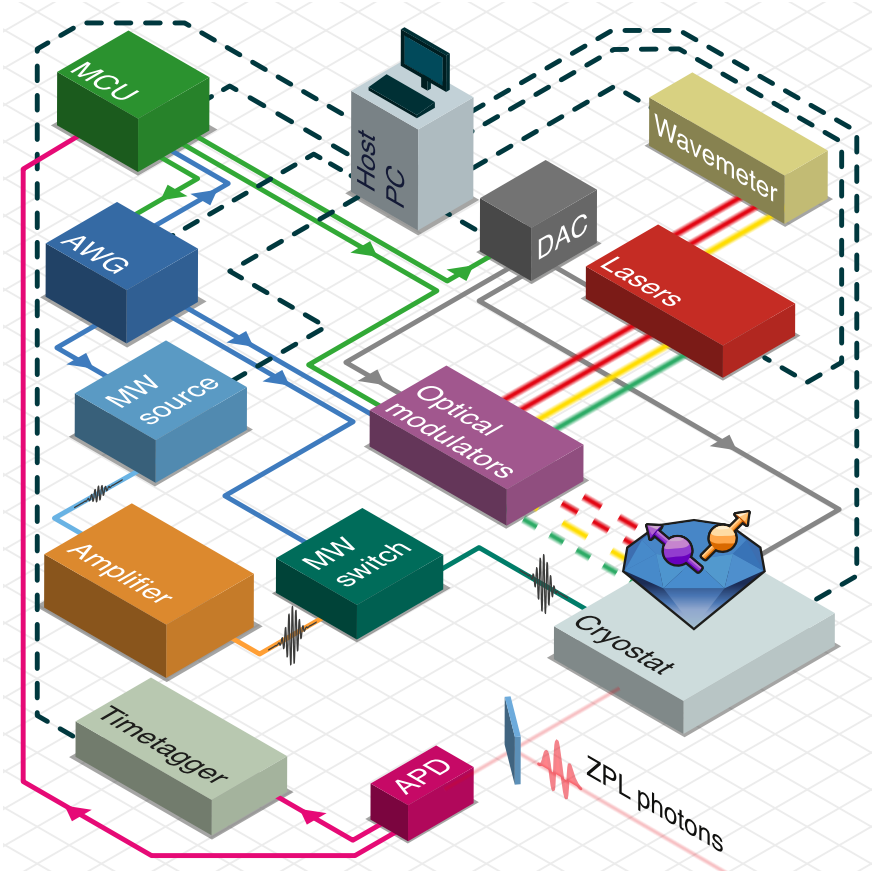

Figure 2.8: **Experimental setup of a single quantum network node.** The sample with the NV center and surrounding nuclear spins are cooled to 4 K in a cryostat. The host PC orchestrates the experiment and stores the measured data. It employs a microcontrol unit (MCU) for microsecond real-time control of the setup and an arbitrary waveform generator (AWG) for nanosecond control sequences. The NV center is controlled in two ways: MW and laser pulses. The AWG sends the MW pulses with IQ modulation to the MW source. The MW source upconverts the pulses to the required GHz qubit frequency, after which they are amplified. A MW switch improves the attenuation and reduces noise when no pulses are generated. The laser pulses are shaped by acoustic-optic modulators (AOMs) with a rise time of 25 ns and electric-optic modulators (EOM) with a rise time of 200 ps. These modulators are controlled by the MCU and the AWG. The frequency of the lasers is stabilized by a PID loop on the host PC, using a wavemeter as a reference. The electric field tuning of the optical transitions of the NV center is controlled by a DC signal generated by a digital-to-analog converter, which is controlled by the MCU. The fluorescence of the NV center is split into ZPL and PSB photons. The ZPL photons are sent to a beamsplitter for entanglement generation. An avalanche photodiode detects the PSB photons, which are used for the readout of the electron spin. The detection events are recorded with sub-nanosecond resolution on a timetagger and microsecond resolution on the MCU. Adapted from Pompili [70].

2.7. EXPERIMENTAL SETUPS

The experiments on the three-node network in chapters 4 and 5 have three independent setups. The individual nodes all have a configuration as depicted in Fig. 2.8. A more detailed description of the optical part of the setups can be found in Fig. 4.6.

The experiments in chapter 6 with SnV centers are controlled by a setup that is very similar to the one described in Fig. 2.8. The main differences are the lasers and cryostat that are used. The cryostat for the NV center experiments cools the sample to 4 K, whereas the cryostat in the SnV center experiments can cool the sample down to 0.4 K. A description of that setup can be found in section 6.9.1.

REFERENCES

[1] M. W. Doherty *et al.*, *The nitrogen-vacancy colour centre in diamond,* Physics Reports The Nitrogen-Vacancy Colour Centre in Diamond, **528**, 1 (2013).

[2] W. Pfaff, *Quantum Measurement and Entanglement of Spin Quantum Bits in Diamond.*, Ph.D. thesis, Delft University of Technology, Delft (2013).

[3] H. Bernien, *Control, Measurement and Entanglement of Remote Quantum Spin Registers in Diamond*, Ph.D. thesis, Delft University of Technology, Delft (2014).

[4] H. Bernien *et al.*, *Heralded entanglement between solid-state qubits separated by three metres,* Nature **497**, 86 (2013).

[5] N. Kalb, *Diamond-Based Quantum Networks with Multi-Qubit Nodes*, Ph.D. thesis, Delft University of Technology, Delft (2018).

[6] G. Thiering and A. Gali, *Ab Initio Magneto-Optical Spectrum of Group-IV Vacancy Color Centers in Diamond,* Physical Review X **8**, 021063 (2018).

[7] U. Wahl *et al.*, *Direct Structural Identification and Quantification of the Split-Vacancy Configuration for Implanted Sn in Diamond,* Physical Review Letters **125**, 045301 (2020).

[8] A. E. Rugar *et al.*, *Quantum Photonic Interface for Tin-Vacancy Centers in Diamond,* Physical Review X **11**, 031021 (2021).

[9] A. Faraon, C. Santori, Z. Huang, V. M. Acosta and R. G. Beausoleil, *Coupling of Nitrogen-Vacancy Centers to Photonic Crystal Cavities in Monocrystalline Diamond,* Physical Review Letters **109**, 033604 (2012).

[10] A. Sipahigil *et al.*, *An integrated diamond nanophotonics platform for quantum-optical networks,* Science **354**, 847 (2016).

[11] M. K. Bhaskar *et al.*, *Quantum Nonlinear Optics with a Germanium-Vacancy Color Center in a Nanoscale Diamond Waveguide,* Physical Review Letters **118**, 223603 (2017).

[12] E. Neu *et al.*, *Single photon emission from silicon-vacancy colour centres in chemical vapour deposition nano-diamonds on iridium,* New Journal of Physics **13**, 025012 (2011).

[13] D. D. Sukachev *et al.*, *Silicon-Vacancy Spin Qubit in Diamond: A Quantum Memory Exceeding 10 ms with Single-Shot State Readout,* Physical Review Letters **119**, 223602 (2017).

[14] T. Iwasaki *et al.*, *Tin-Vacancy Quantum Emitters in Diamond,* Physical Review Letters **119**, 253601 (2017).

[15] S. Ditalia Tchernij *et al.*, *Single-Photon-Emitting Optical Centers in Diamond Fabricated upon Sn Implantation,* ACS Photonics **4**, 2580 (2017).

[16] M. E. Trusheim *et al.*, *Transform-Limited Photons From a Coherent Tin-Vacancy Spin in Diamond,* Physical Review Letters **124**, 023602 (2020).

[17] R. Debroux *et al.*, *Quantum Control of the Tin-Vacancy Spin Qubit in Diamond,* Physical Review X **11**, 041041 (2021).

[18] M. Pasini, *Nanophotonics with Diamond Color Centers,* Ph.D. thesis, Delft University of Technology (2024).

[19] C. J. Hepp, *Electronic Structure of the Silicon Vacancy Color Center in Diamond*, Ph.D. thesis, school Universität des Saarlandes, Saarlandes (2014).

[20] S. Meesala *et al.*, *Strain engineering of the silicon-vacancy center in diamond,* Physical Review B **97**, 205444 (2018).

[21] A. M. Stramma, *The Tin-Vacancy Centre in Diamond: A Coherent Spin-Photon Interface for Quantum Network Nodes,* Ph.D. thesis, Cambridge University (2024).

[22] I. Karapatzakis *et al.*, *Microwave Control of the Tin-Vacancy Spin Qubit in Diamond with a Superconducting Waveguide,* Physical Review X **14**, 031036 (2024).

[23] E. Neu *et al.*, *Low-temperature investigations of single silicon vacancy colour centres in diamond,* New Journal of Physics **15**, 043005 (2013).

[24] J. Becker and C. Becher, *Coherence Properties and Quantum Control of Silicon Vacancy Color Centers in Diamond,* physica status solidi (a) **214**, 1700586 (2017).

[25] T. Iwasaki *et al.*, *Germanium-Vacancy Single Color Centers in Diamond,* Scientific Reports **5**, 12882 (2015).

[26] P. Siyushev *et al.*, *Optical and microwave control of germanium-vacancy center spins in diamond,* Physical Review B **96**, 081201 (2017).

[27] E. A. Ekimov *et al.*, *Germanium–vacancy color center in isotopically enriched diamonds synthesized at high pressures,* JETP Letters **102**, 701 (2015).

[28] J. Görlitz *et al.*, *Spectroscopic investigations of negatively charged tin-vacancy centres in diamond,* New Journal of Physics **22**, 013048 (2020).

[29] P. Wang *et al.*, *Transform-Limited Photon Emission from a Lead-Vacancy Center in Diamond above 10 K,* Physical Review Letters **132**, 073601 (2024).

[30] L. Robledo *et al.*, *High-fidelity projective read-out of a solid-state spin quantum register,* Nature **477**, 574 (2011).

[31] N. Kalb, P. C. Humphreys, J. J. Slim and R. Hanson, *Dephasing mechanisms of diamond-based nuclear-spin memories for quantum networks,* Physical Review A **97**, 062330 (2018).

[32] K. D. Jahnke *et al.*, *Electron–phonon processes of the silicon-vacancy centre in diamond,* New Journal of Physics **17**, 043011 (2015).

[33] X. Guo *et al.*, *Microwave-Based Quantum Control and Coherence Protection of Tin-Vacancy Spin Qubits in a Strain-Tuned Diamond-Membrane Heterostructure,* Physical Review X **13**, 041037 (2023).

[34] S. Niese, *Measuring Microwave Pulse Induced Heating Using Decoherence of the Tin-Vacancy Spin in Diamond*, MSc Thesis, Delft University of Technology (2022).

[35] L. J. Rogers *et al.*, *All-Optical Initialization, Readout, and Coherent Preparation of Single Silicon-Vacancy Spins in Diamond,* Physical Review Letters **113**, 263602 (2014).

[36] B. Pingault *et al.*, *Coherent control of the silicon-vacancy spin in diamond,* Nature Communications **8**, 15579 (2017).

[37] Y.-I. Sohn *et al.*, *Controlling the coherence of a diamond spin qubit through its strain environment,* Nature Communications **9**, 2012 (2018).

[38] E. I. Rosenthal *et al.*, *Microwave Spin Control of a Tin-Vacancy Qubit in Diamond,* Physical Review X **13**, 031022 (2023).

[39] M. Klotz *et al.*, *Prolonged Orbital Relaxation by Locally Modified Phonon Density of States for the Si V - Center in Nanodiamonds,* Physical Review Letters **128**, 153602 (2022).

[40] G. L. van de Stolpe, *Quantum Sensing in Diamond and Silicon Carbide: Mapping Spins and Taming Charges*, Ph.D. thesis, Delft University of Technology (2024).

[41] O. S. M. Ubbens, *A Unified Model to Predict Excited State Cyclicity of Nitrogen Vacancy Centres in Diamond*, MSc Thesis, Delft University of Technology (2022).

[42] E. I. Rosenthal *et al.*, *Single-Shot Readout and Weak Measurement of a Tin-Vacancy Qubit in Diamond,* Physical Review X **14**, 041008 (2024).

[43] J. Görlitz *et al.*, *Coherence of a charge stabilised tin-vacancy spin in diamond,* npj Quantum Information **8**, 45 (2022).

[44] J. M. Brevoord *et al.*, *Heralded initialization of charge state and optical-transition frequency of diamond tin-vacancy centers,* Physical Review Applied **21**, 054047 (2024).

[45] J. Arjona Martínez *et al.*, *Photonic Indistinguishability of the Tin-Vacancy Center in Nanostructured Diamond,* Physical Review Letters **129**, 173603 (2022).

[46] M. H. Abobeih *et al.*, *One-second coherence for a single electron spin coupled to a multi-qubit nuclear-spin environment,* Nature Communications **9**, 2552 (2018).

[47] Y. Herrmann *et al.*, *Coherent Coupling of a Diamond Tin-Vacancy Center to a Tunable Open Microcavity,* Physical Review X **14**, 041013 (2024).

[48] F. W. Sun and C. W. Wong, *Indistinguishability of independent single photons,* Physical Review A **79**, 013824 (2009).

[49] A. Dietrich *et al., Isotopically varying spectral features of silicon-vacancy in diamond,* New Journal of Physics **16**, 113019 (2014).

[50] R. Høy Jensen *et al., Cavity-Enhanced Photon Emission from a Single Germanium-Vacancy Center in a Diamond Membrane,* Physical Review Applied **13**, 064016 (2020).

[51] Y. N. Palyanov, I. N. Kupriyanov, Y. M. Borzdov and N. V. Surovtsev, *Germanium: A new catalyst for diamond synthesis and a new optically active impurity in diamond,* Scientific Reports **5**, 14789 (2015).

[52] I. P. Radko *et al., Determining the internal quantum efficiency of shallow-implanted nitrogen-vacancy defects in bulk diamond,* Optics Express **24**, 27715 (2016).

[53] D. Riedel *et al., Deterministic Enhancement of Coherent Photon Generation from a Nitrogen-Vacancy Center in Ultrapure Diamond,* Physical Review X **7**, 031040 (2017).

[54] T. Legero, T. Wilk, A. Kuhn and G. Rempe, *Time-resolved two-photon quantum interference,* Applied Physics B **77**, 797 (2003).

[55] S. Aghaeimeibodi, D. Riedel, A. E. Rugar, C. Dory and J. Vučković, *Electrical Tuning of Tin-Vacancy Centers in Diamond,* Physical Review Applied **15**, 064010 (2021).

[56] L. De Santis, M. E. Trusheim, K. C. Chen and D. R. Englund, *Investigation of the Stark Effect on a Centrosymmetric Quantum Emitter in Diamond,* Physical Review Letters **127**, 147402 (2021).

[57] G. Clark *et al., Nanoelectromechanical Control of Spin–Photon Interfaces in a Hybrid Quantum System on Chip,* Nano Letters **24**, 1316 (2024).

[58] C. M. Knaut *et al., Entanglement of nanophotonic quantum memory nodes in a telecom network,* Nature **629**, 573 (2024).

[59] A. Stolk *et al., Telecom-Band Quantum Interference of Frequency-Converted Photons from Remote Detuned NV Centers,* PRX Quantum **3**, 020359 (2022).

[60] T. H. Taminiau *et al., Detection and Control of Individual Nuclear Spins Using a Weakly Coupled Electron Spin,* Physical Review Letters **109**, 137602 (2012).

[61] S. Kolkowitz, Q. P. Unterreithmeier, S. D. Bennett and M. D. Lukin, *Sensing Distant Nuclear Spins with a Single Electron Spin,* Physical Review Letters **109**, 137601 (2012).

[62] N. Zhao *et al., Sensing single remote nuclear spins,* Nature Nanotechnology **7**, 657 (2012).

[63] C. E. Bradley *et al., A Ten-Qubit Solid-State Spin Register with Quantum Memory up to One Minute,* Physical Review X **9**, 031045 (2019).

[64] C. Cabrillo, J. I. Cirac, P. García-Fernández and P. Zoller, *Creation of entangled states of distant atoms by interference,* Physical Review A **59**, 1025 (1999).

[65] S. Bose, P. L. Knight, M. B. Plenio and V. Vedral, *Proposal for Teleportation of an Atomic State via Cavity Decay,* Physical Review Letters **83**, 5158 (1999).

[66] S. L. N. Hermans *et al.*, *Entangling remote qubits using the single-photon protocol: An in-depth theoretical and experimental study,* New Journal of Physics **25**, 013011 (2023).

[67] P. C. Humphreys *et al.*, *Deterministic delivery of remote entanglement on a quantum network,* Nature **558**, 268 (2018).

[68] S. D. Barrett and P. Kok, *Efficient high-fidelity quantum computation using matter qubits and linear optics,* Physical Review A **71**, 060310(R) (2005).

[69] B. Hensen, *Quantum Nonlocality with Spins in Diamond*, Ph.D. thesis, Delft University of Technology, Delft (2016).

[70] M. Pompili, *Multi-Node Quantum Networks with Diamond Qubits*, Ph.D. thesis, Delft University of Technology (2021).

3

REMOTE-ENTANGLEMENT PROTOCOLS FOR QUBITS WITH PHOTONIC INTERFACES

H. K. C. Beukers*, M. Pasini*, H. Choi*, D. Englund, R. Hanson and J. Borregaard

Generating entanglement between distant quantum systems is at the core of quantum networking. In recent years, numerous theoretical protocols for remote entanglement generation have been proposed, of which many have been experimentally realized. Here, we provide a modular theoretical framework to elucidate the general mechanisms of photon-mediated entanglement generation between single spins in atomic or solid-state systems. Our framework categorizes existing protocols at various levels of abstraction and allows for combining the elements of different schemes in new ways. These abstraction layers make it possible to readily compare protocols for different quantum hardware. To enable the practical evaluation of protocols tailored to specific experimental parameters, we have devised numerical simulations based on the framework with our codes available online.

The results of this chapter have been published in PRX Quantum **5**, 010202 (2024).
* Equally contributing authors

3.1. INTRODUCTION

Remote entanglement of quantum systems is a vital component in quantum networks and computing[1–3]. Since remote stationary qubits cannot interact directly, a “flying qubit" is needed to mediate the interaction and generate entanglement. Photons offer versatility, as they can transfer quantum information over long distances with low-loss optical fibers, operate at room temperature, and be easily detected with single-photon detectors. In a photon-mediated entanglement protocol, stationary qubits interact selectively with photons, usually via an optical transition, resulting in the entanglement between the photon and the stationary qubit. This entanglement between photons and spins can be used to create entanglement between two distant qubits. The entanglement generated can have high fidelity even in the presence of photonic loss, as photon detection can be used to herald a successful entanglement attempt[4–10], as long as sources of false heralding are limited. These individual entanglement links between quantum nodes can then be combined to distribute the entanglement through a quantum network[11]. This distributed entanglement has been used to perform unconditional quantum teleportation between nodes without a direct optical link[12]. Overall, these technologies pave the way toward network-based quantum computing[13], entanglement-based quantum communications[14], distributed quantum sensing, and long-distance interferometry[15].

Photon-mediated remote entanglement of stationary qubits has been demonstrated in numerous quantum systems, including trapped ions[16], neutral atoms[17,18], semiconductor quantum dots[19,20], and color centers in diamond[21,22]. Different demonstrations rely on different entanglement generation protocols, where the choice of protocol implementation is dictated by the features or limitations of the experimental platform. As a result, the implementation of the entanglement protocol is often tailored to specific hardware.

Here, we present a theoretical framework for comparing and understanding different photon-mediated remote-entanglement protocols (REPs). The modular framework consists of four layers, with modules assembled by connecting the output of one to the input of another. The advantage of this framework is that it gives insights into the common features of remote-entanglement protocols. Moreover, it allows easy modification of the modules to compare a protocol with different types of quantum hardware or to rearrange the quantum hardware and test different protocols with the same hardware (which is done in Section 3.8). Dedicated simulations of entanglement generation for a given experiment usually lack this flexibility.

We start by explaining the high-level idea and how the first layer (the “logical building block and topology” layer) can describe REPs in a generic manner. Next, we introduce the encoding and physical building block layers, which link the protocol to specific hardware. Finally, the quantum optical modeling layer provides a detailed and quantitative description of the physical building blocks. Our focus is on qubits realized with a single spin in atomic or solid-state systems, but the framework can incorporate other

systems such as the spin wave in an atomic ensemble and optomechanical resonators, as well as superconducting qubits. These single entangled links between qubits could later be extended to multi-pin encoding for error correction for fault-tolerant quantum networks[23].

We have released a simulation software package titled QuREBB (Quantum Remote-Entanglement Building Blocks) which is available in an accompanying GitHub repository (Sec. 3.7)[24]. This package offers a comparison of three exemplary entanglement protocols. For each protocol, we review every layer, from the idealized version to its practical implementation. As an example, we assume that the protocols are implemented with silicon-vacancy color centers in diamond nanophotonic cavities. This serves as a tutorial on how to effectively employ our theoretical framework for the construction and quantitative analysis of the performance of the protocol. The modular structure of our software implementation mirrors the framework, enabling the implementation of complex quantum systems from the physical to the network levels. Users can easily add new physical devices or logical units without interfering with existing functionality. Our "named quantum object" simplifies the tensor operations of different quantum subsystems by indexing them by names instead of numerical values.

Note that in each layer, we have descriptions of photons, spins, and spin-photon interfaces. In this work, we elaborate spin-photon interfaces in the most detail for their critical role in the creation of entanglement. We also systematically analyze the photonic and spin operations focusing on the construction of REPs. We refer readers interested in more details on spin or photon operations to Refs.[25–27].

3.2. REMOTE-ENTANGLEMENT-PROTOCOL FRAMEWORK

Figure 3.1 shows our modular framework for REPs. The framework consists of four layers, each becoming more specific and detailed in terms of hardware. Throughout the paper, we refer to stationary qubits as spins for convenience.

In the first layer, we choose the topology of the protocol and construct it using logical building blocks (LBBs) (Fig. 3.1(a)). The topology, i.e., how the photons travel between the nodes, determines the generic high-level quantum circuit and the LBBs are the idealized quantum operations, such as the spin-photon interface, the photon source, and the photodetector. The LBBs act on the spin qubit or the photonic qubit, or both. This layer simplifies and categorizes REPs, giving insight into the entanglement generation. The REP topology is classified into detection-in-midpoint, sender-receiver, and source-in-midpoint protocols[28], as shown in Fig.3.1(a). We use the sender-receiver topology as an example in the figure.

In the second layer, we choose the qubit encoding, in particular the photonic encoding which is the most relevant for the REP: Fock state, polarization, dual rail, frequency encoding, or time-bin encoding, the latter is shown in Fig.3.1(b). This layer translates the abstract photonic and spin qubits into a specific implementation in the system.

Entanglement link
a)
Logical Building Blocks and Topology
Sec 5.3
SPIN-PHOTON INTERFACE
Mode Mixing
Detection
SINGLE PHOTON SOURCE
PHOTON PAIR SOURCE
b)
Encoding
Sec. 5.4
Spin Init.
Ph
Gate
Measure
|E⟩
|L⟩

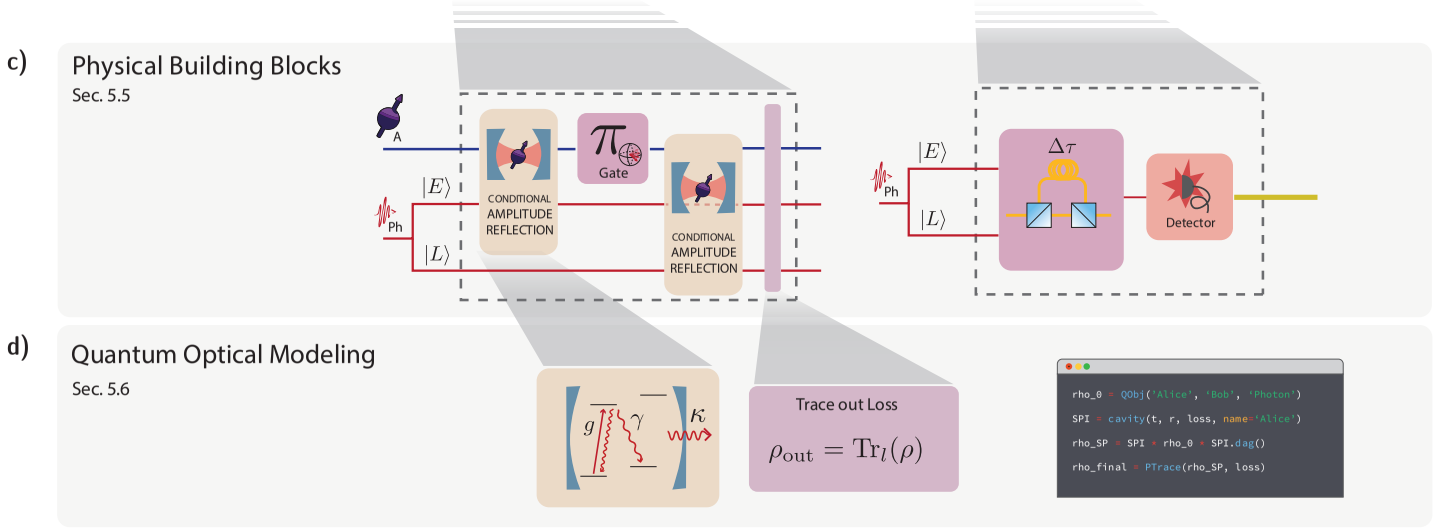

Figure 3.1: **An overview of remote-entanglement-protocol modular framework. Entanglement link** - The objective of entanglement protocols is to entangle two remote spins (purple) where the entanglement is created by photons (red). (a) **Logical Building Blocks and Topology** (Sec. 3.3) - The topology for remote entanglement generation is deconstructed in logical building blocks (LBBs). From left to right, we consider three main REP topologies: the detection-in-midpoint, sender-receiver, and source-in-midpoint topologies. (b) **Encoding** (Sec. 3.4)- The encoding layer chooses the basis for the photonic qubits and the levels for the spin qubit. We illustrate the time-bin encoding of sender-receiver topology with spin-photon gates. (c) **Physical Building Blocks** (Sec. 3.5) - The physical building blocks (PBBs) are the quantum channels describing the operations of the physical systems including imperfections. This layer shows the REP at the physical level. The first panel describes the construction of spin-photon gates with an overcoupled cavity-QED system for state conditional amplitude reflection. The second panel shows the implementation of a measurement of the time-bin qubit in the X basis, using a Mach-Zehnder interferometer (see Figs 3.3 and 3.4). (d)**Quantum optical modeling** (Sec. 3.6) - This layer models the hardware used in the PBB. In this example the relevant parameters for the PBBs (e.g. the state-dependent reflection coefficient, $r_{|0\rangle,|1\rangle}$) can be calculated from physical variables (e.g. the spin-cavity coupling rate, g) using a detailed quantum optical model. We implemented these descriptions in a software package publicly available on GitHub (Sec. 3.7). Sec. 3.8 shows the simulation and benchmarking results with our framework.

In the third layer, we get closer to the hardware and implement the protocol in physical building blocks (PBBs). We implement the LBB with the desired hardware and encoding in PBBs as shown in Fig. 3.1(c). This requires the idealized quantum operations of the LBB to be compiled to the available PBBs. For example, in Figure 3.1, the spin-photon interface block is implemented as three PBBs, namely, the reflection of the early time bin, a single-qubit rotation, and a reflection of the late time bin. The PBBs are a native operation for the hardware and are modeled as a quantum channel.

The final layer is quantum optical modeling, where the exact physics of PBBs are modeled. This layer is added to reuse the quantum modeling of a system for different PBBs. For example, a critically coupled or an overcoupled cavity both require the same quantum optical modeling but are used in different PBBs.

3.3. LOGICAL BUILDING BLOCKS AND TOPOLOGY

The first layer of our framework is the choice of protocol topology and its description in terms of logical building blocks (LBBs). The operation of the protocol topology can be described by the circuit diagrams (Fig. 3.2(a)). LBBs are high-level quantum operations in a quantum network that can be chained together to form an entanglement protocol, such as photon sources, spin-photon emission, and photon detection. In Fig. 3.2(b), we show how LBBs compare to elementary circuit diagrams, and in Fig. 3.2(c), how they can be used to construct different protocol topologies. The LBBs are not hardware-specific, as the practical details on what generates this operation and the dependence on physical parameters are described in the physical building block layer.

3.3.1. TOPOLOGY OF THE PROTOCOL

In this work, we consider three topologies for REPs, described in Fig. 3.1(a); namely, detection-in-midpoint (ingoing), sender-receiver, and source-in-midpoint (outgoing) [28].

In the detection-in-midpoint topology, both end points generate spin-photon entanglement. The photons are then measured in the middle, in an entangled basis using a Bell-state measurement. This projects the two spins in an entangled state. The detection-in-midpoint topology has an advantage in its simplicity. At its most basic, this topology requires only photon emission from the spins, beam-splitter interference of the photons, and single-photon detections at the central station. Efficient spin-photon interfaces such as optical cavities, while helpful, are not necessary to get high-fidelity entanglement. Furthermore, the time overhead for classical communication is reduced by half compared to the other topologies, since the end points communicate solely with the detection point, eliminating the need for direct communication between them.

In the sender-receiver topology, the first end point generates spin-photon entanglement, and the photon is then sent to the second end point, where it interacts with the spin, such that entanglement between the spins is achieved. This interaction can be a gatelike behavior (e.g., by using an optical cavity) after which the photon is

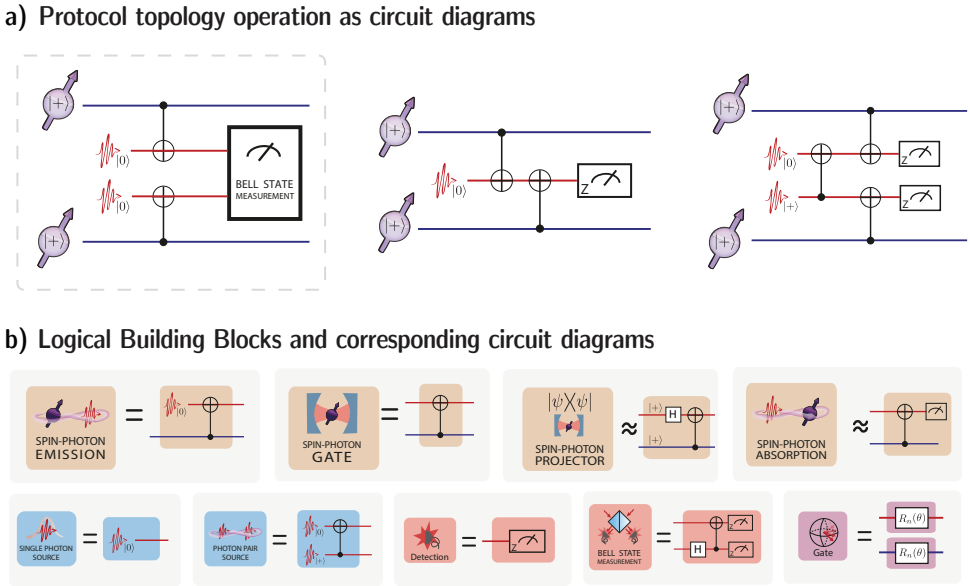

Figure 3.2: **The remote-entanglement-protocol topologies and logical building blocks (LBBs).** (a) The three available topologies for REP — detection-in-midpoint, sender-receiver topology, and source-in-midpoint — and depiction of their operation with circuit diagrams. Here we use the notation $|+\rangle = (|0\rangle + |1\rangle)/\sqrt{2}$. (b) The LBBs available to construct the REP. The circuit description outlines their idealized operations, which the user can match with the diagrams in (a). For the spin-photon projector and the spin-photon absorption, an approximate gate diagram is given. This can be used to see how they can be used in the quantum circuits in (a). The exact gate description for these LBBs would be a projector operation and a SWAP gate. (c) Three different implementations of the midpoint detector, as an example. In this case, the spin-photon emission, spin-photon gate, and spin-photon projector are used as the spin-photon interface, respectively.

measured. Alternatively, the photon can be absorbed by the spin-photon interface in which case this topology matches the workings of quantum state transfer[17,29]. The sender-receiver topology does not necessitate an intermediary station for the spins to become entangled. However, the classical communication time for the heralding signal is twice as long compared to a detection-in-midpoint topology, as it needs to travel the full distance as opposed to half of it.

The source-in-midpoint topology has an entangled photon source in the middle that sends these photons to the end points. The end points have an entangling interaction between the spin and the photon, after which the photons are measured and the spins will be projected into an entangled state. The source-in-midpoint topology is useful in satellite-assisted entanglement protocols. The ground-to-satellite channel (uplink) has a higher overall loss than the satellite-to-ground channel (downlink). Phenomenologically, this phenomenon is collectively referred to as the "shower-curtain effect" of the atmosphere[30]. In particular, the diffraction and deflection by air turbulence are more severe in the early stage of transmission than in the late stage on the dispersed beam. Moreover, practical factors such as limited onboard optics on the satellite result in a larger pointing error in the uplink than in the downlink[31].

Remote entanglement between two stationary qubits has been experimentally realized with sender-receiver topology using trapped atoms embedded in optical cavities[32], and with detection-in-midpoint using several platforms including nitrogen-vacancy (NV) centers in diamond[21], quantum dots[19], trapped ions[16], and atoms[18].

3.3.2. SPIN-PHOTON-INTERFACE BLOCKS

The key logical building block of an REP is the spin-photon-interface block since this is the interaction between the stationary and flying qubits. In this work, we focus on REPs that are heralded, using single-photon detection to screen out photon-loss errors. Absorption-based spin-photon interfaces generally allow heralding only through additional energy levels in the stationary qubit[17]. Thus, we give only a cursory treatment of absorption-based spin-photon interfaces. We identify four main categories of spin-photon-interface blocks, as follows.

Spin-Photon Emission. A spin-photon-emission block creates a photonic qubit entangled with the qubit state of the spin by emission through a higher-level excited state. This is commonly achieved by the emission of a photon after spin-dependent excitation with a laser pulse. As an example, optical excitation of a spin in a superposition state will emit a photon depending on the spin state, $\frac{1}{\sqrt{2}}(|0\rangle_s + |1\rangle_s) \xrightarrow{\text{laser}} \frac{1}{\sqrt{2}}(|0\rangle_s + |\text{excited}\rangle_s) \rightarrow \frac{1}{\sqrt{2}}(|0\rangle_s|0\rangle_p + |1\rangle_s|1\rangle_p)$, where the subscript s (p) labels the state of the spin (photonic mode) and $|1\rangle_s$ is the bright state of the spin that is excited and emits a single photon. Alternatively, the system can be brought to an excited state in which two different decay channels lead to two different spin states. The emitted photons can, e.g., have a different polarization entangled with the spin state. Various optically active quantum systems

have realized spin-photon emission through spin-dependent optical excitation or decay to different spin states, including NV centers in bulk diamonds[33], neutral atoms[34], trapped ions[16], and quantum dots[19].

Spin-Photon Gate. A spin-photon-gate block is a conditional gate between the spin and a photon. Depending on the exact implementation, this will act as a controlled-Z or controlled-X rotation on the photonic qubit. Spin-photon-gate blocks require a strong coupling of photons with the stationary qubit, and this is realized by confining the light with photonic cavities or waveguides. In some cases, the need for strong coupling can be relaxed at the expense of a nondeterministic but heralded gate operation. Examples of practical implementation of spin-photon-gate LBB are trapped atoms in Fabry-Perot cavities[32], SiV centers in diamond photonic crystal cavities[35], and quantum dots in photonic crystal waveguides[36].

Spin-Photon Projector. A spin-photon-projector block selects only specific states from the input state. With the right input state and the right selection, this results in spin-photon entanglement. This method is sometimes referred to as "carving"[37]. An example is where the input state is in a superposition for both the photon and spin qubit (note that the $|0\rangle_p$ is referring to the qubit state, not the vacuum state), $\frac{1}{2}(|0\rangle_s|0\rangle_p + |0\rangle_s|1\rangle_p + |1\rangle_s|0\rangle_p + |1\rangle_s|1\rangle_p)$, and the spin-photon interface has a photonic loss that depends on both the spin and photon state. In this example, a spin-photon interface that has photon loss for the photon in the scenarios $|0\rangle_s|1\rangle_p$and $|1\rangle_s|0\rangle_p$ would create, with a 50% chance, the state $\frac{1}{2}(|0\rangle_s|0\rangle_p + |1\rangle_s|1\rangle_p)$. So heralding no photon loss by photon detection ensures that only (an entangled) part of the incoming state is selected. This approach has been used for entangling two neutral atoms in a cavity[37] and with silicon-vacancy centers in diamond photonic crystal cavities for the demonstration of an asynchronous Bell-state measurement between two photons[35]. The downside is that it has intrinsic losses as it rejects part of the incoming state rather than performing a deterministic gate.

Spin-Photon Absorption. The spin-photon absorption block transfers the photon state to the spin state. The block often implements a strong interaction using a cavity[38] or a spin ensemble[39]. The absorption of a photon from lossy channels results in the vacuum field and does not herald the entanglement by photodetection, resulting in low fidelities. Instead, spin-photon absorption can be useful if used carefully. For example, one can read the spin state after the absorption, effectively constructing a heralded protocol. Alternatively, one can make a high optical-depth spin ensemble absorb a single photon from a photon-pair source and use the other photon from the source[40]. If the channel loss is negligible, the spin-photon absorption can directly implement quantum state transfer without classical communications[41].

3.3.3. PHOTON BLOCKS

Photon source. Photon source blocks can be considered as the initialization of photonic qubits. High-rate entanglement generation with photon sources requires the de-

terministic generation of single photons with high-efficiency quantum emitters[42,43] or photon-pair generation followed by the heralding[44]. For high fidelities, single photons need to be indistinguishable, which is often challenging in a solid-state environment[45–47]. The distinguishability problem is considered in the quantum optical modeling layer.

Photon-pair sources. Photon-pair sources provide entangled photon pairs, which can be used for REPs with source-in-midpoint topology. This can be understood as two photons initialized in an entangled state. Midpoint on-demand entangled photon-pair sources have been proposed based on correlated photon decay from quantum emitters[28], mode mixing of single photons[48] or multiplexing spontaneous pair sources[49]. We note that at the LBB level, photon-pair sources output perfect Bell states in the logical basis, $|0\rangle$ and $|1\rangle$. The photonic basis of the states is determined in the photonic encoding layer (Sec. 3.4) and imperfections, such as probabilistic photon-pair generation, are detailed in the quantum optical modeling of PBBs (Sec. 3.6).

Photon measurement. Generally in the REPs, the photon is still entangled with the spins before detection. For example in the sender-receiver topology (middle circuit of Fig 3.2(a)), the state before the measurement is

$$\frac{1}{2}\left(|0\rangle_p\left(|00\rangle_{AB}+|11\rangle_{AB}\right)+|1\rangle_p\left(|01\rangle_{AB}+|10\rangle_{AB}\right)\right), \tag{3.1}$$

where A and B refer to the two separate spins. This means that the photon needs to be measured on a basis that preserves entanglement between the spins — this is in the Z basis for this situation. In this measurement of the photonic qubit, the outcome heralds a different entangled state on the spins; in this example, measurement of $|0\rangle$ for the photon heralds $\frac{1}{\sqrt{2}}(|00\rangle+|11\rangle)$. One can choose to feed back on one of the spins to always generate the same entangled state or use the measurement outcome in postprocessing.

Bell-State Measurement. Photonic Bell-state measurement projects the state of two photons into one of four Bell states, $|\Psi^{\pm}\rangle = |01\rangle \pm |10\rangle$, $|\Phi^{\pm}\rangle = |00\rangle \pm |11\rangle$. When it is required to have a quantum operation between two photons — e.g., in the detection-in-midpoint topology — the Bell state measurement can be used. This is advantageous, as in linear optics the photons do not interact. This can be achieved with a beam splitter and photon measurement after the beam splitter. The Bell-state measurement projects two photons into an entangled state. It is usually used for entanglement swapping of two spin-photon-entangled pairs to yield entangled spins. Note that the Bell-state measurement with linear optics is probabilistic, with only a 50% chance of succeeding. However, with auxiliary single photons, one can boost the success probability to 75%[50]

Photon gates. Gates on the photonic qubit are essential in some entanglement protocols. How easily these can be implemented depends completely on the photonic encoding used and this is discussed in Sec.3.5.1.

3.3.4. SPIN BLOCKS

Operations on the spin such as initialization, gates, and measurements are their own logic building blocks. They are the standard set of initialization, qubit gates, and qubit measurement[27]. In some cases, entanglement protocols require the spin to be initialized and put in a superposition for each entanglement attempt.

3.3.5. OTHER LOGICAL BUILDING BLOCKS

The blocks discussed earlier are the logical operations required for the working of the REPs. On top of these there are processes that in an ideal scenario do not do anything to the photonic and spin qubits. Their implementation will, however, add noise; e.g., a photonic loss in a fiber or quantum frequency conversion of the photons. These blocks do not change the logical states of qubits in the ideal situation, so they appear as identity operators in the circuit diagrams of the LBB layer and they can be modeled in detail as PBBs. For example, a photonic loss block can be added, which takes care of the losses in the system: this does not change the ideal operation of the protocol but will impact the rate and fidelity in the simulations (which is implemented in the PBB).

For a long-distance entanglement generation, it is advantageous to use photons in the telecom band to improve photon transmission using ultralow-loss fibers. As the physical platforms used for spin-photon interfaces have limited access to those wavelengths, quantum frequency conversion[51,52] is often used to match the photon wavelength of the spin-photon interface with the desired communication band. In this case, one can model and add a frequency-conversion block to protocols.

3.3.6. COMBINING TOPOLOGY AND LOGICAL BUILDING BLOCKS

In a given topology, a user can implement different combinations of LBBs. Figure 3.2(c) demonstrates the detection-in-middle topology implemented with the spin-photon emission, gate, and projector logical building blocks.

3.4. ENCODING

In Sec 3.3, the ideal operation of an REP has been outlined. To translate this to the quantum hardware, the abstract spin and photonic qubits need to be encoded in the desired and available spin and photon levels. In this section, the photonic encodings are discussed in detail, as these are very general. The spin encoding is much more platform dependent and therefore is discussed more briefly.

3.4.1. PHOTONIC ENCODING

Optical photons are the best option to send quantum information over a long distance for remote entanglement. Quantum information can be encoded into a photon using various degrees of freedom: amplitude (Fock-state encoding), timing (time-bin encoding), spatial modes (dual-rail encoding), polarization (polarization encoding), and frequency (frequency encoding) (see Fig. 3.3). In the literature, dual-rail encoding can also refer to general two-mode encodings; e.g., time-bin and frequency encoding. In this tu-

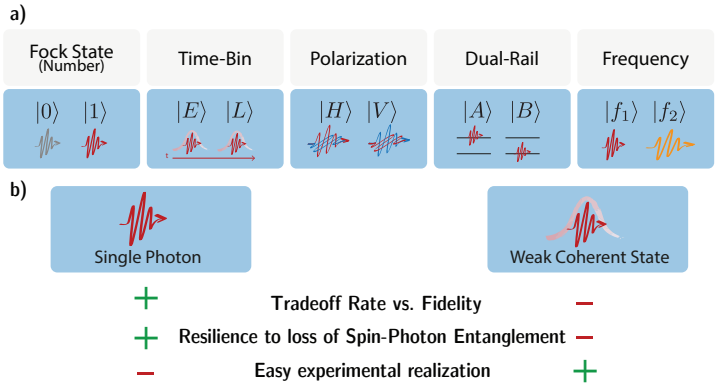

Figure 3.3: **The encoding of photonic qubits.** (a) The basis states of photonic encoding. (b) In every basis choice, the basis can be implemented with single photons or those can be approximated with a weak coherent state.

torial, we will use the term "dual-rail" exclusively for the encoding into spatial modes. Each of the encoding schemes has two states acting as the qubit basis. In general, the other degrees of freedom are kept the same to simplify the operations and allow for the interference of encoded photons for a Bell measurement, which requires indistinguishable photons unless precise measurement of conjugate variable is available and the measurement result is mutually unbiased (for frequency-mismatching case see, e.g., Refs.[53,54]).

PHOTON NUMBER OF THE PHOTONIC QUBIT

All encoding except Fock-state encoding have a single photon in the basis states. The advantage is that the loss of photons can be detected. The entanglement protocols discard the cases with photon loss for high-fidelity entanglement generation, so-called heralded entanglement[21,22].

As high-efficiency indistinguishable single-photon sources are technologically demanding, the single photons are frequently replaced with weak coherent sources (attenuated lasers). They have Poisson statistics with a small mean photon number, well below one. The wave function of a weak coherent state is dominantly vacuum ($|0\rangle$), with a small fraction of single-photon state ($|1\rangle$) and an even smaller fraction of two-photon states ($|2\rangle$):

$$|\alpha\rangle \propto |0\rangle + \alpha|1\rangle + \frac{\alpha^2}{\sqrt{2}}|2\rangle + \ldots \tag{3.2}$$

where α is the complex amplitude and $|\alpha|^2 \ll 1$ is the mean photon number. The vacuum component $|0\rangle$ reduces the rate of entanglement generation, since it cannot herald entanglement through photodetection. The $|2\rangle$ state reduces the fidelity of the spin-photon entangled state, as the loss of one of the two photons leaks information to the environment. There is, therefore, a trade-off between rate and fidelity for choosing

α, when using weak coherent states as approximate single-photon states in heralded-entanglement-generation protocols.

ENCODING BASIS

Fock-state encoding. Fock-state encoding stores quantum information in the photon-number eigenstates with zero photons and one photon ($|n=0\rangle$ and $|n=1\rangle$, where n is the photon number). $n>1$ states are not considered in the encoding due to technical difficulties in preparing those states. However, the problem is that loss takes one qubit state to the other and therefore directly impacts the fidelity (compared to other encodings where loss can be detected as the vacuum state is not part of the encoding space). The relative phase of the two bases evolves as the optical phase, so the optical path length needs to be stabilized or at least known for correction. Despite these complications, Fock-state encoding has a significant advantage in that Bell measurement is possible with the detection of a single photon, while the other encodings need the detection of two single photons. The success probability of a heralded protocol scales linearly with the probability of photon loss if only single-photon detection is needed, while it scales quadratically for two-photon detection (in all but Fock-state encoding). In cases in which photon losses are significant, due to long-distance transmission or devices with low efficiency, the linear scaling given by Fock-state encoding can provide a key advantage over other encodings.

Time-bin encoding. Time-bin encoding counteracts the drawbacks of Fock-state encoding at the expense of the requirement of two-photon detection for Bell measurement. Two time bins (early and late) are chosen to encode the photons. Photon loss can always be detected, in the ideal case of detectors with no dark counts, as this would result in no detection of photons. Therefore, the fidelity of protocols with time-bin encoding is not compromised, as long as dark counts are negligible with respect to the signal but the rate decreases. Another advantage is relaxed phase stability: the optical phases should be stable on the time scale of the spacing of the time bins. However, arbitrary qubit operations are hard to implement but the encoding is quite robust against noise sources such as dispersion or birefringence in the transmission medium. Therefore, this encoding is mostly used in sending quantum information over long fibers and not in situations that require full control over the photonic qubit state[55].

Polarization. The polarization encoding defines the qubit state in two perpendicular polarizations: horizontal (H) and vertical (V), diagonal (D) and anti-diagonal (A), or left (L) and right (R) circular. Single-qubit gates are easily implemented, as all single-qubit rotations can be performed with wave plates (see Sec. 3.5.1). Moreover, polarization encoding requires phase stability between the two polarization bases. This stability can be readily attained in free space. In single-mode optical fibers, the polarization is preserved but temperature and stress fluctuations in the fiber can rotate the polarization: stabilization and calibration are therefore required. Polarization-maintaining (PM) fibers decouple the two different polarization bases by using orthogonal modes with different effective indices. This preserves only the amplitude in each basis and not the phase relation between them. In remote-entanglement experiments using polarization encoding,

single-mode fibers are usually used[32,56].

Dual-rail encoding. The dual-rail encoding uses two spatial modes for photons. This encoding has one significant drawback, as it requires twice the physical elements. The phase between two separate paths is extremely stable on the integrated photonic device; however, in fiber or free space, the requirements are comparable to those for phase stabilization for Fock-state encoding. This encoding can implement operations that are hard to perform in another encoding because path separation gives the most flexibility to use optical elements separately in two modes (see Sec. 3.5.1).

Note that in some literature the term “dual-rail encoding” is used to refer to a single excitation out of two orthogonal bosonic degrees of freedom, encompassing spatial modes, polarizations, time bins, frequencies, wave vectors, and orbital angular momentum. In these instances, “Fock-state encoding" is referred to as “single-rail encoding"[55]. In this tutorial, we use “dual-rail encoding" specifically for the single excitation in two spatial photonic modes and specify the degree of freedom in other cases.

Frequency encoding. In frequency encoding, photonic qubits utilize two distinct frequency modes as basis states. Single-qubit gates in frequency encoding require nonlinear optical devices such as electro-optic modulators that suffer from low efficiencies. To measure frequency-encoded photons, the frequency separation of two frequency modes must exceed the spectral resolution of a grating or a cavity. One can also directly detect a frequency-encoded photon in a time-separated manner by using group-velocity dispersion in optical fibers[57] or Bragg gratings[58]. Note that group velocity-dispersion does not convert the frequency encoding to time-bin encoding. Even if a photon of one frequency is time shifted relative to a photon of another frequency, the two photons still occupy distinct frequency bins.

3.4.2. SPIN ENCODING

Besides the photonic qubit, the spin qubit also needs to be encoded in the physical states of the system. The encoding of the stationary qubit depends on the system at hand. An important requirement for the spin-photon interface is that at least one of the states has an efficient and stable optical transition. Besides, there should be ways to initialize, control, and read out with high fidelity. Lastly, the coherence time of the qubit should be long enough to bridge at least the time of flight of the photons to the midpoint or another quantum node, as this allows for heralded-entanglement generation, which is required for applications beyond point-to-point quantum key distribution[3]. Examples of the levels that are used to encode the spin qubit in various systems are the electronic spin for NV centers in diamond[21] or cold atoms[17], spin-orbital hybrid states for group-IV centers in diamond[35], hyperfine levels in trapped ions[16], and angular momentum states in quantum dots[19].

3.5. PHYSICAL BUILDING BLOCKS

After the REP topology is constructed with LBBs and the encoding is chosen, we can construct the REP with the physical systems that are available. The LBBs are ideal circuit elements acting on the qubits of photons and spins, while the PBBs are physical processes on the optical modes (e.g., early and late) and spin states. Therefore, the PBB layer translates the abstract operations to allow hardware implementation.

For example, to generate spin-photon entanglement, a spin-photon-interface LBB can be composed of several PBBs that perform operations on different photonic states. As shown in Fig. 3.1, a spin-photon-interface LBB with time-bin encoding consists of a conditional-amplitude-reflection PBB in early mode, a qubit-rotation PBB on the spin, and a conditional-amplitude-reflection PBB acting again on the late mode.

3.5.1. PHOTON OPERATIONS

The PBBs of the photonic operations are described in Fig. 3.4. Polarization and dual-rail encoding are convenient with regard to the implementation of quantum gates and are often used in linear optics quantum computation[59]. The photonic PBBs, of which we describe photonic loss, mode mixing, and photodetection in Sec. 3.6.3, are often studied in standard quantum optics textbooks.

MEASUREMENT

Measurement in all photon encodings is done by means of single-photon detectors. Fock-state encoding can be measured directly. However, a single-photon state ($|1\rangle$) after photon loss cannot be distinguished from the vacuum state ($|0\rangle$). Time-bin encoding requires time-resolving detectors. Polarization and frequency-encoded qubits cannot be detected directly and are usually converted to dual-rail (see Sec 3.5.1) where both modes are then measured with a separate detector.

PHOTON GATES

An arbitrary gate can be made with the combination of rotations around the X and Z axes of the qubit Bloch sphere. For a Z rotation, the phase between the qubit basis states needs to be changed. Also, this is directly the phase that needs to be stable for the use of the encoding. For an X rotation, the operation needs to change the basis states. This can be readily implemented for polarization encoding with waveplates. For a Fock state encoding, this is not trivial and has not been demonstrated to the best of our knowledge, and the time-bin needs to be converted to dual-rail. In dual-rail encoding a Mach-Zehnder interferometer is used.

BELL-STATE MEASUREMENT

The Bell-state measurement can be performed with linear optics with a 50% success probability[55]. It can only detect the $|\Psi^{\pm}\rangle = |01\rangle \pm |10\rangle$ state, as it requires the detection of both modes after the beam splitter. The $|\Phi^{\pm}\rangle = |00\rangle \pm |11\rangle$ state cannot be detected as measuring the same modes after the beam splitter reveals both their individual states. The Bell-state measurement is done by using a beam splitter for mode mixing and two

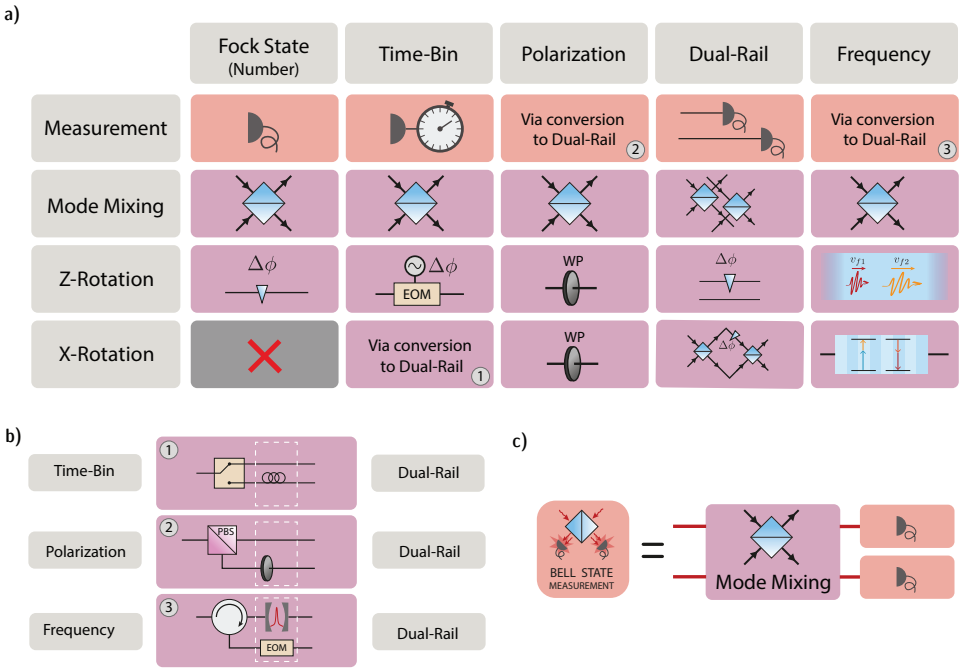

Figure 3.4: **The photonic PBBs for the different photon encodings.** (a) Each basis has its own implementation of the quantum operations, but some do not have natural implementation without converting them to a different basis (usually to dual-rail). The *measurement* in the computational basis is performed with a single-photon detector. For time-bin encoding, it needs to be time resolved. For polarization and frequency, the qubit is usually converted to and detected in dual-rail encoding. Two-qubit gates are implemented using *mode mixing* with a beam splitter. The mode mixing lets two photonic qubits interfere with each other. For a *Z rotation* the phase between the two basis states needs to be altered. This is implemented in Fock-state encoding with a delay line, in time-bin encoding with an electric optic modulator (EOM) shifting one time-bin, in polarization encoding with a wave plate, in dual-rail encoding with delaying one of the lines, and in frequency encoding with a dispersive medium. The *X rotation* requires changing the photon between the two eigenstates, which is not feasible for Fock-state encoding, goes via dual-rail for time-bin encoding, can be easily implemented with a wave plate in polarization encoding, and uses a Mach-Zehnder interferometer for dual-rail and nonlinear processes for frequency encoding. (b) The conversion between the basis that can be used for the easier physical implementation of quantum operations. Fock-state encoding cannot easily be converted. All other encodings can be converted to and from dual-rail. For this, one element adds a new encoding (switch, PBS, or cavity or grating), and another removes the old encoding (in the white dashed box, a delay, wave plate, or frequency-shifting EOM). The latter can be omitted if the photon is detected afterward, as no indistinguishability is required. (c) The LBB of Bell-state measurement can be constructed using mode mixing and single-photon detection in each of the encodings.

detectors to tell which of the two detectable entangled states ($|\Psi^+\rangle$ or $|\Psi^-\rangle$) has been measured (Fig 3.4(c)).

CONVERSION BETWEEN ENCODINGS

Figure 3.4(b) shows the possible conversion between the encodings. In practice, dual-rail encoding is a versatile encoding that can be converted directly into the others and vice versa. For the conversion, one needs the separation of the photons in different modes into different spatial paths (e.g. using a polarizing beam splitter) and compensating elements to remove the character from the previous encoding (e.g. using a wave plate). The compensation can be omitted if one does not need indistinguishable photons after conversion; e.g., if the photons are detected directly.

The conversion between time-bin encoding and dual-rail is used often as this is the only viable way to perform X gates on the photonic qubit. In this case, the switch is often replaced by a beam splitter by accepting the 50% loss, as this reduces the complexity of the experiment and as the time delay between time bins can be short compared to the switching time. When using a beam splitter, there are also possible optical paths involving the unwanted output ports that cause the photon to be delayed and fall outside of the defined time-bin window; however, these cases can be discarded upon measurement using time-resolving detectors.

3.5.2. SPIN OPERATIONS

The exact PBB spin operations depend considreably on the chosen spin encoding. We discuss the most common ones below.

INITIALIZATION

Initialization of the spin is usually achieved in one of the following ways. When a nonperfectly cycling optical transition is present, which means that under continuous driving there is a (small) probability of spontaneously decaying to a different state than the ones involved in the transition, it is possible to use optical pumping[60]. By laser excitation of the noncycling transition, the system will eventually decay to the desired qubit state and remain there, as this is not driven by the laser. In systems with a very good readout, it can be advantageous to read and generate the desired initialized state with a control pulse conditional on the readout result[35]. If one wants to prepare the system in a superposition a quantum gate can be used. Alternatively, one can prepare a state by stimulated Raman adiabatic passage (STIRAP)[61].

CONTROL

Quantum control of the qubit is usually achieved by direct Rabi driving of the transition. This is usually a microwave [25] or optical field but it can also be done with other coupled fields, such as an oscillating strain field[62]. If the transition frequency is experimentally hard to reach or is only weakly allowed, two driving fields in a lambda configuration can be used, in which the qubit states are coupled to a common excited state. By driving both transitions, a coherent rotation on the qubit can be achieved with a two-photon Raman transition[63]. In some systems, mostly based on solid-state implementations, coupling to

fluctuating magnetic fields in the surrounding environment, such as nuclear spin baths, can affect the coherence of spin-based qubits. With the control in place, it is usually possible to extend the coherence time of the spin qubit in these platforms by means of dynamical decoupling[64].

READOUT

The qubits that we are considering have a good spin-photon interface, which allows for optical readout of the spin. The spin can be read out by the detection of the state-dependent fluorescence. For high fidelity of this readout, a high collection efficiency and good cyclicity of the optical transition are needed. A good cyclicity results in a transition that can be driven for a long time, generating as many photons as possible before the qubit decays to an unwanted state[65], while a high collection efficiency allows for measuring enough photons for a high-fidelity readout with a shorter driving time and lower probability of the qubit changing state. When a conditional-phase-reflection PBB (see Sec. 3.5.3) is used, the spin state can be read out by phase readout[66].

AUXILIARY QUBITS

To go beyond a single entangled link, it is essential to have auxiliary qubits for storage of quantum states in the system[67]. This is required for, e.g., entanglement distillation[68–71] and entanglement swapping in repeater schemes. The available auxiliary qubits are highly dependent on the system and can go from nuclear spins in solid-state emitters to different species of atoms or ions in those systems. The most difficult requirement to fulfill for these qubits is often that they need to be resilient for entanglement attempts on the spin qubit, which typically involves a lot of initialization and control pulses. This can result in a competition between the coupling required for two-qubit gates and the isolation required for resilience during entanglement attempts[60].

3.5.3. SPIN-PHOTON INTERFACE

The spin-photon interface is an essential part of the entanglement protocols, as it connects the stationary and flying qubits. We discuss five different spin-photon-interface PBBs (see Fig 3.5). The first three are suitable to make spin-photon entanglement for a spin-photon-emission LBB: spontaneous emission, coherent scattering, and Raman scattering. These PBBs are all controlled with a classical laser control pulse and the output is a single photon (or a weak coherent state depending on the exact implementation) entangled with the spin. When the interaction between the light and the emitter is very strong, we can get a reflection of a single-photon or weak coherent state in which the amplitude or phase of the reflected light is controlled by the spin state. The conditional-amplitude-reflection or conditional-phase-reflection PBB can be used to build the LBB of a spin-photon projection or a spin-photon gate.

SPONTANEOUS EMISSION

The conceptually most simple way to implement a spin-photon interface is the emission-based spin-photon interface, where the spin-photon entanglement is generated through spontaneous emission. In this case, a short high-power optical π pulse is used to excite the system to the excited state. If this excitation or the spontaneous

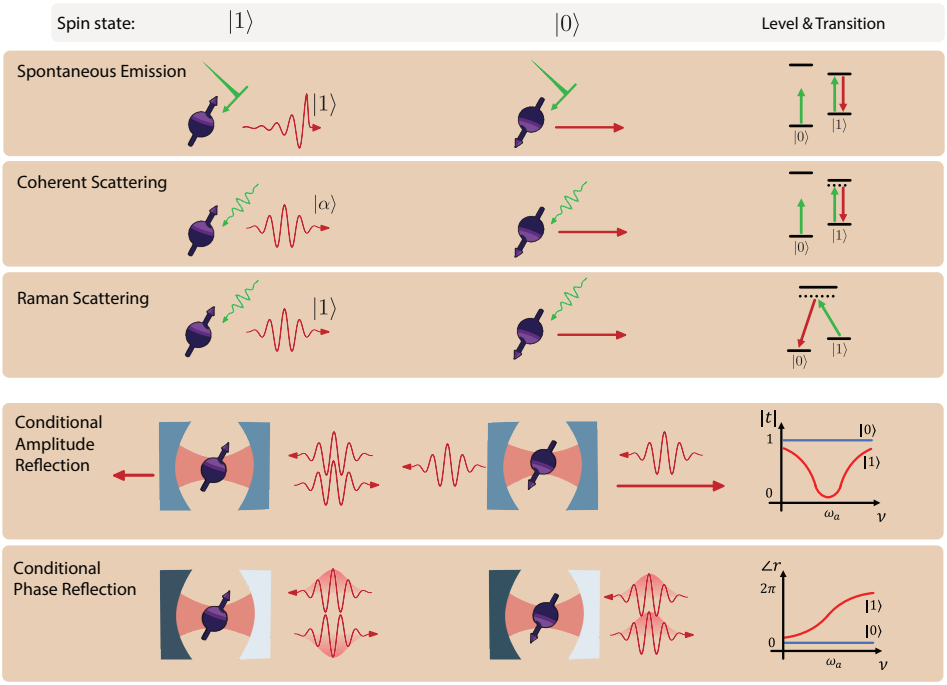

Figure 3.5: **Spin-photoninterface PBBs**. State-selective optical transitions as spin-photon interfaces. For the *spontaneous-emission* spin-photon interface, the excitation pulse is much shorter than the optical lifetime and excites the $|1\rangle$ transition: it will emit a single photon by spontaneous emission. The *coherent-scattering* spin-photon interface scatters a weak pulse from the $|1\rangle$ optical transition, resulting in a photon with a weak coherent state. The *Raman-scattering* spin-photon interface is excited with a pulse but as the optical excitation ends up in a different spin state only a single photon is emitted. In the **conditional-phase-reflection** spin-photon interface a photon is reflected from the cavity with a coupled spin. For $|1\rangle$, the phase is flipped and therefore entangled with the spin state. An overcoupled cavity is used for this purpose. In the *conditional-amplitude-reflection* spin-photon interface, the photon is transmitted or reflected depending on the spin state. A critically coupled cavity is used for this case.

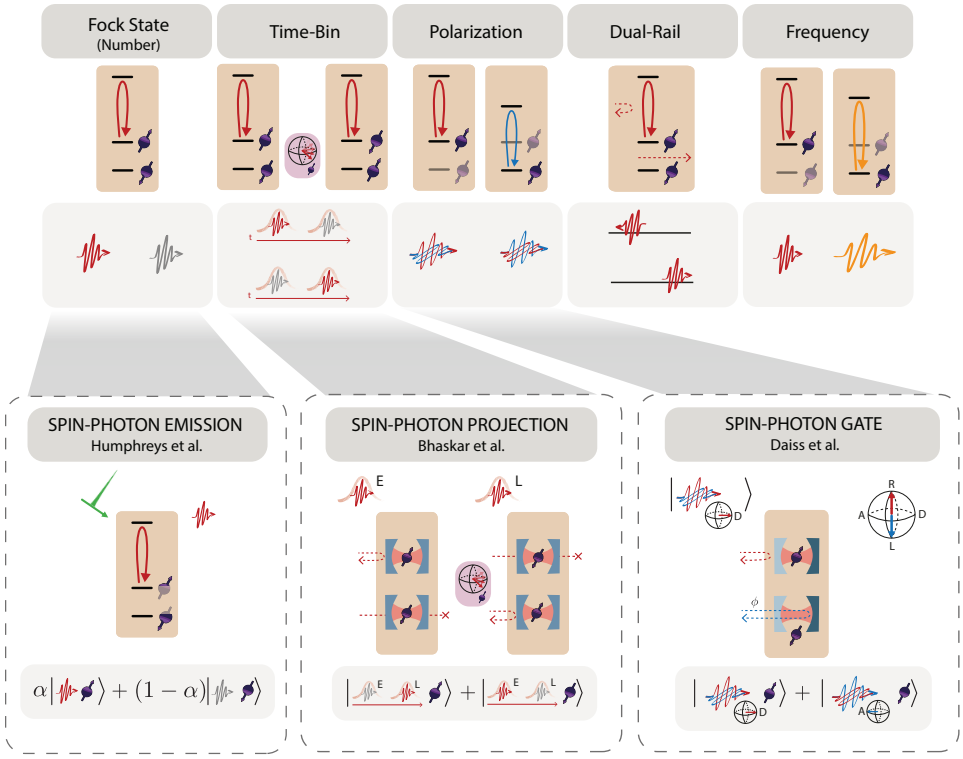

Figure 3.6: **Spin-photon interface PBBs**. A schematic example of how a spin-photon-interface LBB can be implemented in the different photonic encodings, starting from a spin-photon PBB. Below are examples of experimental realizations of the emission [22], projection [35], and gate [32] LBBs in different encodings.

emission depends on the spin state we can create spin-photon entanglement.

With this PBB, we can create a spin-photon-emission LBB. For Fock-state encoding we prepare the spin in a superposition and apply a spin state-dependent optical π pulse such that the presence of a photon is entangled with only one of the spin states. For the time-bin encoding, we initialize the spin state in an equal superposition and apply the excitation twice with a π-pulse of the spin in the middle. For the polarization or frequency encoding, both spin states need to have an optical transition with a different polarization or frequency. The entanglement can either be generated by initializing the spin in an equal superposition and exciting both transitions or by relying on an optical transition that has an equal chance of decaying to either state, correlated with a different polarization or frequency. An example of polarization encoding can be found in Ref. [72].

The photon coming from such a process will have a frequency and exponential temporal shape determined by the optical properties of the emitter. The line width is determined by the lifetime and the inhomogeneously broadened line width and the indistinguishability are determined by the dephasing processes of the optical transition. This requires favorable properties of the emitter to make the photons suitable for entanglement generation. The optical π pulse needs to be much shorter than the optical lifetime; otherwise, in the case of fast spontaneous decay, the same pulse can cause reexcitation of the transition and a second photon emission, which can lead to an error in the protocol. On the other hand, it needs to be not too short, as this increases the line width of the excitation pulse and can therefore couple to and cause photon emission from unwanted off-resonant transitions that are close in frequency. A common method to separate the single photon from the excitation laser is to use the delayed emission of the photons compared to the arrival of the laser pulse. By delaying the detection window compared to the arrival of the excitation pulse, one can filter out the laser pulse in the time domain. This PBB has been used to make entanglement between NV centers [22] (see Fig 3.6).

COHERENT SCATTERING

In the coherent-scattering PBB a long and weak pulse is scattered elastically from the emitter. Under the condition that the exciting pulse is weak and long enough that, on average, only one photon interacts with the emitter within the optical lifetime, the scattered light will inherit the temporal shape, photon statistics, and frequency of the excitation field [67]. One can detune the laser from the emitter, making it more resilient to the spectral instability of the emitter. However, as the light has the same character as the laser, filtering the excitation light is experimentally much more challenging. This PBB allows for a spin-photon-emission LBB in a similar way to spontaneous emission.

RAMAN SCATTERING

The third way to make a spin-photon-emission LBB is to use the PBB of Raman scattering. In this case, the driving field and the emitted photon are coupled in a lambda scheme, where they both couple to a virtual state (see Fig 3.5, third row). In this inelastic scattering event, the temporal wave form and frequency are determined by the driving field, but now only a single photon is emitted. The driving field and the spontaneously emitted photons, which would act as noise sources, can be separated and filtered out

from the scattered photons since they have different frequencies. There is usually a trade-off between efficiency and noise in this PBB by choosing the detuning of the virtual level from the excited state. This PBB has been used for entangling trapped ions over hundreds of meters[56].

Raman transition can be also used for spin-photon absorption. In this case, the spin absorbs the incoming photon with one transition and the other transition is driven so that the spin is in another state upon absorption. If there is no photon interacting with the first transition — e.g., because there is no photon or it is in a different polarization — then there is no change in the spin state, because the driving addresses the transition with no population.

CONDITIONAL AMPLITUDE REFLECTION

When the interaction between the spin and the photon becomes strong, a single spin can modulate the single photon. This is different from the three previous situations in which the driving field is "classical" and only the photon emitted or scattered is in the single-photon regime. As emitters have a limited dipole, the light field needs to be confined spatially to achieve strong interaction, which can be achieved in an optical cavity or a waveguide. In the conditional-amplitude-reflection PBB, the emitter acts as a quantum switch, reflecting the light if it is in one spin state while transmitting the light in the other spin state.

In the dual-rail encoding, this can clearly be used to realize a spin-photon gate, as the spin interacts directly with the two spatial paths. For the other photonic encodings, we can use this PBB to make the spin-photon-projector LBB: the photon is only reflected if the transition is on resonance and otherwise is lost. This PBB has been used to show an asynchronous Bell-state measurement with the silicon vacancy in diamond[35], where a time-bin photonic qubit and a nanophotonic optical cavity have been used (see Fig 3.6).

CONDITIONAL PHASE REFLECTION

To perform a spin-photon gate, the conditional-amplitude-reflection PBB works only for the dual-rail encoding. For the other encodings, the problem is that photons are lost in transmission depending on the spin state, which is not compatible with a spin-photon gate. To apply a spin-photon gate, we need an unconditional reflection of the photon. The conditionality of the interaction should therefore be encoded in the phase of the photon. This is achieved with an overcoupled cavity, where the back side of the cavity has a much higher reflectivity than the front, such that the photon will not be transmitted. The emitter will alter the cavity response in such a way that, depending on the spin state, the photon will be reflected on the cavity or will enter the cavity and leave it again. When calibrated well, this can result in a π-phase-shift difference between the two types of reflection. The cavity can, in principle, also be replaced by a waveguide with a mirror at the end.

The conditional phase reflection with polarization-encoded photonic qubits has been the central PBB in the realization of a nonlocal gate with cold atoms in cavities[32] (see Fig 3.6.

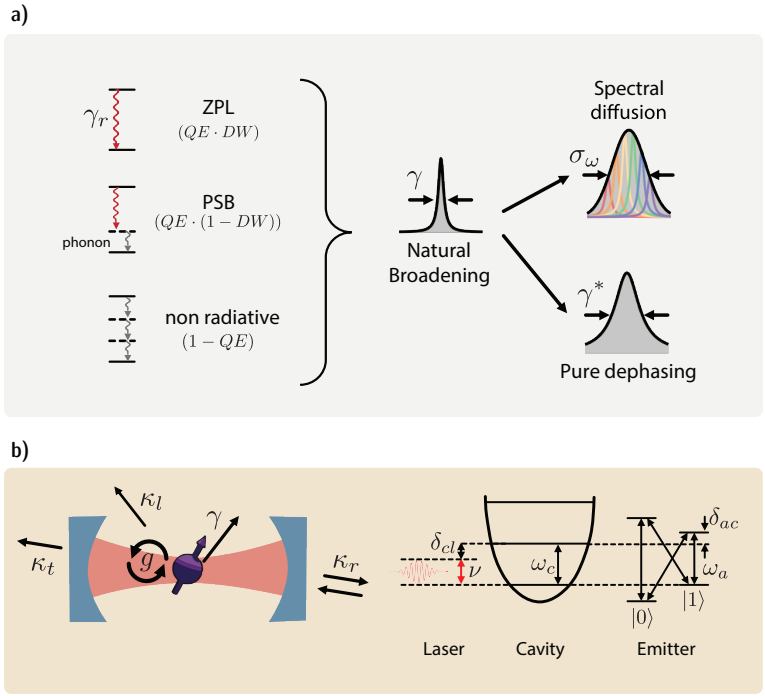

Figure 3.7: **The quantum modeling layer — spin-photon interface.** (a) The inefficiencies and noises of the optical transition in the spin-photon interface. Left: zero-phonon-line (ZPL) decay (γ_r), phonon-sideband (PSB) decay, and nonradiative decay combined give a total decay rate γ, resulting in the natural broadening (Lorentzian). The ratios of the transitions are expressed with an internal quantum efficiency (QE) and Debye-Waller factor (DW). Right: additional slow noise adds Gaussian spectral diffusion with a standard deviation of σ_ω, while the fast noise gives Lorentzian pure dephasing of line width γ^*. (b) Left: the cavity-QED system parameters. g is the vacuum Rabi frequency, γ is the spontaneous-emission rate, and κ_r, κ_t, and κ_l are the cavity decay rates to the reflection, transmission, and loss ports, respectively. Right: the level diagram of the laser, cavity, and spin. We assume that the $|1\rangle$ state of spins is desirably interacting with photons; interaction with the $|0\rangle$ state is negligible when $\gamma \ll \delta_{01}, g$.

3.6. QUANTUM OPTICAL MODELING

In the quantum optical modeling layer, the devices used are simulated at the quantum optics level. The aim of this layer is to calculate the action of the PBB on the photonic modes and spin states. The operations of the PBBs are modeled as quantum channels, which are completely positive trace-preserving maps. The PBBs map an input density matrix to an output density matrix. We emphasize that the mathematical modeling of PBBs can be done in different levels of detail. Thus, one can choose the PBB model as exhaustive or approximate depending on the purpose. The quantum optical modeling layer is separated from the PBB layer, as many PBBs rely on the same physical systems and therefore the same modeling; e.g., the conditional-amplitude- and conditional-phase-reflection PBBs both use an emitter coupled to a cavity. Moreover, the same PBBs can be modeled in different ways with different details. We will first discuss the intrinsic properties of the emitter, then how they can be enhanced and modified by an optical cavity, and, finally, the modeling of a couple of PBBs.

Using the modeling of a hardware-specific implementation, an REP can be benchmarked and optimized with respect to relevant experimental parameters. Having a realistic description of the building blocks also allows us to take into account noise sources and practical limitations.

3.6.1. EMITTER

For the spin-photon interface to perform well, the properties of the optical interface are important. The optical transition of an ideal emitter (Fig. 3.7(a)) has a naturally broadened line width γ related to its excited-state lifetime. In practice, noises in the surrounding environment of the emitter generally cause the optical line to broaden[47,73].

The noises can be divided into spectral diffusion and dephasing by their time scales. Especially for solid-state emitters, the fluctuation of the local charge environment is often slower than the nanoseconds lifetime of the transition. These charge fluctuations can change the spacing of the energy levels involved in the optical transition by the Stark effect, causing the frequency to change. This effect is called spectral diffusion. Spectrally diffused transitions have a fluctuating resonance frequency, shot-to-shot, that can be modeled with a Gaussian distribution of standard deviation σ_ω. The fidelity of spectrally diffused spin-photon interfaces can be calculated by a Monte Carlo simulation, statistically averaging over the distribution function[47]. On the other hand, fast noise sources such as mobile charges on the surfaces of photonic nanostructures or acoustic phonon scattering induce homogeneous broadening of the transition. In this limit, the frequency and phase noises are indistinguishable: $S_{\delta\omega_1}(\omega) = S_{\delta\phi_1}(\omega) \cdot \omega^2$, where $S(\omega)$ is the power spectral density and the subscript of S refers to the random process. The noise is modeled as random phase flips or, equivalently, pure dephasing without longitudinal relaxation. For pure dephasing γ^*, the transition is further broadened by γ^* from radiative broadening and the line shape is Lorentzian. If the fluctuation time scale of a noise is in an intermediate regime, the dynamics of the spin-photon interfaces and the resulting fidelity of entanglement requires a complete specification of the noise

as a stochastic random process.

Furthermore, especially in solid-state emitters, in addition to the coherent transition without the involvement of phonons — the zero-phonon line — there are phonon-assisted optical transitions, called phonon sidebands. Moreover, nonradiative, multi-phonon processes make the excited-state population decay without emitting photons. The quantum efficiency (QE) is defined as the ratio between the rates of all radiative processes to those of all processes:

$$QE = \frac{\Gamma_{\text{rad}}}{\Gamma_{\text{rad}} + \Gamma_{\text{nonrad}}}. \tag{3.3}$$

The decay rate of the zero-phonon line relative to the phonon sideband is the Debye-Waller factor (DW). In remote-entanglement settings, a large $QE \cdot DW$ is helpful for an efficient spin-photon interface, since only the coherent photons of the zero-phonon line are usable for entanglement protocols.

Other noise sources, such as a magnetic field or strain fluctuations, can also influence the transition through Zeeman shifts or mechanical deformation of the substrate, altering the energy levels. Moreover, in platforms other than solid-state emitters, such as trapped ions or superconducting qubits, other sources of noise, such as thermal fluctuations or coupling to nearby qubits, can play a significant role.

3.6.2. PHOTONIC CAVITY

A bare emitter can be used as a spin-photon interface, but it is advantageous to enhance the emitter properties and the collection efficiency of photons by means of an optical cavity. Other devices can be used to achieve the same goal, such as coupling the emitter to (photonic crystal) waveguides or optical fibers. However, the use of a cavity is the most common approach and, often, other devices can be described as a special case of cavity-emitter coupling[74,75]. Quantum optical modeling of a two-level system coupled to an optical cavity is a well-studied subject[38]. See also Refs.[76,77] for various cavity designs and the operations of cavities, including ring resonators[78].

Figure 3.7(b) shows relevant quantities of the emitter-cavity system. The dynamics of an emitter-cavity coupled system are governed by three parameters, γ, κ, and g. The emitter (cavity) transition line width γ (κ) is the inverse time of emitter decay (cavity relaxation). Photons spontaneously emitted into free space, nonradiative decays, and decays into phonon sidebands fall outside the coherent cavity-emitter interactions and are considered as a relaxation channel of the system, incorporated in γ. The dynamics of a cavity-emitter coupled system are governed by the coupling rate g. Physically, g is the Rabi frequency when the emitter is driven by a vacuum cavity electric field (the zero-point electric field multiplied by the transition dipole moment).

The cooperativity of the system is defined as

$$C = \frac{4g^2}{\kappa\gamma}. \tag{3.4}$$

The cooperativity gauges the strength of coherent interaction relative to the dissipation and a higher cooperativity improves the efficiency of spin-photon interfaces. In REPs, this translates directly to the rate and the fidelities, as we will see in Sec. 3.8.

While κ, g, and γ are usually set parameters once the device is realized, the operation point of the cavity-emitter system can often be tuned. On the right-hand side of Fig. 3.7(b), we indicate the energy relations that determine the operation point. The frequencies ω_c, ω_a, and ν are related to the energies of the cavity mode, the atomic transition, and the external source (laser or single photon). The detuning between the cavity and emitter, δ_{ac}, determines how the emitter and cavity couple and what is the amplitude and phase response of the system. The external source frequency, which we define with respect to the cavity as δ_{cl}, can be optimized to obtain the desired phase or amplitude when interacting with the cavity. Realistically, there are often additional optical transitions that couple (or are close) to the cavity. Here, we depict a common level scheme for solid-state emitters, the Voigt configuration. When the energy difference between the target transition (here involving the bright state $|1\rangle$) and other transitions is comparable to the cavity line width, the emitter line width, or the oupling rate, or the input light is not far detuned, undesired interaction of the dark $|0\rangle$ state can lead to errors.

The cavity loss channels, $\kappa_{t,r,l}$, determine the cavity behavior. It is useful to relate the losses to the cavity input channel, which we take to be κ_r. In this way, we can define the cavity output coupling as critically coupled ($\kappa_l + \kappa_t = \kappa_r$), undercoupled ($\kappa_l + \kappa_t > \kappa_r$) or overcoupled ($\kappa_l + \kappa_t < \kappa_r$). The first and latter regimes are particularly interesting for a cavity-based spin-photon interface: an overcoupled cavity is sometimes called a single-sided cavity as the preferential output channel is the one used for probing the cavity; therefore emitted photons will be funneled in the collected optical mode, while an incident photon will almost always be reflected back to the same port; this cavity is used in the conditional-phase-reflection PBB. A critically coupled cavity allows both transmission and reflection to potentially be used as output channels. This is the cavity used for a conditional-amplitude-reflection PBB.

Emission-based spin-photon interfaces can be realized using a bare emitter, though this can pose a severe limitation to the entanglement-generation rate when quantum efficiencies and/or Debye-Waller factors are low. In addition, especially for spontaneous emission, spectral diffusion and dephasing directly affect the photon indistinguishability and thus the entanglement fidelity. The efficiency and the fidelity of a spin-photon interface can be improved with a cavity: the Purcell effect enhances the emission of the optical transition by decreasing the lifetime and increasing the fraction of photons emitted by the target transition (e.g., the zero-phonon line for solid-state spins). At the same time, the optical-line-width broadening coming from the lifetime reduction decreases the relative effect of incoherent broadening mechanisms. The Purcell factor is defined as

$$F_p = 4g^2/\kappa\gamma_r = \frac{3}{4\pi^2}\frac{Q}{V}\left(\frac{\lambda}{n}\right)^3, \tag{3.5}$$

where Q is the cavity quality factor, λ is the resonant wavelength, n is the refractive index of the host material, and V is the effective mode volume. The effective mode volume is calculated with the electric field profile of the cavity mode, $E(\vec{r})$:

$$V = \int dV \epsilon(\vec{r})|E(\vec{r})|^2 / \epsilon(\vec{r}_e)|E(\vec{r}_e)|^2, \tag{3.6}$$

for the emitter located at $\vec{r}_e$, where $\epsilon(\vec{r})$ is the permittivity as a function of the coordinates[38,79]. If the cavity has a sufficiently high quality factor and a small mode volume, resulting in $g > \kappa, \gamma$, the system enters the strong-coupling regime[38], and the overall outcoupling efficiency of the emitted photons can become inefficient. This is because the cavity photon can be reabsorbed into the emitter before escaping the cavity. In the strong-coupling regime, the outcoupling efficiency is

$$\eta_{\text{out}} = \frac{\kappa_r}{\kappa} \cdot \frac{\kappa}{\kappa + \gamma}, \tag{3.7}$$

assuming that $\kappa_t = 0$ and where κ_r is the output port of the emitted photons. Equation (3.7) separates the contribution of cavity outcoupling and the fractional photon decay through the cavity. Thus, for example, reducing κ_r does not help the efficiency, as it decreases both factors. Furthermore, in the strong-coupling regime, the wave packet of photons oscillates with a coupling rate g, which makes the indistinguishability significantly susceptible to both g and $\kappa + \gamma$. When designing a cavity for entanglement, optimal parameters should be chosen within the trade-off space, rather than just strengthening the interaction, which often places the system in weak-coupling or bad-cavity regimes ($\kappa \gg g \gg \gamma$).

Spin-photon-gate and spin-photon-projector LBBs, by contrast, are based on the efficient coherent scattering of a single-photon or a weak coherent state by the emitter, which in turn requires strong interaction between the dipole of the emitter and a photonic mode. Spatial confinement of an optical mode by means of optical cavities or light-guiding structures (i.e., waveguides or optical fibers) enables this strong interaction. Here, we will focus on the use of cavities, as the scattering and emission of an emitter are similar[74,75] except for the numerical calculation of the coupling (for multiemitter cases, see Ref.[80]). In the strong-coupling regime, the response of the cavity to incoming photons with the cavity system is modulated in amplitude and phase by the state of the emitter. The cavity-emitter parameters and chosen operation points (in terms of the cavity-emitter detuning and the photon frequency) can be used together with the system input-output formalism relations (see Sec. 3.10.3 and Refs.[74,75]) to determine the response of the system, in terms of reflection and transmission coefficients and loss. The spin-dependent reflection and transmission coefficients are complex valued and describe the amplitude and phase of the photon after the interaction. They are used to realize spin-photon gates and spin-photon projectors. In practice, this can be changing either the amplitude or the phase of the photonic state, conditioned on the spin being in the bright state, as shown in the last two rows of Fig. 3.5. When modulating phase, it is convenient to use a single-sided cavity, as almost all photons will be reflected optimizing the efficiency, while amplitude modulation benefits from a critically coupled

cavity, maximizing the contrast of the field amplitudes. As anticipated, it is possible that the unwanted transition is spectrally close in frequency and it also couples to the cavity. In such cases, the relative phase or amplitude contrast between the system responses has to be optimized for high fidelity of the spin-photon emission. This can be done by changing the operation point, i.e. the emitter-cavity detuning and the input photon frequency.

3.6.3. QUANTUM CHANNEL DESCRIPTION OF PBB

The systematic and modular treatment of quantum channels is the key role of the PBB layer. Quantum channels can be additive and multiplicative; e.g., an optical π-pulse emission spin-photon interface and a weak excitation spin-photon interface, respectively. Table 3.1 lists the representative PBBs, which we use in Sec. 3.8 for benchmarking REPs. In the following sections, we explain the items of Table 3.1.

SPIN PBB

The state-preparation block outputs the desired state $|\psi\rangle$ with fidelity F_{state}. Our model assumes that a probabilistic error switches the state to an orthogonal state with probability $1 - F_{\text{state}}$. The density matrix of the system is an incoherent mixture of the two components weighted with the probabilities $\hat{\rho} = F_{\text{state}} |\psi\rangle \langle\psi| + (1 - F_{\text{state}}) |\psi^{\perp}\rangle \langle\psi^{\perp}|$.

Note that the quantum channel description of PBBs depends on the model of the physical systems. Let us assume that one rotates a perfectly prepared $|0\rangle$ state for the preparation of $\hat{R}_x(\theta)|0\rangle$, where $\hat{R}_x(\theta)$ is the single-qubit rotation around the x axis by θ. However, if θ has a bias error of ϵ, then $\rho_{\text{out}} = \hat{R}_x(\theta+\epsilon)|0\rangle\langle 0|\hat{R}_x^{\dagger}(\theta+\epsilon)$ will be more accurate. Choosing a realistic and accurate model is important. Our model-flexible description of PBBs enables the framework to cover all possible quantum hardware, as far as its quantum modeling can be made.

The most widely used error model for qubit operations (gates) is the depolarization channel. This channel maps the portion of the qubits population into a maximally mixed state, which is achieved with the uniformly probable application of Pauli operators (for n-qubit gates, the n-tensor product of Paulis and the identity operator, except for $I^{\otimes n}$). Table 3.1 lists the one- and two-qubit gate errors as they are often used,

$$\hat{\rho}_{\text{out}} = F_1 \hat{\rho}_{\text{in}} + \frac{1-F_1}{3}(\hat{\sigma}_x^{\dagger}\hat{\rho}_{\text{in}}\hat{\sigma}_x + \hat{\sigma}_y^{\dagger}\hat{\rho}_{\text{in}}\hat{\sigma}_y + \hat{\sigma}_z^{\dagger}\hat{\rho}_{\text{in}}\hat{\sigma}_z) \tag{3.8}$$

$$\hat{\rho}_{\text{out}} = F_2 \hat{\rho}_{\text{in}} + \frac{1-F_2}{15} \sum_{\substack{\hat{A},\hat{B}=\hat{I},\hat{\sigma}_x,\hat{\sigma}_y,\hat{\sigma}_z \\ \hat{A}\otimes\hat{B}\neq\hat{I}\otimes\hat{I}}} (\hat{A}^{\dagger}\otimes\hat{B}^{\dagger})\hat{\rho}_{\text{in}}(\hat{A}\otimes\hat{B}). \tag{3.9}$$

In the simulation of color centers in Sec. 3.8, we assume that spin PBBs are perfect because these operations have errors that are an order of magnitude smaller than those of photonic or spin-photon PBBs.

PHOTONIC PBB

A photon lost while traveling through the fiber by absorption or scattering can project the spin-photon entangled state to a trivial state. A popular way to describe the process

Table 3.1: Physical building blocks as a quantum channel.

PBB	Quantum Channel	Operator
Spin PBB		
State Preparation	$\rho_{\text{out}} = F_{\text{state}} \lvert\psi\rangle\langle\psi\rvert + (1 - F_{\text{state}}) \lvert\psi^{\perp}\rangle\langle\psi^{\perp}\rvert$	$\langle\psi\rvert\psi^{\perp}\rangle = 0$
Qubit Error	$\hat{\rho}_{\text{out}} = F_1 \hat{\rho}_{\text{in}} + \frac{1-F_1}{3}(\hat{\sigma}_x \hat{\rho}_{\text{in}} \hat{\sigma}_x + \hat{\sigma}_y \hat{\rho}_{\text{in}} \hat{\sigma}_y + \hat{\sigma}_z \hat{\rho}_{\text{in}} \hat{\sigma}_z)$	
Two-Qubit Error	$\hat{\rho}_{\text{out}} = F_2 \hat{\rho}_{\text{in}} + \frac{1-F_2}{15} \sum_{\substack{\hat{A},\hat{B}=\hat{I},\hat{\sigma}_x,\hat{\sigma}_y,\hat{\sigma}_z \\ <\hat{A},\hat{B}>\neq \hat{I}\otimes\hat{I}}} (\hat{A}^{\dagger} \otimes \hat{B}^{\dagger}) \hat{\rho}_{\text{in}} (\hat{A} \otimes \hat{B})$	
Photonic PBB		
Photonic Loss	$\rho_{\text{out}} = \text{tr}_L \left[\hat{U}(\rho_{\text{in}} \otimes \lvert 0_L\rangle\langle 0_L\rvert) \hat{U}^{\dagger} \right]$	$\hat{U} = \exp[\theta_L (\hat{a}\hat{a}_L^{\dagger} - \hat{a}^{\dagger}\hat{a}_L)]^{*}$
Mode Mixing	$\rho_{\text{out}} = \hat{U} \rho_{\text{in}} \hat{U}^{\dagger}$	$\hat{U} = \exp[\pi/4 (\hat{a}\hat{b}^{\dagger} - \hat{a}^{\dagger}\hat{b})]$
Photodetection	$\rho_{\text{out}} = \hat{\Pi} \rho_{\text{in}} \hat{\Pi}^{\dagger}$	$\hat{\Pi} = \hat{I} - \lvert 0_p\rangle\langle 0_p\rvert \ (\lvert 1_p\rangle\langle 1_p\rvert)$
Entangled Pair Source (SPDC)	$\rho_{\text{out}} = \hat{S}_2(\zeta) \lvert 0000\rangle\langle 0000\rvert \hat{S}_2^{\dagger}(\zeta)$	$\hat{S}_2(\zeta) = \exp\left[\zeta (\hat{a}_H^{\dagger}\hat{b}_V^{\dagger} + \hat{a}_V^{\dagger}\hat{b}_H^{\dagger}) + \text{h.c.}\right]$
Spin-photon PBB		
Spontaneous Emission (optical π-pulse)	$\rho_{\text{out}} = C \rho_{\text{in}} C^{\dagger} + p_{\text{incoh}} \hat{C}_{\text{incoh}} \rho_{\text{in}} \hat{C}_{\text{incoh}}^{\dagger} + p_{2\text{ph}} \hat{C}_{2\text{ph}} \rho_{\text{in}} \hat{C}_{2\text{ph}}^{\dagger}$	$\hat{C} = \sqrt{p_{\text{coh}}}\hat{C}_{\text{coh}} + \sqrt{p_{\text{loss}}}\hat{C}_{\text{loss}}$ $\hat{C}_{\text{coh}} = \lvert 0_s\rangle\langle 0_s\rvert \otimes \hat{I} + \lvert 1_s\rangle\langle 1_s\rvert \otimes \hat{a}^{\dagger}$ $\hat{C}_{\text{loss}} = \lvert 1_s\rangle\langle 1_s\rvert \otimes \hat{a}_{\text{loss}}^{\dagger}$ $\hat{C}_{\text{incoh}} = \lvert 1_s\rangle\langle 1_s\rvert \otimes \hat{a}_{\text{incoh}}^{\dagger}$ $\hat{C}_{2\text{ph}} = \lvert 1_s\rangle\langle 1_s\rvert \otimes \frac{1}{\sqrt{2}}\hat{a}^{\dagger}\hat{a}^{\dagger}$
Coherent Scattering	$\rho_{\text{out}} = \sum_k P_{\beta}(k) \hat{C}_{\text{incoh}}(k) (\hat{C} \rho_{\text{in}} \hat{C}^{\dagger}) \hat{C}_{\text{incoh}}^{\dagger}(k)^{\dagger}$	$\hat{C} = \lvert 0_s\rangle\langle 0_s\rvert \otimes \hat{I} + \lvert 1_s\rangle\langle 1_s\rvert \otimes \hat{D}_a(\alpha) \otimes \hat{D}_{a_{\text{loss}}}(\alpha_L)$ $\hat{C}_{\text{incoh}}(k) = \lvert 0_s\rangle\langle 0_s\rvert \otimes \hat{I} + \lvert 1_s\rangle\langle 1_s\rvert \otimes \frac{1}{\sqrt{k!}}(\hat{a}_{\text{incoh}}^{\dagger})^k$
Conditional Phase Reflection	$\rho_{\text{out}} = \text{tr}_L \left(\hat{C}_z \rho_{\text{in}} \hat{C}_z^{\dagger} \right)$	$\hat{C}_z = \sum_{k_s=0,1} \lvert k_s\rangle\langle k_s\rvert \otimes \exp(i(\angle r_k \hat{a}^{\dagger}\hat{a} + \angle l_k \hat{a}_{\text{loss}}^{\dagger}\hat{a}_{\text{loss}})) \exp\left[\theta_k (\hat{a}^{\dagger}\hat{a}_{\text{loss}} - \hat{a}\hat{a}_{\text{loss}}^{\dagger})\right]^{\ddagger}$

* $\theta_L = \arcsin(\sqrt{L})$.

† $P_{\beta}(k) = \frac{|\beta|^{2k} \exp^{-|\beta|^2}}{k!}$. Note that this assumes perfect incoherent photon filtering afterward. For the case of imperfect filtering, two incoherent modes for collection and loss should be counted separately (then, filtering modifies the collection incoherent mode only).

‡ $\theta_k = \arcsin\left(\sqrt{L_k}\right)$, r_k (l_k) are the complex coefficient of reflection (loss) of a photon for spin state $\lvert k_s\rangle$. "$\angle(\cdot)$" is the phase of the following complex coefficient.

is via the Lindblad master equations[81]. This is equivalent to unitary evolution with an auxiliary mode and partial tracing (see the Table 3.1 element). The unitary evolution is equivalent to the beam-splitter operation, the angle of which is determined from the loss ($\theta_L = \arcsin\sqrt{L}$; see Sec. 3.10.3). The same unitary evolution also describes the mode mixing for erasing "which path information". Here, we have listed the perfect mode mixing with $\theta = \pi/4$ but imperfect mode mixing can be set with different values of θ for the biased case or even combinations of θ values for stochastic description.

We can implement the photodetection on a specific mode (p subscription in Table 3.1) with a projection operator. Here, we have used the projection of a Fock-state encoded photonic mode but one can use the eigenstate of a different basis for the projection operator.

Lastly, we present the PBB for entangled photon-pair sources. Among many implementations and photon encodings, we specifically consider spontaneous parametric down-conversion (SPDC), the polarization-encoded photon-pair state[82,83],

$$\rho_{\text{out}} = |\text{SPDC}\rangle\langle\text{SPDC}|, \tag{3.10}$$

$$|\text{SPDC}\rangle = \hat{S}_2(\zeta)|0000\rangle = e^{-|\zeta|^2/2}\cdot\Big[|0000\rangle + \zeta\big(|1_{a,H}0_{a,V}0_{b,H}1_{b,V}\rangle + |0_{a,H}1_{a,V}1_{b,H}0_{b,V}\rangle\big) + \ldots\Big], \tag{3.11}$$

where $\hat{S}_2(\zeta) = \exp\left[\zeta(\hat{a}_H^\dagger\hat{b}_V^\dagger + \hat{a}_V^\dagger\hat{b}_H^\dagger) + \text{h.c.}\right]$ is the SPDC operator, ζ denotes the numerical parameter determined by pump field, $\hat{a}$ and $\hat{b}$ are two spatial photonic modes, H and V indicate two polarization modes, and "h.c." refers to Hermitian-conjugate terms. It is worth noting that $|HV\rangle + |VH\rangle = |1_{a,H}0_{a,V}0_{b,H}1_{b,V}\rangle + |0_{a,H}1_{a,V}1_{b,H}0_{b,V}\rangle$ in the literature for simplicity, whereas we explicitly specify photon numbers in each photonic mode to align with other PBBs.

SPIN-PHOTON PBB

The ideal operation of the emission spin-photon interface using an optical π pulse is described with the coherent channel subscripted with "coh". When the spin is in the dark state ($|0\rangle$), it does not affect the state of the photonic mode ($\hat{I}$). When the spin is in the bright state ($|1\rangle$), the desired outcome is the creation of a single photon in the mode of interest, $\hat{a}$. This results in the Kraus operator $\hat{C}_{\text{coh}} = |0_s\rangle\langle 0_s|\otimes\hat{I} + |1_s\rangle\langle 1_s|\otimes\hat{a}^\dagger$.

In realistic devices, ideal events only happen with probability p_{coh}. With probability, p_{incoh}, the incoherent channel, labeled by "incoh", adds a photon with a random phase that does not coherently interfere, which reflects the non-unity indistinguishability. This can be modeled with the addition of photon to the incoherent mode $\hat{a}_{\text{incoh}}$ that will not be interfered with by the mode-mixing PBB. Likewise, double excitation and finite efficiencies contribute additively to the density matrix through $\hat{C}_{2\text{ph}}$ and $\hat{C}_{\text{loss}}$, with $p_{2\text{ph}}$ and p_{loss} (see Table 3.1 and Sec. 3.10.4). Again, these PBBs can add more channels such as ionization or remove some if they are not wanted.

All the parameters including probabilities are calculated at the quantum optical modeling layer, and PBBs require these numerical values for the calculation of ρ_{out}. For the calculation of PBB parameters from physically characterized ones, see Sec. 3.10.4.

Instead of a short strong optical pulse, one can weakly drive the transition by coherently scattering the field. Scattered in this way, the field is in a coherent state with amplitude α. The process can be encapsulated by the displacement operator $\hat{D}_{\hat{a}}(\alpha)$ where $\hat{a}$ represents the mode that the operator acts on ($\hat{D}(\alpha)|0\rangle = |\alpha\rangle$). At the same time, the excitation field is also scattered to unwanted mode $\hat{a}_{\text{loss}}$. Moreover, incoherent scattering due to noise adds photons to another mode with Poisson statistics. We can express the loss-mode part of the density matrix as

$$\hat{\rho}_{\text{loss}} = \sum_i \frac{n_{\text{loss}}^i \exp(-n_{\text{loss}})}{i!} |i\rangle\langle i|, \tag{3.12}$$

where n_{loss} is the average number of photons added to the loss mode. $|n \neq 0\rangle$ components of the density matrix reduce the fidelity of the fidelity of spin-photon entanglement and subsequent spin-spin entanglement, because they leak information on the quantum state (only the bright state, $|1_s\rangle$, adds the photon to the loss mode).

3.7. SOFTWARE IMPLEMENTATION OF THE FRAMEWORK

The layered and modular framework lends itself well to implementation in simulation code. Our QuREBB (Quantum Remote-Entanglement Building Blocks) simulation repository is available on GitHub[24] and we have used it to simulate and compare different REPs (Sec. 3.8). One can reuse implemented codes with minimal corrections due to our modular framework, even for different protocol topologies (with modifications of LBBs) or different physical systems (with modifications of quantum modeling).

The code is based on the QuTiP package[84], written in (python). For the simulation of REPs, it is important to represent composite quantum systems (involving stationary qubits and multiple photonic modes), track all modes, and trace out photonic loss modes when needed. QuTiP references subsystems by indices and partial traces modify the indices. We have improved the indexing capabilities of the quantum object (Qobj) in QuTiP and we refer to a quantum mode with a string such that each subsystem can be properly named (a dictionary). We have created an inherited class, "named quantum object" (NQobj), that is compatible with the QuTiP standard functions and we have described the names of the subsystems in an attribute "names". With this new attribute in place, one can allow for operations with NQobjs of different sizes. For example, when a density matrix evolves with a unitary, one can omit the identities for the subsystems that are not involved, as this is inferred from the names of the objects. For a modular use of the code, this is an essential feature, as it allows us to write code for the building blocks without knowledge of the whole system. Moreover, it allows us to trace out loss modes anywhere in the calculations, as they can be indexed by name, without the risk of shifting all the indices of the other modes by removing the loss mode.

The state of the system is represented by a non-normalized density matrix. In this way, both the state and the success probability are represented by one object. The state is the normalized density matrix and the success probability is the trace of the density matrix. These non-normalized density matrices act as the interface between the PBBs, which are the quantum operators on the density matrix.

The quantum modeling of the spin-photon interface favors the description with creation and annihilation operators (the Heisenberg picture), while the nonunitary evolution of quantum systems favors density matrices (the Schrödinger picture). To bridge the gap, one needs descriptions such as one of the beam splitters in Table 3.1: $\hat{U} = \exp[\theta(\hat{a}\hat{b}^\dagger - \hat{a}^\dagger\hat{b})]$. We have modeled the cavities as a composite system of beam splitters and phase shifters (see Sec. 3.10.3). The method is advantageous in directly describing arbitrary big Fock-state space in QuTiP as users can choose the size of the creation and annihilation operators accordingly. The code is directly extendable to the simulation of weak coherent states with non-negligible multiphoton states.

While our package covers the low-level description of quantum systems to the protocol-level description of elementary entanglement links, it complements other tools at the link layer or above. This includes NetSquid[85], an event-driven network simulator that can cover a link layer[86] or a higher level with a large number of nodes[2], as well as QuNetSim[87] and others[88,89].

3.8. SIMULATING AND BENCHMARKING ENTANGLEMENT PROTOCOLS

In this section, we show an example of how the proposed framework can be used to break down three different entanglement protocols into realistic PBBs, and we use the software introduced in Sec. 3.7 to simulate the performance and compare them. We set the physical platform used for all the protocols to be the silicon-vacancy (SiV) center in a diamond coupled to an optical cavity.
We outline our simulation comparison in Fig. 3.8. The hardware platform that we have chosen is the SiV color center in diamond, and we consider photonic crystal cavities to either enhance the spin-photon emission or to realize spin-photon projectors in the strong-coupling regime. The protocols that we compare are one emission-based protocol with detection-in-midpoint topology, where we use Fock-state encoding for the photon (protocol A in Fig. 3.8(b) and two projector-based (protocols B and C) with the conditional-amplitude-reflection and the time-bin encoding, with a sender-receiver and detection-in-midpoint topology. The detailed implementation in terms of PBBs is shown for all protocols in Figs. 3.8(c) and 3.8(d). More details on the quantum optical modeling used can be found in Sections 3.10.3 and 3.10.4.

We compare the performance of the protocols according to the simulation results. For each simulation, we start with realistic experimental values for the particular system that can be found in the literature (see Table 3.3) and we search for the optimal operation point of the spin-photon interface by sweeping a subset of the parameters

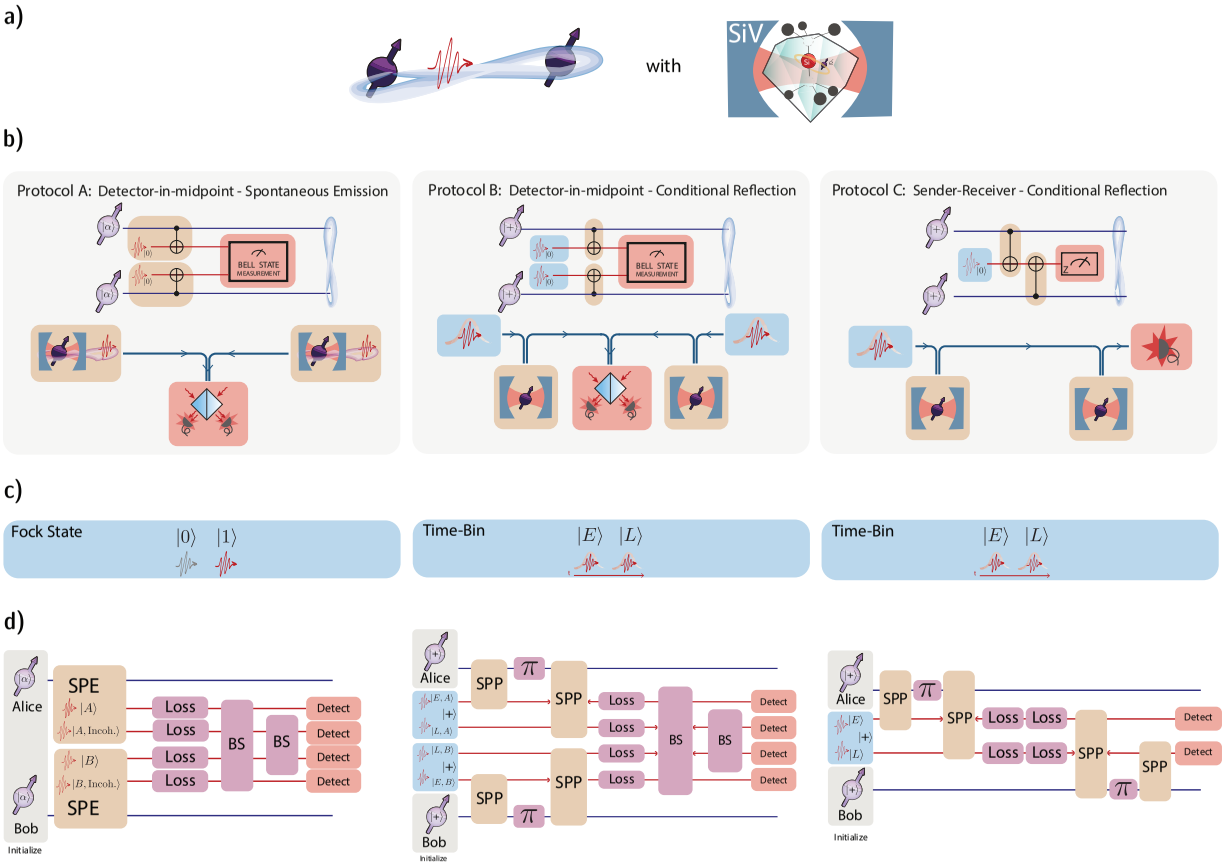

Figure 3.8: **A comparison of different protocols for entanglement generation** using the SiV center in diamond coupled to an optical cavity as a spin-photon interface. (b) The circuit diagram and LBB descriptions of the protocols under investigation. (c) The photonic encodings for each protocol. (d) The protocol after the LBBs are compiled to hardware-aware PBBs and including imperfections such as loss. The photon states are labeled by node of interaction (A and B for Alice and Bob), by time-bin encoding (E and L for the early and late modes), and whether the photon is resulting from incoherent emission (Incoh.). The initial photon state is defined as $|+\rangle = 1/\sqrt{2}(|E\rangle + |L\rangle)$.

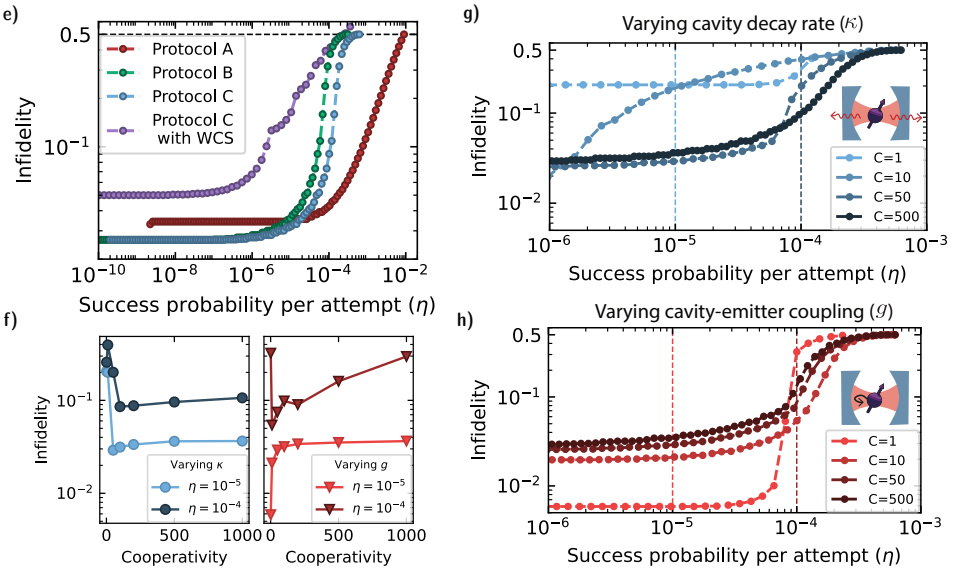

Figure 3.9: **Comparison of different protocols for entanglement generation - Simulations.** (e) Simulated success probability-infidelity curves for the different protocols using the parameters of Table 3.3. Protocol C is also simulated for a weak-coherent-state (WCS) input instead of single photons. (f)-(h) The performance of protocol C when the cooperativity is changed by improving either the cavity decay rate κ or the emitter-cavity coupling g, following Eq. (3.4). (f) The fidelity for two different success probabilities η when varying κ or g (left and right graphs, respectively) (g), (h) The success-probability-infidelity curves for some of the cooperativities. The dashed lines mark the values of η shown in (f).

("sweep parameters", indicated as *variable* in Table 3.3) and for each configuration we calculate the protocol outcome. We choose to optimize only parameters that are easily controllable in an experimental setting: the detuning between the cavity and the emitter and the detuning between the input photon and the cavity (which we call the operation frequency). The frequency difference between the two optical transitions involved, δ_{01}, can in principle be tuned by applying an external magnetic field and this can have a big impact on the performance of the protocol. However, as the magnetic field is intertwined with other features of the system, such as the cyclicity of the optical transition and the qubit frequency, we do not consider it here as a sweep parameter. Similarly, intrinsic properties of the cavity or the emitter are considered to be fixed parameters for the protocol optimization. Ultimately, the simulation gives us the infidelity and success probability with which the protocol achieves a definite target state, which is one of the four Bell states, as a function of the swept parameters. To benchmark the protocols we compare the trade-off between the infidelity and the success probability. We report the success probability of the protocol for each attempt, as obtained from the density matrix of the final state. The effective rate can be extracted from the success probability by accounting for the repetition rate of the protocol: this can give a more consistent comparison. Figure 3.9(e) shows the rate-infidelity curves for the three protocols with the starting values reported in Table 3.3. From these curves, one can see how, with these parameters and protocol implementations, protocol A is advantageous with respect to the others, except at low rates where the fidelity is limited by the incoherent emission due to dephasing. Here, protocols B and C allow us to obtain lower infidelity. We also simulate protocol C using a weak-coherent-state (WCS) input to approximate single photons. In this case, the success probability drops faster than in the single-photon implementation, as it scales with the average photon number in the WCS, and the infidelity is higher since the multiphoton components in the input cause protocol errors.

Finally, we simulate how protocol C performs for different values of the cooperativity. Again, we optimize for each point by sweeping the "sweep parameters" as above and, in addition to that, we vary only one of the intrinsic cavity parameters to change the cooperativity. The rate-infidelity curves are reported in Fig. 3.9(g) and (h). We test two ways to change the cooperativity, as can be seen from Eq. (3.4). In Fig. 3.9(g) we do this by varying the cavity decay rate κ, which is related to the cavity quality factor Q, at fixed cavity-emitter coupling g. In Fig. 3.9(h), we keep κ fixed and we vary the cavity-emitter coupling g, which can be realized in practice by changing the cavity-mode volume, the overlap between the emitter dipole and the field distribution, or the quantum efficiency and Debye-Waller factor of the optical system. In Fig. 3.9(f), we report the infidelity at two different success probabilities. Interestingly, increasing the cooperativity by only optimizing a subset of the parameters does not always lead to better performance. This can be attributed to the Purcell broadening of the optical line width which, when a second optical transition is close in frequency (δ_{01} is small compared to the Purcell-broadened line width and cannot be optimized), can cause a decrease in fidelity due to undesired interaction with the wrong spin state. Varying the cavity line width (κ) or varying the coupling g can affect this phenomenon differently, especially at low cooperativities. Fur-

thermore, when increasing the cooperativity in Fig. 3.9 by only changing either κ or g, we pass from the bad-cavity regime ($\kappa \gg g$) to the strong-coupling one ($g \gg \kappa$). As discussed in Sec. 3.6.2, this regime is not necessarily optimal for entanglement generation, especially if the system is not optimized accordingly.

3.9. CONCLUSIONS

In this work, we have introduced a modular framework to describe photon-mediated remote-entanglement protocols. Our framework divides the remote-entanglement protocols into four different layers, allowing a perspective of the entanglement protocol from an abstract and hardware-agnostic overview to a detailed description of each component and physical implementation. We have described the function of the different layers and provided examples of their realization, including detailed modeling of cavity-based spin-photon interfaces. Finally, using a software implementation that directly reflects the modular approach of the framework, we have simulated different remote-entanglement-protocol topologies based on a realistic experimental platform and investigated how they perform under different parameter regimes.

For future work, our framework can be expanded into both higher-level uses and lower-level descriptions. At the higher level, leveraging the logical operations of the LBB layer can construct error-corrected encoded quantum networks[23]. The incorporation of error-correction schemes into our framework would enable the simulation of fault-tolerant quantum applications. On the other hand, the integration of material-level details of physics (for the case of color centers see, e.g., Ref.[90]), into our quantum optical modeling can help the choice of quantum systems to optimally configure the network. This inclusion of finer-grained aspects will enhance the accuracy of our simulations as well. In addition, we believe that our framework can be extended to apply to continuous-variable entanglement distribution[91] and qudit entanglement distribution[92].

3.10. SUPPLEMENTARY INFORMATION

3.10.1. NOMENCLATURE

Table 3.2: Nomenclature used in this tutorial

Topology	
Detection-in-midpoint	
Sender-receiver	
Source-in-midpoint	
Logical Building Blocks	
Spin	Initialization
	Gate
	Measurement
Photon	Photon source
	Photon pair source
	Measurement
	Bell state measurement
	Photon gate
Spin-Photon	Spin-photon emission
	Spin-photon gate
	Spin-photon projector
	Spin-photon absorption
Encoding	
Fock state	
Time-bin	
Polarization	
Dual-rail	
Frequency	
Physical Building Blocks	
Spin	Initialization
	Gate
	Measurement
Photon	Initialization
	Measurement
	Mode mixing
	Z-Rotation
	X-Rotation
Spin-photon	Spontaneous emission
	Coherent scattering
	Raman scattering
	Conditional amplitude reflection
	Conditional phase reflection

3.10.2. NOTATION AND SIMULATION PARAMETERS

Table 3.3: SiV parameters for simulations

Name	Symbol	Spin-Photon Projector	Spin-Photon Emission
Emitter Resonance Frequency	ω_a	406.706 THz	
Cavity Resonance Frequency	ω_c	Variable	
Laser Frequency	ν	Variable	
Laser-Cavity Detuning	Δ_{lc}	Variable	
Cavity-Emitter Detuning	Δ_{ce}	Variable	
Laser-Emitter Detuning	Δ_{le}	Variable	
Emitter Radiative Decay Rate (ZPL)	γ_r	13.1 MHz [a]	
Emitter Total Decay Rate	γ	92.5 MHz [a]	100 MHz
Pure Dephasing	γ^*	30.5 MHz [b,c]	
Spectral Diffusion	σ_ω	N/A[d]	
Total Emitter Linewidth	Γ	123 MHz [b]	N/A
Optical Transitions Detuning	δ_{01}	1 GHz	
Emitter-Cavity Coupling	g	8.38 GHz [b]	6.81 GHz
Cavity Decay Rate	κ	21.8 GHz [b]	$\kappa_l + \kappa_t = 89$ GHz, $\kappa_r = 240$ GHz [e]
Cavity Quality Factor	Q	18,700 [b]	1,237
Cavity Cooperativity	C	105	4.3 [f]
Debye-Waller Factor	DW	0.7 [g]	
Quantum Efficiency	QE	0.2	
Link Loss	-	0.9	
Device Insertion Loss	-	0.5	

a 90

b 35

c This data for over-coupled cavity does not exist. We assume that it is the same as the critically-coupled case.

d To the best of our knowledge, there are no spectroscopic results resolving pure dephasing and spectral diffusion of SiV. In this work, we simply assume that the broadening in [35] is from the pure dephasing considering the Lorentzian lineshape.

e 93

f Note that this number is converted with pure dephasing assumed.

g 94

3.10.3. MODELING CONDITIONAL REFLECTION SPIN-PHOTON INTERFACE WITH UNITARIES

We model the conditional reflection spin-photon interfaces using input-output formalism [74,75]. This describes the response of the system in terms of r, t, and l as the complex

coefficients of reflection, transmission, and loss, respectively. To calculate the unitary operator in the Fock state basis, we use the beamsplitter configuration in Fig. 3.10 and the description of a beamsplitter

$$U = \exp\left[\theta(a^\dagger b - a b^\dagger)\right] \tag{3.13}$$

$L = |l|^2$ is the loss. For example, if 30% of photons are lost, then $L = 0.3$.

$$U_1 = \exp\left[\theta_1(a^\dagger l - a l^\dagger)\right]. \tag{3.14}$$

$$\theta_1 = \arctan\left(\frac{\sqrt{L}}{\sqrt{1-L}}\right). \tag{3.15}$$

Then, from r and t, we calculate the normalized r' and t';

$$r' = r/\sqrt{|r|^2 + |t|^2} \tag{3.16}$$

$$t' = t/\sqrt{(|r|^2 + |t|^2)}. \tag{3.17}$$

The unitary for the splitting is

$$U_2 = \exp\left[\theta_2(a^\dagger b - a b^\dagger)\right] \tag{3.18}$$

$$\theta_2 = \arctan\left(\frac{|t'|}{|r'|}\right) \tag{3.19}$$

For adjusting the phases,

$$U_3 = \exp\left[i(\angle r a^\dagger a + \angle t b^\dagger b)\right] \tag{3.20}$$

The total unitary for loss-reflection-transmission is,

$$U = U_3 \cdot U_2 \cdot U_1. \tag{3.21}$$

One can use both ports of the cavity with dual rail encoding. The interference of fields is reflected in the interference of the reflection/transmission coefficient derived from the coherence of the spins. Figure 3.10 shows the two-port-to-three-port unitary decomposition. The splitting ratio of BS1 is determined by the loss of input port 1, while that of BS2 is by the loss of input port 2. BS3 combines the output ports of BS1 and BS2 to generate reflection and transmission. A total of five phase shifters are added between the beamsplitters and at the output port for the phase adjustment.

For a larger number of input/output ports, we can use Reck[95] or Clements[96] decomposition.

3.10.4. QUANTUM MODELED PHYSICAL PARAMETERS

Here, we discuss the PBB parameters calculated from the quantum modeling layer.

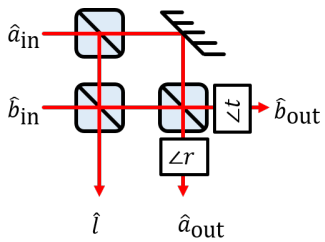

Figure 3.10: Two-port-to-three-port unitary construction with beamsplitters.

SPONTANEOUS-EMISSION PBB

$$p_{\text{coh}} = \langle 1|\rho_{\text{in}}|1\rangle \cdot \frac{\kappa_r}{\kappa} \cdot \frac{C}{C+1} \cdot \frac{F_p\gamma_r}{\Gamma + F_p\gamma_r} + \langle 0|\rho_{\text{in}}|0\rangle \tag{3.22}$$

$$p_{\text{incoh}} = \langle 1|\rho_{\text{in}}|1\rangle \cdot \frac{\kappa_r}{\kappa} \cdot \frac{C}{C+1} \cdot \frac{\gamma* + \sigma_\omega}{\Gamma + F_p\gamma_r} \tag{3.23}$$

$$p_{2\text{ph}} = 0 \tag{3.24}$$

$$p_{\text{loss}} = 1 - p_{\text{coh}} - p_{\text{incoh}} - p_{2\text{ph}} \tag{3.25}$$

$$\tag{3.26}$$

The double-excitation probability $p_{2\text{ph}}$ is a function of the lifetime, pulse width, and ionization probability. Here, we neglect the two-photon emission for simplicity. This is made possible by adjusting the pulse area so that one transition is an odd-multiple π pulse and the other is an even-multiple π pulse.

COHERENT-SCATTERING PBB

$$\alpha_{\text{tot}} = \alpha + \alpha_L \tag{3.27}$$

$$\alpha_{\text{tot}} = \eta\alpha \tag{3.28}$$

$$\alpha_L = \frac{1-\eta}{\eta}\alpha \tag{3.29}$$

$$\eta = \frac{\kappa_r}{\kappa} \cdot \frac{F_p}{F_p+1} \tag{3.30}$$

$$|\beta|^2 = \left[\frac{\gamma*}{\Gamma' - \gamma*} + \frac{1 - QE' \cdot DW'}{QE' \cdot DW'}\right] |\alpha_{\text{tot}}|^2 \tag{3.31}$$

$$\Gamma' = \Gamma + F_p\gamma_r \tag{3.32}$$

$$DW' = \frac{(F_p+1)DW}{F_p \cdot DW + 1} \tag{3.33}$$

$$QE' = \frac{QE \cdot (F_p \cdot DW + 1)}{1 + F_p \cdot QE \cdot DW} \tag{3.34}$$

where η is the collection efficiency of the coherent emission. The prime represents the cavity-modified rate or the ratio of transitions. In Eq. (3.31), the first term is for incoherent emission and the second term is for inefficiencies.

3.10.5. SIMULATIONS PARAMETER SWEEP AND DETAILS

To optimize the fidelity and success probability of the simulations in Fig. 3.8 we perform the parameter sweep in Table 3.4.

Protocol	Parameters	Range	Number of points
A	α (initial spin state)	$[10^{-7}, 0.3]$	500
B,C	Δ_{la}	$[-18, 0]$ GHz	1000
	Δ_{ac}	$[0, 120]$ GHz	60
C (WCS)	α (WCS)	$[0.001, 2]$	10
	Δ_{la}	$[-15, -2]$ GHz	1200
	Δ_{ac}	$[0, 120]$ GHz	50

Table 3.4: Sweep parameters for simulations of Fig. 3.8

For the cooperativity sweep, by varying κ we use the same values as in the table. For the sweep by varying g, the cavity-emitter spectrum changes significantly; therefore, the range has to be optimized for each simulation. The ranges can be found in the simulation notebooks[24].

The simulations were run on a desktop computer (Intel Xenon CPU, 3.50 GHz, quad core, eight threads, 32-GB RAM). The simulation of a single protocol run takes approximately 350 ms for protocols A and C and approximately 550 ms for protocol B (mostly dependent on the size of the Hilbert space). By using basic PYTHON multiprocessing functions, we can speed up the parameter sweep by a factor ~ 5 compared to just looping the protocol over the whole parameter space. This results on a runtime of ~ 2 min for Protocol A, ~ 2 hours for Protocol B, ~ 1 hour for protocol C and ~ 10 hours for the WCS simulation.

REFERENCES

[1] H. J. Kimble, *The quantum internet,* Nature **453**, 1023 (2008).

[2] S. Wehner, D. Elkouss and R. Hanson, *Quantum internet: A vision for the road ahead,* Science **362**, eaam9288 (2018).

[3] M. Ruf, N. H. Wan, H. Choi, D. Englund and R. Hanson, *Quantum networks based on color centers in diamond,* Journal of Applied Physics **130**, 070901 (2021).

[4] C. Cabrillo, J. I. Cirac, P. García-Fernández and P. Zoller, *Creation of entangled states of distant atoms by interference,* Physical Review A **59**, 1025 (1999).

[5] L.-M. Duan, M. D. Lukin, J. I. Cirac and P. Zoller, *Long-distance quantum communication with atomic ensembles and linear optics,* Nature **414**, 413 (2001).

[6] D. E. Browne, M. B. Plenio and S. F. Huelga, *Robust Creation of Entanglement between Ions in Spatially Separate Cavities,* Physical Review Letters **91**, 067901 (2003).

[7] L.-M. Duan and H. J. Kimble, *Efficient Engineering of Multiatom Entanglement through Single-Photon Detections,* Physical Review Letters **90**, 253601 (2003).

[8] C. Simon and W. T. M. Irvine, *Robust Long-Distance Entanglement and a Loophole-Free Bell Test with Ions and Photons,* Physical Review Letters **91**, 110405 (2003).

[9] S. D. Barrett and P. Kok, *Efficient high-fidelity quantum computation using matter qubits and linear optics,* Physical Review A **71**, 060310 (2005).

[10] N. Sangouard *et al.*, *Long-distance entanglement distribution with single-photon sources,* Physical Review A **76**, 050301 (2007).

[11] M. Pompili *et al.*, *Realization of a multinode quantum network of remote solid-state qubits,* Science **372**, 259 (2021).

[12] S. L. N. Hermans *et al.*, *Qubit teleportation between non-neighbouring nodes in a quantum network,* Nature **605**, 663 (2022).

[13] N. H. Nickerson, J. F. Fitzsimons and S. C. Benjamin, *Freely Scalable Quantum Technologies Using Cells of 5-to-50 Qubits with Very Lossy and Noisy Photonic Links,* Physical Review X **4**, 041041 (2014).

[14] W. J. Munro, K. Azuma, K. Tamaki and K. Nemoto, *Inside Quantum Repeaters,* IEEE Journal of Selected Topics in Quantum Electronics **21**, 78 (2015).

[15] E. T. Khabiboulline, J. Borregaard, K. De Greve and M. D. Lukin, *Optical Interferometry with Quantum Networks,* Physical Review Letters **123**, 070504 (2019).

[16] D. L. Moehring *et al.*, *Entanglement of single-atom quantum bits at a distance,* Nature **449**, 68 (2007).

[17] S. Ritter *et al.*, *An elementary quantum network of single atoms in optical cavities,* Nature **484**, 195 (2012).

[18] J. Hofmann *et al.*, *Heralded Entanglement Between Widely Separated Atoms,* Science **337**, 72 (2012).

[19] A. Delteil *et al.*, *Generation of heralded entanglement between distant hole spins,* Nature Physics **12**, 218 (2016).

[20] R. Stockill *et al.*, *Phase-Tuned Entangled State Generation between Distant Spin Qubits,* Physical Review Letters **119**, 010503 (2017).

[21] H. Bernien *et al.*, *Heralded entanglement between solid-state qubits separated by three metres,* Nature **497**, 86 (2013).

[22] P. C. Humphreys *et al.*, *Deterministic delivery of remote entanglement on a quantum network,* Nature **558**, 268 (2018).

[23] L. Jiang *et al.*, *Quantum repeater with encoding,* Physical Review A **79**, 032325 (2009).

[24] H. K. C. Beukers *et al.*, *QuREBB, GitHub repository,* `https://github.com/QuTech-Delft/QuREBB` (2023).

[25] V. Dobrovitski, G. Fuchs, A. Falk, C. Santori and D. Awschalom, *Quantum Control over Single Spins in Diamond,* Annual Review of Condensed Matter Physics **4**, 23 (2013).

[26] F. Flamini, N. Spagnolo and F. Sciarrino, *Photonic quantum information processing: A review,* Reports on Progress in Physics **82**, 016001 (2018).

[27] M. A. Nielsen and I. L. Chuang, *Quantum Computation and Quantum Information*, 10th ed. (Cambridge University Press, Cambridge ; New York, 2010).

[28] C. Jones, D. Kim, M. T. Rakher, P. G. Kwiat and T. D. Ladd, *Design and analysis of communication protocols for quantum repeater networks,* New Journal of Physics **18**, 083015 (2016).

[29] J. I. Cirac, P. Zoller, H. J. Kimble and H. Mabuchi, *Quantum State Transfer and Entanglement Distribution among Distant Nodes in a Quantum Network,* Physical Review Letters **78**, 3221 (1997).

[30] I. Dror, A. Sandrov and N. S. Kopeika, *Experimental investigation of the influence of the relative position of the scattering layer on image quality: The shower curtain effect,* Applied Optics **37**, 6495 (1998).

[31] S. Pirandola, *Satellite quantum communications: Fundamental bounds and practical security,* Physical Review Research **3**, 023130 (2021).

[32] S. Daiss *et al.*, *A quantum-logic gate between distant quantum-network modules,* Science **371**, 614 (2021).

[33] H. Bernien *et al.*, *Two-Photon Quantum Interference from Separate Nitrogen Vacancy Centers in Diamond,* Physical Review Letters **108**, 043604 (2012).

[34] C. W. Chou *et al.*, *Measurement-induced entanglement for excitation stored in remote atomic ensembles,* Nature **438**, 828 (2005).

[35] M. K. Bhaskar *et al.*, *Experimental demonstration of memory-enhanced quantum communication,* Nature **580**, 60 (2020).

[36] M. L. Chan *et al.*, *Quantum state transfer between a frequency-encoded photonic qubit and a quantum-dot spin in a nanophotonic waveguide,* Physical Review A **105**, 062445 (2022).

[37] S. Welte, B. Hacker, S. Daiss, S. Ritter and G. Rempe, *Cavity Carving of Atomic Bell States,* Physical Review Letters **118**, 210503 (2017).

[38] A. Reiserer and G. Rempe, *Cavity-based quantum networks with single atoms and optical photons,* Reviews of Modern Physics **87**, 1379 (2015).

[39] L. Heller, J. Lowinski, K. Theophilo, A. Padrón-Brito and H. de Riedmatten, *Raman Storage of Quasideterministic Single Photons Generated by Rydberg Collective Excitations in a Low-Noise Quantum Memory,* Physical Review Applied **18**, 024036 (2022).

[40] N. Piro *et al.*, *Heralded single-photon absorption by a single atom,* Nature Physics **7**, 17 (2011).

[41] A. D. Boozer, A. Boca, R. Miller, T. E. Northup and H. J. Kimble, *Reversible State Transfer between Light and a Single Trapped Atom,* Physical Review Letters **98**, 193601 (2007).

[42] I. Aharonovich, D. Englund and M. Toth, *Solid-state single-photon emitters,* Nature Photonics **10**, 631 (2016).

[43] N. Somaschi *et al.*, *Near-optimal single-photon sources in the solid state,* Nature Photonics **10**, 340 (2016).

[44] P. J. Mosley *et al.*, *Heralded Generation of Ultrafast Single Photons in Pure Quantum States,* Physical Review Letters **100**, 133601 (2008).

[45] C. P. Anderson *et al.*, *Electrical and optical control of single spins integrated in scalable semiconductor devices,* Science **366**, 1225 (2019).

[46] T. Grange *et al.*, *Cavity-Funneled Generation of Indistinguishable Single Photons from Strongly Dissipative Quantum Emitters,* Physical Review Letters **114**, 193601 (2015).

[47] H. Choi, D. Zhu, Y. Yoon and D. Englund, *Cascaded Cavities Boost the Indistinguishability of Imperfect Quantum Emitters,* Physical Review Letters **122**, 183602 (2019).

[48] Q. Zhang *et al.*, *Demonstration of a scheme for the generation of "event-ready" entangled photon pairs from a single-photon source,* Physical Review A **77**, 062316 (2008).

[49] K. C. Chen *et al.*, *Zero-Added-Loss Entangled-Photon Multiplexing for Ground- and Space-Based Quantum Networks,* Physical Review Applied **19**, 054029 (2023).

[50] F. Ewert and P. van Loock, *$3/4$-Efficient Bell Measurement with Passive Linear Optics and Unentangled Ancillae,* Physical Review Letters **113**, 140403 (2014).

[51] K. De Greve *et al.*, *Quantum-dot spin–photon entanglement via frequency downconversion to telecom wavelength,* Nature **491**, 421 (2012).

[52] A. Tchebotareva *et al.*, *Entanglement between a Diamond Spin Qubit and a Photonic Time-Bin Qubit at Telecom Wavelength,* Physical Review Letters **123**, 063601 (2019).

[53] J. Metz and S. D. Barrett, *Effect of frequency-mismatched photons in quantum-information processing,* Physical Review A **77**, 042323 (2008).

[54] T.-M. Zhao *et al.*, *Entangling Different-Color Photons via Time-Resolved Measurement and Active Feed Forward,* Physical Review Letters **112**, 103602 (2014).

[55] P. Kok *et al.*, *Linear optical quantum computing with photonic qubits,* Reviews of Modern Physics **79**, 135 (2007).

[56] V. Krutyanskiy *et al.*, *Entanglement of Trapped-Ion Qubits Separated by 230 Meters,* Physical Review Letters **130**, 050803 (2023).

[57] A. Pickston *et al.*, *Optimised domain-engineered crystals for pure telecom photon sources,* Optics Express **29**, 6991 (2021).

[58] A. O. C. Davis, P. M. Saulnier, M. Karpiński and B. J. Smith, *Pulsed single-photon spectrometer by frequency-to-time mapping using chirped fiber Bragg gratings,* Optics Express **25**, 12804 (2017).

[59] C. Figgatt *et al.*, *Parallel entangling operations on a universal ion-trap quantum computer,* Nature **572**, 368 (2019).

[60] A. Reiserer *et al.*, *Robust Quantum-Network Memory Using Decoherence-Protected Subspaces of Nuclear Spins,* Physical Review X **6**, 021040 (2016).

[61] K. Bergmann, N. V. Vitanov and B. W. Shore, *Perspective: Stimulated Raman adiabatic passage: The status after 25 years,* The Journal of Chemical Physics **142**, 170901 (2015).

[62] S. Maity *et al.*, *Coherent acoustic control of a single silicon vacancy spin in diamond,* Nature Communications **11**, 193 (2020).

[63] B. Pingault *et al.*, *Coherent control of the silicon-vacancy spin in diamond,* Nature Communications **8**, 15579 (2017).

[64] G. de Lange, Z. H. Wang, D. Ristè, V. V. Dobrovitski and R. Hanson, *Universal Dynamical Decoupling of a Single Solid-State Spin from a Spin Bath,* Science **330**, 60 (2010).

[65] C. T. Nguyen *et al.*, *Quantum Network Nodes Based on Diamond Qubits with an Efficient Nanophotonic Interface,* Physical Review Letters **123**, 183602 (2019).

[66] P.-J. Stas *et al.*, *Robust multi-qubit quantum network node with integrated error detection,* Science **378**, 557 (2022).

[67] L. Childress, J. M. Taylor, A. S. Sørensen and M. D. Lukin, *Fault-tolerant quantum repeaters with minimal physical resources and implementations based on single-photon emitters,* Physical Review A **72**, 052330 (2005).

[68] C. H. Bennett *et al.*, *Purification of Noisy Entanglement and Faithful Teleportation via Noisy Channels,* Physical Review Letters **76**, 722 (1996).

[69] D. Deutsch *et al.*, *Quantum Privacy Amplification and the Security of Quantum Cryptography over Noisy Channels,* Physical Review Letters **77**, 2818 (1996).

[70] E. T. Campbell and S. C. Benjamin, *Measurement-Based Entanglement under Conditions of Extreme Photon Loss,* Physical Review Letters **101**, 130502 (2008).

[71] N. Kalb *et al.*, *Entanglement distillation between solid-state quantum network nodes,* Science **356**, 928 (2017).

[72] T. Wilk, S. C. Webster, A. Kuhn and G. Rempe, *Single-Atom Single-Photon Quantum Interface,* Science **317**, 488 (2007).

[73] G. Wolfowicz *et al.*, *Quantum guidelines for solid-state spin defects,* Nature Reviews Materials **6**, 906 (2021).

[74] A. H. Kiilerich and K. Mølmer, *Input-Output Theory with Quantum Pulses,* Physical Review Letters **123**, 123604 (2019).

[75] A. H. Kiilerich and K. Mølmer, *Quantum interactions with pulses of radiation,* Physical Review A **102**, 023717 (2020).

[76] B. E. Saleh and M. C. Teich, *Chapter 11,* in *Fundamentals of Photonics* (Wiley, 2019).

[77] A. Yariv and P. Yeh, *Photonics: Optical Electronics in Modern Communications* (Oxford University Press, 2007).

[78] K. Ngan, Y. Zhan, C. Dory, J. Vučković and S. Sun, *Quantum Photonic Circuits Integrated with Color Centers in Designer Nanodiamonds,* Nano Letters **23**, 9360 (2023).

[79] H. Choi, M. Heuck and D. Englund, *Self-Similar Nanocavity Design with Ultrasmall Mode Volume for Single-Photon Nonlinearities,* Physical Review Letters **118**, 223605 (2017).

[80] A. S. Sheremet, M. I. Petrov, I. V. Iorsh, A. V. Poshakinskiy and A. N. Poddubny, *Waveguide quantum electrodynamics: Collective radiance and photon-photon correlations,* Reviews of Modern Physics **95**, 015002 (2023).

[81] M. O. Scully and M. S. Zubairy, *Quantum Optics* (Cambridge University Press, 1999).

[82] P. G. Kwiat *et al.*, *New High-Intensity Source of Polarization-Entangled Photon Pairs,* Physical Review Letters **75**, 4337 (1995).

[83] C. Couteau, *Spontaneous parametric down-conversion,* Contemporary Physics **59**, 291 (2018).

[84] J. R. Johansson, P. D. Nation and F. Nori, *QuTiP: An open-source Python framework for the dynamics of open quantum systems,* Computer Physics Communications **183**, 1760 (2012).

[85] T. Coopmans *et al.*, *NetSquid, a NETwork Simulator for QUantum Information using Discrete events,* Communications Physics **4**, 1 (2021).

[86] A. Dahlberg *et al.*, *A link layer protocol for quantum networks,* in *Proceedings of the ACM Special Interest Group on Data Communication,* SIGCOMM '19 (Association for Computing Machinery, Beijing, China, 2019) pp. 159–173.

[87] S. Diadamo, J. Nötzel, B. Zanger and M. M. Beşe, *QuNetSim: A Software Framework for Quantum Networks,* IEEE Transactions on Quantum Engineering **2**, 1 (2021).

[88] T. Matsuo, C. Durand and R. Van Meter, *Quantum link bootstrapping using a RuleSet-based communication protocol,* Physical Review A **100**, 052320 (2019).

[89] B. Bartlett, *A distributed simulation framework for quantum networks and channels,* (2018), arxiv:1808.07047 [physics, physics:quant-ph] .

[90] G. Thiering and A. Gali, *Ab Initio Magneto-Optical Spectrum of Group-IV Vacancy Color Centers in Diamond,* Physical Review X **8**, 021063 (2018).

[91] J. Dias, M. S. Winnel, N. Hosseinidehaj and T. C. Ralph, *Quantum repeater for continuous-variable entanglement distribution,* Physical Review A **102**, 052425 (2020).

[92] Y. Zheng, H. Sharma and J. Borregaard, *Entanglement Distribution with Minimal Memory Requirements Using Time-Bin Photonic Qudits,* PRX Quantum **3**, 040319 (2022).

[93] E. N. Knall *et al., Efficient Source of Shaped Single Photons Based on an Integrated Diamond Nanophotonic System,* Physical Review Letters **129**, 053603 (2022).

[94] R. E. Evans, *An Integrated Diamond Nanophotonics Platform for Quantum Optics*, Ph.D. thesis, Harvard University (2018).

[95] M. Reck, A. Zeilinger, H. J. Bernstein and P. Bertani, *Experimental realization of any discrete unitary operator,* Physical Review Letters **73**, 58 (1994).

[96] W. R. Clements, P. C. Humphreys, B. J. Metcalf, W. S. Kolthammer and I. A. Walmsley, *Optimal design for universal multiport interferometers,* Optica **3**, 1460 (2016).

4

A MULTINODE QUANTUM NETWORK OF REMOTE SOLID-STATE QUBITS

M. Pompili*, S. L. N. Hermans*, S. Baier*, H. K. C. Beukers, P. C. Humphreys, R. N. Schouten, R. F. L. Vermeulen, M. J. Tiggelman, L. dos Santos Martins, B. Dirkse, S. Wehner & R. Hanson

The distribution of entangled states across the nodes of a future quantum internet will unlock fundamentally new technologies. Here, we report on the realization of a three-node entanglement-based quantum network. We combine remote quantum nodes based on diamond communication qubits into a scalable phase-stabilized architecture, supplemented with a robust memory qubit and local quantum logic. In addition, we achieve real-time communication and feed-forward gate operations across the network. We demonstrate two quantum network protocols without postselection: the distribution of genuine multipartite entangled states across the three nodes and entanglement swapping through an intermediary node. Our work establishes a key platform for exploring, testing, and developing multinode quantum network protocols and a quantum network control stack.

The results of this chapter have been published in Science, **372**, 259-264 (2021).
* Equally contributing authors

4.1. INTRODUCTION

Future quantum networks sharing entanglement across multiple nodes[1,2] will enable a range of applications such as secure communication, distributed quantum computing, enhanced sensing, and fundamental tests of quantum mechanics[3–8]. Efforts in the past decade have focused on realizing the building blocks of such a network: quantum nodes capable of establishing remote entangled links as well as locally storing, processing, and reading out quantum information.

Entanglement generation through optical channels between a pair of individually controlled qubits has been demonstrated with trapped ions and atoms[9–12], diamond nitrogen-vacancy (NV) centers[13,14], and quantum dots[15,16]. In addition, a number of quantum network primitives have been explored on these elementary two-node links, including nonlocal quantum gates[17,18] and entanglement distillation[19]. Moving these qubit platforms beyond two-node experiments has so far remained an outstanding challenge owing to the combination of several demanding requirements. Multiple high-performance quantum nodes are needed that include a communication qubit with an optical interface as well as an efficient memory qubit for storage and processing. Additionally, the individual entanglement links need to be embedded into a multinode quantum network, requiring a scalable architecture and multinode control protocols.

Here, we report on the realization and integration of all elements of a multinode quantum network: optically mediated entanglement links connected through an extensible architecture, local memory qubit and quantum logic, and real-time heralding and feed-forward operations. We demonstrate the full operation of the multinode network by running two key quantum network protocols. First, we establish Greenberger-Horne-Zeilinger (GHZ) entangled states across the three nodes. Such distributed genuine multipartite entangled states are a key ingredient for many network applications[2] such as anonymous transmission[20], secret sharing[21], leader election[22], and clock stabilization[8]. Second, we perform entanglement swapping through an intermediary node, which is the central protocol for entanglement routing on a quantum network enabling any-to-any connectivity[23,24]. Owing to efficient coherence protection on all qubits, combined with real-time feed-forward operations, these protocols are realized in a heralded fashion, delivering the final states ready for further use. This capability of heralding successful completion of quantum protocols is critical for scalability; its demonstration here presents a key advance from earlier experiments using photons[25] and quantum memories[26].

Our network is composed of three spatially separated quantum nodes (Figure 4.1, A and B), labeled Alice, Bob, and Charlie. Each node consists of an NV center electronic spin as a communication qubit. In addition, the middle node Bob uses a carbon-13 nuclear spin as a memory qubit. Initialization and single-shot readout of the communication qubits are performed through resonant optical excitation and measurement of state-dependent fluorescence[14]. Universal quantum logic on the electronic-nuclear register is achieved through tailored microwave pulses delivered on chip (Section 4.6).

The nodes are connected through an optical fiber network for the quantum signals, as well as classical communication channels for synchronizing the control operations and relaying heralding signals (see below).

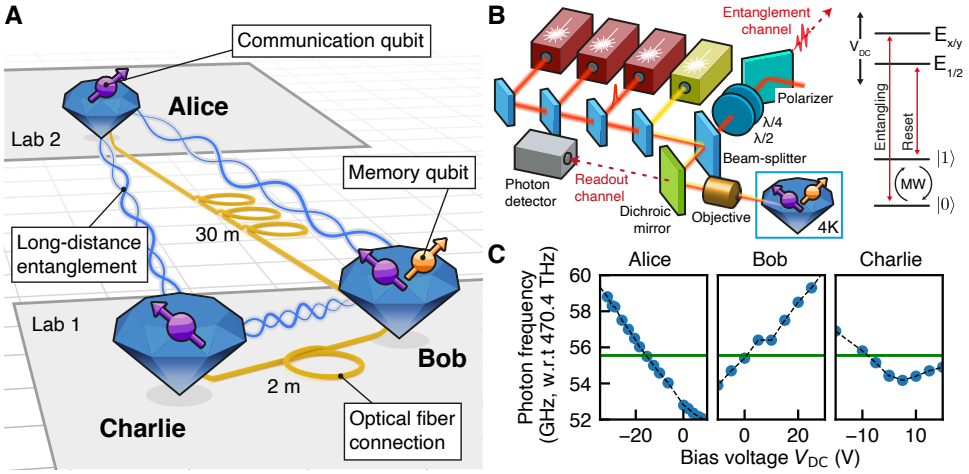

Figure 4.1: **The three-node quantum network.** **(A)** Layout of the network. Three nodes, labeled Alice, Bob, and Charlie, are located in two separate labs. Each node contains an NV center communication qubit (purple). At Bob, an additional nuclear spin qubit (orange) is used in the presented experiments. Fiber connections between the nodes (lengths indicated) enable remote entanglement generation on the links Alice-Bob and Bob-Charlie, which, combined with local quantum logic, allow for entanglement to be shared between all nodes (wiggly lines). **(B)** On the left is a simplified schematic of the optical setup at each node (see Figure 4.6, Table 4.1, and Section 4.6 for additional details). On the right is a diagram of the relevant levels of the electronic spin qubit, showing optical transitions for remote entanglement generation and readout ("entangling"), qubit reset ("reset"), and resonant microwaves ("MW") for qubit control (see Figures 4.7 and 4.14 for additional details). The memory qubit at Bob is initialized, controlled, and read out via the electronic qubit (Figure 4.8). Optical transition frequencies are tuned via the dc bias voltages (V_{DC}). $\lambda/2$ ($\lambda/4$) is a half-waveplate (quarter-waveplate); $E_{x/y}$ and $E_{1/2}$ are electronic excited states. **(C)** Tuning of the optical "entangling" transition at each of the three nodes. The solid line is the working point, 470.45555 THz; the dashed line is a guide to the eye. w. r. t. , with respect to.

Remote entanglement generation hinges on indistinguishability between emitted photons. For NV centers in high-purity low-strain diamond devices, the optical transition frequencies show relatively minor variations (few GHz). We remove the remaining offsets by using dc Stark tuning at each node with bias fields generated on chip (Figure 4.1C). We are thus able to bring the relevant optical transitions of all three nodes to the same frequency, which we choose to be the zero-bias frequency of Bob.

4.2. ESTABLISHING REMOTE ENTANGLEMENT IN A NETWORK ARCHITECTURE

To generate remote entanglement between a pair of nodes (i.e., one elementary link), a single-photon protocol is used[27,28] (Figure 4.2A). The communication qubits of the nodes are each prepared in a superposition state $|\alpha\rangle = \sqrt{\alpha}|0\rangle + \sqrt{1-\alpha}|1\rangle$. At each node,

pulsed optical excitation, which is resonant only for the $|0\rangle$ state, and subsequent photon emission deterministically create an entangled state between the communication qubit and the presence-absence of a photon (the flying qubit). The photonic modes from the two nodes are then interfered on a beam splitter, removing the which-path information. The beam splitter closes an effective interferometer formed by the optical excitation and collection paths. Detection of a single photon after the beam splitter heralds the state $|\psi^{\pm}\rangle \approx (|01\rangle \pm e^{i\Delta\theta}|10\rangle)/\sqrt{2}$ between the two communication qubits, where the $\pm$ sign depends on which of the two detectors clicked and $\Delta\theta$ is the optical phase difference between the two arms of the effective interferometer (Section 4.6). Experimentally, this phase difference is set to a known value by stabilizing the full optical path using a feedback loop [14,16]. This scheme yields states at maximum fidelity $1-\alpha$ at a rate $\approx 2\alpha p_{\text{det}} r_{\text{attempt}}$, with p_{det} the probability that an emitted photon is detected and r_{attempt} the entanglement attempt rate.

Scaling this entangling scheme to multiple nodes requires each elementary link to be phase-stabilized independently (Figure 4.2B), posing a number of new challenges. The different links, and even different segments of the same link, will generally be subject to diverse noise levels and spectra. Additionally, the optical power levels used are vastly different, from microwatts for the excitation path to attowatts for the single-photon heralding station, requiring different detector technologies for optimal signal detection. We solve these challenges with a hybrid phase-stabilization scheme that is scalable to an arbitrary number of nodes. We decompose the effective interferometer for each link into three independently addressable interferometers and stabilize each separately (see Figure 4.2C for the Alice-Bob link; the link Bob-Charlie is phase-stabilized in an analogous and symmetric way; see Figures 4.9 and 4.12).

First, each node has its own local stabilization that uses unbalanced heterodyne phase detection (Figure 4.2C, left). In comparison to the previous homodyne stabilization method [14], this enables us to obtain a higher bandwidth phase signal from the small part of the excitation light that is reflected from the diamond surface ($\approx$ 1%) by boosting it with a strong reference-light beam at a known frequency offset. Moreover, this scheme allows for optimal rejection of the reflected excitation light by polarization selection, thus preventing excitation light from entering the single-photon path toward the heralding detectors and creating false entanglement heralding events. The measured phase signals are fed back on piezoelectric-mounted mirrors to stabilize the local interferometers.

Second, the global part of the effective interferometer (Figure 4.2C, right) is stabilized by single-photon-level homodyne phase detection with feedback on a fiber stretcher: A small fraction of the strong reference-light beam is directed into the single-photon path, and the interference is measured using the same detectors used for entanglement generation.

This architecture provides scalability in the number of nodes and a higher feedback bandwidth compared with our previous implementation on a single link (Figure 4.13;

see Section 4.6 for details). In our current implementation, the central node – Bob – has combining optics to merge the signals coming from Alice and Charlie, so that the single-photon detectors can be shared by the two links.

Crucially, this architecture enables the successive generation of entanglement on the two elementary links as required for network protocols exploiting multinode entanglement. We benchmark its performance by running entanglement generation on both elementary links within a single experimental sequence (Figure 4.2D).

We achieve fidelities of the entangled Bell states exceeding 0.8 for both links (Figure 4.2E), on par with the highest fidelity reported for this protocol for a single link[14]. For the same fidelity, the entangling rates are slightly higher than in Ref.[14] (9 and 7 Hz for links Alice-Bob and Bob-Charlie, respectively), despite the additional channel loss from connecting the two links. The main sources of infidelity are the probability α that both nodes emit a photon, remaining optical phase uncertainty, and double excitation during the optical pulse (see Table 4.2 and Section 4.6). A detailed physical model that includes known error sources is used here and below for comparison to the experimental data (Section 4.6); predictions by the model are indicated by the gray bars in the correlation and fidelity plots.

4.3. MEMORY QUBIT PERFORMANCE AND REAL-TIME FEED-FORWARD OPERATIONS

To distribute entangled states across multiple nodes, generated entangled states must be stored in additional qubits while new entanglement links are created. Carbon-13 nuclear spins are excellent candidates for such memory qubits, thanks to their long coherence times, controllability, and isolation from the control drives on the electronic qubit[29]. Recent work[30] indicated that their storage fidelity under network activity is mainly limited by dephasing errors resulting from the coupling to the electronic spin that is randomized on failed entanglement generation. It was suggested that the memory robustness to such errors may be further improved by operating under an increased applied magnetic field. Here, we use a magnetic field of 189 mT for our central node, as opposed to $\approx$ 40 mT used in past experiments[19,30].

This higher field puts much stricter demands on the relative field stability in order to not affect the qubit frequencies; we achieve an order of magnitude reduction in field fluctuations by actively stabilizing the temperature of the sample holder, which in turn stabilizes the permanent magnet inside the cryostat (Section 4.6). Additionally, the higher magnetic field splits the two optical transitions used for electronic spin initialization, hindering fast qubit resets; the addition of a second initialization laser, frequency locked to the first one with an offset of 480 MHz, enables us to maintain high-fidelity (> 0.99) and fast (few microsecond) resets (Section 4.6).

We measure the fidelity of stored states on Bob's memory qubit for a varying number of entanglement generation attempts (Figure 4.3). The two eigenstates ($\pm Z$) do not show

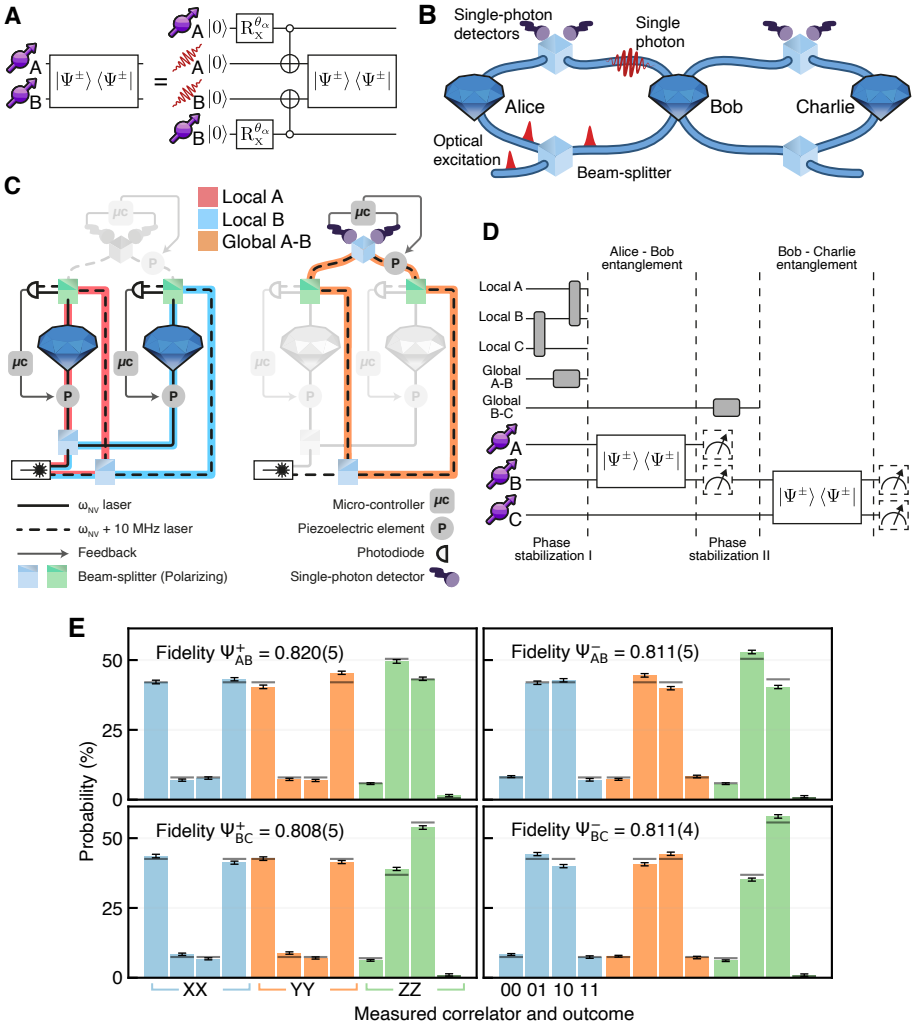

Figure 4.2: **Establishing remote entanglement in a network architecture.** **(A)** Circuit diagram of the single-photon entanglement protocol, where $R_X^{\theta_\alpha}$ is a rotation around the x axis with angle θ_α, $\theta_\alpha = 2\cos^{-1}(\sqrt{\alpha})$. **(B)** Sketch of three quantum network nodes in line configuration, showing the two effective interferometers. **(C)** Phase stabilization diagram of the Alice-Bob link, highlighting the local interferometers (left) and the global interferometer (right). See Section 4.6 for further details. **(D)** Experimental sequence to generate Bell pairs on both Alice-Bob (A-B) and Bob-Charlie (B-C) links. Dashed boxes display measurements used in (E). **(E)** Correlation measurements on entangled states on A-B (top) and B-C (bottom) links. The left plots correspond to $|\Psi^-\rangle$ states; the right plots correspond to $|\Psi^+\rangle$ states. Shown are observed probabilities for outcomes (from left to right) 00, 01, 10, and 11 for correlation measurements in the bases XX (blue), YY (orange), and ZZ (green). Gray bars depict values from the theoretical model. Error bars indicate one standard deviation.

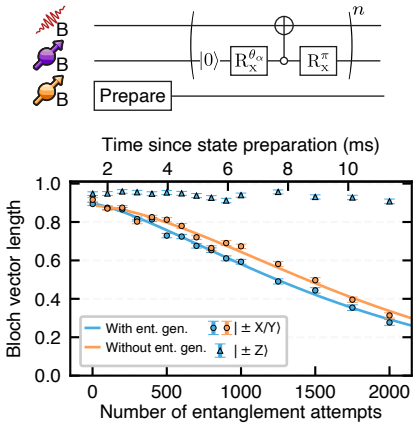

Figure 4.3: **Memory qubit coherence under network activity. (Top)** Circuit diagram displaying the experimental sequence, where n is the number of entanglement attempts. **(Bottom)** Blue represents the measured Bloch vector length of memory qubit eigenstates (triangles) and superposition states (circles) versus entanglement attempts, for $\alpha = 0.05$. Orange represents measured superposition decay versus time in the absence of entanglement attempts. Solid lines are fits, yielding decay constants of $N_{1/e} = 1843 \pm 32$ (2042 ± 36) with (without) entanglement generation attempts (see Table 4.5 and Section 4.6 for additional details).

appreciable decay as we increase the number of entanglement generation attempts, as expected from the pure dephasing nature of the process[30]. The superposition states degrade with an average decay constant of $N_{1/e} \approx 1800$ attempts. To gain insight into the contribution of network activity to this decay, we repeat these measurements in the absence of entanglement attempts, in which case dephasing of the memory qubit is mainly due to uncontrolled interactions with nearby nuclear spins. We find this intrinsic dephasing time to be $T_2^\star = 11.6(2)$ ms, equivalent to the duration of ≈ 2000 entanglement generation attempts. We conclude that the intrinsic dephasing accounts for most of the decay observed under network activity, indicating the desired robustness. For the experiments discussed below, we use a timeout of 450 attempts before the sequence is restarted, as a balance between optimizing entanglement generation rate and fidelity of the stored state.

Executing protocols over quantum networks requires real-time feed-forward operations among the various nodes: measurement outcomes at the heralding station or at nodes need to be translated into quantum gates on other nodes. We implement an asynchronous bidirectional serial communication scheme between microcontrollers at the nodes, enabling both the required timing synchronization of the nodes and the exchange of feed-forward information for the quantum network protocols (Section 4.6). Furthermore, we integrate the feed-forward operations with local dynamical decoupling protocols that actively protect the communication qubits from decoherence. The resulting methods enable us to run multinode protocols in a heralded fashion: *Flag* signals indicate in real time the successful execution of (sub)protocols and generation of desired states that are then available for further use, thus critically enhancing the efficiency and

removing the need for any postselection.

4.4. DEMONSTRATION OF MULTINODE NETWORK PROTOCOLS

We now turn to the full operation of the three-node network that combines the different elements discussed above. We perform two canonical network protocols: the distribution of genuine multipartite entanglement and entanglement swapping to two non–nearest-neighbor nodes.

In both protocols, the sequence depicted in Figure 4.4A is used to establish a remote entangled state on each of the two links. This sequence starts with a preparation step (depicted only in Figure 4.15) that synchronizes the microcontrollers of the nodes and makes sure that the NV centers in each node are in the desired charge state and in resonance with all the relevant lasers. After initialization of the memory qubit, the first entangled state is prepared on the link Alice-Bob. We interleave blocks of entanglement generation attempts with phase-stabilization cycles. Once Alice-Bob entanglement is heralded, Alice's entangled qubit is subject to a dynamical decoupling sequence while awaiting further communication from the other nodes. At Bob, deterministic quantum logic is used to swap the other half of the entangled state to the memory qubit.

The second part of the phase stabilization is then executed, followed by the generation of remote entanglement between the communication qubits of Bob and Charlie. In case of a timeout (no success within the preset number of attempts), the full protocol is restarted. In case of success, a dynamical decoupling sequence is started on Charlie's communication qubit analogous to the protocol on Alice. At Bob, a Z-rotation is applied to the memory qubit to compensate for the acquired phase that depends linearly on the (a priori unknown) number of entanglement attempts. This gate is implemented through an XY4 decoupling sequence on the communication qubit, with a length set in real time by the microcontroller based on which entanglement attempt was successful (Section 4.6). After this step, the two links each share an entangled state ready for further processing: one between the communication qubit at Alice and the memory qubit at Bob and one between the communication qubits of Bob and Charlie.

The first protocol we perform is the generation of a multipartite entangled GHZ state across the three nodes. The circuit diagram describing our protocol is depicted in Figure 4.4B. We first entangle the two qubits at Bob, followed by measurement of the communication qubit in a suitably chosen basis. The remaining three qubits are thereby projected into one of four possible GHZ-like states, which are all equivalent up to a basis rotation. The specific basis rotation depends both on the measurement outcome at Bob and on which Bell states ($|\Psi^+\rangle$ or $|\Psi^-\rangle$) were generated in the first part of the sequence, which in turn depends on which two photon detectors heralded the remote entangled states. These outcomes are communicated and processed in real time and the corresponding feed-forward operations are applied at Charlie. As a result, the protocol is able to achieve delivery of the same GHZ state $|\mathrm{GHZ}\rangle_{\mathrm{ABC}} = (|000\rangle + |111\rangle)/\sqrt{2}$, irrespective of the intermediate outcomes. Here, we choose to herald only on Bob

reporting the $|0\rangle$ readout outcome, because the asymmetry in the communication qubit readout fidelities renders this outcome more faithful (Section 4.6). Additionally, this choice automatically filters out events in which the NV center of Bob was in the incorrect charge state or off resonance (occurrence $\approx$ 10% in this experiment; see Section 4.6). With this heralding choice, the protocol delivers GHZ states at a rate of about 1/(90s).

We extract the fidelity to the ideal GHZ state from correlation measurements by using

$$F = (1 + \langle IZZ\rangle + \langle ZIZ\rangle + \langle ZZI\rangle + \langle XXX\rangle - \langle XYY\rangle - \rangle YXY\rangle - \langle YYX\rangle)/8 \tag{4.1}$$

and find $F = 0.538(18)$ (Figure 4.4C). The state fidelity above 0.5 certifies the presence of genuine multipartite entanglement distributed across the three nodes[31].

In this experiment, the fidelities of the entangled states on the elementary links bound the fidelity of the heralded GHZ state to about 0.66. Other relevant error sources are the dephasing of the memory qubit and accumulation of small quantum gate errors (see Table 4.3). We emphasize that, contrary to earlier demonstrations of distributed GHZ states with photonic qubits[25] and ensemble-based memories[26] that relied on postselection, we achieve heralded GHZ state generation: a real-time heralding signal indicates the reliable delivery of the states.

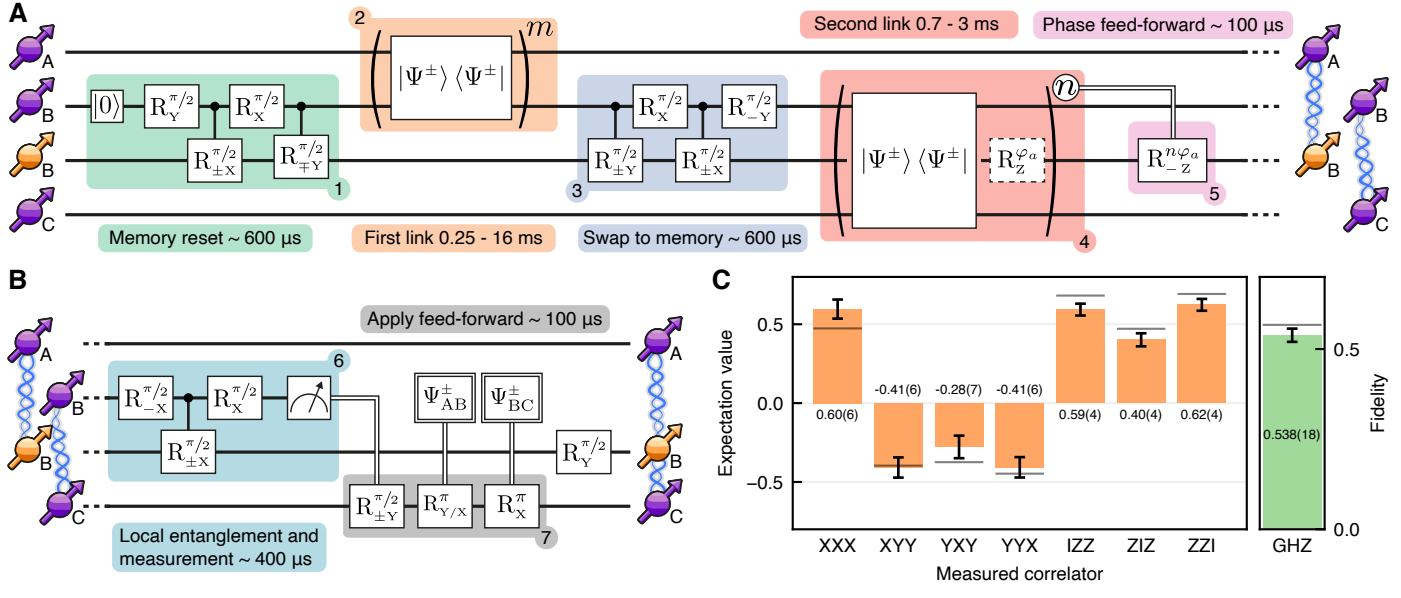

Figure 4.4: **Distribution of genuine multipartite entanglement across the quantum network.** **(A)** Circuit diagram displaying the experimental sequence used to establish entanglement on both elementary links. **(B)** Circuit diagram displaying the experimental sequence for distributing a three-partite GHZ state across the three nodes. **(C)** Outcomes of correlation measurements and the resulting fidelity of the heralded GHZ state, demonstrating genuine multipartite entanglement. Gray bars depict values from the theoretical model. Error bars indicate one standard deviation.

The second protocol, illustrated in Figure 4.5A, demonstrates entanglement swapping of the two direct links into an entangled state of the outer two nodes. Once entanglement is established on the two links as described above, the central part of the entanglement swapping is executed: Bob, the central node, performs a Bell state measurement (BSM) on its two qubits. One way to read this protocol is that the BSM induces teleportation of the state stored on Bob's memory qubit to Charlie, by consuming the entangled state shared by Bob's communication qubit and Charlie. Because the state teleported to Charlie was Bob's share of an entangled state with Alice, the teleportation establishes direct entanglement between Alice and Charlie.

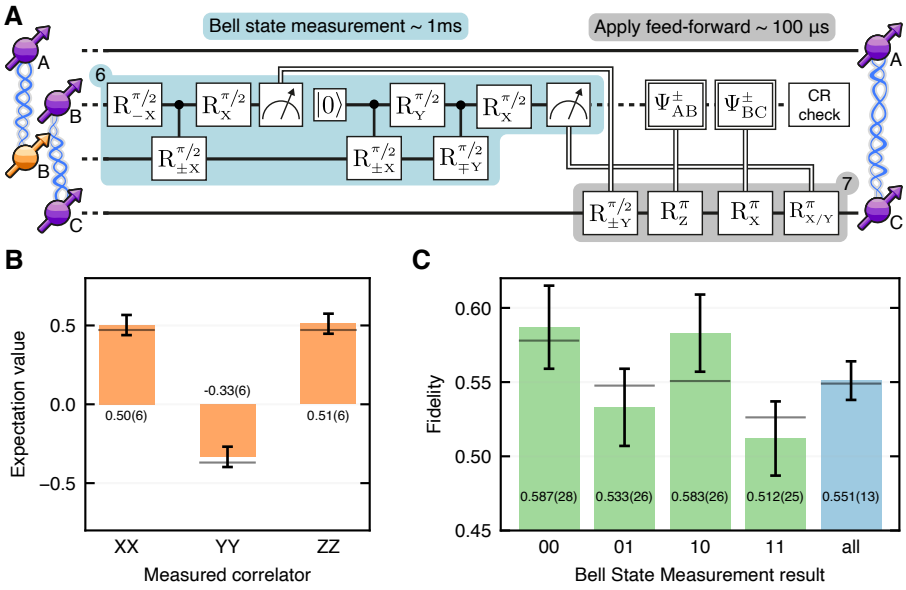

Figure 4.5: **Entanglement swapping on a multinode quantum network.** **(A)** Circuit diagram displaying the experimental sequence for entanglement swapping, yielding an entangled state shared between the two non-connected nodes. **(B)** Outcomes of correlation measurements on the heralded entangled state shared between Alice and Charlie for the selected Bell-state measurement outcome (see main text). **(C)** State fidelities for different outcomes of Bob's Bell-state measurement (green) and the state fidelity averaged over all outcomes (blue). In (B) and (C), gray bars depict values from the theoretical model, and error bars indicate one standard deviation.

After the BSM is completed, we perform a charge and resonance (CR) check on Bob to prevent heralding on events in which the NV center of Bob was in the incorrect charge state or off resonance. We note that this CR check was not used in the heralding procedure of the GHZ generation protocol because its current implementation induces decoherence on Bob's memory qubit, which is part of the final GHZ state to be delivered. To complete the entanglement swapping, feed-forward operations are performed at Charlie to account in real time for the different measurement outcomes, analogous to the previous protocol, resulting in the delivery of the Bell state $|\Phi^+\rangle_{AC} = (|00\rangle + |11\rangle)/\sqrt{2}$.

We assess the performance of the entanglement swapping by measuring three two-node correlators on the generated Bell state shared by Alice and Charlie. Because the BSM is performed with local quantum logic and single-shot readout, it is (except for the CR check step) a deterministic operation. However, given the asymmetry in the readout errors as discussed above, the fidelity of the final state will depend on the readout outcomes. Figure 4.5B shows the results of the correlation measurements on the delivered state for heralding on Bob obtaining twice the outcome $|0\rangle$, yielding a state fidelity of $F = 0.587(28)$. Figure 4.5C compares the state fidelities across the different BSM outcomes, displaying the expected lower fidelities for outcomes of $|1\rangle$ and an average fidelity over all outcomes of $F = 0.551(13)$. The combined heralding rate is $1/(40\text{s})$. The sources of infidelity are similar to the ones discussed above (see Table 4.4). This experiment constitutes the first demonstration of entanglement swapping from previously stored remote entangled states, enabled by the network's ability to asynchronously establish heralded elementary entanglement links, to store these entangled states, and then to efficiently consume them to teleport entanglement to distant nodes.

4.5. CONCLUSION AND OUTLOOK

We have demonstrated the realization of a multinode quantum network. We achieved multipartite entanglement distribution across the three nodes and any-to-any connectivity through entanglement swapping. It is noteworthy that the data acquisition for the network protocols has been performed fully remotely because of the COVID-19 pandemic, highlighting the versatility and stability of our architecture. Near-term advances in the capabilities and performance of the network will be driven by further reducing the infidelities of the elementary links (Section 4.6), by adding new subprotocols such as control methods[29], decoupling sequences[30], and repetitive readout[32] for the nuclear spin qubits; by improved photonic interfaces to enhance the entangling rates[33–35]; and by improved control over the charge state of the NV center[36].

Our results open the door to exploring advanced multinode protocols and larger entangled states, for instance, by extending the local registers at the nodes. We note that a fully controlled 10-qubit register has recently been demonstrated on a similar device[29]. Furthermore, the network provides a powerful platform for developing and testing higher-level quantum network control layers[37–39], such as the recently proposed link layer protocol for quantum networks[40]. Quantum frequency conversion of the NV photons[41] can be used to interface the network nodes with deployed telecom fiber, paving the way to near-term quantum network tests over metropolitan distances. Finally, we expect the methods developed here to provide guidance for similar platforms reaching the same level of maturity in the future[42–45].

4.6. SUPPLEMENTARY INFORMATION

4.6.1. EXPERIMENTAL SETUP

Our experiments are performed on three quantum network nodes. Each node houses a Nitrogen-Vacancy (NV) center in a high-purity type-IIa chemical-vapor-deposition diamond cut along the ⟨111⟩ crystal orientation (Element Six). All three samples have a natural abundance of carbon isotopes. Fabrication of solid immersion lenses and an anti-reflection coating on the diamond samples enhances the photon-collection efficiencies from the NV centers. The samples are housed in home-built cryogenic confocal microscope setups at 4 K. Experimental equipment used for each node is summarized in Table 4.1. In the following we use the letters A, B and C to identify nodes Alice, Bob and Charlie. The numbers 0, 1 refer to the computational basis $|0\rangle, |1\rangle$. Node A is in a different laboratory than nodes B and C, 7 m away. Nodes B and C are on the same optical table, approximately 2 m apart, see also Figure 4.1A of the main text. The optical fiber that connects A with B is 30 m long, while the one that connect B to C is 2 m long.

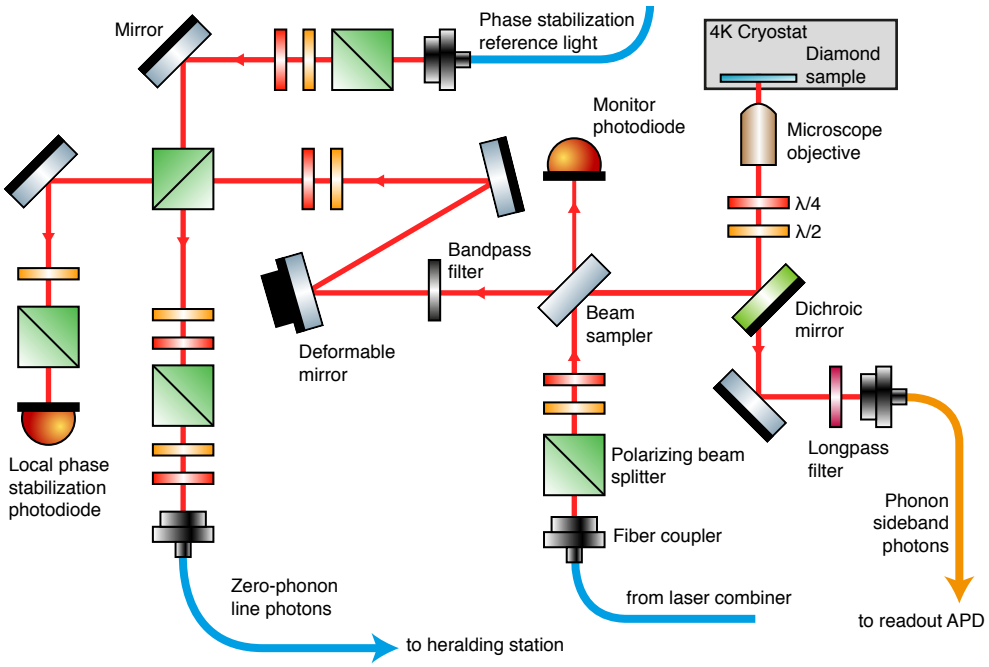

Figure 4.6: **Schematic of the optics used for each node.** The red lines indicate the optical path used both by the laser beams and the single photons. Blue fibers are single-mode polarization maintaining fiber. The orange fiber is a multi-mode fiber. The laser combiner (not depicted) combines, via beam-splitters and dichroic mirrors, the various laser beams and couples them into the single-mode fiber shown in the diagram. The laser combiner also includes a piezoelectric-mounted mirror that is used for the local phase stabilization feedback. The monitor photodiode records the 90% of excitation light that goes through the beam-sampler (and that would otherwise be discarded). We monitor this signal on a digital oscilloscope connected to the measurement computers for debugging purposes.

Table 4.1: **Experimental equipment used in the three nodes.** Non-listed equipment is unchanged from previous experiments and identical for the three setups.

	Alice	Bob	Charlie
Cryostat	attocube attoDRY800	Montana Instruments Cryostation S50	Montana Instruments Cryostation S50
Positioner	Sample on attocube xyz stack	Microscope objective on PI P-615	Microscope objective on PI P-615
Micro-controller	Jäger ADwin-Pro II T12	Jäger ADwin-Pro II T12	Jäger ADwin-Pro II T12
Arbitrary Waveform Generator (AWG)	Tektronix AWG5014	Tektronix AWG5014C	Tektronix AWG5014C
MW source	R&S SGS100A SGMA - up to 6 GHz	R&S SGS100A SGMA - up to 12.75 GHz	R&S SGS100A SGMA - up to 6 GHz
MW amplifier	AR 40S1G4	AR 25S1G4A	AR 40S1G4
Entangling and qubit readout laser	Toptica TA-SHG pro 637 nm	Toptica DL pro 637 nm	Toptica TA-SHG pro 637 nm
Qubit reset laser	Toptica DL pro 637 nm	1 - Toptica TA-SHG pro 637 nm 2 - New Focus Velocity 637 nm	New Focus Velocity 637 nm
Charge reset laser	Toptica DL-SHG pro 575 nm	Cobolt 515 nm	Toptica DL-SHG pro 575 nm
EOM	Jenoptik AM635		Jenoptik AM635
Deformable mirror	Boston Micromachines 12x12	Boston Micromachines 12x12	Boston Micromachines 12x12

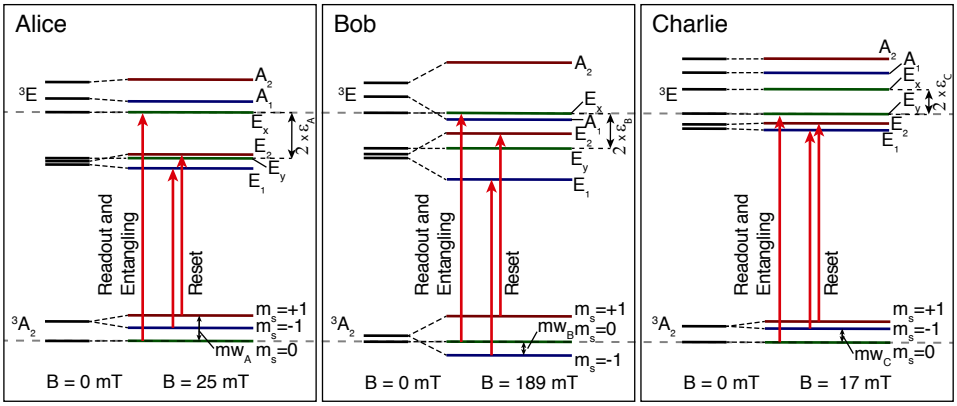

Figure 4.7: **Level structure for the three NV centers.** The optical transitions used within this work are indicated by red solid arrows. DC stark tuning brings all readout transitions to the same frequency, ensuring that the photons generated via the optical excitation pulse are indistinguishable. The spin state $m_S = 0/+1/-1$ of each level is indicated by color (green/red/blue). The communication qubits of nodes A, B and C are encoded in the NV center electronic spin states $|0/1\rangle_A \equiv |m_S = 0/+1\rangle$, $|0/1\rangle_B \equiv |m_S = 0/-1\rangle$ and $|0/1\rangle_C \equiv |m_S = 0/-1\rangle$. The memory qubit of node B is encoded in the nuclear spin state of the addressed ^{13}C atom, $|0/1\rangle \equiv |m_I = \pm\frac{1}{2}\rangle$.

Figure 4.6 depicts the optics used to deliver and collect light to each sample. For phonon-sideband (PSB) detection, a dichroic mirror (Semrock) and an additional long-pass filter (Semrock) are used to block reflections of the excitation lasers. Photon emission is detected via an avalanche photo-diode (APD, Laser components, quantum efficiency approximately 80 %), with a total collection efficiency of approximately 10 %. For zero-phonon line (ZPL) detection, we isolate the single photons first with a narrow bandpass filter (5 nm, Semrock), then by blocking the reflected excitation light via two polarising beam-splitters (Thorlabs and Semrock). Spatial mode shaping via a deformable mirror (Boston Micromachines) enhances coupling to a polarization-maintaining single-mode fiber. The optical signals from each node are combined on in-fiber polarization-maintaining beam-splitters (Evanescent Optics). The final beam-splitter (where the single photons interfere) has an integrated fiber stretcher used for optical phase stabilization. Finally, the single photons are detected on superconducting nanowire single photons detectors (Photon Spot). They are optimized for 637 nm, have a detection efficiency >95 % and a dark count rate < 1 Hz.

The level structures of the three nodes are depicted in Figure 4.7. Each structure depends on local strain, electric fields and the applied magnetic field B. For nodes A and B the magnetic field is created with a permanent neodymium magnet inside the cryostat, which is located close to the sample and attached to the sample holder. The magnetic field is fine-tuned to be along the symmetry axis of the NV center using permanent neodymium magnets outside the cryostat. Node C has only a single permanent magnet outside the cryostat.

For optical excitation we set the laser frequencies (red arrows in Fig. 4.7) to the

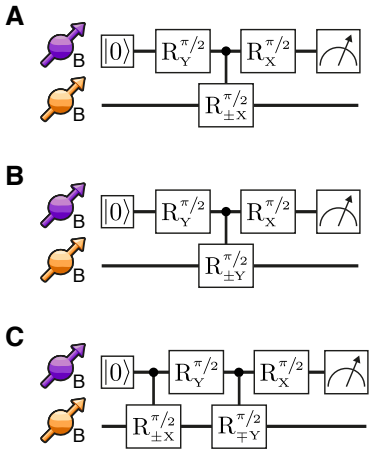

Figure 4.8: **Memory qubit readout sequences. (A-C)** Readout sequences of the nuclear spin memory qubit expectation values for $\hat{X}, \hat{Y}, \hat{Z}$ via the communication qubit. The controlled rotations are to be read as follows: $R_{\pm X}^{\pi/2}$ is a rotation of the memory qubit around the X axis with an angle of $\pi/2$ if the communication qubit is in $|0\rangle$, and with an angle of $-\pi/2$ if the communication qubit is in $|1\rangle$.

corresponding $^3A_2$ to ^3E transition. Spin-selective excitation of ZPL transitions (λ = 637.25 nm, $\omega = 2\pi \times 470.45$ THz) enables qubit readout ("Entangling" in Fig. 1B of the main text, $m_s = 0 \longleftrightarrow E_{x/y}$) and qubit reset via optical spin-pumping ("Reset" in Fig. 1B of the main text, $m_s = \pm 1 \longleftrightarrow E_{1,2}$). While at low field a single laser is sufficient to address both qubit reset transitions, in case of node B, which operates at 189 mT, we find a reset transitions splitting of 480 MHz. An additional laser is implemented in order to drive both reset transitions efficiently.

In order to tune the readout transitions of each NV center into resonance we employ the DC Stark effect via DC-biasing the strip-line that is used to deliver microwave (MW) signals. The feedback sequence is analogous to the one used in Ref.[46]. Node B operates at 0 V tuning (it is grounded), and it uses non resonant charge reset with a green laser (515 nm). We observe small day to day drift in the readout frequency of node B that we attribute to slow ice build-up on the sample as the transition frequency can be brought back to its original value by a warm-up cool-down cycle. Nodes A and C, which use resonant charge reset with a yellow laser (575 nm), are brought into resonance with node B before starting a measurement.

The memory qubit of node B is the nuclear spin of a ^{13}C atom in the proximity of the NV center. Its electronic-spin-dependent precession frequencies are $\omega_0 = 2\pi \times 2025$ kHz and $\omega_{-1} = 2\pi \times 2056$ kHz, resulting in parallel hyperfine coupling of $A_\parallel \approx 2\pi \times 30$ kHz. The nuclear spin is controlled using dynamical decoupling sequences[19,29]. The conditional $\pi/2$-rotations on the nuclear spin are performed with 56 decoupling pulses with an inter-pulse delay of $2\tau = 2 \times 2.818$ μs. Gate sequences to readout the memory qubit via the communication qubit are summarized in Fig. 4.8.

For synchronization purposes, the micro-controllers at each node (Jäger ADwin-Pro II T12) share a common 1 MHz clock. To increase the on-off ratio of the AOM RF drivers, and therefore reduce unwanted light leakage, we use home-built fast (150 ns rise-time) RF switches, based on the HMC8038 (Analog Devices), to disconnect the RF drivers from the AOMs when no power should be delivered. We terminate the MW delivery line on each cryostat with a home-built MW envelope detector, that allows us to see on an oscilloscope the microwave pulses being delivered to each sample. We use this for debugging purposes. Parts that are not mentioned in the description above are the same as in Refs. [14,19,46].

4.6.2. MODEL OF THE GENERATED STATES

MODEL AND SOURCES OF ERROR

The Python code to model all the generated states and to produce the figures in the main text can be found at[47]. The Jupyter notebooks that generate the figures make direct use of that code to plot the simulated states. The communication qubits of nodes A, B and C are encoded in the NV center electronic spin states $|0/1\rangle_A \equiv |m_S = 0/+1\rangle$, $|0/1\rangle_B \equiv |m_S = 0/-1\rangle$ and $|0/1\rangle_C \equiv |m_S = 0/-1\rangle$. The memory qubit of node B is encoded in the nuclear spin state of the addressed ^{13}C atom, $|0/1\rangle \equiv |m_I = \pm\frac{1}{2}\rangle$.

Regarding the generation of Bell states on the Alice-Bob and Bob-Charlie links, we extend the model presented in Ref. [14] to allow for different values of the parameters α in the two nodes. We find that to obtain maximum state fidelity the condition $\alpha_A p_A^{\text{det}} \approx \alpha_B p_B^{\text{det}}$ must hold, where $\alpha_{A,B}$ are the populations of the $|0\rangle$ state of each node and $p_{A,B}^{\text{det}}$ is the probability of detecting a photon emitted by the respective node in the detection window. The state that is heralded by the protocol is the following (assuming $p^{\text{det}} \ll 1$):

$$\rho_{AB}^{\pm} = \frac{1}{p_{\text{tot}}} \begin{pmatrix} p_{00} & 0 & 0 & 0 \\ 0 & p_{01} & \pm\sqrt{V p_{01} p_{10}} & 0 \\ 0 & \pm\sqrt{V p_{01} p_{10}} & p_{10} & 0 \\ 0 & 0 & 0 & p_{11} \end{pmatrix}, \tag{4.2}$$

$$p_{00} = \alpha_A \alpha_B (p_A^{\text{det}} + p_B^{\text{det}} + 2p_{\text{dc}}), \tag{4.3}$$

$$p_{01} = \alpha_A (1-\alpha_B)(p_A^{\text{det}} + 2p_{\text{dc}}), \tag{4.4}$$

$$p_{10} = \alpha_B (1-\alpha_A)(p_B^{\text{det}} + 2p_{\text{dc}}), \tag{4.5}$$

$$p_{11} = 2(1-\alpha_A)(1-\alpha_B) p_{\text{dc}}, \tag{4.6}$$

$$p_{\text{tot}} = p_{00} + p_{01} + p_{10} + p_{11} \tag{4.7}$$

where V is the visibility of the two-photon quantum interference, $p_{\text{dc}} \ll 1$ is the probability of detecting a dark count (or in general a non-NV photon) in the detection window, the $\pm$ sign depends on which detector clicked. The off-diagonal terms neglect the contribution due to the dark counts with respect to the contribution due to $p_{A,B}^{\text{det}}$, i.e. we assume $p_{\text{dc}} \ll p_{A,B}^{\text{det}}$.

Table 4.2: **Error budget of the generated Bell states and experimental parameters.** The error due to the probability that both nodes emit a photon is related to the values of α (see section 4.6.2) and is therefore intrinsic to the protocol. The infidelity contribution for each of the other errors is estimated as if that error were the only other error present, this way one can easily compare the relative effect of the different infidelity sources. When combined we take into account all the errors at the same time.

Source of infidelity	Expected state infidelity	
	Alice - Bob	Bob - Charlie
Probability that both nodes emit a photon	6.1e-2	8.0e-2
Phase uncertainty	6.0e-2	1.5e-2
Double excitation	5.5e-2	7.0e-2
Photon distinguishability	2.4e-2	2.3e-2
Non-NV and dark counts	5e-3	5e-3
Combined	0.191	0.186
Measured Ψ^+ infidelity	0.180(5)	0.192(5)
Measured Ψ^- infidelity	0.189(5)	0.189(4)
Experimental parameters	Alice - Bob	Bob - Charlie
p_{det}	$p_A^{\text{det}} = 3.6e-4$ $p_B^{\text{det}} = 4.4e-4$	$p_B^{\text{det}} = 4.2e-4$ $p_C^{\text{det}} = 3.0e-4$
α	$\alpha_A = 0.07$ $\alpha_B = 0.05$	$\alpha_B = 0.05$ $\alpha_C = 0.10$
p_{dc}	1.5e-7	1.5e-7
Visibility V	0.90	0.90
Phase uncertainty	30^o	15^o
Entanglement attempt duration	3.8 μs	5.0 μs
Probability of double excitation	0.06	0.08

If one assumes $p_{\text{det}} = p_A^{\text{det}} = p_B^{\text{det}}$, $p_{\text{dc}} = 0$, $\alpha = \alpha_A = \alpha_B$ and $V = 1$, then the fidelity of ρ_{AB} with the closest Bell state is $F = 1 - \alpha$, and the generation rate is $r_{AB} = 2\,\alpha\,p_{\text{det}}\,r_{\text{attempt}}$, with r_{attempt} the attempt rate.

Additional sources of infidelity are uncertainty in the phase of the entangled state and double excitation. See Ref.[14] for details on how they are modeled. We summarize in Table 4.2 the infidelity arising from the aforementioned sources, which is reasonably in agreement with the measured state fidelities. The Bell states between Alice and Bob were generated with $\alpha_A, \alpha_B = 0.07, 0.05$, while the ones between Bob and Charlie with $\alpha_B, \alpha_C = 0.05, 0.10$. These values have been chosen as a trade-off between protocol success rate and fidelity.

To model the states generated in the two demonstrated protocols (GHZ state between Alice Bob and Charlie, and Bell state between Alice and Charlie) we take into account:

- the Bell states generated between Alice and Bob and between Bob and Charlie,

Table 4.3: **Error budget of the generated GHZ states.** For each source of infidelity considered we estimate two quantities: the infidelity induced on the state as if it were the only source of error present; the improvement in fidelity if that error were to be removed while all other errors remain present. When combined we take into account all the errors at the same time.

Source of infidelity	Expected infidelity if only source present	Expected improvement once removed
Ψ_{AB} state infidelity	0.191	0.120
Ψ_{BC} state infidelity	0.186	0.122
Memory qubit depolarising noise	8.3e-2	4.4e-2
Memory qubit dephasing noise	2.8e-2	1.5e-2
Dynamical decoupling of A and C	3.7e-2	1.9e-2
At least one node is in NV^0	1.6e-2	8e-3
Feed-forward errors	6e-3	3e-3
Ψ_{AB} and Ψ_{BC} combined	0.337	0.275
Combined	0.433	
Measured GHZ infidelity	0.462(18)	

- the dephasing of the nuclear spin during the entanglement generation between Bob and Charlie,
- depolarising noise on the nuclear spin that combines initialisation, swap and readout error,
- communication qubit readout errors at Bob that would generate a wrong feed-forward operation at Charlie,
- the depolarising noise on the communication qubits of Alice and Charlie during their dynamical decoupling sequences,
- the possibility that Alice and/or Charlie are in the wrong charge state (NV^0) at the end of the sequence.

Table 4.3 and Table 4.4 summarize the error budget of the generated states. In the case of the entanglement swapping we also report the expected infidelity when accepting any Bell state measurement (BSM) result.

In the protocol demonstrating GHZ distribution across the three nodes we chose to herald on readout outcome “0" only, as explained in the main text. Our model predicts that GHZ states heralded on measurement outcome “1" would have had an additional 3% infidelity (due to the asymmetry in the electron readout infidelities).

FUTURE IMPROVEMENTS TO THE REMOTE ENTANGLEMENT LINKS

The remote entanglement fidelity can be increased in the near term by improving phase stabilization at Alice to a similar level as Bob and Charlie, by lowering the double-excitation probability through a reduction of the optical excitation pulse width,

Table 4.4: **Error budget of the generated Alice-Charlie states.** For each source of error considered we estimate two quantities: the infidelity induced on the state as if it were the only source of error present; the improvement in fidelity if that error were to be removed while all other errors remain present. When combined we take into account all the errors at the same time. Errors reported for different Bell state measurement (BSM) results.

Source of infidelity	Expected infidelity if only source present	Expected improvement once removed
Ψ_{AB} state infidelity	0.191	0.115
Ψ_{BC} state infidelity	0.186	0.109
Memory qubit depolarising noise	8.2e-2	4.0e-2
Memory qubit dephasing noise	2.8e-2	1.2e-2
Dynamical decoupling of A and C	3.7e-2	1.7e-2
At least one node is in NV^0	1.6e-2	6e-3
Feed-forward errors (00 BSM result)	1.3e-2	6e-3
Feed-forward errors (any BSM result)	7.5e-2	3.4e-2
Combined (00 BSM result)	0.422	
Combined (any BSM result)	0.451	
Measured Φ_{AC} infidelity (00 BSM result)	0.413(28)	
Measured Φ_{AC} infidelity (any BSM result)	0.449(13)	

and by using similar devices with higher collection efficiency[46] allowing for operation at smaller α. Additionally, an improvement in fidelity of approximately $\eta_{\mathrm{PSB}}(\alpha + p_{2e})$ (where η_{PSB} is the probability to collect a photon in the phonon sideband emission and p_{2e} is the probability of double excitation during the optical pulse) can be obtained by rejecting heralding events for which simultaneously a photon was detected in the phonon sideband emission channel on one of the nodes. In the same way, this filtering will reduce the errors due to double excitation during the optical pulse as well as errors due to heralding on dark counts. This rejection could be implemented in real-time using an additional FPGA on each node. The combination of these improvements would bring the entanglement fidelity above 0.90.

Going beyond the current hardware, the entanglement generation rates may be increased by up to two orders of magnitude by enhancing the collection of coherent NV photons through the use of optical cavities[33,35]. Alternatively, the development of other color centers in optical waveguides and/or cavities may bring a similar improvement in rates[42–45].

4.6.3. PHASE STABILIZATION

Inherent to an implementation where active phase stabilization is interleaved with free evolution time, there is a trade-off between phase stability (or fidelity of the entangled state) and the free evolution time (which is the time used for entanglement generation). The more often the system is stabilized, the higher the bandwidth of the stabilization and the lower the final uncertainty in $\Delta\theta$ will be.

Our previous implementation used a single homodyne phase detection scheme[14]. While that method allows for the stabilization of the phase of the entangled state, there are several aspects that can be improved; The small fraction of excitation light that is reflected from the diamond surface is partially coupled in the single-photon detection path. By measuring the interference signal after the beam-splitter at the heralding station it is possible to obtain the phase of the interferometer. But leaking some of the reflected excitation light into the single-photon path for phase stabilization purposes increases the chance that, during entanglement generation, some of the reflected excitation light will be detected and mistakenly herald an entangled state. To counteract this effect, the amount of leaked light was somewhat minimized by polarization selection (but never completely, since some light is needed to detect a phase signal) and long integration times (24 ms) were used during phase detection, reducing the phase stabilization bandwidth. Furthermore, exposing the NV center to a relatively long and strong laser pulse makes it more susceptible to spectral jumps and ionization.

To solve these challenges we devised and implemented a new phase stabilization scheme that combines higher bandwith and optimal rejection of the excitation light from the single-photon paths, while maintaining robustness against power level fluctuations and scalability to a higher number of nodes.

PHASE DETECTION METHODS

In a homodyne phase detection scheme the light has the same frequency in both arms of the interferometer. Depending on the optical phase difference $\Delta\theta$, light will constructively or destructively interfere on the output ports of the beam-splitter. Assuming common polarization and perfectly overlapping spatial modes, the intensity $I_{3,4}$ in the output ports is

$$I_{3,4} = I_1 + I_2 \pm 2\sqrt{I_1 I_2}\cos\Delta\theta. \tag{4.8}$$

For known input levels $I_{1,2}$, $\Delta\theta$ can be calculated from the difference in intensity in the output ports of the beams-splitter. Fluctuations in the intensity of the input signals will lead to an error in the phase measurement, except for the case $\cos\Delta\theta = 0$ which gives $I_3 = I_4$ independent of the input intensity.

In a heterodyne phase detection scheme the light has different frequencies in the two arms of the interferometer. Again, assuming common polarization and perfectly overlapping modes, the light will interfere in the output ports resulting in a signal with amplitude

$$I_{3,4} = I_1 + I_2 \pm \sqrt{I_1 I_2}\big(\cos((\omega_1 - \omega_2)t - \Delta\theta) + \cos((\omega_1 + \omega_2)t + \Delta\theta)\big) \tag{4.9}$$

where $\omega_{1,2}$ are the angular frequencies of the light. When we pick a relatively small frequency difference, $(\omega_1 - \omega_2)/2\pi \approx 10$ MHz, we can ignore the last term in Eq. 4.9 and the resulting 10 MHz beat signal can be measured with a photodiode and efficiently filtered from the DC background signal (the last term of Eq. 4.9 will have a frequency in the optical domain and will not be picked up by the photodiode due to the limited bandwidth). The phase of this beat signal corresponds to the optical phase difference in the two paths. Since the phase information is not translated to the amplitude of the beat signal, fluctuations in the input intensity will not cause an error in the measurement. Moreover, this method is very suitable to measure small signals: if the signal is very small in one of the arms, the amplitude of the beat signal can be increased by increasing the intensity in the other arm.

SPLITTING THE INTERFEROMETER IN PARTS

In the experiments with three quantum nodes we have two effective interferometers that share part of their optical paths. We split the interferometers into six parts, see Figures 4.9, 4.10. In total there are four local interferometers and two global interferometers, where the local interferometer comprises the excitation path and free space optical path close to the cryostat of each node and the global interferometer includes the fibers connecting the nodes to the central beam-splitter. With the measured phase, an error signal is computed and feedback is applied to the optical path, either with a mirror on a piezoelectric element or a fiber stretcher.

The two global interferometers, using homodyne phase detection, stabilize the optical path to the beam-splitter and single photon detectors used for entanglement heralding. Since the detectors are shared for the two entanglement links, the optical phase measurement for the two global interferometers has to be multiplexed in time. The local interferometers are stabilized using heterodyne phase detection. The excitation light

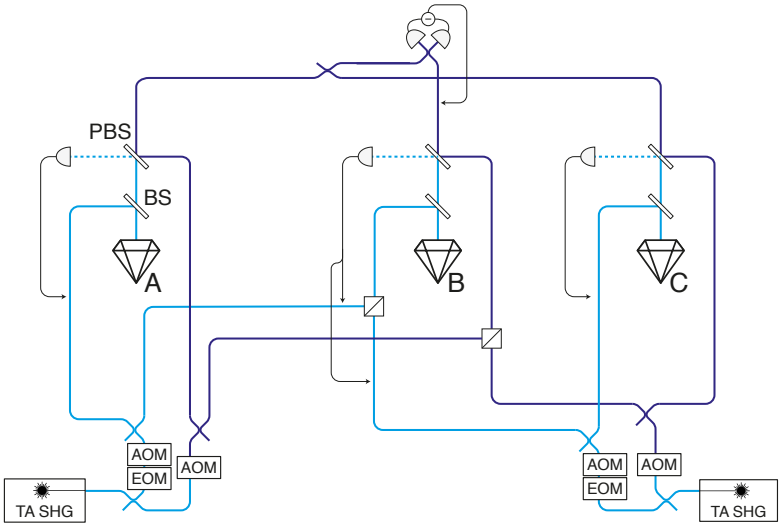

Figure 4.9: **Diagram of the entire layout.** Shown are the paths used by the excitation laser (solid light-blue lines) and the phase light (solid dark-blue lines), which has a frequency offset of $\approx 10MHz$ with respect to the excitation laser. The frequency offset is generated using different frequency modulation set-points for the acousto-optic modulators (AOM) in the excitation and phase path respectively.

(the same we use for the optical excitation pulse that generates spin-photon entanglement) is reflected off the diamond surface and since it has (close to) orthogonal polarization with the NV centers emitted photons it can be separated from the single photons using a polarizing beam-splitter (PBS). Afterwards, the weak reflected excitation pulse interferes with a strong laser pulse from the other arm with the frequency offset. The beat signal is measured with a photodiode and the optical phase difference is extracted using an electronic reference signal. The middle node has two local interferometers, one for each link. When all separate interferometers are stabilized, the paths of the excitation light and the single photons used for entanglement heralding will be phase stable.

TECHNICAL DESCRIPTION OF THE LOCAL INTERFEROMETER

For all the local interferometers we use a heterodyne phase detection scheme. A diagram of the optics and electronics is plotted in Figure 4.11. For each entanglement link (Alice-Bob and Bob-Charlie) the phase and excitation light are provided by the outer nodes (Alice and Charlie). To generate the known 10 MHz frequency offset between the light paths, we take advantage of the acousto-optic modulators (AOMs) we use to generate light pulses. By driving two AOMs at respectively 200 MHz and 210 MHz, we establish the required frequency difference between the light paths. Part of the RF signals used to drive the AOMs are tapped off and combined in a mixer to obtain an electronic reference signal. The light from the AOMs is launched in a free space path with several optical elements. The first polarizing beam-splitter (PBS) ensures the phase light to be linearly polarized. The second PBS separates the reflected excitation light from the sin-

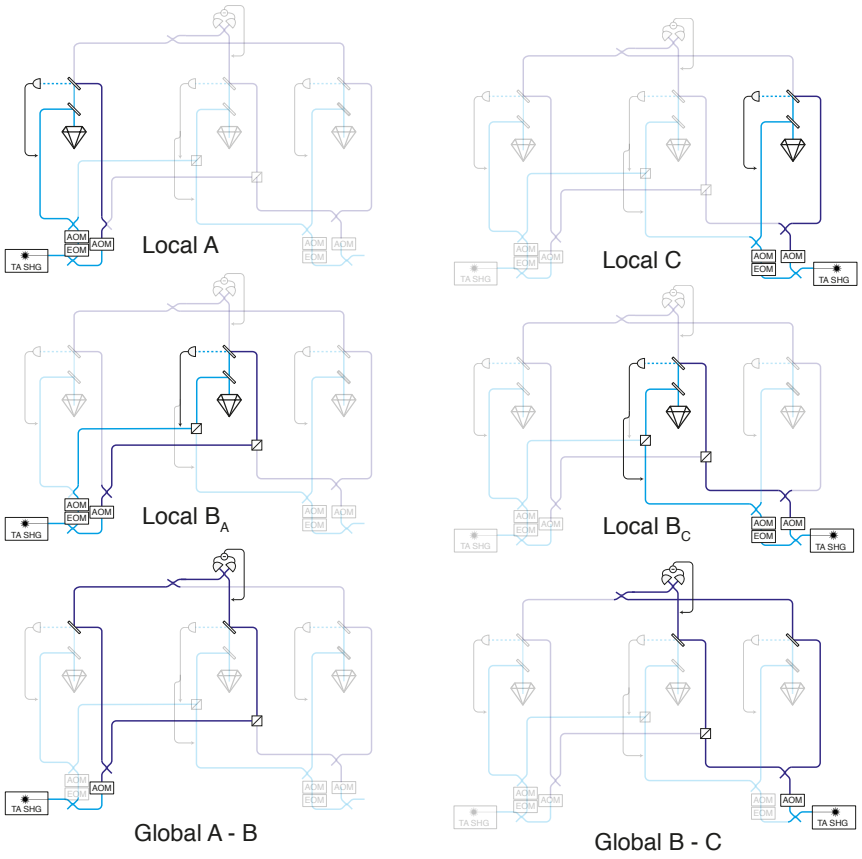

Figure 4.10: **Diagrams of the six interferometers in which the optical set-up is divided.** For the local interferometers, the heterodyne beat signal (dashed light-blue lines) is measured, compared to an electronic reference signal and feedback is applied to the optical path via piezo-electric mounted mirrors. For the global interferometers, the interference is measured by the single photon detectors. The detectors are shared for the two entanglement links using a beam-splitter that combines the photons from Alice with photons from Charlie. A feedback signal is applied to a fiber stretcher which is also shared by the two global interferometers.

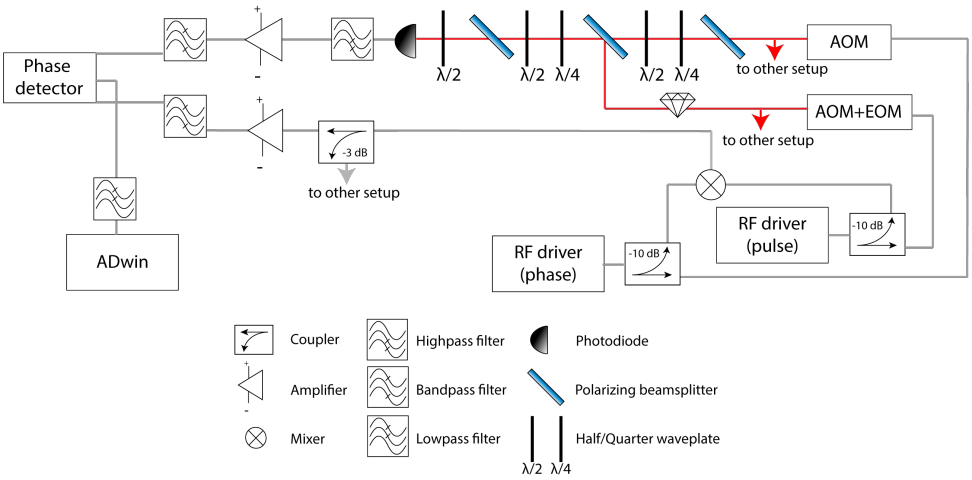

Figure 4.11: **Diagram of the electronics and optics for a local interferometer using a heterodyne phase detection scheme.** Both the electronic reference signal and the excitation light are shared with another setup.

gle photons. At this point the phase-reference light and the reflected excitation light have orthogonal polarization. The waveplates in front of the third beam-splitter rotate their polarization such that they can be interfered on the third PBS. This interference leads to a beating signal that can be detected with the photodiode. Consequently, the beating signal is filtered, amplified and, together with the electronic reference signal, used as inputs for the phase detector (Mini-Circuits ZRDP-1+). The output of the phase detector is filtered and impedance matched to an analog to digital converter (ADC) input of the micro-controller, the ADwin.

TIMINGS

The phase stabilization requires synchronization between the different nodes. Nodes A and C provide the phase and excitation light, but all nodes measure the phase of at least one local interferometer. Some of the detectors used for the phase measurements are shared among different interferometers, so not all measurements can be done at the

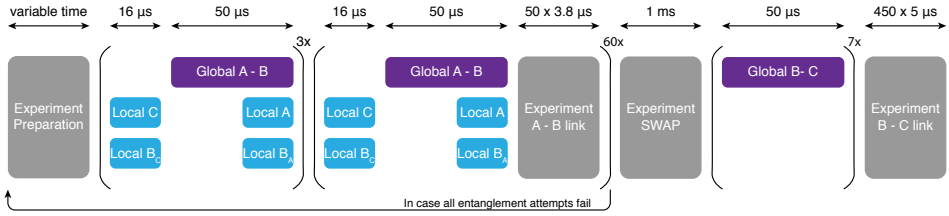

Figure 4.12: **Overview of the timings related to the phase stabilization.** Experimental time (gray blocks) is interleaved with phase stabilization cycles, which include a phase measurement and a feedback. The subscript to B indicates which light is used, either from setup A or C. The local phase stabilization of A and B_A and the global phase stabilization A−B can be performed at the same time since they use the same light sources.

same time. Figure 4.12 shows how the various phase stabilization cycles are interleaved with entanglement generation time.

The choice of free evolution time is governed by the noise sources in the different parts of the system. The local interferometer of node A experiences noise with high frequency components (compared to the other intereferometers) hence the free running time must be short enough to achieve the necessary feedback bandwith. The duration of the preparation part of the experiment, which includes charge and resonance checks, as well as synchronization steps between nodes, can vary from approximately 50 μs to a few seconds. When the phase is completely scrambled due to a too long free running time, it is not possible to reach the set-point in a single feedback round. For this reason we start with multiple rounds of phase stabilization without any free evolution time in between.

PHASE STABILITY

To characterize the performance of the phase stabilization we look at three different aspects: the free evolution of the phase without any stabilization, the frequency spectrum of the noise and the distribution of the phase while actively stabilizing. All the results for the six interferometers are plotted in Figure 4.13 (see Fig. 4.10 for the labeling). The differences in performance can be explained by the noise sources present in our experimental lay-out. We identify two main sources of noise: the relatively noisy fiber connection between nodes A and B and the positioning stages of each node. The three nodes are built in two separates rooms and we use optical fibers (30 m) to connect node A to node B. All nodes have a microscope objective for optically accessing the diamond samples. On node B and C this microscope objective is mounted on a piezo-electric stage. For node A the design is different: here the sample is mounted on a piezo-stack and the microscope objective is fixed. All these piezo-electric stages are susceptible to the vibrations generated by the operation of the cryostats.

The sample stage of node A cause relatively-strong high-frequency (> 500 Hz) noise; the microscope objective stage of nodes B and C cause lower-frequency noise and the optical fiber connection between nodes A and B causes relatively-strong low-frequency components. In the experimental sequence we interleave experimental time with rounds of phase stabilization. With the used timings (see Fig. 4.12) we are able to stabilize frequencies ≤ 500 Hz. Due to its relatively high-frequency components, the noise of the local interferometer of node A is the limiting factor in terms of phase stability of the overall apparatus. We expect that fixing the sample to the cold-finger of the cryostat, and only moving the microscope objective (like we do on nodes B and C) will allow us to lower the phase noise on node A in the future.

ENTANGLED-STATE PHASE DRIFTS

While the phase stabilization scheme allows us to access the entangled state generated by the single photon protocol by fixing the phase $\Delta\theta$, we observe that the phase of the generated entangled state undergoes small drifts on a timescale of hours. That is, even though all the interferometers are stabilized to the same value, the phase of the entangled state will slowly drift by $\approx 10^o$/hour. We hypothesize that these drifts are due to

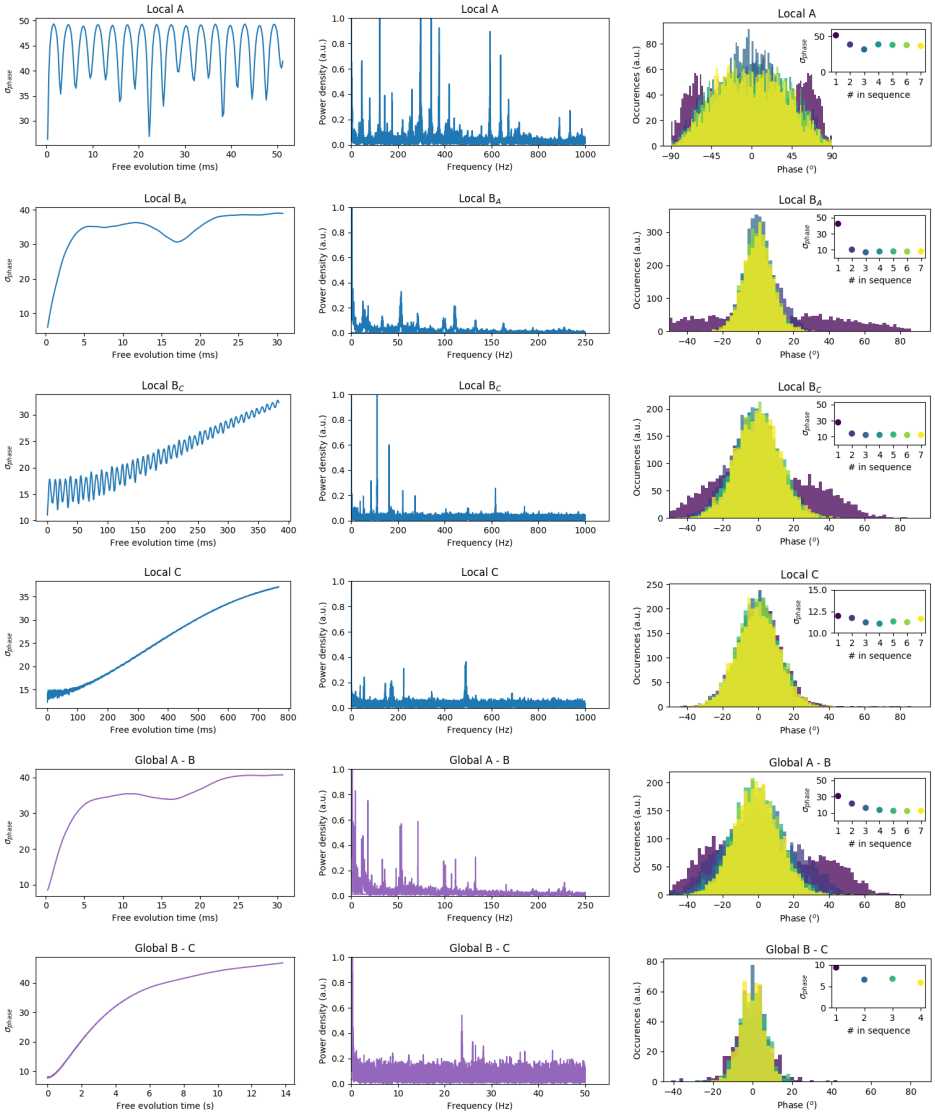

Figure 4.13: **Characterization of the phase stabilization of all six interferometers. (Left)** Standard deviation of the measured phase while changing the free evolution time. **(Center)** Frequency spectrum of the measured noise. **(Right)** Phase distribution for the different rounds of phase stabilization. **(Insets)** Standard deviation of the phase per stabilization round.

the relative position of the microscope objective and the NV center: while the light used for phase stabilization is reflected off the diamond surface, the NV-emitted photons are generated inside the diamond. Small changes in distance and angle of the microscope objective would not lead to observable differences in the fluorescence measurement we use for position optimization, but may slightly alter the path the photons have to travel. To solve this challenge, after every position optimization (≈ once every hour), we re-calibrate the phase of the generated entangled state (≈ 5 minute measurement per link). More robust positioning systems (both for the sample and the microscope objective) may reduce the phase drifts and alleviate the need for entangled-phase re-calibration.

4.6.4. SINGLE-SHOT READOUT CORRECTION

We correct tomography-related single-shot readouts (SSROs) for known error in order to obtain a reliable estimate of the actual generated states.

SINGLE QUBIT CASE

For a single qubit:

$$\vec{m} = \hat{R}\,\vec{p}, \tag{4.10}$$

where $\vec{p} = (p_0, p_1)^T$ is the (column) vector of expected populations, $\vec{m} = (m_0, m_1)^T$ is the (column) vector of measured populations, and

$$\hat{R} = \begin{pmatrix} r_{00} & r_{01} \\ r_{10} & r_{11} \end{pmatrix} = \begin{pmatrix} F_0 & 1-F_1 \\ 1-F_0 & F_1 \end{pmatrix}$$

is the SSRO operator that connects the two. For example:

$$m_0 = F_0\,p_0 + (1-F_1)\,p_1,$$

i.e. the measured population in $|0\rangle$ is given by the correctly assigned population in $|0\rangle$ plus the incorrectly assigned population in $|1\rangle$. From Eq. 4.10 it follows that:

$$\vec{p} = \hat{R}^{-1}\vec{m}, \tag{4.11}$$

which is what we use in practice to apply the readout correction. This allow us to obtain the vector of expected populations given the measured populations and the SSRO error operator. Experimentally we cannot directly measure $\vec{m}$. We measure events in which the communication qubit is either in $|0\rangle$ or in $|1\rangle$. We repeat this process N times, obtaining N_0 times the outcome $|0\rangle$ and N_1 times the outcome $|1\rangle$. From this we estimate the measured populations $\vec{m}$:

$$m_0 = N_0/N, m_1 = N_1/N \tag{4.12}$$

The probability distribution of the number of events N_0 is a Binomial distribution with expected value $N m_0$ and variance $N m_0(1-m_0)$. From this it is possible to calculate the experimental value and uncertainty for m_0 (and m_1):

$$m_0 = N_0/N \tag{4.13}$$

$$m_1 = 1 - m_0 \tag{4.14}$$

$$\sigma_{m_0} = \sigma_{m_1} = \sqrt{\frac{m_0}{N}(1-m_0)} \tag{4.15}$$

The covariance between m_0 and m_1 is:

$$\mathrm{Cov}(m_0, m_1) = -\frac{m_0(1-m_0)}{N} \tag{4.16}$$

Once Eq. 4.11 has been calculated it is possible to evaluate the expectation value of $\vec{p}$ and its uncertainty. In the one qubit scenario it is easy to invert the expression analytically:

$$p_0 = \frac{F_1\ m_0 + (F_1 - 1)\ m_1}{F_0 + F_1 - 1} = \frac{F_1 + m_0 - 1}{F_0 + F_1 - 1} \tag{4.17}$$

$$p_1 = \frac{(F_0 - 1)\ m_0 + F_0\ m_1}{F_0 + F_1 - 1} = \frac{F_0 - m_0}{F_0 + F_1 - 1} = 1 - p_0 \tag{4.18}$$

$$\sigma_{p_0} = \sigma_{p_1} = \frac{\sigma_{m_0}}{F_0 + F_1 - 1} \tag{4.19}$$

and it is straightforward to propagate uncertainties in $F_{0/1}$ to p_0 and p_1.

TWO AND THREE QUBIT CASE

For two (and more) qubits, the measurement outcomes will be distributed according to a Multinomial distribution (as opposed to a Binomial). While the expectation values of $p_0, \ldots, p_i$ can still be computed analytically relatively straightforwardly, their uncertainties need to take into account the non-trivial covariances in the m_i. Additionally, taking into account uncertainties in the $F_{0/1}$ makes the error propagation even more tedious. We therefore use a Monte Carlo simulation that takes into account the Multinomial distribution as well as the $F_{0/1}$ of each setup to estimate uncertainties on the correlation measurements and the state fidelities, without having to assume normality of the data. The code to run the Monte Carlo simulation is included in the Jupyter notebooks that produce the figures of the main text[47].

4.6.5. PHASE FEED-FORWARD ON THE MEMORY QUBIT

The nuclear spin memory qubit of Bob precesses at a frequency that depends on the spin state of the electronic spin (the communication qubit). Throughout the experimental sequence we keep track of the phase acquired by the nuclear spin to be able to readout and apply gates in the correct bases. While most operations are deterministic in time (nuclear spin initialisation, gates on the electronic spin, etc.) and the phase evolution of the nuclear spin can be calculated in advance, entanglement generation is a probabilistic process. This means that it is not known in advance how long the entanglement operation (number of entanglement attempts) is going to take, and therefore how much phase the nuclear spin is going to acquire. To solve this challenge, we implement a phase feed-forward mechanism that applies a Z-rotation to the nuclear spin that cancels this acquired phase. Since the used Arbitrary Waveform Generator (AWG) only has limited real-time programming capability, we implement this mechanism via a real-time interaction between our node micro-controller (ADwin) and the AWG. Once entanglement is heralded between Bob and Charlie, the AWG of Bob jumps out of the entanglement generation subroutine and starts an XY4 decoupling sequence on the communication qubit. During this XY4, the AWG interacts with the ADwin of Bob (which has recorded how much phase the nuclear spin has acquired during the entanglement operation) to

select, via a binary decision tree, the time in between microwave pulses. The binary decision tree allows us to vary the (additional) duration of the XY4 element in steps of 2 ns up to 512 ns, which is more than a 2π precession for the nuclear spin (τ_L =490 ns, feed-forward resolution $\approx 1.5^o$). Regardless of the inter-pulse time selected, the communication qubit will be decoupled. Consequently, the needed additional phase to re-phase the nuclear spin can be conveniently set via the length of the XY4 sequence. We pre-compile the timings that the ADwin will communicate to the AWG to reduce the computational load on the ADwin. We anticipate that an AWG with an integrated programmable FPGA will be able to completely take over the task of phase tracking without need for interaction with the node micro-controller, reducing experimental overhead.

4.6.6. MEMORY QUBIT LIFETIME AND INCREASED MAGNETIC FIELD

An important resource in our experiments is the ability to store entanglement in the nuclear spin memory qubit of Bob while performing further operations on the node. While we have implemented methods to keep track and actively compensate for the phase acquired during entanglement generation (see previous section), additional dephasing may occur. The major source of nuclear spin dephasing during entanglement generation was found to be[30] failed electronic spin control (initialization errors or MW pulse errors).

An entanglement attempt can be broken into the following pieces: communication qubit reset (via optical pumping), MW pulse that creates the communication qubit superposition (named in the following the α pulse), optical excitation pulse that creates the spin-photon entanglement, and a decoupling MW π pulse. The time τ between the α and the de-coupling pulse is chosen such that it equals the time between the decoupling pulse and the average reset time in the subsequent entanglement attempt (see Ref.[30] for details). This ensures that regardless of its initial state, the communication qubit spends an equal amount of time in the $|0\rangle$ and $|1\rangle$ states. However, an error in the MW π pulse will result in an unknown acquired phase on the nuclear spin and lead to dephasing. Previous work[30] suggested that such dephasing can be mitigated when working at a higher magnetic field, which allows for a shorter spacing between subsequent MW pulses.

In order to work at higher fields we have installed a stronger permanent magnet inside the cryostat of Bob reaching a field of 189 mT at the location of the NV center. At such fields, temperature fluctuations of the magnet, mainly due to the MW pulses applied to the sample, can result in a significant change of the magnetic field amplitude. Hence, we stabilize the sample holder via an active feedback loop, ensuring a stable temperature of the permanent magnet. We reach a stability of 1 μT, which results in a maximum variation of the nuclear spin precession frequency of $\approx$ 10 Hz, one order of magnitude below the dephasing rate due to interactions with other spins in its environment.

These improvements allow us to shorten the interpulse spacing to 942 ns, limited by the waiting time after the optical excitation pulse that we need to include in order to

allow the AWG to respond in real time to a successful entanglement attempt and jump out of the entangling sequence. As Figure 4.3 of the main text shows, a similar nuclear memory lifetime is observed when applying entanglement attempts or when idling. This shows that the lifetime of the memory qubit, in our magnetic field regime, is mainly limited by natural dephasing and not by electronic spin control errors. We fit the two decays with the following function:

$$f(N) = A\exp\left(-\left(\frac{N}{N_{1/e}}\right)^n\right), \tag{4.20}$$

with N the number of entanglement generation attempts, $N_{1/e}$ the N at which the Bloch vector length has decayed to $1/e$ of its initial value A, and n the exponent of the decay. The results of the fit are reported in Table 4.5. For the results *Without ent. gen.* the entanglement generation attempt is replaced by the equivalent free evolution time.

Table 4.5: **Fit results of memory qubit lifetime curves.** Fit results for the curves displayed in Figure 4.3 with and without entanglement generation (Ent. Gen.). See section 4.6.6 for details on the fitting function.

	With Ent. Gen.	Without Ent. Gen.
$N_{1/e}$	1843(32)	2042(36)
n	1.37(5)	1.61(6)
A	0.895(6)	0.885(6)

4.6.7. MICROWAVE PULSE FIDELITY

Errors in the MW pulses can limit the control of the communication qubit as well as induce decoherence on the nuclear spin memory qubit[30]. We use Hermite MW pulse envelopes[29] to perform rotations of the communication qubit spin:

$$h(t) = \left(1 - p\left(\frac{t}{T}\right)^2\right)e^{-\left(\frac{t}{T}\right)^2}, \tag{4.21}$$

where p affects the shape of the pulse and T changes the length of the pulse. The pulses get distorted by the transmission line before they get to the sample. We apply a linear pre-distortion in frequency domain to compensate part of the error via the following IQ signals:

$$I = a \cdot h(t) \tag{4.22}$$

$$Q = ab\frac{t}{\pi T^2}\left(p + 1 - p\left(\frac{t}{T}\right)^2\right)e^{-\left(\frac{t}{T}\right)^2}, \tag{4.23}$$

where a is the amplitude of the pulse and b is the skewness (slope) of the pre-distortion in frequency domain.

The MW π-pulses are calibrated by initializing the qubit in the $|0\rangle$ state, applying an odd number of consecutive pulses and reading out the final state. If the pulses were perfect one would measure $|1\rangle$ as outcome. The effect of the skewness on the pulse fidelity is

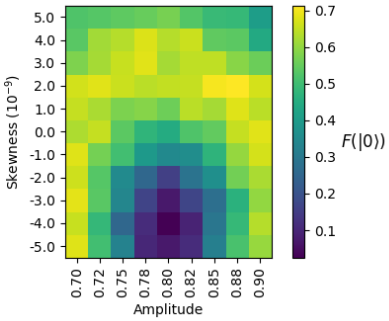

Figure 4.14: **Calibrating the pre-distorted microwave (MW) Hermite pulses**. The π pulses are calibrated by applying 11 sequential pulses: the probability of being in $|0\rangle$ at the end of the sequence is measured for different amplitudes (a) and skewness (b) of the Hermite pulse. The linear frequency pre-distortion allows us to achieve lower errors for the MW pulses.

investigated with a two dimensional scan; evaluating the fidelity for pulses with different amplitudes (a) and skewness (b). Figure 4.14 shows an example of such a scan, where it is clear one can calibrate a and b almost independently. We find that different set-ups require different levels of pre-distortion b, ranging from e-11 to e-8. We estimate that the current errors of our MW pulses are between 0.1 % and 1 % for all the three nodes.

4.6.8. CLASSICAL COMMUNICATION

The three nodes can share information in several ways. The slowest method is based on Python socket interfaces between the measurement computers that allow us to share necessary values and information at a rate of approximately 10 Hz; this method is used for example to frequency lock the lasers, to coordinate calibrations on all nodes from a single computer and to share and record environmental data such as the temperature in the different laboratories. The second, and fastest, method is a direct connection between the micro-controller and the AWGs. This enables the triggering of all the AWGs from a single node, reducing jitter on the output waveforms. The third method is implemented on the micro-controllers and is used for the feed-forward operations across the nodes. Each micro-controller has one input and one output communication port (physically it is a normal digital input-output coaxial port). Bob, which receives signals from both Alice and Charlie, has a digital summing box (OR gate) at its input port, that combines the signals coming from the other two nodes. We designed the experimental sequence such that it is clear who sent a specific message depending on when it arrives. Messages are sent over an off-the-shelf coaxial cable, using a serial communication scheme, with an average bit interval of 60 ns(the shortest the micro-controller can achieve). At the input port of each micro-controller, a fast edge detection (100 MHz) stores changes in the signal level (and the time at which they occur). It is therefore possible to reconstruct what pattern (i.e. message) was sent from one node to the other, directly on the micro-controller. Sending a message takes up to 300 ns (we send up to 5 bits at a time). Receiving and decoding take up to 2 μs combined. A flowchart of

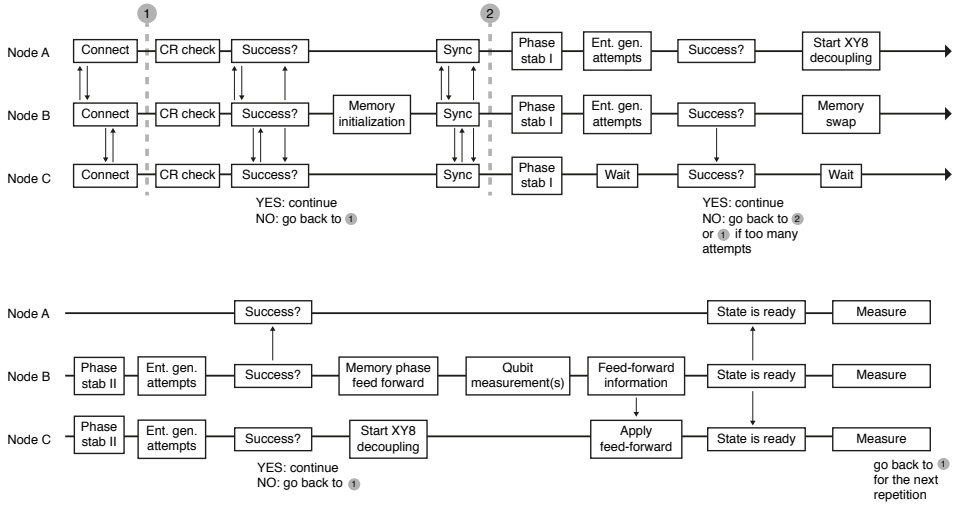

Figure 4.15: **Flowchart of the network protocols demonstrations.** The micro-controllers of the three nodes exchange information to synchronize the experimental sequence and apply feed-forward operations. Vertical lines between the nodes represent communication steps.

the communication steps between the micro-controllers used in the networks protocols demonstrated in the main text is shown in Figure 4.15.

4.6.9. FEED-FORWARD OPERATIONS BETWEEN NODES

We implement the feed-forward operations needed for our experimental protocols by combining the classical communication just discussed with a real-time pulse selection sequence by the micro-controller on the AWG. For both network protocols demonstrated we need to apply gates on the communication qubit of Charlie conditional on measurement outcomes at Bob. Once Bob has performed the required readout operations (on the communication qubit for the GHZ state generation or on both qubits for the entanglement swapping) it combines the readout results with the Bell states generation outcomes (i.e. which detectors clicked in the A-B and B-C entanglement generation) to obtain one of four possible feed-forward messages. Combining this information on Bob is an optimization of our communication resources; we could, alternatively, send the bits of information one by one to Charlie and combine the information there should that be a requirement of the protocol (for example in a blind quantum computation scenario). At this point a *FAIL* message could also be sent from Bob to all the nodes in order to abort the whole sequence, for example if the Bell State Measurement result is not the one that gives high-fidelity (see main text). We choose to not send *FAIL* messages and instead continue with the protocol to be able to assess the protocol performance for the less faithful Bell State Measurement outcomes (see Fig. 5C of the main text). In the meantime, Charlie has been applying an XY8 decoupling sequence to the communication qubit to protect its coherence while Bob performed the readout operations. Once Charlie receives the feed-forward information, its micro-controller starts a decision-tree

sequence with its AWG to select the required microwave pulse-sequence. This decision tree is incorporated into an XY8 block of the AWG, such that the slow response time of the AWG (1 μs per bit of information) does not affect the coherence of the communication qubit. The microwave pulse sequence selected via the decision tree is appended to the aforementioned XY8 block. After the feed-forward operations are performed, the delivery of the states by the network protocol is completed. Finally, the delivered states are analyzed using a readout sequence (composed of an optional basis rotation and state readout).

4.6.10. DATA ACQUISITION AND CALIBRATIONS

The data supporting the protocol demonstrations in the main text (Figures 4C, 5B, 5C) was gathered in the month of October 2020. Due to the restrictions imposed by the COVID19 pandemic, we operated the setups remotely (from home) and went to the laboratories only when something needed in-situ intervention (like a broken power-supply).

The data has been collected in blocks of approximately 1 hour, interleaved by calibration routines of approximately 20 minutes. For the GHZ state generation protocol we set the target number of data points at 2000. For the entanglement swapping we set the target number of data points at 4000. We stopped the experiment once the measurement block was completed in which the target number of data points was surpassed.

For the GHZ state generation we acquired 55 blocks over 10 days (effective measurement time $\approx$ 50 hours), obtaining 2028 events, equivalent to a rate of $r_{\mathrm{GHZ}} \approx (90\mathrm{s})^{-1}$.

For the entanglement swapping demonstration we acquired 53 blocks over 7 days (effective measurement time $\approx$ 45 hours), obtaining 853 events with BSM result "00", equivalent to a rate of $r_{\mathrm{swapping}} \approx (3\mathrm{min})^{-1}$. The other BSM results were: "01": 1030 events, "10": 1004 events, "11": 1168 events. The ratio of events between the BSM results matches the readout characteristics of node B: measured (expected) share of the events, $0.21:0.25:0.25:0.29$ ($0.23:0.25:0.25:0.27$). Combining all the BSM results we obtained a total of 4055 events, equivalent to a rate $r'_{\mathrm{swapping}} \approx (40\mathrm{s})^{-1}$.

Every three measurement blocks we performed a fidelity check on the entangled states between Alice-Bob and Bob-Charlie at the target α (total duration 20 minutes). These fidelity checks, combined over the GHZ and Entanglement Swapping datasets, are used for Figure 4.2E of the main text. We performed a total of 58 fidelity checks, that combined generated: 24197 Ψ^+_{AB} events, 25057 Ψ^-_{AB} events, 26383 Ψ^+_{BC} events and 27459 Ψ^-_{BC} events. The asymmetry in the number of events between the Ψ^+ and the Ψ^- states is due in part to the beam-splitter having a non ideal splitting ratio ($0.493:0.507$), to a slight difference in detector efficiencies ($\approx 1\%$) and to the brightnesses ($\alpha\ p_{\mathrm{det}}$) of the two setups involved not being completely balanced. The asymmetry between the number of events for the Ψ_{AB} and the Ψ_{BC} states is due to the different probability for node B to be in the wrong charge state (NV^0) at the end of the sequence for the two links. To obtain a reliable estimate of the fidelities of the Bell states, we discard events in which

a CR (charge and resonance) check performed after readout gives a negative result. We remark that, as mentioned in the main text, we do not perform such an operation for the network protocols demonstrations, which are free from any post-selection. For the GHZ state generation, by heralding only on the $|0\rangle$ readout outcome of the communication qubit of Bob, we automatically reject events in which the NV center of Bob was either in the wrong charge state or off resonant. For the Entanglement Swapping demonstration, we perform a CR check after the Bell state measurement is performed on node B, and we herald success of the whole protocol only if this final CR check gives a positive result. We find that the test gives a positive result in approximately 90% of the cases.

4.6.11. EXPERIMENTAL MONITORING

Analogous to what reported in section J of the SI of Ref.[46], we implement checks while the experiment is running to ensure that the nodes are performing as expected. If one of the checks does not pass, we mark all future data to be disregarded (until the check is passed) and / or pause the experiment to perform further calibrations. Following is a list of all the checks that we use to mark future data to be disregarded (if they don't pass):

- Check that the measured phase of each interferometer is below 50^o before the last piezo feedback is performed.
- Check that the number of photons collected during the qubit reset by optical pumping part of the entanglement generation sequence, averaged over the preceding second, is above a pre-set threshold. If the check does not pass within a matter of seconds, we pause the experiment and scan the laser frequency to find back the qubit reset transition frequency.
- Check that the number of photons collected during the spin-photon entanglement part of the entanglement generation sequence, averaged over the preceding second, is above a pre-set threshold. If the check does not pass within a matter of seconds, we pause the experiment and scan the bias voltage of the setup.

4.6.12. AUTHOR CONTRIBUTIONS

M.P., S.L.N.H., S.B., and R.H. devised the experiment. M.P., S.L.N.H., S.B., and H.K.C.B. carried out the experiments and collected the data. M.P., S.L.N.H., S.B., H.K.C.B., P.C.H., R.N.S., R.F.L.V., M.J.T., and L.d.S.M. prepared the experimental apparatus. M.P. and R.H. wrote the main manuscript with input from all authors. M.P., S.L.N.H., S.B., H.K.C.B., and R.H. wrote the supplementary materials. M.P., S.L.N.H., and S.B. analyzed the data and discussed with all authors. R.H. supervised the research.

REFERENCES

[1] H. J. Kimble, *The quantum internet,* Nature **453**, 1023 (2008).

[2] S. Wehner, D. Elkouss and R. Hanson, *Quantum internet: A vision for the road ahead,* Science **362** (2018).

[3] L. Jiang, J. M. Taylor, A. S. Sørensen and M. D. Lukin, *Distributed quantum computation based on small quantum registers,* Physical Review A **76**, 1 (2007).

[4] A. Broadbent, J. Fitzsimons and E. Kashefi, *Universal blind quantum computation,* Proceedings - Annual IEEE Symposium on Foundations of Computer Science, FOCS , 517 (2009), 0807.4154 .

[5] D. Gottesman, T. Jennewein and S. Croke, *Longer-baseline telescopes using quantum repeaters,* Physical Review Letters **109**, 1 (2012), 1107.2939 .

[6] A. Ekert and R. Renner, *The ultimate physical limits of privacy,* Nature **507**, 443 (2014).

[7] N. H. Nickerson, J. F. Fitzsimons and S. C. Benjamin, *Freely scalable quantum technologies using cells of 5-to-50 qubits with very lossy and noisy photonic links,* Physical Review X **4**, 1 (2014), 1406.0880 .

[8] P. Kómár *et al.*, *A quantum network of clocks,* Nature Physics **10**, 582 (2014), 1310.6045 .

[9] D. L. Moehring *et al.*, *Entanglement of single-atom quantum bits at a distance,* Nature **449**, 68 (2007).

[10] S. Ritter *et al.*, *An elementary quantum network of single atoms in optical cavities,* Nature **484**, 195 (2012).

[11] J. Hofmann, M. Krug, N. Ortegel, L. Gérard and M. Weber, *Heralded Entanglement Between Widely Separated Atoms,* Science **337**, 72 (2012).

[12] L. J. Stephenson *et al.*, *High-Rate, High-Fidelity Entanglement of Qubits Across an Elementary Quantum Network,* Physical Review Letters **124**, 1 (2020).

[13] H. Bernien *et al.*, *Heralded entanglement between solid-state qubits separated by three metres,* Nature **497**, 86 (2013), 1212.6136 .

[14] P. C. Humphreys *et al.*, *Deterministic delivery of remote entanglement on a quantum network,* Nature **558**, 268 (2018), 1712.07567 .

[15] A. Delteil *et al.*, *Generation of heralded entanglement between distant hole spins,* Nature Physics **12**, 218 (2016).

[16] R. Stockill *et al.*, *Phase-Tuned Entangled State Generation between Distant Spin Qubits,* Physical Review Letters **119**, 1 (2017).

[17] P. Maunz *et al.*, *Heralded quantum gate between remote quantum memories,* Physical Review Letters **102**, 2 (2009).

[18] S. Daiß *et al.*, *A quantum-logic gate between distant quantum-network modules,* Science **371**, 614 (2021).

[19] N. Kalb *et al.*, *Entanglement distillation between solid-state quantum network nodes,* Science **356**, 928 (2017), 1703.03244 .

[20] M. Christandl and S. Wehner, *Quantum Anonymous Transmissions,* in *Advances in Cryptology - ASIACRYPT 2005* (2005) pp. 217–235.

[21] M. Hillery, V. Bužek and A. Berthiaume, *Quantum secret sharing,* Physical Review A **59**, 1829 (1999).

[22] A. Ambainis, H. Buhrman, Y. Dodis and H. Röhrig, *Multiparty quantum coin flipping,* Proceedings of the Annual IEEE Conference on Computational Complexity **19**, 250 (2004).

[23] H. Briegel, W. Dür, J. I. Cirac and P. Zoller, *Quantum Repeaters The Role of Imperfect Local Operations in Quantum Communication,* Physical Review Letters **81**, 5932 (1998).

[24] M. Pant *et al.*, *Routing entanglement in the quantum internet,* npj Quantum Information **5**, 1 (2019).

[25] D. Bouwmeester, J.-w. Pan, M. Daniell, H. Weinfurter and A. Zeilinger, *Observation of Three-Photon Greenberger-Horne-Zeilinger Entanglement,* Physical Review Letters **82**, 1 (1999).

[26] B. Jing *et al.*, *Entanglement of three quantum memories via interference of three single photons,* Nature Photonics **13**, 210 (2019).

[27] C. Cabrillo, J. I. Cirac, P. Garcia-Fernandez and P. Zoller, *Creation of entangled states of distant atoms by interference,* Physical Review A **59**, 1025 (1999).

[28] S. Bose, P. L. Knight, M. B. Plenio and V. Vedral, *Proposal for teleportation of an atomic state via cavity decay,* Physical Review Letters **83**, 5158 (1999), 9908004 [quant-ph] .

[29] C. E. Bradley *et al.*, *A Ten-Qubit Solid-State Spin Register with Quantum Memory up to One Minute,* Physical Review X **9**, 31045 (2019), 1905.02094 .

[30] N. Kalb, P. C. Humphreys, J. J. Slim and R. Hanson, *Dephasing mechanisms of diamond-based nuclear-spin memories for quantum networks,* Physical Review A **97**, 1 (2018), 1802.05996 .

[31] O. Gühne and G. Tóth, *Entanglement detection,* Physics Reports **474**, 1 (2009).

[32] L. Jiang *et al.*, *Repetitive readout of a single electronic spin via quantum logic with nuclear spin ancillae,* Science **326**, 267 (2009).

[33] D. Riedel *et al.*, *Deterministic enhancement of coherent photon generation from a nitrogen-vacancy center in ultrapure diamond,* Physical Review X **7**, 1 (2017), 1703.00815 .

[34] E. Janitz, M. K. Bhaskar and L. Childress, *Cavity quantum electrodynamics with color centers in diamond,* Optica **7**, 1232 (2020).

[35] M. Ruf, M. J. Weaver, S. B. Van Dam and R. Hanson, *Resonant Excitation and Purcell Enhancement of Coherent Nitrogen-Vacancy Centers Coupled to a Fabry-Perot Microcavity,* Physical Review Applied **15**, 1 (2021).

[36] S. Baier *et al.*, *Orbital and Spin Dynamics of Single Neutrally-Charged Nitrogen-Vacancy Centers in Diamond,* Physical Review Letters **125**, 1 (2020).

[37] R. Van Meter, *Quantum Networking* (John Wiley & Sons, Inc., 2014).

[38] A. Pirker and W. Dür, *A quantum network stack and protocols for reliable entanglement-based networks,* New Journal of Physics **21** (2019).

[39] W. Kozlowski and S. Wehner, *Towards Large-Scale Quantum Networks,* in *NANOCOM* (2019).

[40] A. Dahlberg *et al.*, *A link layer protocol for quantum networks,* SIGCOMM 2019 - Proceedings of the 2019 Conference of the ACM Special Interest Group on Data Communication , 159 (2019).

[41] A. Tchebotareva *et al.*, *Entanglement between a Diamond Spin Qubit and a Photonic Time-Bin Qubit at Telecom Wavelength,* Physical Review Letters **123**, 1 (2019).

[42] B. C. Rose *et al.*, *Observation of an environmentally insensitive solid-state spin defect in diamond,* Science **361**, 60 (2018).

[43] C. T. Nguyen *et al.*, *Quantum Network Nodes Based on Diamond Qubits with an Efficient Nanophotonic Interface,* Physical Review Letters **123**, 1 (2019).

[44] M. E. Trusheim *et al.*, *Transform-Limited Photons from a Coherent Tin-Vacancy Spin in Diamond,* Physical Review Letters **124**, 1 (2020).

[45] N. T. Son *et al.*, *Developing silicon carbide for quantum spintronics,* Applied Physics Letters **116**, 190501 (2020).

[46] B. Hensen *et al.*, *Loophole-free Bell inequality violation using electron spins separated by 1.3 kilometres,* Nature **526**, 682 (2015).

[47] R. H. M. Pompili, S. Hermans, S. Baier, H. Beukers, P. Humphreys, R. Schouten, R. Ver- meulen, M. Tiggelman, L. d. S. Martins, B. Dirkse, S. Wehner, *Data and software supporting "Realization of a multi-node quantum network ofremote solid-state qubits",* (2021).

5

QUBIT TELEPORTATION BETWEEN NON-NEIGHBORING NODES IN A QUANTUM NETWORK

S. L. N. Hermans*, M. Pompili*, H. K. C. Beukers, S. Baier, J. Borregaard & R. Hanson

Future quantum internet applications will derive their power from the ability to share quantum information across the network. Quantum teleportation allows for the reliable transfer of quantum information between distant nodes, even in the presence of highly lossy network connections. While many experimental demonstrations have been performed on different quantum network platforms, moving beyond directly connected nodes has so far been hindered by the demanding requirements on the pre-shared remote entanglement, joint qubit readout and coherence times. Here we realize quantum teleportation between remote, non-neighboring nodes in a quantum network. The network employs three optically connected nodes based on solid-state spin qubits. The teleporter is prepared by establishing remote entanglement on the two links, followed by entanglement swapping on the middle node and storage in a memory qubit. We demonstrate that once successful preparation of the teleporter is heralded, arbitrary qubit states can be teleported with fidelity above the classical bound, even with unit efficiency. These results are enabled by key innovations in the qubit readout procedure, active memory qubit protection during entanglement generation and tailored heralding that reduces remote entanglement infidelities. Our work demonstrates a prime building block for future quantum networks and opens the door to exploring teleportation-based multi-node protocols and applications.

The results of this chapter have been published in Nature, **605**, 663-668 (2022).
* Equally contributing authors

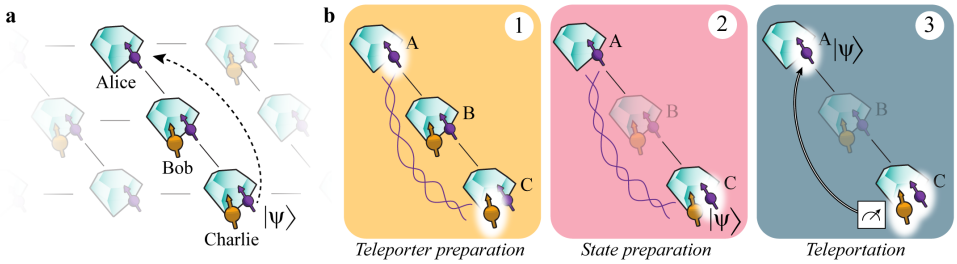

Figure 5.1: **Teleporting a qubit between non-neighboring nodes of a quantum network. (a)** Three network nodes, Alice (A), Bob (B) and Charlie (C) are connected via optical fiber links (lines) in a line configuration. Each setup has a communication qubit (purple) that enables entanglement generation with its neighboring node. Additionally, Bob and Charlie contain a memory qubit (yellow). **(b)** The steps of the teleportation protocol: (1) We prepare the teleporter by establishing entanglement between Alice and Charlie using an entanglement swapping protocol on Bob, followed by swapping the state at Charlie to the memory qubit. (2) The qubit state to be teleported is prepared on the communication qubit on Charlie. (3) A Bell-state measurement is performed on Charlie's qubits and the outcome is communicated to Alice over a classical channel. Dependent on this outcome, Alice applies a quantum gate to obtain the teleported qubit state.

5

5.1. INTRODUCTION

Quantum teleportation is the central routine for reliably sending qubits across lossy network links[1] as well as a key primitive of quantum network protocols and applications[2–4]. Using a teleporter in the form of a pre-shared entangled state, the quantum information is transferred by performing a joint Bell-state measurement on the sender's part of the entangled state and the qubit state to be teleported. The state is recovered on the receiving node by a gate operation conditioned on the Bell-state measurement outcome[1]. Since the quantum information is not transmitted by a physical carrier, the protocol is insensitive to loss in the connecting photonic channels and on intermediate nodes. A deterministic Bell-state measurement combined with real-time feed-forward enables unconditional teleportation, in which state transfer is achieved each time a qubit state is inserted into the teleporter.

Pioneering explorations of quantum teleportation protocols were performed using photonic states[5–7]. Following the development of quantum network nodes with stationary qubits, remote qubit teleportation was realized between trapped ions[8], trapped atoms[9,10], diamond NV centers[11] and memory nodes based on atomic ensembles[12].

While future quantum network applications will widely employ teleportation between non-connected nodes in the network, the demanding set of requirements on the pre-shared entanglement, the Bell-state measurement and the coherence times for enabling real-time feed-forward has so far prevented the realization of teleportation beyond directly connected stationary network nodes.

Here, we overcome these challenges by a set of key innovations and achieve qubit teleportation between non-neighboring network nodes (see Figure 5.1a). Our quantum

network consists of three nodes in a line configuration, Alice, Bob and Charlie. Each node contains a nitrogen-vacancy (NV) center in diamond. Using the NV electronic spin as the communication qubit we are able to generate remote entanglement between each pair of neighboring nodes. In addition, Bob and Charlie each employ a nearby ^{13}Cnuclear spin as a memory qubit. The steps of the teleportation protocol are shown in Figure 5.1b. To prepare the teleporter we use an entanglement swapping protocol mediated by Bob, similar to a quantum repeater protocol[13], to establish entanglement between Alice and Charlie. Once successful preparation of teleporter is heralded, the input qubit state is prepared on Charlie and finally teleported to Alice.

5.2. ENTANGLEMENT FIDELITY OF THE NETWORK LINKS

A key parameter for quantum teleportation is the fidelity of the pre-shared entangled state between Alice and Charlie. As we generate this state by entanglement swapping, its fidelity is upper bounded by the errors on the individual links. Therefore, mitigating error sources on the individual links is critical. Our network generates entanglement between neighboring nodes using a single-photon protocol[14,15] in an optical-phase-stabilized architecture[16]. The building block of this protocol is a qubit-photon entangled state created at each node. To generate this entangled state we initialize the communication qubit in a superposition state $|\psi\rangle = \sqrt{\alpha}|0\rangle + \sqrt{1-\alpha}|1\rangle$ and apply a state-selective optical pulse that transfers the population from $|0\rangle$ to an optically excited state. Following spontaneous emission, the qubit state is entangled with photon number (0 or 1 photon). We perform this protocol on both nodes and interfere the resonant photonic states on a beam splitter (Figure 5.2a). Detection of a single photon in one of the beam splitter output ports ideally heralds the generation of an entangled state $|\psi\rangle = (|01\rangle \pm |10\rangle)/\sqrt{2}$, where the $\pm$ phase is set by which detector clicked. Figure 5.2b displays the joint outcomes of qubit measurements in the computational basis after entanglement is heralded, showing the expected correlations.

The infidelity of the generated state has three main contributions: double $|0\rangle$ state occupancy, double optical excitation and finite distinguishability of the photons[16,17] (see Section 5.7.9). In the case of double $|0\rangle$ state occupancy (which occurs with probability α), both communication qubits are in the $|0\rangle$ state and have emitted a photon. Detection of one of these photons leads to false heralding of an entangled state. The second effect, double excitation, is due to the finite length of the optical pulse compared to the emitter's optical lifetime. There is a finite chance that the communication qubit emits a photon during this pulse, is subsequently re-excited during the remainder of the pulse and then emits another photon resulting in the qubit state being entangled with two photons. Detection or loss of the first photon destroys the coherence of the qubit-photon entangled state and detection of the second photon can then falsely herald the generation of an entangled state.

Crucially, false heralding events due to double $|0\rangle$ state occupancy and double excitation are both accompanied by an extra emitted photon. Therefore, detection of this additional photon allows for unambiguous identification of such events and thus

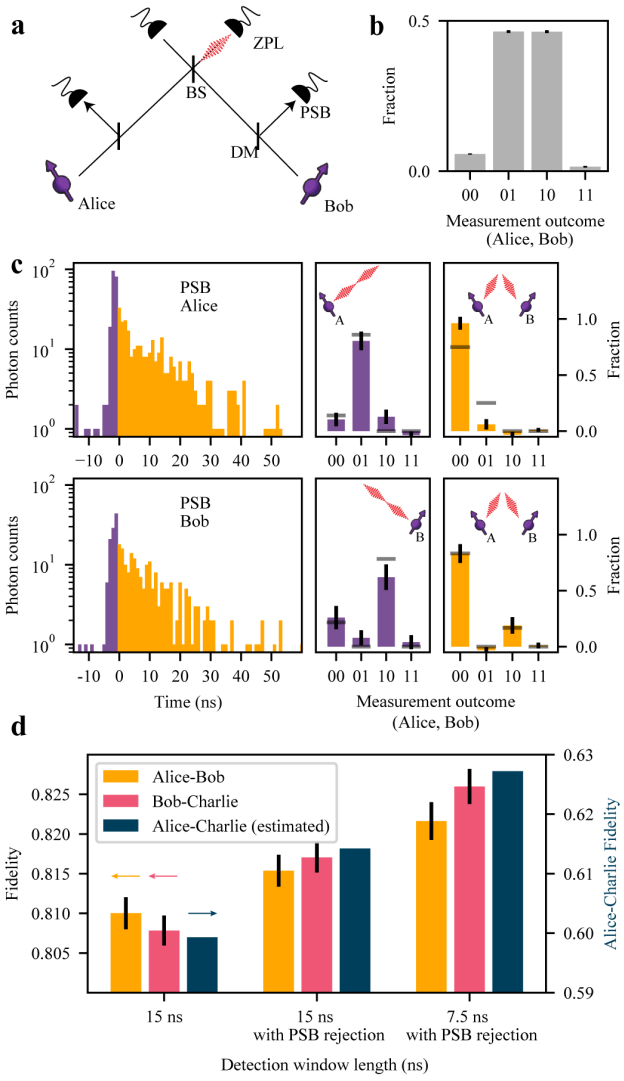

Figure 5.2: **High-fidelity entangled network links.** **(a)** Simplified schematic of the optical link used for generating entanglement between neighboring nodes. Photons emitted by the communication qubits are filtered by a dichroic mirror (DM) to separate the resonant (zero-phonon line, ZPL) photons (3% of emission) from the off-resonant (phonon-side band, PSB) photons (97% of emission). The resonant photons are sent to the beam splitter (BS); detection of a single photon at one of the ZPL detectors heralds successful generation of an entangled state between the two nodes. **(b)** Measured correlations of the communication qubits in the computational basis, conditioned on a heralding event on the ZPL detectors. **(c)** (left) Histograms of the PSB photon detection times on Alice (top) or Bob (bottom), conditioned on a simultaneous ZPL detection in the same entanglement generation attempt. Gray lines show expected correlations based on a quantum-optical model (see Section 5.7.3). **(d)** Measured fidelity of the network links, without PSB rejection (left), with PSB rejection (middle) and with PSB rejection plus shortened detection window (right). The dark blue bars indicate the corresponding expected fidelity on Alice-Charlie after entanglement swapping for each case (Section 5.7.9)). All error bars represent one standard deviation.

for real-time rejection of the corresponding false heralding signals. We implement this rejection scheme by monitoring the off-resonant phonon-side band (PSB) detection path on both setups during and after the optical excitation (see Figure 5.2a).

To investigate the effect of this scheme, we generate entanglement on the individual links and extract the entanglement heralding events for which the PSB monitoring flagged the presence of an additional photon. For these events, we again analyze the corresponding qubit measurements in the computational basis (Figure 5.2c).

We identify two separate regimes: one during the optical pulse (purple) and one after the optical pulse (yellow). When a photon is detected on Alice's (Bob's) PSB detector during the optical pulse we see that the outcome 01 (10) is most probable (purple data in Figure 5.2c) showing that only one setup was in the $|0\rangle$ state and thus that both detected photons originated from Alice (Bob). The detection of PSB photons during the optical pulse thus primarily flags double excitation errors. In contrast, when a photon is detected after the optical pulse in either Alice's or Bob's PSB detector, the outcome 00 is most probable (yellow data in Figure 5.2c), indicating that both setups were in the $|0\rangle$ state and both emitted one photon. PSB photon detection after the optical pulse thus flags the double $|0\rangle$ state occupancy error. We find similar results to Figure 5.2c for the entangled states generated on the Bob-Charlie link, see Section 5.7.3. The improvement in fidelity from rejecting these false heralding events in our experiment is set by the combined probability of occurrence ($\approx 9\%$, see Section 5.7.9) multiplied by the probability to flag them (given here by the total PSB photon detection efficiency of $\approx 10\%$).

The third main source of infidelity, the finite distinguishability, can arise from frequency detunings between the emitted photons[18]. While most of these detunings are eliminated upfront by the charge-resonance (CR) check before the start of the protocol (Section 5.7.1), the communication qubits may still be subject to a small amount of spectral diffusion. In our single-photon protocol, this leads to dephasing that is stronger for photons that are detected later relative to the optical pulse. By shortening our detection window, we can increase the fidelity of the entangled state at the expense of a lower entangling rate. For the experiments below (unless mentioned differently) we use a detection window length of 15ns. Figure 5.2d summarizes the measured improvements on the individual links. For the teleporter, we estimate that their combined effect is an increase in Alice-Charlie entangled state fidelity by $\approx 3\%$. This increase is instrumental in pushing the teleportation fidelity above the classical bound.

5.3. MEMORY QUBIT COHERENCE

In the preparation of the teleporter it is crucial that the first entangled state between Alice and Bob is reliably preserved on the memory qubit while the second link between Bob and Charlie is being generated. For this reason we abort the sequence and start over when the second entangled state is not heralded within a fixed number of attempts, the timeout.

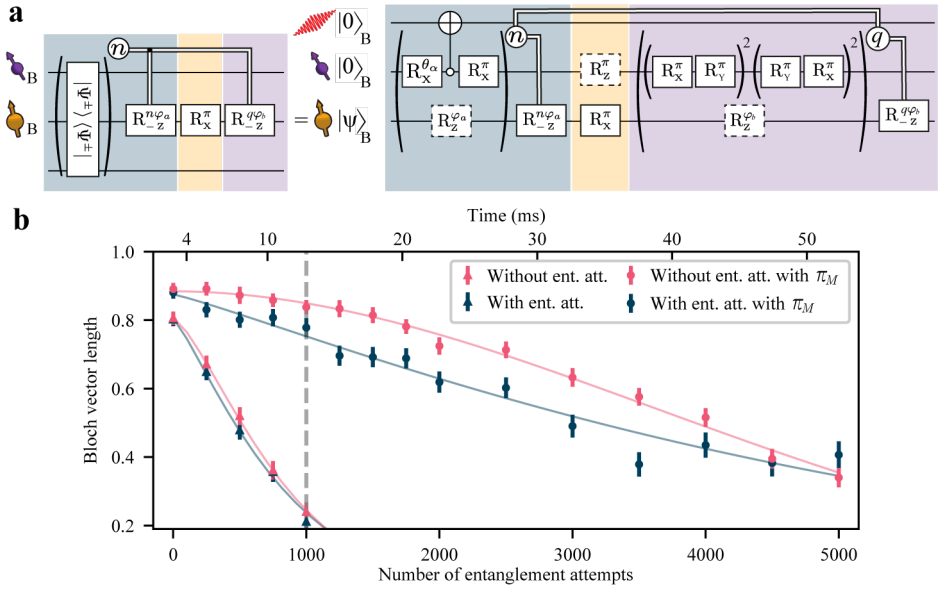

Figure 5.3: **Memory qubit coherence. (a)** Gate sequence on Bob for entanglement generation with the communication qubit while preserving states stored on the memory qubit. Entanglement generation attempts are repeated until success or a predetermined timeout. Upon success in the n^{th} attempt, a phase feed-forward is applied to maintain the correct reference frame of the memory qubit [16], followed by a decoupling pulse on the memory qubit. The decoupling π_M pulse causes a Z-rotation on the communication qubit. Afterwards, we rephase the memory qubit for the same amount of time as it took to herald entanglement (by applying q blocks of XY8 decoupling sequences on the communication qubit, where q depends on the number of entanglement attempts needed n) and we end with another phase feed-forward on the memory qubit, to compensate for any phase picked up during this decoupling. **(b)** Bloch vector length of a superposition state stored on the memory qubit for different number of entanglement attempts or a time-equivalent wait element. In the case of no decoupling (no π_M) on the memory qubit, the gates in the yellow shaded box in (a) are left out. The gray dashed line indicates the chosen timeout of 1000 entanglement attempts. All error bars represent one standard deviation.

The ^{13}C memory qubits can be controlled with high fidelity via the communication qubit while they can be efficiently decoupled when no interaction is desired. Recent work showed that in a magnetic field of 189 mT entanglement generation attempts with the communication qubit do not limit the memory dephasing time $T_2^{\star}$ [16], opening the door to significantly extending the memory preservation time with active coherence protection from the spin bath [19]. We realize this protection by integrating a decoupling π-pulse on the memory qubit into the experimental sequence that follows a heralding event, while ensuring that all phases that are picked up due to the probabilistic nature of the remote entangling process are compensated in real time (Figure 5.3a).

In Figure 5.3b we check the performance of this sequence by storing a superposition state on the memory qubit and measuring the Bloch vector length. We compare the

results for the sequence with and without the decoupling π-pulse, and with and without entanglement attempts. We observe that without the decoupling pulse the decay of the Bloch vector length is not altered by the entanglement attempts, in line with previous findings [16]. In contrast, when we apply the decoupling pulse the decay is slowed down by more than a factor of 6, yielding a $N_{1/e}$ decay constant of $\approx$ 5300 entanglement attempts, the highest number reported to date for diamond devices. In addition, we observe a difference in the shape of the decay between the cases with and without entangling attempts, indicating that intrinsic decoherence is no longer the only limiting error source. The improved memory coherence enables us to use a timeout of 1000 entangling attempts, more than double that of Ref. [16], which doubles the entanglement swapping rate.

5.4. MEMORY QUBIT READOUT

High-fidelity memory qubit readout is required both in the preparation of the teleporter (at Bob) and during the teleportation protocol itself (at Charlie). The memory qubit is read out by mapping its state onto the communication qubit using quantum logic followed by single-shot readout of the communication qubit using state-dependent optical excitation and detection [20]. Due to limited photon collection efficiency ($\approx$ 10%) and finite cyclicity of the optical transition ($\approx$ 99%), the communication qubit readout fidelity is different for $|0\rangle$ and $|1\rangle$. As a result, for random initial states the probability that the correct state was assigned is significantly larger if one or more photons were detected (assigned outcome 0) than if no photons were detected (assigned outcome 1) [21]. In previous work we circumvented this issue by conditioning on obtaining the outcome 0 [16]. However, this approach scales unfavorably, as it forces the protocol to prematurely abort with probability >50% at each memory qubit readout. Therefore, to access more complex protocols with multiple memory qubit readouts, near-deterministic readout schemes are required.

We resolve this challenge by introducing a basis-alternating repetitive readout for the memory qubit (see Figure 5.3c). The key point of this readout strategy is, in contrast to earlier work [22], to alternatingly map the computational basis states of the memory qubit to the communication qubit state $|0\rangle$. Figure 5.3d shows the readout fidelities of the n-th readout repetition for the two initial states for the memory qubit on Bob (for Charlie, see Section 5.7.6). We clearly observe the expected alternating pattern due to the asymmetry of the communication qubit readout fidelities. Importantly, the readout fidelity decays only by $\approx$ 1% per readout, showing that the readout is mostly non-demolition and multiple readouts are possible without losing the state. We model the readout procedure using measured parameters (see Section 5.7.6) and plot the model's predictions as dashed lines in Figure 5.3d-f.

Next, we assign the state using the first readout and continue the sequence only when the consecutive readouts are consistent with the first readout. The subsequent readouts therefore add confidence to the assignment in the case of consistent outcomes, while

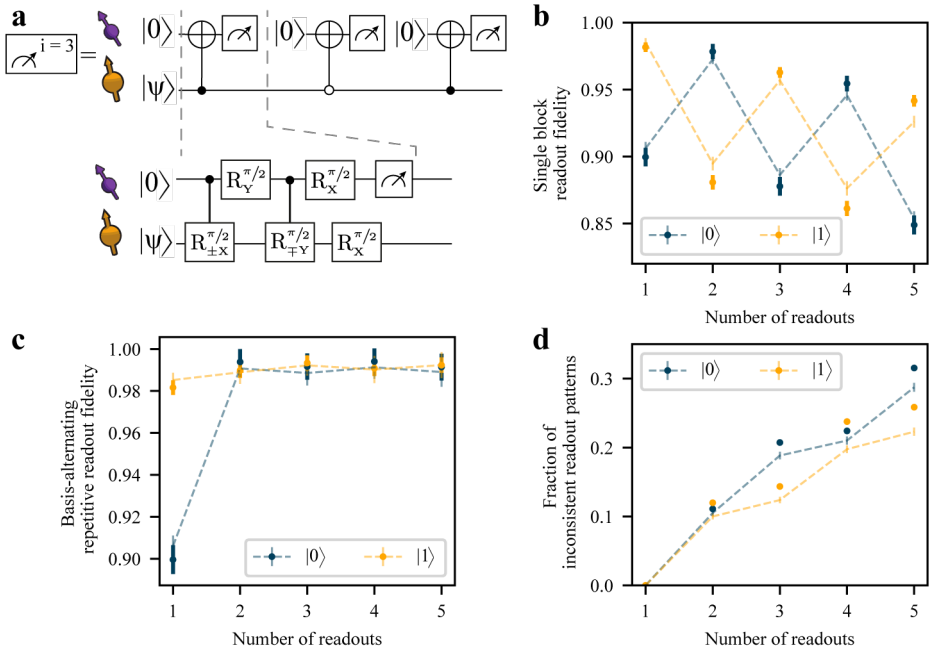

Figure 5.4: **Memory qubit readout.** **(a)** Gate sequence for the basis-alternating repetitive readout of the memory qubit. **(b)** Readout fidelity for each readout repetition, for state $|0\rangle$ and $|1\rangle$. **(c)** Readout fidelity of the basis-alternating repetitive readout scheme for different number of readout repetitions. s **(d)** Fraction of inconsistent readout patterns for different number of readout repetitions. In (d-f) the dashed lines show a numerical model using measured parameters. All error bars represent one standard deviation.

cases of inconsistent outcomes (which have a higher chance of indicating an incorrect assignment) are filtered out. In Figure 5.3e we plot the readout fidelity resulting from this strategy for up to five readouts, with the corresponding rejected fraction due to inconsistent outcomes plotted in Figure 5.3f. We observe that using two readouts already eliminates most of the asymmetry, reducing the average infidelity from ≈ 6% to below 1%. At this point, the remaining observed infidelity mainly results from cases where the memory qubit was flipped during the first readout block due to imperfect memory qubit gates. While adding further readout blocks does not lead to significant improvements in fidelity, each two additional readouts cut the amount of consistent outcomes by ≈ 10%, due to the communication qubit readout infidelities and gate errors. For the experiments reported below (unless mentioned differently) we use two readout repetitions to benefit from a high average readout fidelity (Bob: 99.2(4)%, Charlie: 98.1(4)%) and a high probability to continue the sequence (Bob and Charlie: ≈ 88%).

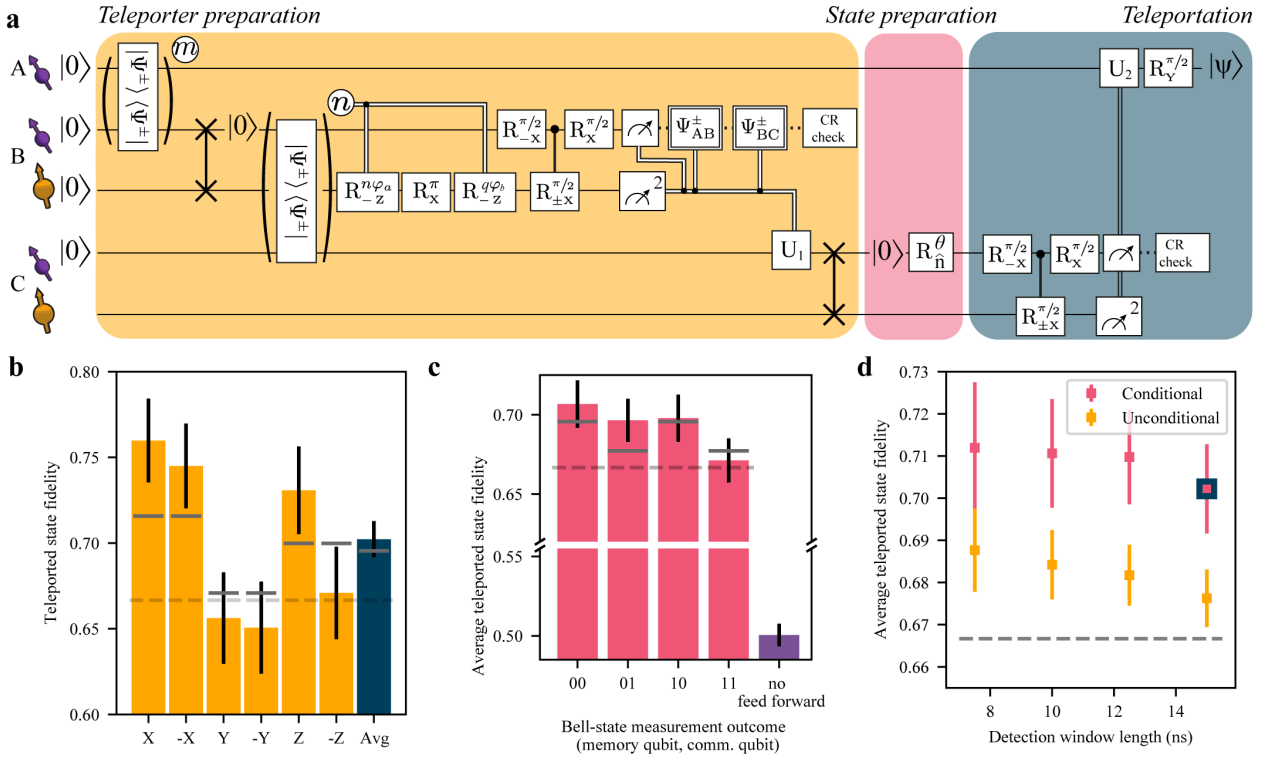

Figure 5.5: **Qubit teleportation between non-neighboring network nodes.** **(a)** Circuit diagram of the teleportation protocol using notation defined in Figure 5.3. m (n) is the number of attempts needed to herald entanglement for the AB (BC) entangled link. See Section 5.7.1for the full circuit diagram. **(b)** Teleported state fidelities for the six cardinal states and their average. The gray lines show the expected fidelities from simulations. The dashed lines in (b-d) represents the classical bound of 2/3. **(c)** Average teleported state fidelity for the different outcomes of the Bell-state measurement on Charlie. The right-most bar shows the resulting fidelity when no feed forward operation on Alice would be applied. **(d)** Average state fidelity for a conditional and unconditional teleportation, for different detection window lengths of the two-node entanglement generation processes. The blue bordered data point is the same point as shown in (b). All error bars represent one standard deviation.

5.5. TELEPORTING QUBIT STATES FROM CHARLIE TO ALICE

With all innovations described above implemented, we perform the protocol as shown in Figure 5.5a. First we generate entanglement between Alice and Bob and store Bob's part of the entangled state on the memory qubit using a compiled SWAP operation. Second, we generate entanglement between Bob and Charlie, while preserving the first entangled state on the memory qubit with the pulse sequence as described in Figure 5.3a. Next, we perform a Bell-state measurement on Bob followed by a CR check. We continue the sequence if the communication qubit readout yields outcome 0, the memory qubit readout gives a consistent outcome pattern and the CR check is passed. At Charlie, we perform a quantum gate that depends on the outcome of the Bell-state measurement and on which detectors clicked during the two-node entanglement generation. Next, we swap the entangled state to the memory qubit. At this point the teleporter is ready and Alice and Charlie share an entangled state with an estimated fidelity of 0.61.

Subsequently, we generate the qubit state to be teleported, $|\psi\rangle$, on Charlie's communication qubit and run the teleportation protocol. First, a Bell-state measurement is performed on the communication and memory qubits at Charlie. With the exception of unconditional teleportation (discussed below), we only continue the sequence when we obtain a 0 outcome on the communication qubit, when we have a consistent readout pattern on the memory qubit and when Charlie passes the CR check. The outcomes of the Bell-state measurement are sent to Alice and by applying the corresponding gate operation we obtain $|\psi\rangle$ on Alice's side.

We teleport the six cardinal states ($\pm$X, $\pm$Y, $\pm$Z), which form an unbiased set [23], and measure the fidelity of the teleported states to the ideally prepared state (Figure 5.5b). We find an average teleported state fidelity of F =0.702(11) at an experimental rate of 1/(117 s). This value exceeds the classical bound of 2/3 by more than three standard deviations, thereby proving the quantum nature of the protocol. We note that this value provides a lower bound to the true teleportation fidelity, as the measured fidelity is lowered by errors in the preparation of the qubit states at Charlie (estimated to be 0.5%, see Section 5.7.11).

The differences in fidelity between the teleported states arise from an interplay of errors in different parts of the protocol that either affect all three axes (depolarizing errors) or only two axes (dephasing errors). These differences are qualitatively reproduced by our model (gray bars in Figure 5.5b). In Figure 5.5c we plot the teleportation fidelity for each possible outcome of the Bell-state measurement. Due to the basis-alternating repetitive readout, the dependence on the second bit (from the memory qubit readout) is small, whereas for the first bit (communication qubit readout) the best teleported state fidelity is achieved for outcome 0 due to the asymmetric readout fidelities. We also analyze the case in which no feed-forward is applied at Alice (Section 5.7.12); as expected, the average state fidelity reduces to a value consistent with a fully mixed state (fidelity F =0.501(7)), emphasizing the critical role of the feed-forward in the

teleportation protocol.

Finally, we demonstrate that the network can achieve unconditional teleportation between Alice and Charlie. Unconditional teleportation requires that, following preparation of the teleporter by establishing the remote entangled state, the protocol runs deterministically (each qubit state prepared at Charlie ends up at Alice) while surpassing the classical fidelity bound. We thus require that the Bell-state measurement at Charlie and the subsequent feed-forward operations are performed deterministically. To this end, we revise the protocol at Charlie to accept both communication qubit outcomes, use all memory qubit readout patterns including the inconsistent ones and disregard the outcome of the CR check after the Bell-state measurement. Using this fully deterministic Bell-state measurement lowers the average teleportation fidelity by a few percents (Figure 5.5d). At the same time, shortening the detection windows of the two-node entanglement generation is expected to yield an improvement in the fidelity, as discussed above. We find indeed that the average unconditional teleportation fidelity increases with shorter window lengths, reaching F =0.688(10) for a length of 7.5 ns and a rate of 1/(100 s). The current quantum network is thus able to perform teleportation beyond the classical bound, even under the strict condition that every state inserted into the teleporter be transferred.

5.6. OUTLOOK

In this work we have realized unconditional qubit teleportation between non-neighboring nodes in a quantum network. The innovations introduced here on memory qubit readout and protection during entanglement generation, as well as the real-time rejection of false heralding signals, will be instrumental in exploring more complex protocols [2–4,24,25]. Also, these methods can be readily transferred to other platforms such as the group-IV color centers in diamond, the vacancy-related qubits in SiC and single rare-earth ions in solids [26–32].

The development of an improved optical interface for the communication qubit[33] will increase both the teleportation protocol rate and fidelity. Because of the improved memory qubit performance reported here, the network already operates close to the threshold where nodes can reliably deliver a remote entangled state while preserving previously stored quantum states in their memory qubits. With further improvements, for instance by integrating multi-pulse memory decoupling sequences[19] into the entanglement generation, demonstration of deterministic qubit teleportation may come within reach. In that case, the network is able to teleport a qubit state with unit efficiency at any given time, removing the need for heralding successful preparation of the teleporter and opening the door to exploring applications that call the teleportation routine multiple times. In addition, future work will focus on further improving the phase stabilization and extending the current schemes for use in deployed fiber[34].

Finally, by implementing a recently proposed link layer protocol [35], qubit teleportation and applications making use of the teleportation primitive may be executed and

tested on the network through platform-independent control software, an important prerequisite for a large-scale future network.

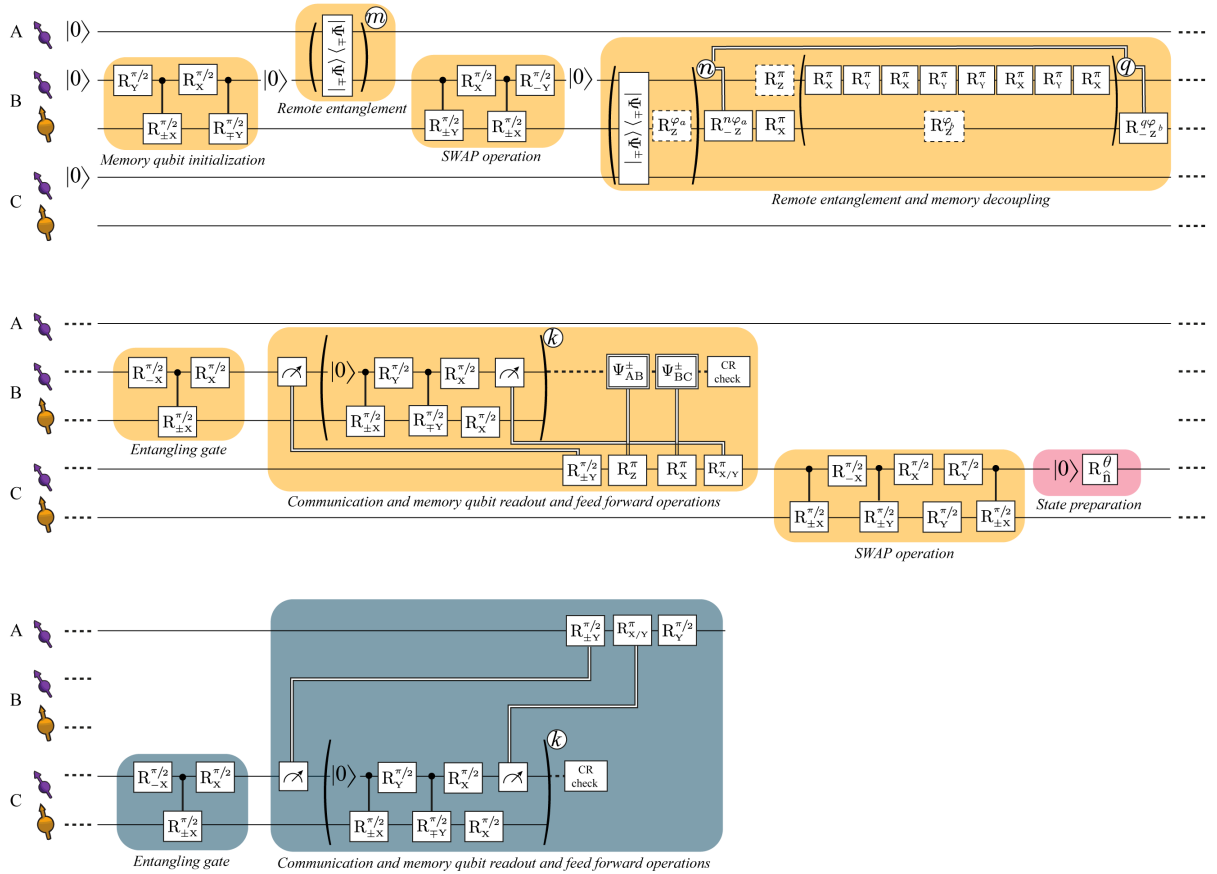

Figure 5.6: Full gate circuit for the teleportation protocol, see text for the description of each element.

5.7. SUPPLEMENTARY INFORMATION

5.7.1. FULL GATE CIRCUIT

Our quantum network consists of three nodes, Alice, Bob and Charlie. In the experiment, we will teleport a qubit from Charlie to Alice, two non-neighboring nodes. The full gate circuit is shown in Figure 5.6. Prior to the sequence, we do a Charge-Resonance (CR) check on each node to ensure that the communication qubits are in the correct charge state (NV^-) and on resonance with the control lasers. Once all the nodes have passed this check, we do a first round of optical phase stabilization of the interferometers, which enables the entanglement generation using the single click protocol[14–17]. After these preparation steps, the sequence is triggered on all setups.

On Bob, we initialize the memory qubit into $|0\rangle$ using the communication qubit[20]. Next, we generate entanglement between the communication qubits of Alice and Bob. When entanglement is heralded, we perform a SWAP operation to store Bob's part of the entangled state on the memory qubit.

We continue with a second round of phase stabilization (not shown in the circuit) and generate entanglement between the communication qubits of Bob and Charlie. Each entanglement attempt slightly decoheres the memory qubit, therefore we limit the number of attempts by a timeout. If we do not succeed within the timeout, we abort the sequence and start over.

During entanglement generation, the memory qubit of Bob picks up an average phase $n\varphi_a$ dependent on the number of entanglement attempts n. Due to the probabilistic nature of the entanglement generation process, we do not know which attempt will be successful, therefore this phase is unknown at the start of the sequence. To maintain the correct reference frame of the memory qubit this phase needs to be corrected in real-time before any other gate can be applied to the memory qubit. We perform this real-time correction by changing the time between pulses on the communication qubit[16]. After the phase correction, the decoupling pulse is applied to the memory qubit via the communication qubit. The back-action of this gate causes a Z-rotation on the communication qubit. To rephase the memory qubit, we wait for the same amount of time as it took to herald the second entangled state while decoupling the communication qubit. This imprints a phase $q\varphi_b$ on the memory qubit, which we compensate in an analogous way.

Bob now shares two entangled states; his memory qubit is entangled with Alice and his communication qubit with Charlie. To establish an entangled state between Alice and Charlie we perform a Bell-state measurement on the two qubits of Bob. To do so, we entangle the communication and memory qubits and do a measurement on the communication qubit. We map its state onto the communication qubit and measure the communication qubit. In the basis-alternating repetitive readout, we repeat the measurement sequence twice. During the first readout we map the $|0\rangle$ state to the $|0\rangle$

state of the communication qubit, and in the second readout we map $|1\rangle$ to $|0\rangle$. The first outcome is used to assign the state and the second outcomes serves as a check. By continuing the sequence only when we measure consistent patterns (for instance $(m1, m2) = (1, 0)$) we increase our average readout fidelity. After the readout procedure, we perform a CR check on Bob to filter out any event where Bob was in the wrong charge state.

Bob communicates to Charlie which gate operation should be done to obtain the correct entangled state. Which operation is required is determined by the outcomes of the Bell-state measurement on Bob and by which detector heralded the individual links. Charlie performs the feed-forward gate operation and subsequently stores its part of the entangled state on the memory qubit using a SWAP gate. At this point in the sequence the teleporter is ready.

To prepare the state that is to be teleported, we initialize the communication qubit at Charlie and perform the desired qubit rotation. To teleport the qubit, we perform a Bell-state measurement on the qubits of Charlie. Locally, we entangle the communication qubit with the memory qubit. We readout the communication qubit and use the basis-alternating repetitive readout for the memory qubit. Additionally, we do a CR check on Charlie. Charlie communicates the results of the Bell-state measurement to Alice, and Alice performs a feed-forward operation to obtain the teleported state. To verify the teleported state, we measure the state of Alice in the corresponding basis. To prevent any bias in the tomography we measure in both directions, e.g. when we teleport $|+Z\rangle$ we measure both along +Z and -Z axes.

5.7.2. EXPERIMENTAL SETUP

The basics of the experimental setup are described in [16]. In the current experiment, Charlie has access to a carbon-13 nuclear spin that acts as a memory qubit. The parameters used for the memory qubits of Bob and Charlie can be found in Table 5.1. Additionally, we have set up a classical communication channel between Charlie and Alice such that Charlie can directly send the results of the Bell-state measurement to Alice.

TEMPORAL SELECTION OF HERALDING PHOTONS

To eliminate any reflected excitation light in the heralding detectors, we make use of a cross-polarization scheme and perform temporal selection of the detected photons as described in Reference [36]. We start the detection windows 4 ns (5 ns) after the highest intensity point of the excitation pulse, for the AB (BC) entangled link, to ensure sufficient suppression of excitation laser light in the detection window.

5.7.3. TAILORED HERALDING OF THE REMOTE ENTANGLED STATES

In the main text we describe several noise mechanisms that reduce the remote two-node entangled state fidelity. Two of these noise mechanisms, double $|0\rangle$ occupancy and double optical excitation, are accompanied by the emission of an extra photon. This extra photon can be detected using the local phonon-side band (PSB) detectors. By

Table 5.1: Memory qubit characteristics. In each setup we use a magnetic field with strength B_z aligned to the NV axis. The nuclear spin precession frequencies ($\omega_{m_s=0}$ and $\omega_{m_s=-1}$) depends on the electron spin state. From the frequency difference, the parallel component $A_\parallel$ of the hyperfine interaction can be estimated. Conditional (unconditional) pulses are applied by doing N_{con} (N_{unc}) pulses on the electron spin with an interpulse delay of τ_{con} (τ_{unc}).

Setup	B_z	$\omega_{m_s=0}$	$\omega_{m_s=-1}$	$A_\parallel$
Bob	1890 Gauss	$2\pi \times 2025$ kHz	$2\pi \times 2056$ kHz	$2\pi \times 30$ kHz
Charlie	165 Gauss	$2\pi \times 177$ kHz	$2\pi \times 240$ kHz	$2\pi \times 63$ kHz

Setup	τ_{con}	N_{con}	τ_{unc}	N_{unc}
Bob	2.818 μs	54	4.165 μs	144
Charlie	6.003 μs	56	11.996 μs	30

monitoring the PSB detectors, we can real-time reject false heralding events.

5

In Figures 5.7 and 5.8, we plot the histograms of the detection times of the PSB photons conditioned on a simultaneous heralding (zero-phonon line, ZPL) photon detection in the same entanglement generation attempt, for the Alice-Bob and Bob-Charlie entangled link respectively. The correlations are measured in the computational (or Z) basis, and in the X and Y basis. In the computational basis we see the behavior dependent on the detection time of the PSB photon as described in the main text together with the simulations (gray bars). In the X and Y basis, all outcomes are equally probable, and the quantum correlations are washed out.

From the data collected, we can extract the probability to detect these additionally emitted PSB photons. We assume the dark counts of the detectors to be negligible, the PSB detections during the pulse to be fully dominated by the double optical excitation error, and the PSB detections after the pulse to be only caused by double $|0\rangle$ occupancy. By correcting for the PSB detection efficiency, we can estimate the probability for double $|0\rangle$ occupancy and double optical excitation errors. The results are given in Table 5.2. The double $|0\rangle$ state error is expected to occur with probability α. The extracted numbers correspond well to the parameter values we use during remote entanglement generation ($\alpha_{\text{Alice}} = 0.07, \alpha_{\text{Bob}} = 0.05, \alpha_{\text{Charlie}} = 0.10$[16]). The probability for the double optical excitation to occur depends on the shape and the amplitude of the optical excitation pulse, and differs per node.

NUMERICAL MODEL

We compare our PSB detection data (previous section) to a numerical model. We model the NV center as a three level system with two stable ground states $|0\rangle, |1\rangle$ and one excited state $|e\rangle$. The optical $|0\rangle \leftrightarrow |e\rangle$ transition is driven by a resonant laser pulse and is assumed to be a closed transition. The Hamiltonian describing the dynamics of the system in a suitable rotating frame is

$$\hat{H} = \Omega(t)\,|e\rangle\langle 0| + \Omega^*(t)\,|0\rangle\langle e|, \tag{5.1}$$

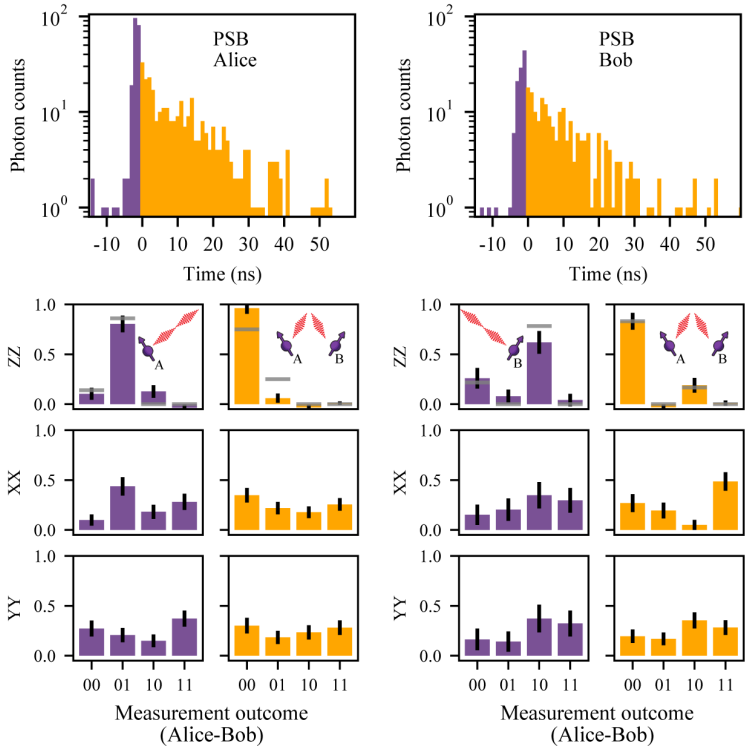

Figure 5.7: (Top) Histograms of the detected PSB photons conditioned on a simultaneous ZPL detection in the entanglement generation attempt, for Alice (left) and Bob (right). (Bottom) Corresponding measured correlations in all bases. The gray bars in the Z basis represent the simulated values. For the X and Y bases, one would expect a probability of 0.25 for all outcomes. All error bars represent one standard deviation.

Table 5.2: Estimated probabilities for the double optical excitation error and the double $|0\rangle$ occupancy error per node (values in percent). All error bars represent one standard deviation.

Node	Double optical excitation probability	Double $\|0\rangle$ occupancy probability
Alice	4.1 ± 0.5	7.6 ± 0.4
Bob (with Alice)	2.6 ± 0.3	4.9 ± 0.3
Bob (with Charlie)	6.9 ± 0.8	4.7 ± 0.8
Charlie	5.7 ± 0.4	9.4 ± 0.4

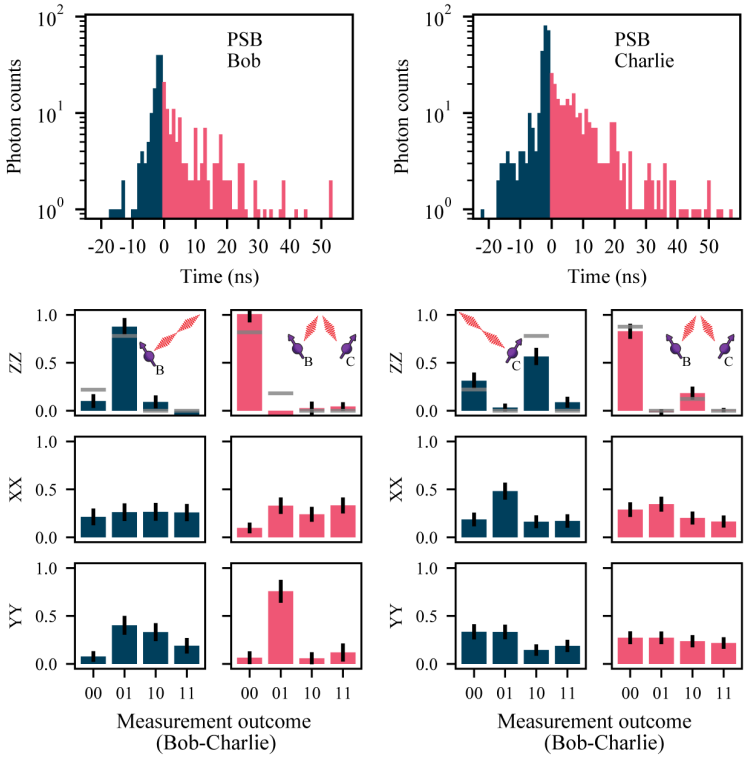

Figure 5.8: (Top) Histograms of the detected PSB photons conditioned on a simultaneous ZPL detection in the entanglement generation attempt, for Bob (left) and Charlie (right). (Bottom) Corresponding measured correlations in all bases. The gray bars in the Z basis represent the simulated values. For the X and Y basis, one would expect a probability of 0.25 for all outcomes. All error bars represent one standard deviation.

Parameter	Description
γ	Spontaneous emission rate of the excited state.
$\Omega(t)$	Optical driving strength.
α	Initial population of the $\|0\rangle$ state.
P_0	Probability of emitting 0 photons (ZPL or PSB).
P_1	Probability of emitting 1 photons (ZPL or PSB).
P_2	Probability of emitting 2 photons (ZPL or PSB or both).
P_z	Probability that an emitted photon is a ZPL photon.
$P_{dz,1}$	Probability that a ZPL photon is within the ZPL detection window, conditioned on a single ZPL photon being emitted.
$P_{db,1}$	Probability that a PSB photon is within the PSB detection window, conditioned on a single PSB photon being emitted.
$P_{dz,2}$	Probability that 2 ZPL photons are within the ZPL detection window, conditioned on two ZPL photons being emitted.
$P_{dz,3}$	Probability that one ZPL photons is within the ZPL detection window and one is not, conditioned on two ZPL photons being emitted.
$P_{db,2}$	Probability that 2 PSB photons are within the PSB detection window, conditioned on two PSB photon being emitted.
$P_{dz,3}$	Probability that one PSB photons is within the PSB detection window and one is not, conditioned on two PSB photons being emitted.
$P_{dzb,1}$	Probability that a ZPL photon is within the ZPL detection window and a PSB photon is within the PSB detection window, conditioned on one ZPL and one PSB photon being emitted.
$P_{dzb,2}$	Probability that a ZPL photon is not within the ZPL detection window and a PSB photon is within the PSB detection window, conditioned on one ZPL and one PSB photon being emitted.
$P_{dzb,3}$	Probability that a ZPL photon is within the ZPL detection window and a PSB photon is not within the PSB detection window, conditioned on one ZPL and one PSB photon being emitte.
η_z	Total transmission and detection efficiency of ZPL photons.
η_p	Total transmission and detection efficiency of PSB photons.

Table 5.3: Explanation of the parameters used in the numerical simulation of the entanglement generation protocol.

where $\Omega(t)$ describes the (time-dependent) driving of the optical transition. From the excited state, the NV can spontaneously emit a photon and decay to $|0\rangle$. Without specifying the particular mode this photon is emitted in, we simply model such an emission with a Lindblad jump operator of the form $\hat{L}_1 = \sqrt{\gamma}|0,1_p\rangle\langle e|$. Here γ is the rate of spontaneous emission, $|0,1_p\rangle$ denotes the state where the NV is in state $|0\rangle$ and one photon was emitted, and we use the convention that when not explicitly stated, there is no emitted photon i.e. $|e\rangle$ denotes the NV in state $|e\rangle$ with zero emitted photons.

To account for double emission errors in the entanglement scheme, we expand the model by letting states $|0,1_p\rangle, |e,1_p\rangle$ be coupled by a similar Hamiltonian as in Eq. (5.1) with the same coupling $\Omega(t)$. Double emission is then captured by a Lindblad jump operator $\hat{L}_2 = \sqrt{\gamma}|0,2_p\rangle\langle 1_p,e|$. For the specific excitation pulses used in

the experiment, we can then numerically solve the Master equation of the system in a basis of $(|0\rangle, |e\rangle, |0,1_p\rangle, |e,1_p\rangle, |0,2_p\rangle)$ to obtain the probability of zero (P_0), one (P_1), or two (P_2) photons being emitted from the system ($P_0 + P_1 + P_2 = 1$). Note that in this model, we neglect the probability of emitting more than two photons from the NV.

Assuming an initial state $\sqrt{\alpha}|0\rangle + \sqrt{1-\alpha}|1\rangle$ of the NV center, the state after the optical excitation is then modeled as

$$|\psi\rangle = \sqrt{\alpha}\left(\sqrt{P_0}|0\rangle + \sqrt{P_1}|0,1_p\rangle + \sqrt{P_2}|0,2_p\rangle\right) + \sqrt{1-\alpha}|1\rangle. \tag{5.2}$$

The emitted photons are either PSB (= 97%) or ZPL (= 3%) photons. We model this by performing a standard beam splitter transformation on the photonic modes. Letting $\hat{a}^\dagger$ be the creation operator of a photon ($|1_p\rangle = \hat{a}^\dagger|0_p\rangle$), we make the transformation $\hat{a}^\dagger \to \sqrt{P_z}\hat{a}_z^\dagger + \sqrt{1-P_z}\hat{a}_b^\dagger$, where $\hat{a}_z^\dagger$ ($\hat{a}_b^\dagger$) is the creation operator of a ZPL (PSB) photon and $P_z = 3\%$. Consequently, $|1_p\rangle \to \sqrt{P_z}|1_z\rangle + \sqrt{1-P_z}|1_b\rangle$, where $|1_z\rangle$ ($|1_b\rangle$) is an emitted ZPL (PSB) photon.

5

The photons can be emitted either inside or outside the detection time window, i.e. the time interval in which detected photons are accepted. This time interval is in general different for the PSB and ZPL photons. This results in the following transformations:

$$|1_z\rangle \to \sqrt{P_{dz,1}}|1_{d,z}\rangle + \sqrt{1-P_{dz,1}}|1_{nd,z}\rangle \tag{5.3}$$

$$|1_b\rangle \to \sqrt{P_{db,1}}|1_{d,b}\rangle + \sqrt{1-P_{db,1}}|1_{nd,b}\rangle \tag{5.4}$$

$$|2_z\rangle \to \sqrt{P_{dz,2}}|2_{d,z}\rangle + \sqrt{P_{dz,3}}|1_{d,z}\rangle|1_{nd,z}\rangle + \sqrt{1-P_{dz,2}-P_{dz,3}}|2_{nd,z}\rangle \tag{5.5}$$

$$|2_b\rangle \to \sqrt{P_{db,2}}|2_{d,b}\rangle + \sqrt{P_{db,3}}|1_{d,b}\rangle|1_{nd,b}\rangle + \sqrt{1-P_{db,2}-P_{db,3}}|2_{nd,b}\rangle \tag{5.6}$$

$$\begin{aligned}|1_z\rangle|1_b\rangle \to\ & \sqrt{P_{dzb,1}}|1_{d,z}\rangle|1_{d,b}\rangle + \sqrt{P_{dzb,2}}|1_{nd,z}\rangle|1_{d,b}\rangle \\ & + \sqrt{P_{dzb,3}}|1_{d,z}\rangle|1_{nd,b}\rangle + \sqrt{1-P_{dz,2}-P_{dz,2}-P_{dz,3}}|1_{nd,z}\rangle|1_{nd,b}\rangle.\end{aligned} \tag{5.7}$$

The probabilities $P_{dz,1}, P_{db,1}, \ldots$ are defined in table 5.3 and are found through the numerical simulation described above.

Finally, we model transmission loss with standard beam splitter transformations acting on the photon modes emitted in the detection window. Letting $\hat{a}_{d,z}^\dagger$ ($\hat{a}_{d,b}^\dagger$) be the creation operator of a ZPL (PSB) photon emitted in the detection time window, we make the transformations

$$\hat{a}_{\mathrm{d,z}}^\dagger \to \sqrt{\eta_z}\hat{a}_{\mathrm{d,z}}^\dagger + \sqrt{1-\eta_z}\hat{a}_{\mathrm{nd,z}}^\dagger \tag{5.8}$$

$$\hat{a}_{\mathrm{d,z}}^\dagger \to \sqrt{\eta_b}\hat{a}_{\mathrm{d,b}}^\dagger + \sqrt{1-\eta_z}\hat{a}_{\mathrm{nd,b}}^\dagger. \tag{5.9}$$

where η_z is the total transmission efficiency from the NV to the central beam splitter while η_b is the total transmission and detection efficiency of the PSB photons. The operators $\hat{a}_{\mathrm{nd,z}}^\dagger$ and $\hat{a}_{\mathrm{nd,b}}^\dagger$ describe the lost/undetected modes. Tracing over the undetected

modes, the output state of a single NV can be written as

$$\rho_\psi = \rho_0 \otimes |0\rangle\langle 0|_{\mathrm{d,b}} + \rho_1 \otimes |1\rangle\langle 1|_{\mathrm{d,b}} + \rho_2 \otimes |2\rangle\langle 2|_{\mathrm{d,b}}\,, \tag{5.10}$$

where we have neglected any coherence between the photonic PSB modes since these are accompanied by undetected non-radiative decay (phonon emission). The unnormalized density matrices ρ_0, ρ_1, and ρ_2 describe the state of the NV center communication qubit and the ZPL photons emitted in the time window of the ZPL detectors and transmitted to the central beam splitter. In the limit $\eta_z \ll 1$, we can neglect terms of $|2_{\mathrm{d,z}}\rangle$ and these density matrices will all be of the form

$$\rho_j = \sum_{i=1}^{4} |\phi_{i,j}\rangle\langle\phi_{i,j}|\,, \tag{5.11}$$

where $|\phi_{i,j}\rangle = (a_{i,j}|1\rangle + b_{i,j}|0\rangle)|0_z\rangle + c_{i,j}|0\rangle|1_{\mathrm{d,z}}\rangle$ and $j = 0,1,2$. In Eq. (5.11) i refers to the different number of lost undetected photons

$i = 1$, zero photons being lost

$i = 2$, one ZPL photon being lost

$i = 3$, one PSB photon being lost

$i = 4$, two photons being lost, either two ZPL, two PSB or one ZPL and one PSB

and j to the number of detected PSB photons. We note that all $a_{i,1}$ and $a_{i,2}$ will be zero since ρ_1 and ρ_2 are accompanied by PSB photons (see Eq. (5.10)) meaning that the NV was in state $|0\rangle$. Furthermore, the only non-zero term in ρ_2 will be $b_{i,2}$ since two PSB photons were emitted, meaning that no ZPL photon was emitted since we neglect higher order emissions.

The only term in Eq. (5.10) from which remote spin-spin entanglement between two NVs can be created is $\rho_0 \otimes |0\rangle\langle 0|_{\mathrm{d,b}}$ since this does not have any detected PSB photons. However, PSB and ZPL photons that were emitted but not detected will still decrease the entangled state fidelity. Such events are responsible for the contributions of $|\phi_{2,0}\rangle, |\phi_{3,0}\rangle$ and $|\phi_{4,0}\rangle$ in ρ_0. The only term where no PSB photons were emitted and no ZPL photons were undetected is $|\phi_{1,0}\rangle = \sqrt{1-\alpha}\,|1\rangle|0_{\mathrm{zpl}}\rangle + \sqrt{\alpha}\,|0\rangle(\sqrt{P_0}\,|0_{\mathrm{zpl}}\rangle + \sqrt{P_1 P_{\mathrm{zpl}} P_{\mathrm{d,zpl}}}\,|1_{\mathrm{d,zpl}}\rangle)$.

The combined state from the two NV centers before the central beam splitter is $\rho_\psi \otimes \tilde{\rho}_\psi$, where $\tilde{\rho}_\psi$ (the state of the second NV) is of the same form as in Eq.5.10 but including that parameters such as initial rotation (α), driving strength (Ω) and transmission efficiencies (η_z, η_b) can be different for the two centers. Furthermore, we include a phase difference between the two paths to the central beam splitter. The central beam splitter is modeled as a perfect 50:50 beam splitter and the finite detection efficiency of the output detectors is assumed to be equal and can be directly included in the transmission efficiencies (η_z) while dark counts are negligible in the experiment and not included. Finally, we include non-perfect visibility between the ZPL photons by reducing the coherence between the output modes of the beam splitter by a factor ν. This visibility is estimated from experimental data and can e.g. originate from slightly off-resonant driving of the NV centers.

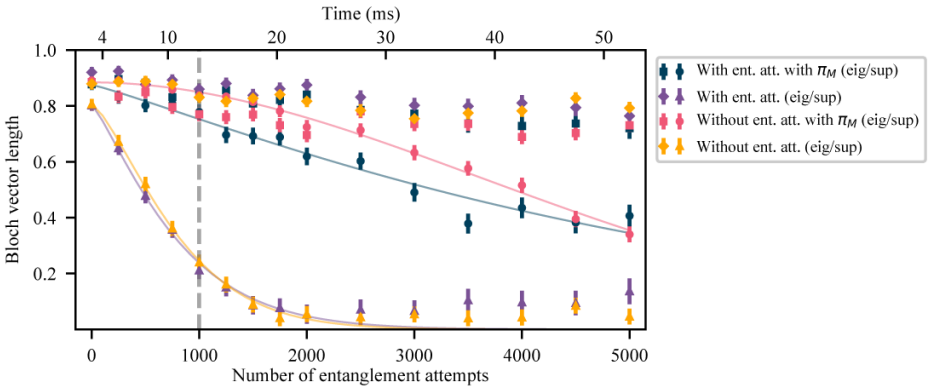

Figure 5.9: Coherence of Bob's memory qubit for superposition states (triangles and circles) and eigenstates (squares and diamonds). We perform the sequence as described in the main text with and without the decoupling pulse π_M on the memory qubit, the dark blue and purple points respectively. Additionally, we perform the sequence with a wait time instead of entanglement attempts with (pink points) and without the decoupling pulse (yellow points). The gray dashed line indicates the timeout of the entanglement generation process used in the teleportation protocol. All error bars represent one standard deviation.

5

5.7.4. MEMORY QUBIT COHERENCE BOB

We use the sequence described in Figure 3a of the main text to preserve the state of the memory qubit during entanglement attempts. To characterize the decoupling sequence, we compare it to the sequence where we do not apply the decoupling pulse on the memory qubit and/or the sequence where we idle instead of performing entanglement attempts. We characterize the coherence of the memory qubit by storing the six cardinal states. We average the results for the eigenstates ($|0\rangle, |1\rangle$) and superposition states ($|\pm X\rangle$ and $|\pm Y\rangle$). In Figure 5.9 we plot the Bloch vector length $b = \sqrt{b_x^2 + b_y^2 + b_z^2}$ with b_i the Bloch vector component in direction i.

Table 5.4: Fitted parameters for the memory coherence decay of the superposition states. All error bars represent one standard deviation.

	A	$N_{1/e}$	n
With ent. att. with π_M	0.875 ± 0.015	5327 ± 319	1.13 ± 0.11
With ent. att. without π_M	0.806 ± 0.019	848 ± 39	1.21 ± 0.09
Without ent. att. with π_m	0.884 ± 0.011	5239 ± 163	1.94 ± 0.16
Without ent. att. without π_M	0.807 ± 0.019	880 ± 34	1.37 ± 0.10

Over the measured range, the eigenstates show little decay. The decay of the superposition states is fitted with the function $f(x) = Ae^{-(x/N_{1/e})^n}$. The fitted parameters can be found in Table 5.4.

The use of the decoupling pulse π_M on the memory qubit increases the $N_{1/e}$ by more

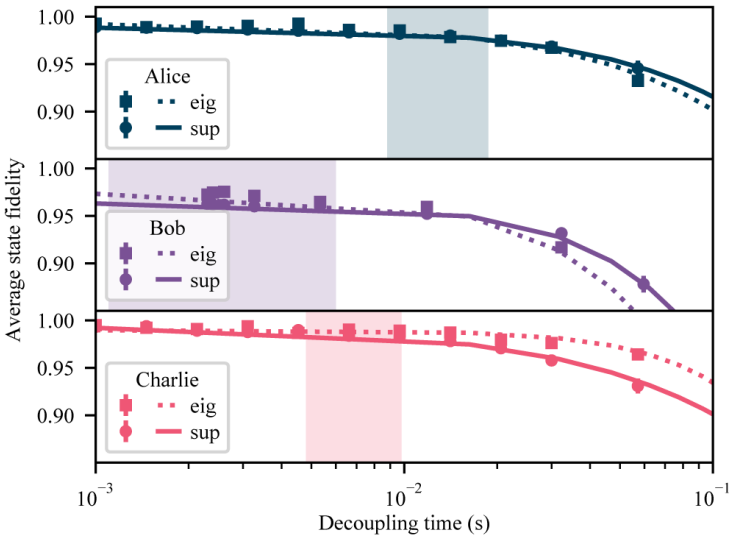

Figure 5.10: Decoupling of the communication qubits. The average state fidelity is plotted for different decoupling times for each setup. The shaded area represent the decoupling times used in the teleportation protocol. All error bars represent one standard deviation.

than a factor 6. Moreover, the initial Bloch vector length A is higher with the π_M pulse. This is mainly explained by the second round of phase stabilization [16] in between swapping the state onto the memory qubit and starting the entanglement generation process. The phase stabilization takes $\approx 350\mu$s and during this time the memory qubit is subject to intrinsic T_2^* dephasing, which can be efficiently decoupled using the π_M pulse.

5.7.5. COMMUNICATION QUBIT COHERENCE

In various parts of the protocol we decouple the communication qubits from the spin bath environment to extend their coherence time. On Alice, we start the decoupling when the first entangled link is established and stop when the results of the Bell-state measurement to teleport the state are sent by Charlie. On Bob, we decouple the communication qubit when the memory qubit is being re-phased. On Charlie, the communication qubit is decoupled from the point that entanglement with Bob is heralded up to the point where Bob has finished the Bell-state measurement, performed the CR check and has communicated the results. All these decoupling times are dependent on how many entanglement attempts are needed to generate the entangled link between Bob and Charlie.

We characterize the average state fidelities for different decoupling times, see Figure 5.10. We investigate eigenstates and superposition states separately. We fit the fidelity with the function $f(t) = Ae^{-(t/\tau_{coh})^n} + 0.5$. The fitted parameters are summarized in Table 5.5. For each setup, the minimum and maximum used decoupling times are in-

Table 5.5: Fitted parameters for average state fidelity state during communication qubit decoupling. All error bars represent one standard deviation.

		A	$\tau_{coh}(s)$	n
Alice	Eigenstate	0.4930 ± 0.0013	0.459 ± 0.012	1.04 ± 0.03
	Superposition	0.4889 ± 0.0018	0.54 ± 0.02	1.07 ± 0.05
Bob	Eigenstate	0.4738 ± 0.0011	0.130 ± 0.003	1.41 ± 0.04
	Superposition	0.4634 ± 0.0015	0.177 ± 0.006	1.47 ± 0.06
Charlie	Eigenstate	0.4897 ± 0.0009	0.357 ± 0.007	1.67 ± 0.06
	Superposition	0.4936 ± 0.0019	0.56 ± 0.02	0.92 ± 0.04

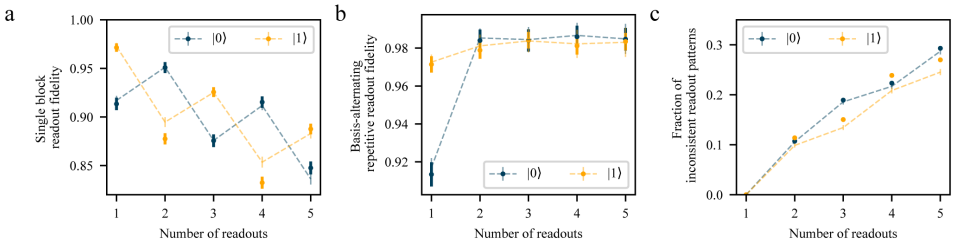

Figure 5.11: Basis-alternating repetitive (BAR) readout results for Charlie's memory qubit. **a** Measured fraction of memory qubit states that were assigned 0 per readout block, for initialization in $|0\rangle$ and in $|1\rangle$. **b** Readout fidelity of the basis-alternating repetitive readout scheme for different number of readout repetitions. **c** Fraction of inconsistent readout patterns for different number of readout repetitions. The dashed lines represent a numerical model using measured parameters. All error bars represent one standard deviation.

dicated by the shaded regions in Figure 5.10. The left-most border is the decoupling time when the first entanglement attempt on Bob and Charlie would be successful, the right-most border when the last attempt before the timeout of 1000 attempts would herald the entangled state.

5.7.6. BASIS-ALTERNATING REPETITIVE READOUT

In the main text we discuss the basis-alternating repetitive readout and the results on Bob's memory qubit are shown in Figure 3. Here we show the results for Charlie's memory qubit. We assign the state using the first readout and only accept the result when the consecutive readouts give a consistent pattern. The results for two different initial states of the memory qubit are plotted in Figure 5.11. We model the expected performance with a Monte Carlo simulation which takes into account the electron readout fidelities, the initial state populations and gate errors, see[37]. In the case of unconditional teleportation, the state is assigned using the first readout and is accepted regardless of the second readout result.

Table 5.6: Numerical values of the data displayed in Figure 4b of the main text. All error bars represent one standard deviation.

	Teleported state fidelity
X	0.760 ± 0.024
-X	0.745 ± 0.025
Y	0.656 ± 0.027
-Y	0.651 ± 0.027
Z	0.731 ± 0.026
-Z	0.671 ± 0.027
Average	0.702 ± 0.011

Table 5.7: Numerical values of the data displayed in Figure 4c of the main text. All error bars represent one standard deviation.

Bell-state measurement outcome (memory qubit, communication qubit)	Average teleported state fidelity
00	0.707 ± 0.015
01	0.696 ± 0.014
10	0.698 ± 0.015
11	0.671 ± 0.014
No feed forward	0.501 ± 0.007

5.7.7. TELEPORTATION RESULTS

The numerical values of the data displayed in Figures 4b and 4c in the main text can be found in Tables 5.6 and 5.7, respectively.

5.7.8. DATA ACQUISITION AND EXPERIMENTAL RATES

At multiple points during the experimental sequence we make a decision on whether to continue the protocol or not. For example, after successful heralding of a two-node entangled state, we can decide to abort the protocol based on whether the flag was raised by any detection of a PSB photon. As all these signals come in real-time, these decisions can be made in real-time, and the sequence can be aborted whenever appropriate. However, we choose to postpone these decisions to the processing after the data acquisition and continue the sequence in any case. In this way, we gain more insight in the performance of the experiment, at the expense of just a marginal increase in experimental time. Processing steps taken after the data acquisition:

- More precise temporal selection than 15 ns.
- PSB rejection.
- Selection of readout outcomes during the Bell-state measurements, including selection on consistent readout patterns for the memory qubit readout.
- Selection on successful Charge-Resonance checks during the sequence.
- Ensure that the last optical phase measurement (before feedback) prior to the heralding event is below $< 50^o$.

- High enough photon count rates on Alice during qubit initialization and optical pulsing, averaged over the second before the heralding signal comes in. (On Alice we perform gate tuning to keep the qubit on resonance with the control lasers. The gate tuning, in combination with the high repetition rate of entanglement attempts, makes the qubit spectrally jumpy. The control loops during the charge-resonance checks should ensure the resonance condition[36], but we use this live-tracking of the photon statistics as an extra check.)

To emphasize, all these processing steps can also be done real-time during the experiment. For the data acquisition, we interleave blocks of measurements with calibrations. The calibrations also serve as an independent measure of the performance of the setups.

We collect the data in blocks of 200 "raw" data points (taking roughly an hour), which result on average in about 30 data points per block after applying the processing steps. We analyzed the data only after completing all data acquisition. Prior to the measurement, we decided on the target total number of data points, the experimental settings, and the processing steps afterwards. The plan was to run a sufficient number of blocks (estimated at 80) such that after processing we would remain with >2,800 data points, and at least 450 per cardinal axis. These target numbers were a trade-off between measurement time and expected violation of the classical bound for the conditional teleportation. Unfortunately, after 80% of the data points were acquired, the setups consistently failed two of the calibrations steps due to the formation of ice on Charlie's diamond sample (the origin of this, either a leak or an outgassing element, is under investigation at time of writing). Therefore, we decided to end the data acquisition, include all data taken up to that point and analyze. In total, we have acquired 79 blocks of data, and we measured 2272 events ($|+X\rangle$ 382, $|-X\rangle$ 385, $|+Y\rangle$ 385, $|-Y\rangle$ 378, $|+Z\rangle$ 375, $|-Z\rangle$ 367) for the conditional teleportation over a time span of 21 days.

We can determine the experimental rate including all overhead (such as CR checks, communication time and phase stabilization) by dividing the number of measured data points by the total measurement time. In Figure 5.12 we plot the experimental rate for both the conditional and unconditional teleportation sequence. In the case of the unconditional teleportation, we accept all Bell-state measurement outcomes on Charlie and therefore the experimental rate is higher. For shorter detection windows during the two-node entanglement, the success probability per attempt is smaller and thus the experimental rate is lower.

5.7.9. MODEL OF THE TELEPORTED STATE

A detailed model of the teleported state can be found at[37]. The model comprises elements from[16] and is further extended for the teleportation protocol. We take the following noise sources into account

- imperfect Bell states between Alice and Bob, and between Bob and Charlie,
- dephasing of the memory qubit of Bob during entanglement generation between Bob and Charlie,

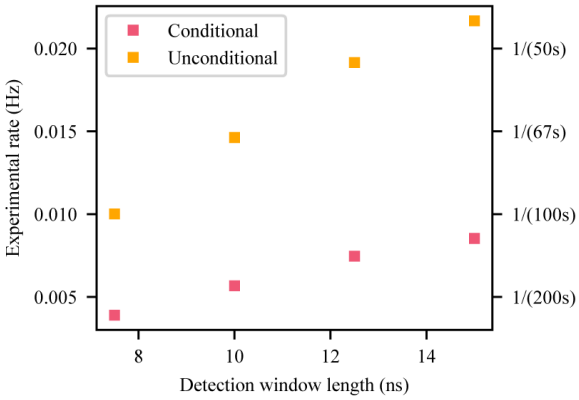

Figure 5.12: Experimental rates of the conditional and unconditional teleportation protocol for different detection window lengths in the two-node entanglement generation.

- depolarizing noise on the memory qubits of Bob and Charlie, due to imperfect initialization and swap gates,
- readout errors on the communication qubits of Bob and Charlie and readouts errors on the memory qubits of Bob and Charlie when using the basis-alternating readout scheme which result in incorrect feed-forward gate operations after the Bell-state measurements,
- depolarizing noise on Alice during the decoupling sequence,
- ionization probability on Alice.

An overview of the input parameters and the effect of the different error sources is given in Tables 5.8 and 5.9.

5.7.10. EFFECT OF THE 3 KEY INNOVATIONS ON THE TELEPORTED STATE FIDELITY AND EXPERIMENTAL RATE

We assess the effect of each innovation on the teleportation protocol. First, we estimate the average state fidelity and experimental rate with a set of baseline parameters based on the performance in [16]. We use a timeout of 1000 entanglement attempts for the second link (between Bob and Charlie) before aborting the protocol and starting over. In both Bell-state measurements, we continue the sequence for the outcomes "00" and "01" (communication qubit, memory qubit), or abort and start over (in the case of conditional teleportation). Then we incrementally add (1) the basis-alternating repetitive readout scheme for the memory qubits,(2) the improved memory qubit coherence and (3) the tailored heralding scheme of the remote entanglement generation. The results are summarized in 5.10.

Table 5.8: Overview of parameters used in the simulations for the two-node entangled states. The error due to the $|0\rangle$ state populations is a result of the single click protocol. For the other error sources we compute the estimated infidelity as if it was the only error source present apart from the protocol error. This allows easy comparison between the different error sources.

	Parameter AB	Parameter BC	Infidelity Ψ_{AB}	Infidelity Ψ_{BC}
Detection window length	15 ns	15 ns		
Detection probability setup 1	3.4×10^{-4}	4.3×10^{-4}		
Detection probability setup 2	5.1×10^{-4}	2.4×10^{-4}		
Average detection probability PSB	0.10	0.12		
$\|0\rangle$ state populations (α_1, α_2)	(0.07, 0.05)	(0.05, 0.1)	5.5×10^{-2}	6.7×10^{-2}
Dark count rate	10 Hz	10 Hz	5.1×10^{-3}	5.3×10^{-3}
Visibility	0.90	0.90	2.4×10^{-2}	2.4×10^{-2}
Average double excitation probability	0.06	0.08	5.5×10^{-2}	7.1×10^{-2}
Optical phase uncertainty	21^o	12^o	3.1×10^{-2}	1.0×10^{-2}
All error sources combined			0.16	0.17

5

5.7.11. ESTIMATED FIDELITY OF STATE TO BE TELEPORTED

The state to be teleported is prepared on the communication qubit of Charlie. Errors in the preparation originate from imperfect initialization and imperfect MW pulses, which are estimated to be $p_{init} = 1.2\times10^{-3}$ and $p_{MW} = 8\times10^{-3}$ [38]. Averaged over the six cardinal states, we estimate the state preparation fidelity to be ≈ 0.995.

5.7.12. CALCULATION OF TELEPORTED STATE FIDELITY WITHOUT FEED-FORWARD OPERATION

Calculation of teleported state fidelity without feed - forward operation In figure 4c in the main text we show the fidelity of the teleported state in case no feed-forward operations would have been applied on Alice. To extract this data we follow the same method as in [11]. We perform classical bit flips on the measurement outcomes to counteract the effect of the feed-forward gate operations (as if the gate was not applied) for each Bell-state measurement outcome. We do this for all six cardinal states and compute the average fidelity. We assume the errors of the gate in the feed-forward operations to be small.

5.7.13. AUTHOR CONTRIBUTIONS

S.L.N.H., M.P. and R.H. devised the experiment. S.L.N.H., M.P. and H.K.C.B. carried out the experiments and collected the data. S.L.N.H., M.P., H.K.C.B. and S.B. prepared the experimental apparatus. J.B. developed the quantum-optical model. S.L.N.H. and R.H. wrote the main manuscript, with input from all authors. S.L.N.H., M.P. and J.B. wrote the supplementary materials, with input from all authors. S.L.N.H. and M.P. analysed the data and discussed with all authors. R.H. supervised the research.

Table 5.9: Overview of parameters used in the simulations for the average teleported state fidelity in case of a conditional Bell-state measurement on Charlie. For each error sources we compute the estimated infidelity as if it was the only error source present apart from the single click protocol errors of the two-node entangled states. This allows easy comparison between the different error sources.

	Parameter	Infidelity
Ionization probability Alice	0.7%	0.6×10^{-2}
Depolarizing noise Alice	0.04	1.7×10^{-2}
Depolarizing noise memory qubit Bob	0.12	5.0×10^{-2}
Dephasing noise memory qubit Bob ($N_{1/e}, n$)	(5300, 1.1)	2.1×10^{-2}
Depolarizing noise memory qubit Charlie	0.14	5.9×10^{-2}
Readout fidelities memory qubit Bob ($\|0\rangle, \|1\rangle$)	(0.99, 0.99)	0.6×10^{-2}
Readout fidelities communication qubit Bob ($\|0\rangle, \|1\rangle$)	(0.93, 0.995)	0.3×10^{-2}
Readout fidelities memory qubit Charlie ($\|0\rangle, \|1\rangle$)	(0.98, 0.98)	1.1×10^{-2}
Readout fidelities communication qubit Charlie ($\|0\rangle, \|1\rangle$)	(0.92, 0.99)	0.6×10^{-2}
Two-node entangled states combined		0.192
All error sources combined		0.305

Table 5.10: Simulated effect of the innovations on the teleported state fidelity and experimental rate.

	Fidelity	Rate (Hz)
Baseline parameters using timeout = 1000, BSM outcomes (communication qubit, memory qubit) = "00" or "01"	0.666	1/(53s)
With basis-alternating repetitive readout	0.679	1/(73s)
With improved memory coherence	0.687	1/(73s)
With tailored heralding scheme	0.695	1/(74s)

REFERENCES

[1] C. H. Bennett *et al.*, *Teleporting an unknown quantum state via dual classical and Einstein-Podolsky-Rosen channels,* Physical Review Letters **70**, 1895 (1993).

[2] S. Wehner, D. Elkouss and R. Hanson, *Quantum internet: A vision for the road ahead,* Science **362** (2018).

[3] M. Ben-Or, C. Crépeau, D. Gottesman, A. Hassidim and A. Smith, *Secure multiparty quantum computation with (only) a strict honest majority,* Proceedings - Annual IEEE Symposium on Foundations of Computer Science, FOCS , 249 (2006), 0801.1544 .

[4] A. S. Arora, J. Roland and S. Weis, *Quantum weak coin flipping,* Proceedings of the Annual ACM Symposium on Theory of Computing , 205 (2019), 1811.02984 .

[5] D. Bouwmeester *et al.*, *Experimental quantum teleportation,* Philosophical Transactions of the Royal Society A: Mathematical, Physical and Engineering Sciences **356**, 1733 (1997).

[6] D. Boschi, S. Branca, F. D. Martini, L. Hardy and S. Popescu, *Experimental Realization of Teleporting an Unknown Pure Quantum State via Dual Classical and Einstein-Podolsky-Rosen Channels,* Physical Review Letters **80**, 1121(5) (1998).

[7] A. Furusawa *et al.*, *Unconditional quantum teleportation,* Science **282**, 706 (1998).

[8] S. Olmschenk, D. N. Matsukevich, P. Maunz, D. Hayes and C. Monroe, *Quantum Teleportation between Distant Matter Qubits,* Science **323**, 486 (2009).

[9] C. Nölleke *et al.*, *Efficient teleportation between remote single-atom quantum memories,* Physical Review Letters **110**, 1 (2013).

[10] S. Langenfeld *et al.*, *Quantum Teleportation between Remote Qubit Memories with only a Single Photon as a Resource,* Physical Review Letters **126**, 130502 (2021).

[11] W. Pfaff *et al.*, *Unconditional quantum teleportation between distant solid-state quantum bits,* Science **345**, 532 (2014), 1404.4369 .

[12] X. H. Bao *et al.*, *Quantum teleportation between remote atomic-ensemble quantum memories,* Proceedings of the National Academy of Sciences of the United States of America **109**, 20347 (2012).

[13] H. Briegel, W. Dür, J. I. Cirac and P. Zoller, *Quantum Repeaters The Role of Imperfect Local Operations in Quantum Communication,* Physical Review Letters **81**, 5932 (1998).

[14] C. Cabrillo, J. I. Cirac, P. Garcia-Fernandez and P. Zoller, *Creation of entangled states of distant atoms by interference,* Physical Review A **59**, 1025 (1999).

[15] S. Bose, P. L. Knight, M. B. Plenio and V. Vedral, *Proposal for teleportation of an atomic state via cavity decay,* Physical Review Letters **83**, 5158 (1999), 9908004 [quant-ph] .

[16] M. Pompili *et al.*, *Realization of a multinode quantum network of remote solid-state qubits,* Science **372**, 259 (2021).

[17] P. C. Humphreys *et al.*, *Deterministic delivery of remote entanglement on a quantum network,* Nature **558**, 268 (2018), 1712.07567 .

[18] T. Legero, T. Wilk, A. Kuhn and G. Rempe, *Time-resolved two-photon quantum interference,* Applied Physics B: Lasers and Optics **77**, 797 (2003).

[19] C. E. Bradley *et al.*, *A Ten-Qubit Solid-State Spin Register with Quantum Memory up to One Minute,* Physical Review X **9**, 31045 (2019), 1905.02094 .

[20] J. Cramer *et al.*, *Repeated quantum error correction on a continuously encoded qubit by real-time feedback,* Nature Communications **7**, 1 (2016).

[21] L. Robledo *et al.*, *High-fidelity projective read-out of a solid-state spin quantum register,* Nature , 5 (2011).

[22] L. Jiang *et al.*, *Quantum repeater with encoding,* Physical Review A **79**, 1 (2009), 0809.3629 .

[23] S. J. Van Enk, N. Lütkenhaus and H. J. Kimble, *Experimental procedures for entanglement verification,* Physical Review A **75**, 1 (2007), 0611219 [quant-ph] .

[24] R. Van Meter, *Quantum Networking* (John Wiley & Sons, Inc., 2014).

[25] A. Broadbent, J. Fitzsimons and E. Kashefi, *Universal blind quantum computation,* Proceedings - Annual IEEE Symposium on Foundations of Computer Science, FOCS , 517 (2009), 0807.4154 .

[26] B. C. Rose *et al.*, *Observation of an environmentally insensitive solid-state spin defect in diamond,* Science **361**, 60 (2018).

[27] C. T. Nguyen *et al.*, *Quantum Network Nodes Based on Diamond Qubits with an Efficient Nanophotonic Interface,* Physical Review Letters **123**, 1 (2019).

[28] M. E. Trusheim *et al.*, *Transform-Limited Photons from a Coherent Tin-Vacancy Spin in Diamond,* Physical Review Letters **124**, 1 (2020).

[29] N. T. Son *et al.*, *Developing silicon carbide for quantum spintronics,* Applied Physics Letters **116**, 190501 (2020).

[30] D. M. Lukin, M. A. Guidry and J. Vučković, *Integrated Quantum Photonics with Silicon Carbide: Challenges and Prospects,* PRX Quantum **1**, 1 (2020).

[31] J. M. Kindem *et al.*, *Control and single-shot readout of an ion embedded in a nanophotonic cavity,* Nature **580** (2020).

[32] S. Chen, M. Raha, C. M. Phenicie, S. Ourari and J. D. Thompson, *Parallel single-shot measurement and coherent control of solid-state spins below the diffraction limit,* Science **370**, 592 (2020).

[33] M. Ruf, N. H. Wan, H. Choi, D. Englund and R. Hanson, *Quantum networks based on color centers in diamond,* Journal of Applied Physics **130**, 070901 (2021), 2105.04341 .

[34] M. E. Grein, M. L. Stevens, N. D. Hardy and P. Benjamin Dixon, *Stabilization of long, deployed optical fiber links for quantum networks,* 2017 Conference on Lasers and Electro-Optics, CLEO 2017 - Proceedings , 1 (2017).

[35] A. Dahlberg *et al.*, *A link layer protocol for quantum networks,* SIGCOMM 2019 - Proceedings of the 2019 Conference of the ACM Special Interest Group on Data Communication , 159 (2019).

[36] B. Hensen *et al.*, *Loophole-free Bell inequality violation using electron spins separated by 1.3 kilometres,* Nature **526**, 682 (2015).

[37] S. Hermans *et al.*, *Data and software supporting "qubit teleportation between non-neighboring nodes in a quantum network",* (2021).

[38] N. Kalb, P. C. Humphreys, J. J. Slim and R. Hanson, *Dephasing mechanisms of diamond-based nuclear-spin memories for quantum networks,* Physical Review A **97**, 1 (2018), 1802.05996 .

6

CONTROL OF SOLID-STATE NUCLEAR SPIN QUBITS USING AN ELECTRON SPIN-1/2

H. K. C. Beukers*, C. Waas*, M. Pasini, H. B. van Ommen, Z. Ademi, M. Iuliano, N. Codreanu, J. M. Brevoord, T. Turan, T. H. Taminiau & R. Hanson

Solid-state quantum registers consisting of optically active electron spins with nearby nuclear spins are promising building blocks for future quantum technologies. For electron spin-1 registers, dynamical decoupling (DD) quantum gates have been developed that enable the precise control of multiple nuclear spin qubits. However, for the important class of electron spin-1/2 systems, this control method suffers from intrinsic selectivity limitations, resulting in reduced nuclear spin gate fidelities. Here we demonstrate improved control of single nuclear spins by an electron spin-1/2 using Dynamically Decoupled Radio Frequency (DDRF) gates. We make use of the electron spin-1/2 of a diamond tin-vacancy center, showing high-fidelity single-qubit gates, single-shot readout, and spin coherence beyond a millisecond. The DD control is used as a benchmark to observe and control a single ^{13}C nuclear spin. Using the DDRF control method, we demonstrate improved control on that spin. In addition, we find and control an additional nuclear spin that is insensitive to the DD control method. Using these DDRF gates, we show entanglement between the electron and the nuclear spin with 72(3) *% state fidelity. Our extensive simulations indicate that DDRF gate fidelities well in excess are feasible. Finally, we employ time-resolved photon detection during readout to quantify the hyperfine coupling for the electron's optically excited state. Our work provides key insights into the challenges and opportunities for nuclear spin control in electron spin-1/2 systems, opening the door to multi-qubit experiments on these promising qubit platforms.*

The results of this chapter have been published in Physical Review X, **15**, 021011 (2025).
* Equally contributing authors

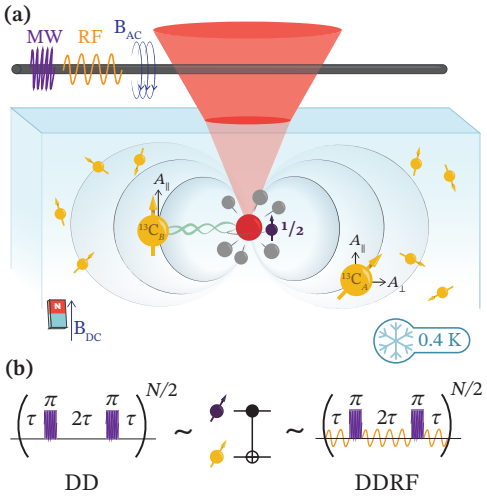

Figure 6.1: **Nuclear spin control with electron spin-1/2.** (a) The electron spin-1/2 of a negatively charged tin-vacancy center in a ⟨100⟩ surface-oriented diamond (purple spin) is initialized and read out by a red laser. The electron spin is controlled using the AC magnetic field of microwave (MW) radiation (purple sine) through a wire (gray line) spanned over the diamond. The surrounding nuclear spins (yellow spins) have a unique parallel and perpendicular hyperfine coupling ($A_\parallel$ and $A_\perp$) to the electron spin. This allows conditional control with the electron spin and generation of entanglement (green link). The nuclear spins can be directly driven using radiofrequency (RF) radiation (yellow sine). (b) Nuclear spin control is achieved by dynamical decoupling (DD) and dynamically decoupled radio frequency (DDRF) gates. For DD gates, interpulse delays τ resonant with the nuclear spin dynamics cause a rotation conditioned on the electron spin state. For DDRF gates, the interpulse delays do not need to follow the dynamics of the target nuclear spin: direct spin-state selective radio frequency driving with tailored phase updating enables a conditional rotation of the nuclear spin. Both techniques perform CNOT-equivalent gates.

6.1. INTRODUCTION

Optically interfaced electron spins in the solid state are promising platforms for quantum networking, computing, and sensing[1]. Prominent examples are color centers[2–7] and single rare-earth ions[8–11]. These electron spins offer fast control[12–14] and high-fidelity readout[15–17]. Moreover, their spin-photon interface enables remote entanglement generation[18], while their solid-state nature facilitates on-chip integration[19]. The use of surrounding nuclear spins as long-lived memory qubits further enhances the functionality of the electron spins. For example, these electron-nuclear registers have enabled recent demonstrations of fault-tolerant quantum computing[20], memory-assisted quantum communication[17] and a multi-node quantum network[21,22].

A key requirement for establishing coherent quantum gates between the electron and nuclear spins is the protection of the electron spin coherence during the gate[23]. For this, different control methods have been developed, such as dynamical decoupling (DD) control[24] and dynamically decoupled radio frequency (DDRF) control[25]. Nuclear spin control using the DD method has been shown in different platforms including color centers in diamond[26–28], silicon carbide[29] and single rare-earth ions[10]. In these

decoherence-protected control methods, the selectivity of the control critically depends on the electron spin magnitude. Notably, the important class of electron spin-1/2 systems, which includes the silicon T centers[30,31] and the diamond group-IV color centers[32–35], has an intrinsically reduced selectivity for the DD control method compared to spin systems with a higher magnitude[10,28,36,37]. It has been hypothesized that the DDRF control method improves the selectivity for these interesting electron spin-1/2 systems[25].

In this work, we experimentally explore and investigate the control of two nuclear spins with the electron spin-1/2 of the negatively charged tin-vacancy (SnV) center in diamond (Fig. 6.1(a)), using both the DD and DDRF control (Fig. 6.1(b)). The SnV center has recently emerged as a highly promising quantum system because of its excellent optical and spin properties, compatibility with nanophotonic integration and operating temperature of above one Kelvin[19,38–46]. We provide a detailed selectivity comparison of spin-1/2 and spin-1 systems in simulation. Furthermore, we investigate the nuclear spins' coupling to the SnV center's excited state during the optical readout of the electron spin.

6.2. ELECTRON SPIN CONTROL

Our experiments are performed on a chemical vapor deposition grown diamond that is implanted with 5×10^{10} ions/cm^2 of spinless ^{120}Sn at a target depth of 88 nm and subsequently annealed at 1100 °C[46]. The diamond contains the natural abundance of carbon isotopes, including 1.1 % ^{13}C, which has a nuclear spin-1/2. A wire is spanned over the diamond sample to deliver the microwave and radio frequency signals. A ^{3}He-cryostat with a confocal optical microscope cools the sample to 0.4 K. We align a bias magnetic field of 0.1 T with the symmetry axis of the SnV center, see Fig. 6.1(a).

We use the negatively charged tin-vacancy (SnV) center throughout this work. The electronic waveform of the SnV center is a spin and orbital doublet in the ground and excited state, as depicted in Fig. 6.2(a). The spin-orbit interaction and lattice strain lift this degeneracy. At temperatures below 1.5 K thermal occupation of the higher levels is negligible, resulting in an effective spin-1/2 system. The other levels are still observable in effects like an anisotropic g-factor, reduced microwave driving efficiency, and an optical cyclicity that depends on the magnetic field alignment[34].

The electron spin qubit is initialized and read out optically with a 619 nm laser. In Fig. 6.2(b), a photoluminescent excitation (PLE) measurement shows the two spin-conserving transitions split by 611(3) MHz due to a difference in the g-factors of the ground and excited states. The SnV center is initialized in the correct charge state and the optical lines are ensured to be on resonance with the laser by a charge-resonance check[47]. The single-shot readout is implemented by spin-selective optical excitation of the spin-down transition[48]. The bright $|0\rangle$ state is assigned in case at least one photon is recorded; otherwise the $|1\rangle$ state is assigned. A finite spin-flipping probability during optical cycling causes readout infidelity of the bright $|0\rangle$ state, whereas noise counts limit the readout fidelity of the dark $|1\rangle$ state. These two contributions are optimized in Fig. 6.2(c), resulting in an average readout fidelity of 77.7(3) %. Note that single-shot readout can be achieved in this setup despite a low collection efficiency of approximately

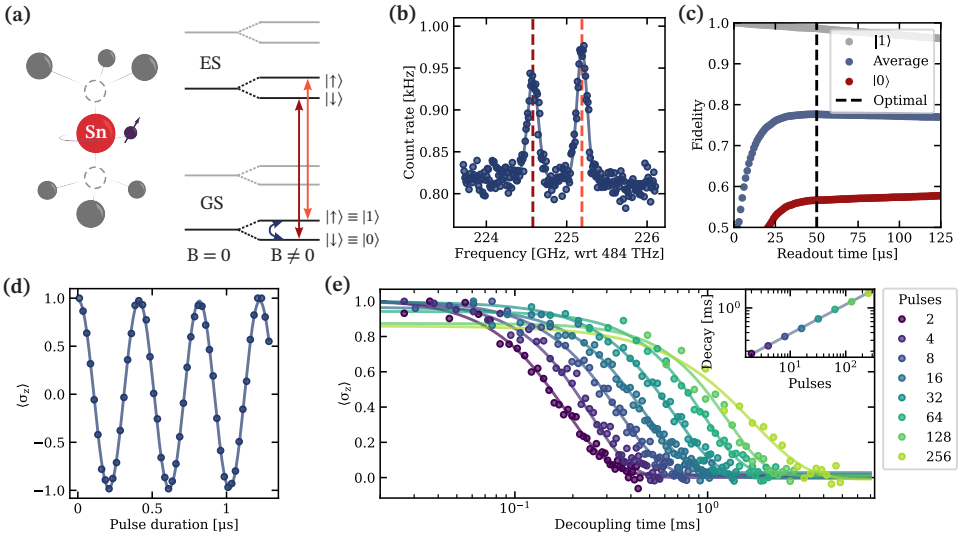

Figure 6.2: **Electronic qubit characterization.** (a) Schematic lattice and level structure of the SnV center. The negatively charged SnV center consists of an interstitial tin atom with two carbon vacancies and an additional electron. The ground and excited states behave as an effective spin-1/2 system at low temperatures. The lowest two levels of the ground state form a spin-1/2 qubit and are connected to the excited state via an optical transition at 619 nm. (b) Photoluminescence excitation measurement of the two spin-conserving transitions in (a). (c) Single-shot readout calibration curve. The splitting of the optical transitions allows for spin-selective readout via optical excitation. The qubit is initialized into an eigenstate. A single-shot readout result of 0(1) is assigned when detecting at least one photon (no photon) during the excitation of the spin-down transition. The best average fidelity determines the optimal readout time. (d) Microwave control of the SnV center electron spin qubit. The fit of this Rabi oscillation is used to determine the duration of $\pi/2$ and π pulses. (e) Electron coherence measurement with dynamical decoupling. We employ XY8 sequences with a varying number of π pulses. Increasing the number of decoupling pulses beyond 100 creates heating in this device, which shows up as a lowered contrast.

0.2 %, thanks to the high cyclicity of approximately 1200 of this SnV center.

Initialization of the qubit is achieved by spin pumping, where a laser, on resonance with the spin-up transition, excites the electron. The finite spin-flipping probability during optical decay causes initialization into the spin-down state. The initialization fidelity of 98.1(5) % is deduced from the residual fluorescence at the end of spin pumping for 300 µs and can be readily improved by implementing a longer spin pumping time or using a higher laser power.

The electron spin is controlled by microwave driving with a Rabi frequency of 2.46 MHz, as shown in Fig. 6.2(d). The average fidelity of the calibrated gates is measured using process tomography to be 98(2) %. The investigated SnV center has a spin dephasing time of $T_2^* = 2.42(4)\,\mu s$, see Appendix 6.9.3. The coherence is extended by XY8 dynamical decoupling of the electron spin to $T_2^{DD} = 1.7(5)$ ms using 256 π pulses[49]. The observed scaling of the coherence during DD in Fig. 6.2(e) matches

$$T_2^{DD} = T_2^{Echo} N^{\chi}, \tag{6.1}$$

where N is the number of decoupling pulses, $T_2^{Echo} = 129(2)\,\mu s$ is the fitted constant equivalent to the single echo coherence, and $\chi = 0.47(1)$ is the scaling factor.

To investigate the limiting effect for the T_2^{Echo}, we perform a double electron-electron resonance (DEER) measurement, see Appendix 6.9.3. In the DEER, we simultaneously apply an echo pulse on the SnV center electron spin and at the MW frequency of free electron spins with a g-factor of 2. This DEER shows a reduced coherence time for the SnV electron spin, which points to the presence of an electron spin bath as a noise source in this device. The found scaling factor χ is close to the one found in the recent experiments in samples with a comparable implantation dose of tin ions[34]. From simulations, they attribute the decoherence to the electron spin bath caused by implantation. Better coherence of the electron spin has been achieved in samples with a hundredfold lower implantation dose[50].

6.3. DYNAMICAL DECOUPLING CONTROL

The hyperfine coupling between the electron spin of the SnV center and the surrounding ^{13}C spins is caused by the dipole-dipole interaction and the Fermi contact hyperfine interaction[51]. Therefore, the coupling is dependent on their relative distance and orientation. A single nuclear spin can be controlled by targeting its unique hyperfine coupling. Strongly coupled ^{13}C can be observed directly in optically detected magnetic resonance (ODMR) of the electron spin[52,53]. However, more weakly coupled spins, where the coupling is smaller than $1/T_2^*$ of the electron spin, are not resolvable by ODMR. To observe and control them, one needs to extend the coherence of the electron spin at the same time. Dynamical decoupling of the electron spin brings the detection limit down to the inverse of the coherence time of the electron spin under dynamical decoupling $1/T_2^{DD}$ [24,54,55].

The Hamiltonian of a single ^{13}C spin, in the secular approximation, is

$$H_{hf} = \omega_L I_z + A_{\parallel} S_z I_z + A_{\perp} S_z I_x, \tag{6.2}$$

where S_i and I_i are the spin operators for the electron and nucleus, respectively, and $\omega_L = \gamma_c B_z$ is the Larmor frequency of the ^{13}C spin with $\gamma_c/2\pi = 10.71\,\mathrm{MHz\,T^{-1}}$. $A_{\parallel}$ and

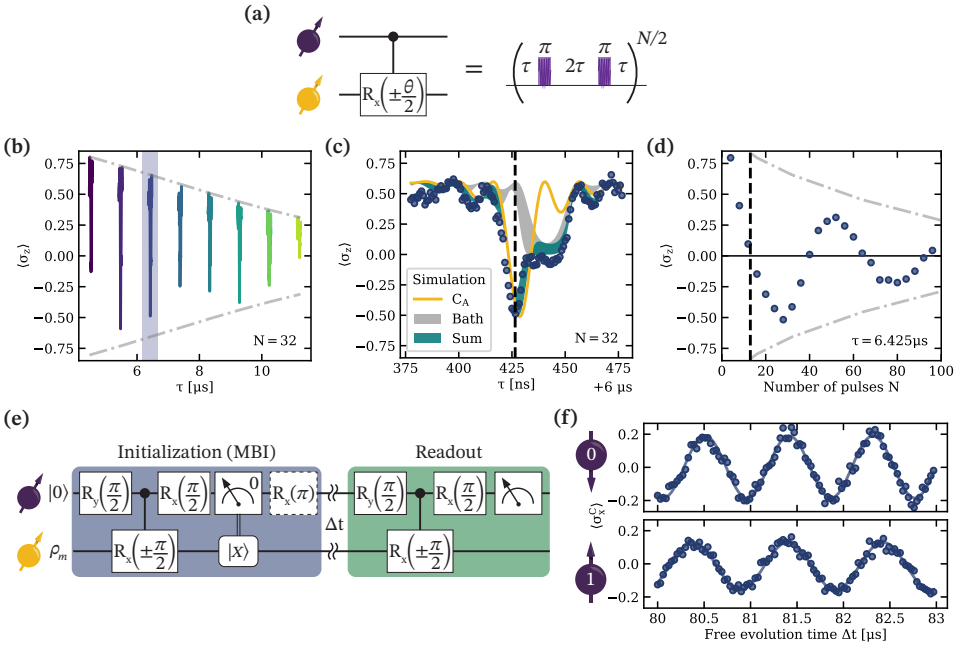

Figure 6.3: **Dynamical decoupling nuclear spin control.** (a) A dynamical decoupling sequence performs a conditional rotation if τ fulfills the resonance condition of the nuclear spin. (b) Dynamical decoupling sequence for varying interpulse delay τ. The dips in the coherence indicate coupling to the nuclear spins around. The dashed line indicates the contrast limit due to the electron coherence. (c) Enlargement of the shaded region of τ in (b). The gray area shows the effect of the spin bath on the electron spin. The spread stems from simulating many different configurations of the spin bath. The narrow dip stems from an individual nuclear spin C_A, where the yellow line is the simulated response. The blue area is the simulated combined effect of the bath and the nuclear spin C_A. Appendix 6.9.5 describes the simulations. (d) Nuclear gate calibration. By fixing $\tau = 6.425\mu$s (dashed line in (b)) and varying the number of decoupling pulses N, coherent control of the nuclear spin can be observed by the oscillation of the electron coherence. The fully entangling gate is achieved when $\langle \sigma_z \rangle = 0$. The gray dashed line indicates the contrast limit due to the electron coherence. (e) Pulse sequence for nuclear Ramsey measurement. The nuclear spin is prepared via a measurement-based initialization (MBI). The controlled gate is achieved by the DD gate characterized in (c) and (d). A measurement of $|0\rangle$ of the electron at the end of the sequence projects the nuclear spin into $|x\rangle$. An optional π pulse allows for measuring the evolution of the nuclear spin for both electron spin states. After a free evolution time Δt, the nuclear spin is measured in the x basis through the electron spin. (f) Ramsey signal of the nuclear spin dependent on the electron spin state. The precession frequency of the nuclear spin changes depending on whether the electron is kept in $|0\rangle$ or flipped to $|1\rangle$ after the MBI. The measured frequencies are $\omega_0/2\pi = 1116.1(2)$ kHz and $\omega_1/2\pi = 985.4(3)$ kHz.

$A_\perp$ are the parallel and perpendicular hyperfine parameters, with respect to the external magnetic field, depicted in Fig. 6.1(a). As a result of this Hamiltonian, the precession axis of the nuclear spin depends on the state of the electron as

$$\vec{\omega}_i = (s_i A_\perp, 0, \omega_L + s_i A_\parallel), \tag{6.3}$$

where s_i is the spin projection of the electron spin for qubit state $|i\rangle$ [36].

Nuclear spins can be detected and controlled using the dynamical decoupling sequence of the electron. The nuclear spin precesses around a different axis depending on the electron spin state. Periodically changing between these two rotation axes can give rise to a conditional rotation of the nuclear spin [24,54,55], as depicted in Fig. 6.3(a). To control a nuclear spin with DD, the π pulses on the electron spin need to be applied in resonance with the dynamics of the nuclear spin. In the high magnetic field regime ($\omega_L \gg A_\parallel, A_\perp$), the resonant condition is met when the τ of the decoupling sequence is

$$\tau_p \approx \frac{(2p+1)\pi}{2\bar{\omega}}, \tag{6.4}$$

where p is the order of the resonance and $\bar{\omega} = (\omega_0 + \omega_1)/2$ is the average nuclear precession frequency. To target a specific nuclear spin, a unique τ_p is required to avoid crosstalk with other spins. Therefore, the selectivity of the DD control method depends on a difference in the average nuclear precession frequency $\bar{\omega}$. Expanding it in hyperfine parameters gives [36]

$$\bar{\omega} = \omega_L \left[1 + \frac{s_0 + s_1}{2} \frac{A_\parallel}{\omega_L} + \frac{s_0^2 + s_1^2}{4} \left(\frac{A_\perp}{\omega_L} \right)^2 \right]. \tag{6.5}$$

The first-order term drops out of the expression if s_0 and s_1 have opposite signs and the same magnitude. In a spin-1/2 system, this is unavoidable, resulting in a second-order selectivity in $A_\perp$. In contrast, in systems with a larger spin magnitude, one can choose the spin projections to achieve a first-order sensitivity in $A_\parallel$.

Low magnetic fields will give a stronger influence of $A_\perp/\omega_L$, which benefits the nuclear spin selectivity in spin-1/2 systems. However, this usually results in a trade-off, as the magnetic field also influences other properties. For the SnV center, for example, a lower field comes at the cost of less separation between the optical transitions and, therefore, reduced optical initialization and readout fidelity for the electron spin qubit.

In Fig. 6.3(b), we first use the DD method to detect the nuclear spins around the SnV center by sweeping τ for 32 decoupling pulses. As this conditional interaction acts like $S_z I_x$, the electron spin can be used as a sensor by applying the conditional gate while the electron is in a superposition. For this, we prepare the electron spin in $|x\rangle = (|0\rangle + |1\rangle)/\sqrt{2}$ using a $\pi/2$ pulse, and, after the decoupling sequence, we use another $\pi/2$ pulse to map the x basis to the z basis for readout. A conditional gate entangles the electron spin with the nuclear spin, which shows up as a loss of coherence of the electron spin in Fig. 6.3(b). A drop in coherence to $\langle \sigma_z \rangle = 0$ can be caused by coupling to many different spins. A value below that shows a coherent interaction with a single spin system [24]. The nuclear spin bath, composed of spins that have small coupling and cannot be resolved individually, shows up at $\tau \approx \frac{2p+1}{4}\tau_L$, where $\tau_L = 2\pi/\omega_L$ is the Larmor period. In Fig. 6.3(c), the dip in coherence around $\tau = 6.45\,\mu$s is shown. Next to the nuclear spin bath, we observe

one dip separate from the bath, which goes well below $\langle\sigma_z\rangle = 0$, indicating coherent coupling. We calibrate a two-qubit gate with this spin based on the DD spectrum by using the τ of the center of the dip. The number of pulses in the DD sequence is swept in Fig. 6.3(d), where $\langle\sigma_z\rangle = 0$ indicates the number of pulses required for a maximally entangling gate (dashed line). The decay of the signal is caused by a combination of loss of coherence of the electron spin and residual crosstalk with the spin bath.

The control over the nuclear spin allows us to perform a Ramsey experiment using the sequence in Fig. 6.3(e), where the nuclear spin is prepared in $|x\rangle$ and read out in the x basis. The state of the nuclear spin can be read out by entangling it with the electron spin and reading out the electron spin. We initialize the nuclear spin using measurement-based initialization (MBI)[56], where measuring the electron spin to be $|0\rangle$ prepares $|x\rangle$ on the nuclear spin. A Ramsey measurement is performed in Fig. 6.3(f) by varying the time between the MBI and measurement. After the MBI, the electron spin is in $|0\rangle$, and the Ramsey shows $\omega_0/2\pi = 1116.1(2)$ kHz. Adding a π pulse after the MBI allows the measurement of $\omega_1/2\pi = 985.4(3)$ kHz.

In the system of the electron spin of the SnV center and the ^{13}C nuclear spin, there is no direct measure of the magnetic field. The electronic g-factor depends on the unknown strain in the lattice. For the nuclear spin, the unknown hyperfine coupling always influences the precession frequency of the ^{13}C spin, as there is no spin-0 projection of the electron. Therefore, we extract the Larmor frequency of the ^{13}C spins from a fit to Fig. 6.3(d), yielding $\omega_L/2\pi = 1048.52(8)$ kHz. From this we extract $A_\parallel/2\pi = -130.9(3)$ kHz and $A_\perp/2\pi = 137(6)$ kHz for this ^{13}C spin C_A. We have corrected for small changes in magnetic field strength between different measurements, see Appendix 6.9.4. We can observe and control this nuclear spin using the DD control method because it has a significantly large $A_\perp$ that separates its resonance enough from the nuclear spin bath, whereas the resonances of other nuclear spins overlap with the nuclear spin bath.

6.4. DYNAMICALLY DECOUPLED RADIO FREQUENCY CONTROL

Dynamical Decoupled Radio Frequency (DDRF) control has been suggested to yield a better selectivity for a spin-1/2 system than DD control[25]. In DDRF, a direct drive of the nuclear spin is combined with coherence protection of the electron spin using dynamical decoupling. The most direct way of driving the nuclear spin is with radio frequency (RF) radiation. The required RF driving frequency ω_i depends on the electron spin state $|i\rangle$ as described by Eq. 6.3. The electron spin coherence must be extended with DD while driving the nuclear spin. To make it work in practice, we need to apply the RF driving pulses in phase with the nuclear spin evolution. Van Ommen *et al.*[57] extend the original work on DDRF[25] with a more precise and generalized analysis that includes the effects of the bandwidths of the RF pulses.

To achieve the desired nuclear spin evolution the phase of the RF pulses is updated after each π pulse on the electron spin with

$$\delta\phi = 2\tau\bar{\omega} + \pi, \tag{6.6}$$

where $\bar{\omega} = (\omega_0 + \omega_1)/2$ is the average nuclear spin precession frequency. The $2\tau\bar{\omega}$ is the

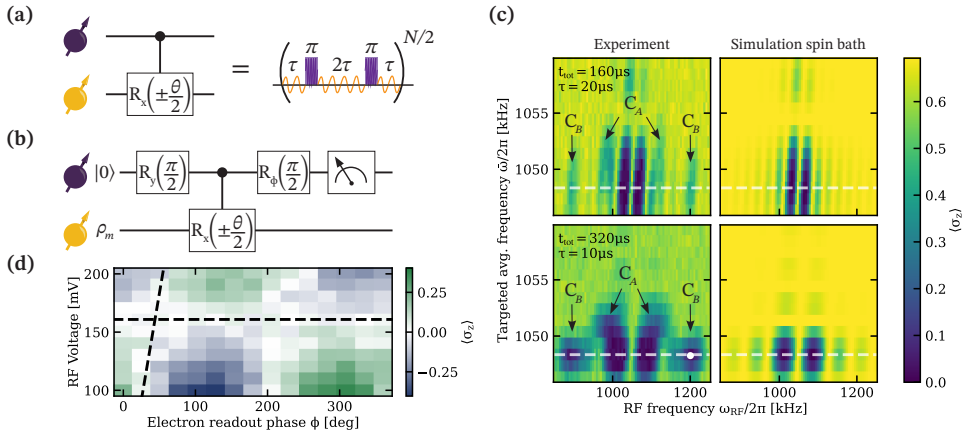

Figure 6.4: **Dynamical decoupled radio frequency (DDRF) control.** (a) A DDRF gate is realized by direct RF driving of the nuclear spin during the interpulse delay of the DD sequence. (b) The sequence to calibrate the gate. The angle θ is calibrated with the applied RF power. The angle ϕ of the second $\pi/2$ gate is calibrated to counteract a phase that the electron picks up due to the RF driving. (c) DDRF spectrum. For each data point in the left panels, the sequence in (b) is measured for multiple electron readout $\pi/2$ pulse phases ϕ and fitted to a sine function to account for phases picked up during the RF pulses. The amplitude of the sine is a measure for $\langle\sigma_z\rangle$. The values for τ are chosen such that for both values of N, the expected electron coherence at the end of the sequence is similar. The right panels show a simulation of the Hamiltonian for a collection of weakly coupled spins to imitate the nuclear spin bath, which is described in Appendix 6.9.5. Additionally to the characteristic bath features, two coupled spins (indicated by the arrows) are observable. The white dashed line indicates ω_L. The solid white circle is the used operating point in (d). (d) Nuclear spin gate calibration. The controlled gate can be calibrated by varying the electron readout $\pi/2$ pulse phase and the RF voltage. A fit of the full data with a heuristic model determines the correct voltage for the controlled gate as well as the additional phase picked up by the electron during the gate (dashed lines). After the RF pulses are generated with the reported voltages, they are amplified by 32 dB.

phase update required to follow the spin evolution such that the RF drive induces rotations along a fixed axis in the rotation frame of the nuclear spin. The π phase makes the rotation conditional as it inverts the rotation axis for the opposite electron spin state. As the phase update rule depends on $\bar{\omega}$, it has a similar selectivity as the DD control. However, the direct driving of the spin RF frequency, typical of DDRF control, increases its selectivity.

The Fourier transform of the pulse's temporal shape determines the frequency response of the RF drive[57]. For a square pulse of length 2τ it is

$$\Omega(\Delta,\tau) \propto \mathrm{sinc}(\Delta\tau), \tag{6.7}$$

where $\Delta = \omega - \omega_{\mathrm{RF}}$ is the detuning from the RF driving frequency, and $\mathrm{sinc}(x) = \sin(x)/x$. For a typical τ used in this work, around 5 µs, this sets an upper bound for the selectivity of the RF drive of around 100 kHz. In our experiments, the power broadening of the nuclear spin transition can be neglected as it is around 2 kHz.

As the DDRF control method also gives an effective $S_z I_x$ interaction, like the DD method, similar detection and control circuit diagrams can be used[24]. The DDRF control method now performs the conditional gate, as depicted in Fig. 6.4(a). The DDRF gate depends on both the used RF frequency ω_{RF} and the targeted average precession frequency $\bar{\omega}$ through the phase update rule, resulting in a two-dimensional DDRF spectrum. This spectrum is achieved by the gates in Fig. 6.4(b).

In Fig. 6.4(c), we show the resulting spectra for two different decoupling sequences, both using a Rabi frequency of 1.64 kHz. We compare the spectra to simulations of the nuclear spin bath. In this way, we can see which resonances are caused by the bath and which ones show the presence of controllable single nuclear spins. Our measurements show the known nuclear spin C_A, as indicated in Fig. 6.4(c). However, there are also resonances belonging to another nuclear spin C_B. This nuclear spin has an average precession frequency close to ω_L (white dashed line), indicating a small $A_\perp$. The splitting between the dips of ω_0 and ω_1 for C_B indicates $A_\parallel/2\pi \approx 300$ kHz. This nuclear spin was not visible in the DD measurements as that method requires a high $A_\perp$ to make it stand out from the bath.

In the spectra, the width of the resonances in targeted $\bar{\omega}$ (vertical) is inversely proportional to the total gate duration, as this is the time over which a difference in $\bar{\omega}$ can build up a phase difference. The width of the resonances in ω_{RF} (horizontal) is inversely proportional to the τ used, as this corresponds to the frequency width of the RF pulse[57].

Nuclear spins have different combinations of $A_\parallel$ and $A_\perp$, resulting in various combinations of $\bar{\omega}$ and ω_{RF} for the resonances. This means that the two parameters need to be searched independently to find the different nuclear spins. This is different in a spin-1 system, such as the nitrogen-vacancy center in diamond, when using $s_0 = 0$ and $s_1 = \pm 1$, where the hyperfine parameters influence only ω_1, with ω_0 being constant. For a spin-1, the search space can be reduced to a one-dimensional slice as ω_0 is known in advance.

The high symmetry of the DD sequence, in combination with the symmetric spin projections of a spin-1/2 system, causes the loss of first-order selectivity in the phase update rule. To circumvent this, we explored the use of the less symmetric Uhrig Dynamical Decoupling (UDD) sequence[58] for the DDRF gate, which is discussed in Appendix 6.9.7. The UDD gives differently shaped resonances, which, in our case, causes separation of

the nuclear spin C_A from the bath. However, in our system where the noise spectrum has no hard cutoff, UDD decoupling is inferior to the XY8 decoupling sequence[49], resulting in lower electron coherence, and is therefore not further pursued.

In previous work[25], only a single driving frequency was used, effectively reducing the nuclear spins' driving to half the time. For the spectroscopy in Fig. 6.4(c) we apply the same approach. However, for calibrated DDRF gates, we drive the nuclear spin at both ω_0 and ω_1, making the driving more efficient and reducing heating. Simulations of our experiments show that a double drive with a driving strength of $\Omega/2$ for both transitions is equivalent to a single drive with Ω. For simplicity and consistency, we describe the experiments and theory in this work as if a single drive was used for the DDRF gates.

The dips in the coherence of the electron spin show which combination of ω_{RF} and $\bar{\omega}$ can be used to control the nuclear spin. We use the right dip of C_B (white dot) to control it. At this operating point, the RF amplitude is swept in the sequence of Fig. 6.4(b) to calibrate the DDRF gate. A fully entangling gate is created by setting the RF amplitude to the point where $\langle\sigma_z\rangle = 0$ (Fig. 6.4(d)). The phase of the electron spin is also calibrated as the magnetic part of the RF radiation adds an extra phase to the electron spin, which needs to be compensated. We measure the nuclear spin precession frequencies using a nuclear magnetic resonance (NMR; see Appendix 6.9.8) experiment extracting $\omega_0/2\pi = 896.02(3)$ kHz and $\omega_1/2\pi = 1200.49(3)$ kHz for ^{13}C spin C_B, which translates to $A_\parallel/2\pi = 304.45(5)$ kHz and $A_\perp/2\pi = 0(13)$ kHz. For C_A, we observe an improved contrast compared to the DD method, indicating that we can better separate this spin from the bath. For the best gate settings, we find a contrast of 0.23 (0.23) for a Ramsey measurement with the electron spin in state $|0\rangle$ ($|1\rangle$) compared to the contrast of 0.19 (0.14) via DD control.

6.5. ELECTRON-NUCLEAR ENTANGLEMENT

To use the DDRF gate on C_B for entangling the electron and nuclear spin, we first optimize the gate through simulation in Fig. 6.5(a), using the hyperfine parameters determined in the previous section. For this, we simulate the required RF Rabi frequencies for fully entangling gates with different total lengths and τ. The effective Rabi frequency depends on the total length of the gate and the amount of off-resonant driving of the other nuclear transition. This off-resonant driving occurs because the RF pulse has a finite sinc-shaped frequency bandwidth[57]. Taking the RF Rabi frequency, total gate time, and τ, we simulate the effect of the presence of a nuclear spin bath. Furthermore, the coherence of the electron needs to be preserved for a high-fidelity gate. Therefore, we calculate the coherence of the electron for different DD sequences based on the measurement in Fig. 6.2(e). By combining these two contributions to the infidelity, we get an estimate for the fidelity of a full two-qubit gate. We choose an operating point that gives the highest fidelity within the region of achievable Rabi frequencies ($\Omega/2\pi < 3.1$ kHz). After the choice of the operation point, the simulation was further refined to the one depicted here, showing that a higher gate fidelity might have been possible.

For the optimization, there is a trade-off between preserving electron coherence and gate performance. Shortening the total gate time improves electron coherence but requires a higher Rabi driving frequency. Increasing τ improves the RF selectivity as the

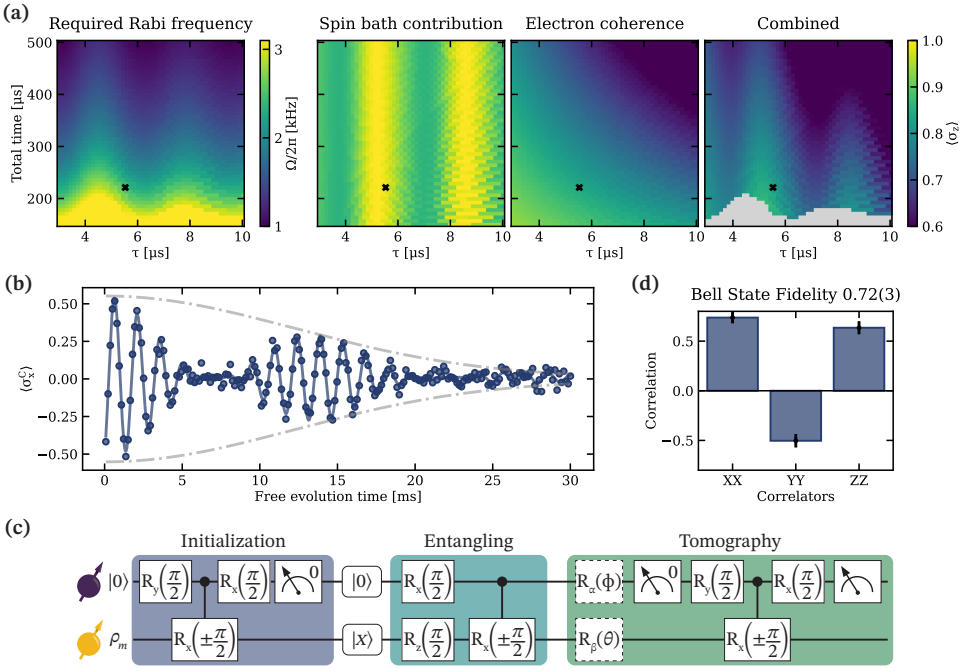

Figure 6.5: **Gate optimization and electron-nuclear entanglement.** (a) Gate parameter simulation. A set of τ and the total gate duration puts a requirement on the Rabi frequency that needs to be achieved for a gate with $\theta = \pi/2$. For specific values of τ, the spectral shape of the RF tone also drives the other nuclear spin transition (i.e. driving ω_0 while targeting ω_1), resulting in a higher required Rabi frequency Ω to compensate for this off-resonant driving[57]. The gate fidelity is determined by the combination of electron coherence during DD and extra coherence loss due to the applied DDRF gate. Considering the fidelity and excluding gates with a Rabi frequency higher than the maximally achievable 3.1 kHz (gray region), we choose the working point indicated by the cross. (b) Measurement of the nuclear T_2^* via a Ramsey sequence. The fit accounts for two coupled spins that induce a beating of the Ramsey signal. The envelope (gray dashed line) has the form $A\exp\left(-(t/T_2^*)^n\right)$ with $n = 2.0(2)$ and decay time $T_2^* = 17.2(6)$ ms. (c) Gate sequence for electron-nuclear entanglement. The nuclear spin is prepared into $|x\rangle$ via MBI. The entangling block creates the Bell state $|\Phi^+\rangle$, which is consecutively measured with different correlators. The tomography pulses on the nuclear spin are realized by Larmor precession (z-rotations) or direct RF driving. (d) Correlators of the $|\Phi^+\rangle$ state. The error bars indicate their standard deviation. The readout of the nuclear spin in the tomography block is corrected for errors in the two-qubit gate, resulting in an entangled state fidelity of $\mathcal{F}_{\text{Bell}} = 0.72(3)$.

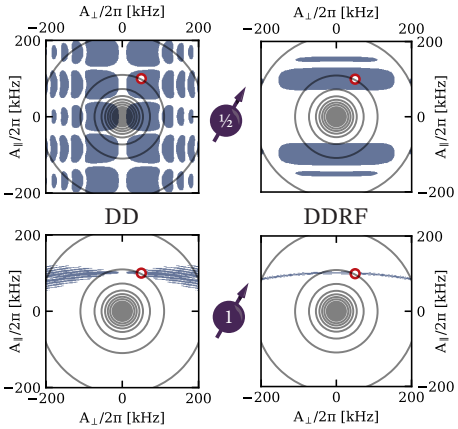

Figure 6.6: **Comparison of nuclear spin control with DD and DDRF methods.** Simulated crosstalk regimes when controlling a target nuclear spin with $A_\parallel/2\pi = 100\,\text{kHz}$ and $A_\perp/2\pi = 50\,\text{kHz}$ (red circle). DD and DDRF control methods are compared for electron spin-1/2 and spin-1. The blue areas correspond to hyperfine parameters for which a bystander nuclear spin would cause more than 5 % decoherence of the electron spin, during a gate performed on the target nuclear spin. The regions between the gray circles contain, for a natural ^{13}C abundance of 1.1 %, on average one bystander ^{13}C nuclear spin. For simulation details, see Appendix 6.9.5.

pulse bandwidth is reduced but lowers the electron coherence. Besides this, higher-order resonances with the nuclear spin bath can be avoided by carefully selecting appropriate values for τ.

In Fig. 6.5(b), the optimized gate is used in an undersampled Ramsey measurement on C_B. The observed beating pattern is explained by a coupling to two different nuclear spins with 67(4) Hz and 71(4) Hz. The $T_2^* = 17.2(6)\,\text{ms}$ of this nuclear spin is comparable to high values measured using the nitrogen-vacancy center in diamond[25]. We extract a two-qubit gate fidelity of $\mathscr{F}_{\text{gate}} = 0.874(4)$ (see Appendix 6.9.6 for details), which is slightly less than the simulated fidelity $\mathscr{F}_{\text{sim}} = 0.915$. We attribute the difference to the decoherence of the electron spin to coupling to undetected spins, which are not captured by the spin bath simulation.

With this two-qubit gate, we have the tools to entangle the SnV electron spin with the ^{13}C spin. For this, we initialize the ^{13}C spin, prepare the electron in a superposition state, and use the two-qubit entangling gate to create the Bell state $|\Phi^+\rangle = \frac{1}{\sqrt{2}}(|00\rangle + |11\rangle)$; see Fig. 6.5(c). The correlators are measured with tomography, from which the fidelity to the Bell state $|\Phi^+\rangle$ is calculated as $\mathscr{F} = (\langle XX\rangle - \langle YY\rangle + \langle ZZ\rangle + 1)/4$. By correcting for known tomography errors, as explained in Appendix 6.9.6, we find a fidelity to the Bell state $|\Phi^+\rangle$ of 72(3) %. As discussed in Appendix 6.9.6, this is mainly limited by the electron coherence loss during the nuclear spin gates.

6.6. COMPARISON CONTROL METHODS

In previous sections, we explored the experimental control of ^{13}C spin with a spin-1/2 electron spin using the DD and DDRF control methods. In this section, we compare the

selectivity of these two methods in simulation. Additionally, we analyze the difference for the case of an electron spin-1 system[24,57]. The different nuclear spins surrounding the electron spin can be characterized by their specific $A_\parallel$ and $A_\perp$. Figure 6.6 visualizes the selectivity of both control methods. We simulate a nuclear spin gate for a nuclear spin with $A_\parallel/2\pi = 100\,\text{kHz}$ and $A_\perp/2\pi = 50\,\text{kHz}$ (red circle). The blue region indicates for which hyperfine parameters a bystander spin would cause more than 5 % coupling to the electron during the same gate.

For each scenario, the most selective gate is found by optimizing the gate parameters under the boundary conditions that the electron has preserved more than 99 % coherence and the gate does not exceed 1 ms. For the simulations, we assume an electron echo time of $T_2^{\text{Echo}} = 1\,\text{ms}$, dynamical decoupling scaling factor $\chi = 2/3$ and a maximum nuclear Rabi frequency of 5 kHz.

The likelihood of having a bystander spin in the blue areas depends on the distribution of hyperfine parameters of the nuclear spins surrounding the color center. The placement of ^{13}C atoms around a color center in the diamond lattice is probabilistic, resulting in a varying arrangement of the bystander spins for different centers. We simulate the distribution of nuclear spin hyperfine parameters by generating many different random spin configurations and calculating their hyperfine parameters. The distribution of hyperfine parameters of bystander spins is visualized by the regions between the gray lines, which contain on average one nuclear spin. More simulation details can be found in Appendix 6.9.5.

We observe that the selectivity for DD in spin-1/2 systems is reduced compared to spin-1[28]. Most notably, there is considerable crosstalk with the nuclear spin bath, i.e., the spins with a weak coupling. We note that the specific analysis depends on the chosen target spin. For example, spins with lower $A_\perp$ have more crosstalk for DD control with electron spin-1/2.

The DDRF method has an enhanced selectivity compared to the DD method as it introduces an extra resonance requirement. Both methods depend on $\bar{\omega}$, DDRF through its phase update rule and DD through the interpulse delay. However, the RF drive in DDRF additionally targets ω_0 or ω_1, which have a first-order dependence on $A_\parallel$, also for electron spin-1/2 systems. This reduces the crosstalk, most notably with the spin bath. The first-order selectivity of the phase update rule scales with the total gate time $2\tau N$ in spin-1 systems and the first-order RF selectivity scales with the interpulse delay 2τ for both systems. Therefore, DDRF for spin-1 systems has a factor N better selectivity[57].

6.7. HYPERFINE COUPLING WITH THE EXCITED STATE

So far, we have considered the hyperfine interaction with the ground state of the SnV electron spin. However, the performed Ramsey measurements also give us insight into the hyperfine interaction in the excited state. We observe that the nuclear spin acquires a phase depending on how much time the electron is in the excited state.

During measurement-based initialization (MBI), we use a readout of the electron that is stopped when a photon is detected. This yields the most reliable assignment of the postmeasurement state but also results in a variable readout time. During the readout, the electron spin gets cycled between the ground and excited states. Therefore,

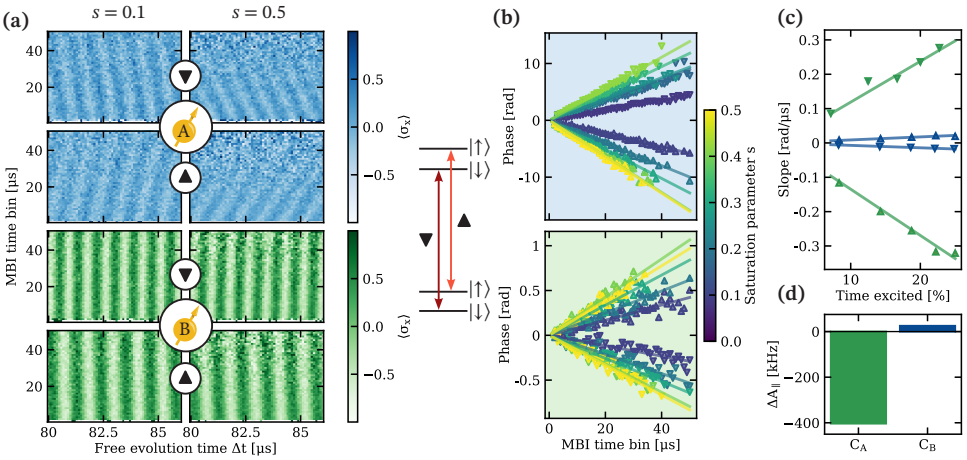

Figure 6.7: **Excited state hyperfine coupling.** (a) The Ramsey measurements of the nuclear spins are binned for the readout time during MBI. We find an additional phase shift depending on the duration of the readout. The blue (green) colored data correspond to C_A (C_B). The rate of acquiring phase increases for higher laser powers (left and right column), i.e., longer occupation of the excited state. Changing the optical transition used for the readout during MBI (▲ or ▼) flips the direction of the phase shift. The difference in contrast stems from the better gate fidelities for C_B compared to C_A. (b) Extracting the phase shift for different MBI durations and saturation numbers s results in linear slopes. (c) The used power in (b) is converted to time spent in the excited state and shows a linear relation with the slope fitted in (b). (d) The difference in parallel hyperfine parameters between the excited and ground states for both nuclear spins.

the time the electron spends in the excited state depends on the optical power and the readout duration.

In Fig. 6.7(a), Ramsey measurements for C_A and C_B are binned by the readout duration during MBI. We observe that the Ramsey fringes are shifted for longer readout durations, indicating that the nuclear spin acquired an extra phase during readout. Furthermore, the shift depends on the readout power. We use the saturation parameter $s = P/P_{\text{sat}}$, to compare the readout power P to the saturation power $P_{\text{sat}} \approx 88\,\text{nW}$. The observed shift is more significant for a readout with $s = 0.5$ in the right column than a readout with $s = 0.1$ in the left column. Lastly, we see that reading out using the spin-down transition (▼ in Fig. 6.7) results in the opposite shift compared to reading out using the spin-up transition (▲ in Fig. 6.7). The more noisy data for longer readout duration are a consequence of the small amount of data resulting from a low probability of detecting the first photon at those times.

We attribute the extra phase to a different hyperfine coupling of the ^{13}C spin to the SnV electron in the ground and the excited states. Note that these effects can be avoided in integer-spin systems such as the diamond nitrogen-vacancy center by using an $m_S = 0$ optical transition. Intuitively, as the excited state exhibits a different electron wave function, the coupling to the ^{13}C can differ from that of the ground state. We can extract the acquired additional phase from the binned Ramsey measurements in the excited state. Figure 6.7(b) shows the fitted phases for the binned Ramsey fringes in Fig. 6.7(a), which are well explained by a constant phase acquisition. Based on saturation measurements,

the readout power can be converted to a fraction of the time spent in the excited state (see Sec. 1.7 in Ref.[59]):

$$t_{\text{exc}}/t = \frac{s}{2s+1}. \tag{6.8}$$

The factor 2 in the denominator stems from the readout being done resonantly, capturing the contribution of stimulated emission. Figure 6.7(c) shows the angular frequency corresponding to the additional phase acquisition as a function of the fraction of time spent in the excited state. Combining this occupancy with the additional phase acquisition in the excited state gives the difference in coupling, which can mainly be assigned to a difference in $A_\parallel$ between the ground and excited states, as a difference in $A_\perp$ has a small second-order effect on the precession frequencies; see Appendix 6.9.9. The extracted difference in parallel hyperfine coupling $\Delta A_\parallel = A_\parallel^e - A_\parallel^g$ is $-404(2)$ kHz and 25.2(4) kHz as displayed in Fig. 6.7(d). The contrast of the Ramsey measurements is mostly preserved for longer readout durations. The exponential decay constant of the Ramsey contrast is $7.5(3) \times 10^2$ and $28(1) \times 10^2$ optical cycles for C_A and C_B respectively, suggesting the nuclear spins are a viable storage of qubit states during optical operations on the electron spin.

6.8. DISCUSSION AND OUTLOOK

We have investigated the nuclear spin control using an electron spin-1/2 system. We have shown an improved selectivity in controlling nuclear spins using Dynamically Decoupled Radio Frequency (DDRF) control compared to the more commonly used Dynamical Decoupling (DD) control. Using these methods, we control two nuclear spins and show entanglement between the nuclear spin of a ^{13}C atom and the electron spin of a tin-vacancy (SnV) center in diamond.

These findings directly translate to other systems with an electron spin-1/2, such as rare-earth ions[10] and many other color centers like the silicon-vacancy and other group-IV vacancy centers in diamond[7,35,53], the T center in silicon[31] and the vanadium center in silicon carbide[60].

Decoupling with longer τ improves the RF selectivity. Longer gates allow for better phase selectivity. Both these factors improve the selectivity for a single gate, allowing the control of more ^{13}C spins. In this work, the electron coherence limits the electron-nuclear gate fidelity. This is not intrinsic to the SnV center or the nuclear spins but can be attributed to the presence of an electron spin bath. Recently, it has been shown that the SnV can indeed have longer coherence times during dynamical decoupling[50], which would improve the nuclear spin control as well.

The selectivity of the nuclear spin gates with DDRF is better than with DD for electron spin-1/2. However, it is still reduced compared to spin systems with a larger magnitude. To counteract this, less symmetric decoupling sequences[61], like the UDD[58], can be explored to increase the selectivity of DDRF further.

The selectivity of the nuclear spin gates in electron spin-1/2 systems can be further improved by interleaving a single DD or DDRF gate by periods in which the electron spin is in an eigenstate. In these periods, the nuclear spins will precess with ω_i as opposed to $\bar{\omega}$ during decoupling, thereby recovering the first-order selectivity to $A_\parallel$ of spin-1 systems. To preserve the state of the electron spin during those periods, it needs to be tem-

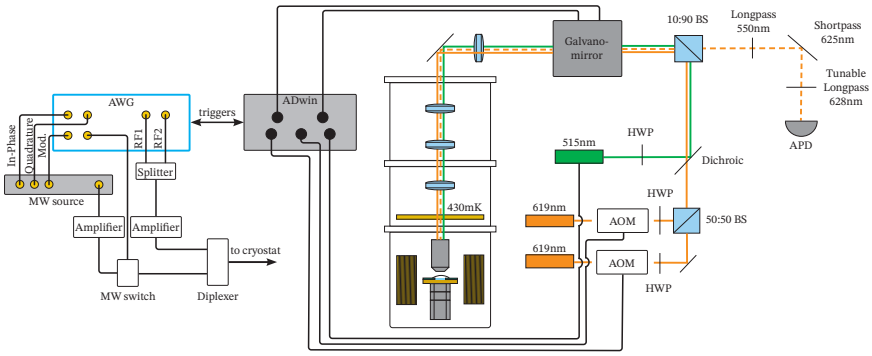

Figure 6.8: **Experimental Setup.** The setup consists of a cryostat with optical access, control electronics, and optical excitation and collection paths. The dashed line represents the fluorescence from the SnV center. A detailed description is provided in the text.

porarily stored in an easily accessible quantum memory[62]. In the SnV center, this role could be fulfilled by the nuclear spin of ^{117}Sn or ^{119}Sn[63].

Lastly, we investigated the hyperfine coupling of the nuclear spins with the excited state of the electron, showing a different coupling in the excited state compared to the ground state of the electron. Additionally, we can conclude that it also showed that the nuclear spins surrounding the SnV center stay coherent while the optical transition is cycled hundreds of times, making these memories robust against the optical readout of the electron spin.

The improved selectivity of the DDRF control and the insights in nuclear spin coupling during readout bring high-fidelity spin control in electron spin-1/2 systems closer.

The data and simulations that support this manuscript are available at 4TU.ResearchData[64].

6.9. SUPPLEMENTARY INFORMATION

6.9.1. EXPERIMENTAL SETUP

The setup is schematically shown in Fig. 6.8. The center of the setup is a BlueFors LD250He system with a base temperature of 430 mK with a 1-1-1 T vector magnet. A positioner stack provides movement of the device. Confocal microscopy experiments are performed with a high-NA objective and a double-4f system with a two-axis galvanomirror. Microwaves and radiofrequency drives are supplied via superconducting coaxial cables (not shown in the figure) and a flex-cable to allow movement of the device (not shown in the figure). To minimize heating, the signal is guided via a custom printed circuit board to a bondwire $\approx 100\,\mu$m above the device. The total microwave losses through the system at the relevant frequency 3.1 GHz are 5 dB.

The experiment is controlled via a home-written software infrastructure based on QMI[65]. A microcontroller (ADwin Pro II, Jäger Messtechnik) controls the experiment, and laser pulses are controlled via its DAC module. For microwave and radio-frequency

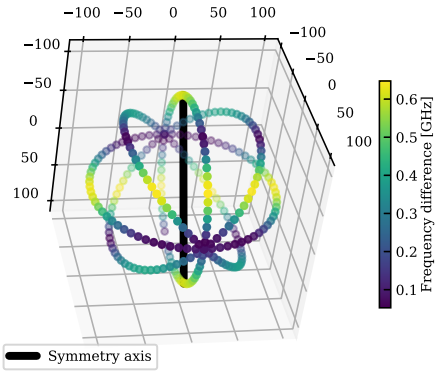

Figure 6.9: **Magnetic field sweep.** The frequency difference of the two spin-conserving optical transitions is shown as a function of the 3D magnetic field in the laboratory frame in units of mT. The solid black line shows the direction of the SnV center symmetry axis. In laboratory spherical coordinates, it is oriented along $(\theta, \phi) = (54.2(1)^\circ, -1.0(2)^\circ)$.

pulses, the ADwin triggers an arbitrary waveform generator (HDAWG, Zurich Instruments). The HDAWG modulates a microwave signal generator (SGS100A, Rohde & Schwarz) with IQ-signals to generate phase-controlled microwave pulses. The microwave pulses are amplified (Model 40S1G4, Amplifier Research) to 26 dBm for all measurements in the main text, which yields an estimated power of 20 dBm at the device location. To prevent the shot noise of the amplifier during free evolution periods from entering the system, a microwave switch and high-pass filter (not in the figure) are employed. The radio frequency signals are directly generated by oscillators of the HDAWG and amplified to 18 dBm. The transmission for these megahertz signals is almost lossless. We use two driving frequencies for the control with DDRF gates and drive both resonance frequencies of the nuclear spin, resulting in a $\sqrt{2}$ improvement of the Rabi frequency for the same power. These two driving tones are combined with a directional coupler and then via a diplexer with the microwave signal. An additional DC-block (not in the figure) after the diplexer completes the chain.

The electron spin is addressed optically via a confocal microscopy setup. Two resonant excitation lasers (DLpro SHG-TA, Toptica) are modulated via the ADwin and AOMs (Fiber-Q 637nm, Gooch&Housego) and combined via a beamsplitter. An off-resonant repump laser at 515nm (Cobolt 06-03-MLD515, Hübner Photonics) is added with a dichroic mirror. The excitation light is coupled into the beam path of the cryostat through a 10:90 beam splitter and the galvanomirror. The collected light is spectrally filtered (FELH0600, Thorlabs; FF625-SDi01 and TLP01-628, Semrock) and detected by a single photon detector (COUNT, LaserComponents). A counter module of the ADwin stores the registered counts in 1 µs time bins.

6.9.2. MAGNETIC FIELD SWEEP

We investigate the behavior of the SnV center by sweeping the magnetic field along four great circles with magnetic field strength 100 mT (see Fig. 6.9). We monitor the frequen-

Table 6.1: Magnetic field fitting parameters.

Term	Value	Origin
$\lambda_g/2\pi$	830 GHz	[34]
$\lambda_e/2\pi$	2988 GHz	[34]
B	97.8 mT	Appendix 6.9.4
θ_{SnV}	54.2(1)°	Fit
ϕ_{SnV}	−1.0(2)°	Fit
Υ_g	352(7) GHz	Fit
Υ_e	674(17) GHz	Fit
f_g	0.171	[34]
f_e	0.072	[34]
δ_g	0.015	[34]
δ_e	0.176	[34]

cies of both spin-conserving transitions with PLE measurements. We model the SnV center Hamiltonian as described in Ref.[34], Eq. B5. To extract relevant parameters from the available data, we have to fix some Hamiltonian parameters. Specifically, our PLE measurements do not give us access to the ground-state splitting.

Fitting the resulting data with the SnV center Hamiltonian with the strain and the laboratory orientation of the SnV center as free parameters, we find a laboratory direction of the SnV center symmetry axis of $(\theta,\phi) = (54.2(1)°, -1.0(2)°)$. Since we use a ⟨100⟩-cut diamond with ⟨110⟩ side faces, these values match the expectation given the alignment of the diamond with respect to the magnet. The strain values result in $\Upsilon_g = 355(8)$ GHz and $\Upsilon_e = 689(20)$ GHz for the ground and excited state, respectively. This moderate strain is smaller than the spin-orbit coupling in both manifolds, yet allows for direct driving of the microwave transition. The fit parameters are summarized in Table 6.1.

6.9.3. ELECTRON COHERENCE

RAMSEY

To investigate the coherence of the electron spin, we conduct a Ramsey measurement. We perform the experiment on resonance and vary the phase of the second $\pi/2$ pulse to artificially introduce the signature of a detuning with $\Delta = 5$ MHz. The resulting signal in Fig. 6.10(a) shows a slow beating in addition to the oscillation with Δ. A fit of two sine functions with a power exponential envelope

$$\langle\sigma_z\rangle(t) = A\exp\left(-\left(\frac{t}{T_2^*}\right)^n\right)\sum_{i=1,2}\left(\sin\left(\omega_i t+\phi_i\right)\right)+c \tag{6.9}$$

reveals a frequency difference of 312(3) kHz of the sines, coinciding with the coupling strength of C_B in the main text. The decay of the envelope with exponent $n = 2.8(2)$ leads to $T_2^* = 2.42(4)$ µs. An exponent bigger than one indicates that the coherence is limited by slow-varying noise in the spin bath, which can possibly be counteracted by dynamical decoupling. This result is in accordance with the expected Ramsey coherence time of color centers in naturally abundant diamond[66].

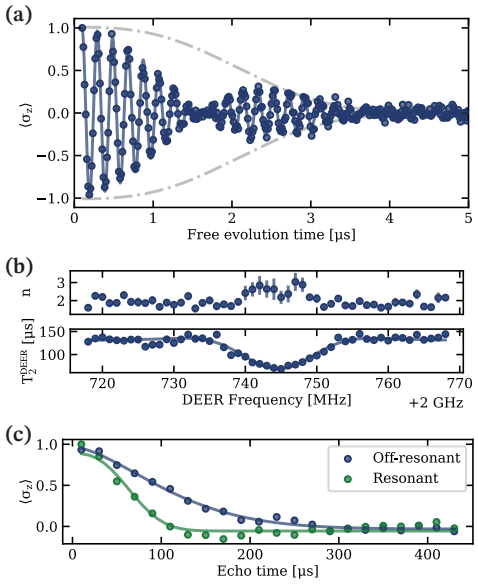

Figure 6.10: **Electron Ramsey and DEER measurements.** (a) Ramsey measurement. The Ramsey measurement is performed with an artificial detuning of 5 MHz, implemented via an evolution time-dependent phase on the second $\pi/2$ gate. The beating frequency of 312(3) kHz. (b) The frequency of the second MW pulse in the DEER measurement is varied to find the resonance of the electron spin bath. Both the echo time and the power of the power exponential fit in Eq. 6.9 are given. The error bars indicate their standard deviation. (c) Two examples of the Hahn echo measurements from (b), where a resonant MW pulse with the electron spin bath decreases the coherence time of the Hahn echo.

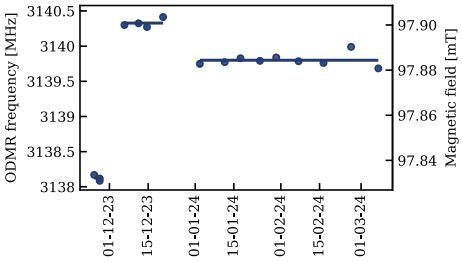

Figure 6.11: **Magnetic field strength over time.** The changes in the magnetic field strength are monitored using the MW frequency of the electron spin, through an ODMR measurement.

DEER

The scaling of the coherence time $T_2^N = T_2^{\text{Echo}} N^{\chi}$ with $T_2^{\text{Echo}} = 129(2)\,\mu\text{s}$ with the number of pulses N via $\chi = 0.47(1)$ is less than we expect for a pure nuclear spin bath limitation[67]. We conduct a double electron-electron resonance (DEER) measurement to verify electron bath noise. When measuring the Hahn echo decay time of the electron spin while applying a microwave pulse with varying frequency simultaneously to the decoupling pulse, we see a clear reduction of the coherence time when driving the surrounding with 2.745 GHz, see Fig. 6.10(b). We extract the decay constant τ and the exponent n from the function

$$T_2^{\text{DEER}} = A \exp\left(-(t/\tau)^n\right). \tag{6.10}$$

We find a spin bath resonance frequency of 2.7446(2) GHz. This corresponds very well with electrons with a g-factor of 2 and a magnetic field of 97.884 mT, as determined in Appendix 6.9.4. The $T_2^{\text{DEER}} = 76(4)\,\mu\text{s}$ has significantly decreased compared to a $T_2^{\text{Echo}} = 128(5)\,\mu\text{s}$. The origin of this spin bath noise is unknown; it might stem from crystal damage due to insufficient annealing or residual tin ions in the surrounding.

6.9.4. MAGNETIC FIELD STRENGTH CHANGES

During the experiments, the magnetic field strength has not been constant as shown in Fig. 6.11, hampering direct comparison between measurements. As we have no direct measure of the magnetic field, we use the MW transition frequency of the electron spin, as measured by the ODMR measurements over time, to keep track of the relative magnitude of the magnetic field. The orientation of the magnetic field also influences the MW transition frequency, but as this is a second-order effect[34] we neglect this contribution. We observe three periods in which the magnetic field was stable. We suspect that switching the superconducting magnet to persistent mode caused the first jump and temporarily warming up to 4 K caused the second one. Using these relative variations in the field strength allowed us to fit Fig. 6.3(d) while using the ω_0 and ω_1 extracted from Fig. 6.3(f) to determine the Larmor frequency. This Larmor frequency could then be converted to an absolute magnetic field strength by using the gyromagnetic ratio of the nuclear spin, as indicated in Fig. 6.11. The reported value of ω_L in the main text is based on the second time period.

6.9.5. SIMULATIONS

All the code to generate the figures in this paper, including the simulations are available in the repository supporting this manuscript[64].

DD

The DD simulations are all based on the analytic formulas from Ref.[36], which describe both electron spin-1/2 and spin-1 systems.

To simulate the nuclear spin bath, we first generate a random distribution of the nuclear spins. For this, we randomly place the nuclear spins in a sphere with radius 30 nm around the electron spin with a density corresponding to 1.1 % ^{13}C atoms. The hyperfine parameters are then calculated by assuming just the dipole-dipole interaction. For the DD spin bath simulations only spins with a hyperfine coupling $A/2\pi < 100\,\text{kHz}$ are included, where $A = \sqrt{A_\parallel^2 + A_\perp^2}$.

For Fig. 6.3(c), ten different realizations of the spin bath are generated, and the region between the highest and lowest line is shown.

DDRF

For the DDRF simulations in Figs. 6.4(b), 6.5(a) and 6.13 numerical methods based on the Python framework QuTiP[68] are used to simulate the Hamiltonian of the RF drive from Ref.[57]. These simulations include the exact pulse shape and length as were used in our experiments. For the comparison in Fig. 6.6 the analytic formulas from Ref.[57] are used.

The simulations of the nuclear spin bath in Figs. 6.4(b), 6.5(a) and 6.13 are based on the spin bath simulations in Ref.[57]. Rather than simulating a randomly generated nuclear spin bath, we approximate it with a probability distribution of the hyperfine parameters. For the distribution of $A_\parallel$, we take the heuristic distribution from the supplement of Ref.[69]. We assume that the nuclear spin bath has $A_\perp = 0\,\text{kHz}$, as the bath has weak coupling and $A_\perp$ has only a second-order effect on ω_0 and ω_1, which are the parameters relevant for the DDRF simulation. In this work, we consider spins with a $|A_\parallel|/2\pi < 20\,\text{kHz}$ to be part of the spin bath for the DDRF simulations as these spins are below our detection limit. We then subdivide the distribution of the bath in bins of $\Delta A_\parallel = 2\,\text{kHz}$ and weigh their effect by the number of expected spins in that bin. Finally, we combine the effect of the different bins on the electron to get the effect of the whole nuclear spin bath.

COMPARISON

The comparison in Fig. 6.6 is performed by finding the coherent and fast two-qubit gate on the target spin that minimizes the crosstalk with bystander spins. We consider it fast and coherent if the electron coherence after the gate is above 99 % and the total gate duration is below 1 ms. A bystander spin is considered to cause crosstalk for a gate if the loss in the coherence of the electron due to this bystander spin is bigger than 5 %. The gate is optimized to cause crosstalk with the fewest possible bystander spins, i.e., minimizing the blue region in Fig. 6.6. This metric is not weighted for the bystander spin density.

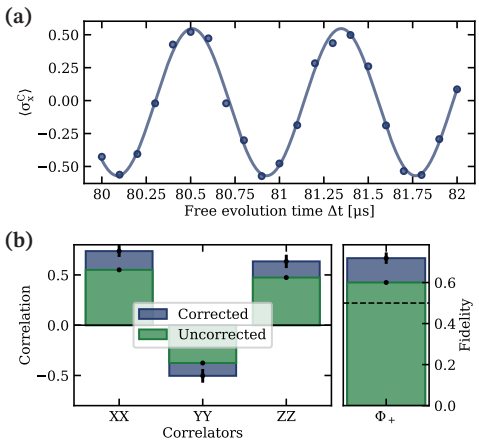

Figure 6.12: **Readout correction for Bell state measurement.** (a) Ramsey measurement to determine two-qubit gate fidelity. The contrast of the Ramsey measurement is reduced due to imperfect two-qubit gates. For the measurement, the two-qubit gate is performed to initialize and read out the nuclear spin. A model based on imperfect state preparation and positive operator-valued measure (POVM) measurements yields $\mathscr{F}_{\text{gate}} = 0.874(4)$. (b) Data for the Bell state measurement in Fig. 6.5(d), including the outcomes without correcting for the two-qubit gate fidelity. The error bars show the standard deviation.

6

For the DD method, the gate with the smallest crosstalk is found by sweeping the interpulse delay τ and the number of decoupling pulses N. For the DDRF method, the interpulse delay τ, the number of decoupling pulses N, and the RF driving strength Ω are swept to find the most selective gate.

The circles indicating the bystander spin density are based on the average of 100 randomly generated spin bath configurations. The spin baths are generated in the same way as for the DD spin bath simulations, see Appendix 6.9.5.

6.9.6. BELL STATE

READOUT GATE CORRECTION

When determining the fidelity of the Bell state $|\Phi^+\rangle$ in the main text, we apply a readout correction to the nuclear spin readout via MBI. To this end, we estimate the two-qubit gate fidelity $\mathscr{F}_{\text{gate}}$ via a Ramsey measurement. The fit of a sinusoidal function to Fig. 6.12(a) shows an amplitude of $\langle\sigma_x\rangle = 0.559(12)$. We model the imperfect initialization and readout of the nuclear spin in the x basis with the preparation of state

$$\rho = \begin{pmatrix} \mathscr{F}_{\text{gate}} & 0 \\ 0 & 1-\mathscr{F}_{\text{gate}} \end{pmatrix}, \tag{6.11}$$

and readout via a POVM measurement with the matrix set

$$E_x = \begin{pmatrix} \mathscr{F}_{\text{gate}} & 0 \\ 0 & 1-\mathscr{F}_{\text{gate}} \end{pmatrix}, \quad E_{-x} = \begin{pmatrix} 1-\mathscr{F}_{\text{gate}} & 0 \\ 0 & \mathscr{F}_{\text{gate}} \end{pmatrix}. \tag{6.12}$$

The expectation value of this model is

$$\langle\sigma_x\rangle = 1\cdot p_x - 1\cdot p_{-x} = 1 - 4\mathscr{F}_{\text{gate}} + 4\mathscr{F}_{\text{gate}}^2, \tag{6.13}$$

Table 6.2: Gate fidelites of electron (e) and nuclear (n) spin.

Gate	Fidelity	Method
Init. (e)	0.981(5)	Calibration
Init. (n)	0.874(4)	Ramsey contrast
$R(\pi/2)$ (e)	0.98(2)	Process tomography
$R_z(\pi/2)$ (n)	1	Calibration
$cR_x(\pm\pi/2)$	0.874(4)	Ramsey contrast
$R_{x,y}(\pi/2)$ (n)	-	Undetermined

with $p_i = \mathrm{Tr}\left(\rho E_i\right)$. Solving for the gate fidelity results in $\mathscr{F}_{\mathrm{gate}} = 0.874(4)$. This value is slightly below the simulated gate fidelity shown in Fig. 6.5(a) of 0.915. We attribute this difference to the coupling of the electron spin to unknown spins.

We use the estimated fidelity to perform a readout correction following the formalism outlined in Ref. [70], Appendix A. The uncorrected and corrected data of the Bell state measurement is shown in Fig. 6.12(b).

ERROR BUDGET ESTIMATION

The measured Bell state does not have perfect fidelity. This section provides an overview of the known and unknown sources of infidelity to estimate the expected fidelity for the Bell state measurements.

The experimental gate sequence as shown in Fig. 6.5(c) is comprised of three logic blocks with single- and two-qubit gates.

In the "Initialization" block, both the electron spin and nuclear spin are prepared into known states $|0\rangle$ and $|x\rangle$. The probability of correctly measuring the electron in state $|0\rangle$ after the two-qubit gate is 98 %, mainly limited by the spin pump fidelity. The correct initialization of the nuclear spin is limited by the two-qubit gate fidelity of 87.4 %.

The "Entangling" block consists of a $\pi/2$ gate on the electron spin, a z rotation of the nuclear spin (implemented by a waiting time, assumed to be perfect) and a two-qubit gate identical to the initialization. We determine the average electron spin gate fidelity to 0.98(2) via process tomography.

The last block, "Tomography", consists of another single-qubit rotation on the electron spin as well as the nuclear spin, followed by a single-shot readout of both qubits individually. To prepare the nuclear spin for a readout in the x or y basis, a z rotation is performed via a waiting time. The error of this gate is determined by the uncertainty of the Ramsey frequency, which we determine to be less than 1×10^{-4} relative error in the main text. For readout in the z basis, a direct RF gate is implemented as reported in Appendix 6.9.8. This gate is calibrated via a Rabi experiment. However, the fidelity of the gate has not been determined. We correct for the readout processes following the description of Appendix A of Ref. [70] for the electron spin and Appendix 6.9.6 for the nuclear spin.

All known and unknown fidelities are listed in Table 6.2.

To estimate the expected fidelity of the Bell state measurement, we use a simplified model in which we assume all gates except the $cR_x(\pm\pi/2)$ to be perfect for simplicity, as their infidelity is small compared to the two-qubit gate. We describe the two-qubit gate

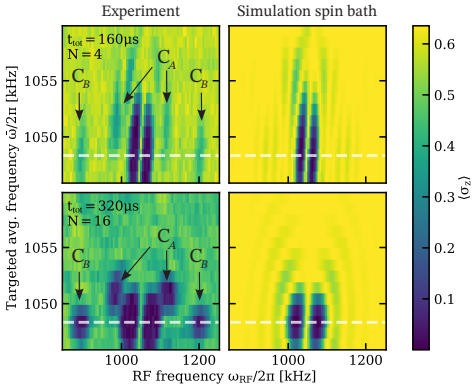

Figure 6.13: **DDRF Spectrum using the UDD sequence.** The same DDRF spectrum as in Fig. 6.4(c) but now implemented with UDD. The upper row is using 4, while the bottom row is using 16 decoupling pulses.

as an ideal gate with probability $p = \mathcal{F}_{\text{gate}}$ and an ideal gate with an additional phase error on the electron with probability $1-p$. With this phase error, we take the loss of coherence of the electron spin during the gate into account, which is the main reason for the gate infidelity, as detailed in Fig. 6.5(a). For the modeling, we exclude the tomography pulses and, hence, compare the calculated value to the readout-corrected measured fidelity.

The estimated fidelity of the created Bell state with the sequence shown in Fig. 6.5(c) is $\mathcal{F}_{\text{ideal}} = 0.76$ with respect to the target state $|\Phi\rangle^+$. This is in good agreement with the measured fidelity of $\mathcal{F}_{\text{Bell}} = 0.72(3)$. We attribute the additional infidelity in the measurement to the single-qubit errors summarized in this section.

6.9.7. DDRF USING UDD

To see if we could improve on the selectivity of DDRF with the symmetric XY8 decoupling sequence, we use Uhrig Dynamical Decoupling[58]. In this sequence, the time between the pulses varies as

$$\delta_j = \sin^2\left(\frac{j\pi}{2N+2}\right), \tag{6.14}$$

where j is the index of the interpulse delay and N is the total number of pulses. The DDRF can be implemented in the same way as for an XY8 decoupling sequence. However, the phase update for the RF driving field is now different between each pulse and needs to be calculated explicitly by keeping track of the phase of the nuclear spin.

In Fig. 6.13, a spectrum similar to Fig. 6.4(c) is shown but now implemented with UDD. The top row shows UDD with $N = 4$, and the bottom row shows $N = 16$. The same two nuclear spins can be observed as with the DDRF with XY8. However, the nuclear spin bath has a different fingerprint, revealing C_A better in the spectrum of $N = 4$.

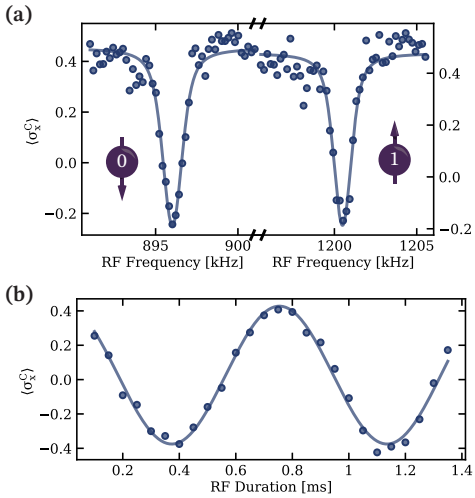

Figure 6.14: **Nuclear spin magnetic resonance and Rabi drive.** (a) Nuclear magnetic resonance experiment. The two resonance frequencies appear as a dip in the readout signal and depend on the state of the electron spin. The frequency matches well with the frequencies determined by Ramsey measurements. (b) Direct RF drive Rabi experiment. The measured Rabi frequency of 1.31(1) kHz matches the expected frequency determined by simulation.

6.9.8. NUCLEAR SPIN NMR AND RABI

In addition to Ramsey measurements to determine the nuclear precession frequencies, we use a direct RF drive on C_B to find the two resonance frequencies. We measure the nuclear magnetic resonance (NMR) spectra by initializing the nuclear spin into state $|x\rangle$, applying the RF signal for 300 µs with varying frequency, and reading out in the x basis. The resonances are shown in Fig. 6.14(a) for both electron spin states during the experiment. We determine $\omega_0/2\pi = 896.02(3)$ kHz and $\omega_1/2\pi = 1200.49(3)$ kHz.

For the tomography of the Bell state, we need to employ an $R_x(\pi/2)$ gate on the nuclear spin. We implement this gate via direct RF drive at ω_0 while the electron is in state $|0\rangle$. In Fig. 6.14(b), a Rabi experiment shows a Rabi frequency $\Omega/2\pi = 1.31(1)$ kHz of the nuclear spin. From this, we calibrate the $\pi/2$ gate employed in the experiments. Furthermore, this measurement allowed us to covert the RF power used in the DDRF spectra in Figs. 6.4 and 6.13 to a Rabi frequency of $\Omega/2\pi = 1.64$ kHz, which was used in the nuclear spin bath simulations.

6.9.9. HYPERFINE COUPLING EXCITED STATE

In Sec. 6.7, we observe that the precession frequency of the nuclear spins depends on whether the electron spin is in the ground or excited state. The difference in precession frequency is

$$\Delta\omega_i = \omega_i^e - \omega_i^g, \tag{6.15}$$

where ω_i^g (ω_i^e) is the precession frequency of the nuclear spin if the electron is in the ground (excited) state. Exciting the electron spin to the excited state with s_i spin projec-

tion gives a way to measure $\Delta\omega_i$. Using Taylor expansion we can write ω_i, the magnitude of Eq. (6.3), as

$$\omega_i = \omega_L \left[1 + \frac{s_i A_\parallel}{\omega_L} + \frac{1}{2} \left(\frac{s_i A_\perp}{\omega_L} \right)^2 \right]. \tag{6.16}$$

This allows us to write Eq. (6.15) as

$$\Delta\omega_i = s_i \left(A_\parallel^e - A_\parallel^g \right) + \frac{s_i^2}{2\omega_L} \left(A_\perp^{e\,2} - A_\perp^{g\,2} \right). \tag{6.17}$$

For our spin system with $s_0 = -1/2$ and $s_1 = 1/2$ this results in

$$A_\parallel^e - A_\parallel^g = \Delta\omega_1 - \Delta\omega_0, \tag{6.18}$$

giving us the difference in parallel hyperfine coupling between the ground and excited states. Extracting the difference in perpendicular hyperfine components is less precise as it shows up as a second-order effect in these measurements.

REFERENCES

[1] D. D. Awschalom, R. Hanson, J. Wrachtrup and B. B. Zhou, *Quantum technologies with optically interfaced solid-state spins,* Nature Photonics **12**, 516 (2018).

[2] J. R. Maze *et al.*, *Nanoscale magnetic sensing with an individual electronic spin in diamond,* Nature **455**, 644 (2008).

[3] M. H. Abobeih *et al.*, *Atomic-scale imaging of a 27-nuclear-spin cluster using a quantum sensor,* Nature **576**, 411 (2019).

[4] A. J. Stolk *et al.*, *Metropolitan-scale heralded entanglement of solid-state qubits,* Science Advances **10**, eadp6442 (2024).

[5] D. M. Lukin, M. A. Guidry and J. Vučković, *Integrated Quantum Photonics with Silicon Carbide: Challenges and Prospects,* PRX Quantum **1**, 020102 (2020).

[6] M. Ruf, N. H. Wan, H. Choi, D. Englund and R. Hanson, *Quantum networks based on color centers in diamond,* Journal of Applied Physics **130**, 070901 (2021).

[7] C. M. Knaut *et al.*, *Entanglement of nanophotonic quantum memory nodes in a telecom network,* Nature **629**, 573 (2024).

[8] A. M. Dibos, M. Raha, C. M. Phenicie and J. D. Thompson, *Atomic Source of Single Photons in the Telecom Band,* Physical Review Letters **120**, 243601 (2018).

[9] A. Ruskuc, C.-J. Wu, J. Rochman, J. Choi and A. Faraon, *Nuclear spin-wave quantum register for a solid-state qubit,* Nature **602**, 408 (2022).

[10] M. T. Uysal *et al.*, *Coherent Control of a Nuclear Spin via Interactions with a Rare-Earth Ion in the Solid State,* PRX Quantum **4**, 010323 (2023).

[11] A. Ruskuc *et al.*, *Scalable Multipartite Entanglement of Remote Rare-earth Ion Qubits,* (2024), arXiv:2402.16224 .

[12] G. D. Fuchs, V. V. Dobrovitski, D. M. Toyli, F. J. Heremans and D. D. Awschalom, *Gigahertz Dynamics of a Strongly Driven Single Quantum Spin,* Science **326**, 1520 (2009).

[13] D. J. Christle *et al.*, *Isolated electron spins in silicon carbide with millisecond coherence times,* Nature Materials **14**, 160 (2015).

[14] D. D. Sukachev *et al.*, *Silicon-Vacancy Spin Qubit in Diamond: A Quantum Memory Exceeding 10 ms with Single-Shot State Readout,* Physical Review Letters **119**, 223602 (2017).

[15] L. Robledo *et al.*, *High-fidelity projective read-out of a solid-state spin quantum register,* Nature **477**, 574 (2011).

[16] J. M. Kindem *et al.*, *Control and single-shot readout of an ion embedded in a nanophotonic cavity,* Nature **580**, 201 (2020).

[17] M. K. Bhaskar *et al.*, *Experimental demonstration of memory-enhanced quantum communication,* Nature **580**, 60 (2020).

[18] H. K. C. Beukers *et al.*, *Remote-Entanglement Protocols for Stationary Qubits with Photonic Interfaces,* PRX Quantum **5**, 010202 (2024).

[19] N. H. Wan *et al.*, *Large-scale integration of artificial atoms in hybrid photonic circuits,* Nature **583**, 226 (2020).

[20] M. H. Abobeih *et al.*, *Fault-tolerant operation of a logical qubit in a diamond quantum processor,* Nature **606**, 884 (2022).

[21] M. Pompili *et al.*, *Realization of a multinode quantum network of remote solid-state qubits,* Science **372**, 259 (2021).

[22] S. L. N. Hermans *et al.*, *Entangling remote qubits using the single-photon protocol: An in-depth theoretical and experimental study,* New Journal of Physics **25**, 013011 (2023).

[23] T. van der Sar *et al.*, *Decoherence-protected quantum gates for a hybrid solid-state spin register,* Nature **484**, 82 (2012).

[24] T. H. Taminiau *et al.*, *Detection and Control of Individual Nuclear Spins Using a Weakly Coupled Electron Spin,* Physical Review Letters **109**, 137602 (2012).

[25] C. E. Bradley *et al.*, *A Ten-Qubit Solid-State Spin Register with Quantum Memory up to One Minute,* Physical Review X **9**, 031045 (2019).

[26] J. Cramer *et al.*, *Repeated quantum error correction on a continuously encoded qubit by real-time feedback,* Nature Communications **7**, 11526 (2016).

[27] S. Maity *et al.*, *Mechanical Control of a Single Nuclear Spin,* Physical Review X **12**, 011056 (2022).

[28] C. T. Nguyen *et al.*, *Quantum Network Nodes Based on Diamond Qubits with an Efficient Nanophotonic Interface,* Physical Review Letters **123**, 183602 (2019).

[29] C. Babin *et al.*, *Fabrication and nanophotonic waveguide integration of silicon carbide colour centres with preserved spin-optical coherence,* Nature Materials **21**, 67 (2022).

[30] D. B. Higginbottom *et al.*, *Optical observation of single spins in silicon,* Nature **607**, 266 (2022).

[31] Photonic Inc *et al.*, *Distributed Quantum Computing in Silicon,* (2024), arXiv:2406.01704 .

[32] C. T. Nguyen *et al.*, *An integrated nanophotonic quantum register based on silicon-vacancy spins in diamond,* Physical Review B **100**, 165428 (2019).

[33] K. Senkalla, G. Genov, M. H. Metsch, P. Siyushev and F. Jelezko, *Germanium Vacancy in Diamond Quantum Memory Exceeding 20 ms,* Physical Review Letters **132**, 026901 (2024).

[34] E. I. Rosenthal *et al.*, *Microwave Spin Control of a Tin-Vacancy Qubit in Diamond,* Physical Review X **13**, 031022 (2023).

[35] P. Wang *et al.*, *Transform-Limited Photon Emission from a Lead-Vacancy Center in Diamond above 10 K,* Physical Review Letters **132**, 073601 (2024).

[36] M. Zahedian, V. Vorobyov and J. Wrachtrup, *Blueprint for efficient nuclear spin characterization with color centers,* Physical Review B **109**, 214111 (2024).

[37] S. Maity *et al.*, *Spectral Alignment of Single-Photon Emitters in Diamond using Strain Gradient,* Physical Review Applied **10**, 024050 (2018).

[38] S. Ditalia Tchernij *et al.*, *Single-Photon-Emitting Optical Centers in Diamond Fabricated upon Sn Implantation,* ACS Photonics **4**, 2580 (2017).

[39] T. Iwasaki *et al.*, *Tin-Vacancy Quantum Emitters in Diamond,* Physical Review Letters **119**, 253601 (2017).

[40] M. E. Trusheim *et al.*, *Transform-Limited Photons From a Coherent Tin-Vacancy Spin in Diamond,* Physical Review Letters **124**, 023602 (2020).

[41] J. Görlitz *et al.*, *Spectroscopic investigations of negatively charged tin-vacancy centres in diamond,* New Journal of Physics **22**, 013048 (2020).

[42] A. E. Rugar *et al.*, *Narrow-Linewidth Tin-Vacancy Centers in a Diamond Waveguide,* ACS Photonics **7**, 2356 (2020).

[43] A. E. Rugar *et al.*, *Quantum Photonic Interface for Tin-Vacancy Centers in Diamond,* Physical Review X **11**, 031021 (2021).

[44] R. Debroux *et al.*, *Quantum Control of the Tin-Vacancy Spin Qubit in Diamond,* Physical Review X **11**, 041041 (2021).

[45] X. Guo *et al.*, *Microwave-Based Quantum Control and Coherence Protection of Tin-Vacancy Spin Qubits in a Strain-Tuned Diamond-Membrane Heterostructure,* Physical Review X **13**, 041037 (2023).

[46] M. Pasini *et al.*, *Nonlinear Quantum Photonics with a Tin-Vacancy Center Coupled to a One-Dimensional Diamond Waveguide,* Physical Review Letters **133**, 023603 (2024).

[47] J. M. Brevoord *et al.*, *Heralded initialization of charge state and optical-transition frequency of diamond tin-vacancy centers,* Physical Review Applied **21**, 054047 (2024).

[48] E. I. Rosenthal *et al.*, *Single-Shot Readout and Weak Measurement of a Tin-Vacancy Qubit in Diamond,* Physical Review X **14**, 041008 (2024).

[49] G. de Lange, Z. H. Wang, D. Ristè, V. V. Dobrovitski and R. Hanson, *Universal Dynamical Decoupling of a Single Solid-State Spin from a Spin Bath,* Science **330**, 60 (2010).

[50] I. Karapatzakis *et al.*, *Microwave Control of the Tin-Vacancy Spin Qubit in Diamond with a Superconducting Waveguide,* Physical Review X **14**, 031036 (2024).

[51] A. P. Nizovtsev *et al.*, *Non-flipping 13C spins near an NV center in diamond: Hyperfine and spatial characteristics by density functional theory simulation of the C510[NV]H252 cluster,* New Journal of Physics **20**, 023022 (2018).

[52] P. Neumann *et al.*, *Multipartite Entanglement Among Single Spins in Diamond,* Science **320**, 1326 (2008).

[53] N. Grimm *et al.*, *Coherent Control of a Long-Lived Nuclear Memory Spin in a Germanium-Vacancy Multi-Qubit Node,* Physical Review Letters **134**, 043603 (2025).

[54] S. Kolkowitz, Q. P. Unterreithmeier, S. D. Bennett and M. D. Lukin, *Sensing Distant Nuclear Spins with a Single Electron Spin,* Physical Review Letters **109**, 137601 (2012).

[55] N. Zhao *et al.*, *Sensing single remote nuclear spins,* Nature Nanotechnology **7**, 657 (2012).

[56] M. Abobeih, *From Atomic-Scale Imaging to Quantum Fault-Tolerance with Spins in Diamond*, Ph.D. thesis, Delft University of Technology (2021).

[57] H. van Ommen *et al.*, *Improved Electron-Nuclear Quantum Gates for Spin Sensing and Control,* PRX Quantum **6**, 020309 (2025).

[58] G. S. Uhrig, *Keeping a Quantum Bit Alive by Optimized π-Pulse Sequences,* Physical Review Letters **98**, 100504 (2007).

[59] R. Loudon, *The Quantum Theory of Light*, 3rd ed., Oxford Science Publications (Oxford University Press, Oxford ; New York, 2000).

[60] T. Astner *et al.*, *Vanadium in silicon carbide: Telecom-ready spin centres with long relaxation lifetimes and hyperfine-resolved optical transitions,* Quantum Science and Technology **9**, 035038 (2024).

[61] J. Casanova, Z.-Y. Wang, J. F. Haase and M. B. Plenio, *Robust dynamical decoupling sequences for individual-nuclear-spin addressing,* Physical Review A **92**, 042304 (2015).

[62] P.-J. Stas *et al.*, *Robust multi-qubit quantum network node with integrated error detection,* Science **378**, 557 (2022).

[63] I. B. W. Harris *et al.*, *Hyperfine Spectroscopy of Isotopically Engineered Group-IV Color Centers in Diamond,* PRX Quantum **4**, 040301 (2023).

[64] H. K. C. Beukers *et al.*, *Data and simulations underlying the research article "Control of solid-state nuclear spin qubits using an electron spin-1/2"*, 4TU.ResearchData (2024).

[65] I. T. Raa *et al.*, *QMI - Quantum Measurement Infrastructure, a Python 3 framework for controlling laboratory equipment,* 4TU.ResearchData (2023).

[66] T. H. Taminiau, J. Cramer, T. van der Sar, V. V. Dobrovitski and R. Hanson, *Universal control and error correction in multi-qubit spin registers in diamond,* Nature Nanotechnology **9**, 171 (2014).

[67] Z.-H. Wang, G. de Lange, D. Ristè, R. Hanson and V. V. Dobrovitski, *Comparison of dynamical decoupling protocols for a nitrogen-vacancy center in diamond,* Physical Review B **85**, 155204 (2012).

[68] J. R. Johansson, P. D. Nation and F. Nori, *QuTiP: An open-source Python framework for the dynamics of open quantum systems,* Computer Physics Communications **183**, 1760 (2012).

[69] G. L. van de Stolpe *et al.*, *Mapping a 50-spin-qubit network through correlated sensing,* Nature Communications **15**, 2006 (2024).

[70] M. Pompili, *Multi-Node Quantum Networks with Diamond Qubits*, Ph.D. thesis, Delft University of Technology (2021).

7

CONCLUSIONS AND OUTLOOK

7.1. SUMMARY

In this thesis, we used the nitrogen-vacancy (NV) center diamond to build a multinode quantum network and showcase important quantum network protocols. To eventually surpass the scale of these experiments, we deemed it necessary to explore a different color center with advantageous properties for quantum networks: the tin-vacancy (SnV) center in diamond. We developed a theoretical framework to understand whether a different physical system benefits from different entanglement protocols. Finally, we realized full control over a SnV center's electron and nuclear spin qubit register, establishing the local control required for future network experiments.

Here, we provide a short summary of the chapters in this thesis:

- In **Chapter 3**, we introduced a modular framework for remote-entanglement protocols. The framework can be used to dissect a protocol in different layers of abstraction, each with its own building blocks. This facilitates understanding and classification of existing remote-entanglement protocols, like the one used in Chapters 4, and 5. It can further be used to assemble new protocols by rearranging the building blocks. Finally, we compared different protocols using the matching simulation suite to show the versatility of the framework.

- In **Chapter 4**, we described the realization of a multinode quantum network based on the nitrogen-vacancy center in diamond. In this network, we devised a new phase stabilization scheme and improved memory coherence by increasing the magnetic field strength. We were able to show entanglement across all three nodes in the form of a GHZ state and implement an entanglement-swapping protocol, connecting two non-neighboring nodes with an entangled link.

- In **Chapter 5**, we built on the results of the multi-node network by adding a fifth qubit to the network. We implemented an improved heralding scheme, increasing the fidelity of the entangled links, designed a new repetitive readout scheme for improved real-time feedback, and implemented a Hahn echo on the memory qubit, extending its coherence. These improvements allowed us to deterministically teleport a quantum state between non-neighboring nodes in the quantum network.

- In **Chapter 6**, we moved our focus to the SnV center. We controlled its electron spin and used that to control two surrounding ^{13}C nuclear spins. The electron spin-1/2 nature of the SnV center reduces the selectivity of the control compared to the spin-1 of the nitrogen-vacancy center. We used the SnV center to investigate different nuclear spin control methods relevant to many important spin-1/2 systems. One of these control methods allowed us to entangle the electron and nuclear spin. Finally, we were able to quantify the hyperfine coupling of the nuclear spin to the electronic excited state, giving insights into the decoherence of the nuclear spin during optical readout.

7.2. SCALING QUANTUM NETWORK EXPERIMENTS

In Chapter 4 and Chapter 5, we used the NV center to scale quantum network experiments beyond two nodes. The question arises what advancements it would take to bring these experiments to the next level, i.e., more nodes, more complex protocols, entanglement distillation or a bigger separation between the nodes. These are the stepping stones towards a quantum internet [1]. However, they are currently limited by a combination of two factors.

First, if a protocol requires multiple entangled pairs to be available simultaneously, such as entanglement swapping or distillation, the balance between the entanglement rate and decoherence rate of the quantum memory is a critical factor for the performance. Their ratio, the quantum link efficiency $\eta_{\text{link}} = r_{\text{entanglement}}/r_{\text{decoherence}}$, has a strong influence on the required amount of hardware [2] and is therefore an essential factor to improve. For the three-node network experiments in Chapter 4 and Chapter 5, the link efficiency was below one. However, with the use of a timeout on the first entangled state, we were able to generate the two entangled links at the same time in a probabilistic way. This came at the price of a reduced entanglement rate, which prohibited scaling to experiments that require the simultaneous availability of more entangled pairs. Hence, improving the quantum link efficiency is paramount.

Second, the rate of generating entanglement is important for any network application or quantum experiment. A recent demonstration of metropolitan distance entanglement with the NV center reiterated the importance of the rate as the added overhead for waiting for a heralding signal reduced the rate to 1.3 min^{-1} [3].

One way to improve the quantum link efficiency is to reduce the decoherence rate $r_{\text{decoherence}}$. An important note is that the decoherence rate is understood to be the one during network operation. Performing entanglement attempts on the electron spin increases decoherence compared to an idling system. Stochastic processes on the electron limit the coherence of the memory qubit during entanglement generation [4], such as failing control gates and spin-pumping. The decoherence scales with both the time that the electron is in an unknown state and the hyperfine coupling of the nuclear spin. Either can be reduced to mitigate the decoherence of the nuclear spin during network operation.

In Chapter 4, we were able to increase the $1/e$ decay constant of the memory from $N_{1/e} \approx 300$ to 2000 entanglement attempts. This was the result of shortening the entanglement sequence, thereby reducing the time the electron is in an unknown state after a failed MW control pulse [4]. This approach allowed us to reach the T_2^* limit of the memory

qubit. In Chapter 5, we were able to improve this to $N_{1/e} \approx 5000$ by adding Hahn echo on the nuclear spin memory. This is, however, still short of the $1/(2p\alpha) \approx 10\,000$ attempts required to make entanglement. Implementing faster conditional logic for the heralding of the entanglement can further shorten the entanglement attempt. Furthermore, the single echo can be extended to dynamical decoupling of the nuclear spin to reduce the effect of quasi-static noise[5]. These improvements can likely bring the link efficiency for the NV center above one, but for now it remains unclear how far this could be taken.

Another approach to improve the memory coherence is to use weaker coupled spins as was done by Bradley et al.[6] where they reached a $N_{1/e} \approx 1 \times 10^5$. In this approach, the effect of stochastic processes during the entanglement attempts has little effect on the nuclear spins as they have such a weak coupling. To control these weakly coupled nuclear spins selectively, it is important to reduce the spectral crowding for those low hyperfine interactions, which was achieved by reducing the concentration of the ^{13}C isotope in isotopically purified samples. The downside of this approach is that the weaker coupled spins provide slower gates of 25 ms.

By improving the probability of success in entanglement generation, both link efficiency and entanglement rate are improved. The most prevalent approach for NV centers is using open microcavities[7–9] as the NV center is optically unstable in nanophotonic devices[10]. This approach improves the optical interface but does not provide a scalable way of increasing the number of communication qubits per node.

7.3. ENTANGLEMENT WITH TIN-VACANCY CENTERS

There are two main reasons why the SnV is an attractive candidate to take over the role of the NV center at the forefront of quantum network experiments. As outlined in Chapter 2, the SnV center has a 10-fold more efficient intrinsic optical interface, improving the rate of entanglement generation 10 to 100-fold depending on whether a single[11] or double[12] click entanglement protocol is used. On top of that, it is compatible with nanophotonic integration, which can be used to enhance the optical interface[13] and improve the collection efficiency[14]. Furthermore, this integration provides a scalable way to increase the number of communication qubits in a single quantum node, which is discussed in Section 7.5.

The properties of a spin-photon interface of a SnV center will depend on whether they are integrated in nanophotonic waveguides or cavities[13,15,16]. In nanophotonic cavities, the optical properties and coupling to a single mode can be enhanced over those of a waveguide. However, they require more complex fabrication capabilities and additional experimental tuning of the cavity[17]. A comparison between the performance of different photonic interfaces cannot be done in isolation. It should also take into account the available entanglement protocols as discussed in Chapter 3. It seems that protocols that have been used for the NV center are attainable for SnV in single-mode waveguides, where the lifetime of the SnV is around 6 ns and compatible with spontaneous emission schemes. SnV centers in cavities will see an improved coherent coupling, but their reduced lifetimes will complicate spontaneous emission schemes[11,12]. Protocols based on spin-dependent reflection of photonic qubits, as they are used for the silicon-vacancy center, are better suited in this case[18]. The strategy that will prevail

for scaling up entanglement with SnV centers is the one with the best tradeoff between fabrication requirements and fabrication scaling. Where the waveguide approach will allow for more relaxed fabrication tolerances, it will require more hardware and overhead to counteract the intrinsic inefficiencies.

All of the required ingredients for quantum network nodes based on SnV centers have been shown in proof-of-principle experiments: transform-limited optical lines[19], single emitter photonic indistinguishalility[20], charge-resonance check[21], single-shot readout[22], electron spin control[23,24], nuclear spin control (Chapter 6), waveguide integration[15,16], cavity integration[13], strain tuning[25] and quantum frequency conversion[26]. The main challenge will be to improve the fidelities of these capabilities and to integrate them all in a scalable design.

An open challenge is to combine all capabilities in a specific strain environment. Strain is required for MW driving and can be used to tune the optical transition, but it also increases the inhomogeneous distribution of the emitters, increasing the requirements of frequency shifting of the photons. Many proof-of-principle experiments have worked around the low fabrication yield and optical instability of the fabricated SnV centers by extensive pre-characterization. High-pressure high-temperature annealing has been able to generate much more stable emitters with a lower inhomogeneous distribution and less crystal damage[27]. However, the process intrinsically relaxes the strain in the diamond. Therefore, the desirable optical properties are accompanied by inefficient microwave spin control[23]. Static strain can be induced in diamond membranes for improving the MW driving efficiency[24]. However, it is an open question whether this method could be combined with integrating SnV centers in nanophotonic structures, as recent experiments show strain relaxation in photonic crystal cavities in bonded membranes[28]. A detailed study on the effect of implantation damage and annealing can direct the field to a method that can improve the optical properties without nullifying the strain. Furthermore, nanophotonic designs have been shown to be compatible with deterministic introduction of static strain[29]. The open question is whether this idea can be combined with other requirements such as photonic integration and strain tuning.

So far, the most complete node with a group-IV vacancy center has been realized with the silicon-vacancy center in diamond[18] and a similar design should be attainable for SnV centers. This node had all the capabilities to make remote entanglement, yet it missed the capability to tune the optical transition of the silicon-vacancy center itself. The tuning of the optical photons was achieved by frequency shifting outside the node with either an electro-optic modulator or during quantum frequency conversion. However, the ability to tune the emitter itself facilitates on-chip entanglement that can be used for quantum information processing or routing of entanglement. Strain tuning of waveguides has been shown[25] and photonic crystal cavities compatible with strain tuning[30] have been simulated to work, however a single node showing all capabilities at the same time has still to be shown.

Given the current advances in the field, entanglement between SnV centers is likely going to be achieved in the coming years. Solving the outstanding questions of integrated design will allow to scale the complexity and scale beyond current NV center experiments.

7.4. QUANTUM MEMORY FOR TIN-VACANCY CENTERS

We discussed the added value the SnV center brings to the generation of entanglement in quantum networks. However, good memory coherence during network operation is also essential for a high link efficiency and, therefore, a quantum network node. Similar to the NV center, this can be realized using weakly coupled nuclear spins and reducing the impact of stochastic processes.

The selectivity of nuclear spin control in electron spin-1/2 systems is reduced, as discussed in Chapter 6. Therefore, controlling weakly coupled spins will require new control techniques. A promising idea for achieving enhanced selectivity is using a quantum memory in addition to the DDRF control. The DDRF gate is then interleaved with periods where the electron spin is put in an eigenstate, which recovers the first-order selectivity for the hyperfine parameters. During these periods, the original state of the electron spin needs to be preserved by storing it in an easily accessible quantum memory. In the SnV center, the nuclear spin of the tin isotope could fulfill this role[31].

The selectivity of the nuclear spin control scales with the total gate length and the interpulse spacing of the dynamical decoupling. The electron spin bath is the limiting factor of the coherence during dynamical decoupling, as became clear in Chapter 6. Implantation damage during fabrication is the most likely source of this bath[23]. Therefore, reducing the implantation damage can improve not only the optical properties but also the nuclear spin control selectivity.

For the SnV center, there is an additional stochastic process on the phase of the nuclear spin compared to the NV center. During optical excitation of the electron, the nuclear spin acquires a phase depending on the time spent in the excited state, as discussed in Chapter 6. This will impact the nuclear spin during readout or entanglement generation. To reduce this effect, the difference between the hyperfine coupling in the ground and excited state needs to be minimized. For weakly coupled spins, this difference will be small, further research must show whether this effect will limit the coherence in practice.

Initialization through spin pumping is a stochastic process in the entanglement sequence causing the dephasing of the nuclear spin[4]. The spin pumping causes an exponentially distributed reset time of the electron. The reset of the electron spin in the SnV center is much slower because of the high cyclicity of its optical transitions, thereby increasing the uncertainty on the electron spin reset time. A measurement-based initialization can completely remove the uncertainty of the electron reset time. This is especially attractive for the SnV center as its high cyclicity improves the readout fidelity.

Control of a local memory register requires many control pulses on the electron, which can cause local heating of the diamond[32]. This limits the number of SnV centers per chip as the cooling power of the cryostat will become limiting. There are a few directions that could be explored to mitigate the heating. Resonant structures can generate high fields with low supply currents but require a well-known operating regime as they lock the qubit frequency during fabrication. Superconducting coplanar waveguides have been shown to reduce the heating[33] in a similar experimental setting as in Chapter 6.

Getting to high fidelity control of ^{13}C will require additional investigation in the pre-

viously mentioned areas. It is a quantum memory available for the SnV center with deterministic gates that can withstand entanglement attempts. Therefore, advancements in ^{13}C spin control will be important for the progress of quantum networks based on group-IV vacancy centers.

7.5. TOWARDS LARGE QUANTUM NETWORKS

A future quantum internet requires high-rate, long-distance entanglement distribution. Quantum repeater require at least hundreds of multiplexed modes and the same amount of qubits in the nodes[34]. Distributed error-corrected computations in the network require at least millions of qubits[35]. Hence, future quantum network nodes will require hardware that is scalable in the number of qubits.

Diamond is a great host material for color centers[36,37]. However, the low nonlinear optical response of diamond and the immature fabrication methods available are unsuited for the optical components such as beamsplitter, phase shifters and switches. More mature phonics platforms such as silicon nitride, aluminum nitride, and lithium niobate offer low loss at visible wavelengths and can realize these optical components[38,39], but they lack good quantum emitters. Hybrid integration of diamond a mature photonic platform gives a systems where these properties are combined[25,40]. These platforms can be combined by the pick-and-place method[40] or transfer printing[41].

In the past decade, there have been many proof-of-principle experiments of quantum network primitive components to build up the capabilities bottom-up where the focus has been on the quantum mechanical implementation of quantum information concepts[5,12,18,42,43]. On the other hand, there have been efforts in the field to make scalable hardware platforms and architectures that are close to a top-down approach where the focus has been on scalability rather than the performance of individual components[25,40,44]. These two approaches will meet in the coming years, where the network primitives can be showcased on scalable platforms.

7.6. EPILOGUE

Color centers have been a versatile building block of the first generation of quantum network experiments. It is exactly their solid-state nature that makes them attractive for the next generation, where integrating them on a chip can give the required scalability. It is now time to get the word "scalable" out of the introduction of quantum network papers and into the main text.

REFERENCES

[1] S. Wehner, D. Elkouss and R. Hanson, *Quantum internet: A vision for the road ahead,* Science **362**, eaam9288 (2018).

[2] C. Monroe *et al.*, *Large-scale modular quantum-computer architecture with atomic memory and photonic interconnects,* Physical Review A **89**, 022317 (2014).

[3] A. J. Stolk *et al.*, *Metropolitan-scale heralded entanglement of solid-state qubits,* Science Advances **10**, eadp6442 (2024).

[4] N. Kalb, P. C. Humphreys, J. J. Slim and R. Hanson, *Dephasing mechanisms of diamond-based nuclear-spin memories for quantum networks,* Physical Review A **97**, 062330 (2018).

[5] C. E. Bradley *et al.*, *A Ten-Qubit Solid-State Spin Register with Quantum Memory up to One Minute,* Physical Review X **9**, 031045 (2019).

[6] C. E. Bradley *et al.*, *Robust quantum-network memory based on spin qubits in isotopically engineered diamond,* npj Quantum Information **8**, 1 (2022).

[7] D. Riedel *et al.*, *Deterministic Enhancement of Coherent Photon Generation from a Nitrogen-Vacancy Center in Ultrapure Diamond,* Physical Review X **7**, 031040 (2017).

[8] M. Ruf, M. Weaver, S. van Dam and R. Hanson, *Resonant Excitation and Purcell Enhancement of Coherent Nitrogen-Vacancy Centers Coupled to a Fabry-Perot Microcavity,* Physical Review Applied **15**, 024049 (2021).

[9] V. Yurgens *et al.*, *Cavity-assisted resonance fluorescence from a nitrogen-vacancy center in diamond,* npj Quantum Information **10**, 112 (2024).

[10] A. Faraon, C. Santori, Z. Huang, V. M. Acosta and R. G. Beausoleil, *Coupling of Nitrogen-Vacancy Centers to Photonic Crystal Cavities in Monocrystalline Diamond,* Physical Review Letters **109**, 033604 (2012).

[11] P. C. Humphreys *et al.*, *Deterministic delivery of remote entanglement on a quantum network,* Nature **558**, 268 (2018).

[12] H. Bernien *et al.*, *Heralded entanglement between solid-state qubits separated by three metres,* Nature **497**, 86 (2013).

[13] A. E. Rugar *et al.*, *Quantum Photonic Interface for Tin-Vacancy Centers in Diamond,* Physical Review X **11**, 031021 (2021).

[14] M. J. Burek *et al.*, *Fiber-Coupled Diamond Quantum Nanophotonic Interface,* Physical Review Applied **8**, 024026 (2017).

[15] A. E. Rugar *et al.*, *Narrow-Linewidth Tin-Vacancy Centers in a Diamond Waveguide,* ACS Photonics **7**, 2356 (2020).

[16] M. Pasini *et al., Nonlinear Quantum Photonics with a Tin-Vacancy Center Coupled to a One-Dimensional Diamond Waveguide,* Physical Review Letters **133**, 023603 (2024).

[17] R. E. Evans, A. Sipahigil, D. D. Sukachev, A. S. Zibrov and M. D. Lukin, *Narrow-Linewidth Homogeneous Optical Emitters in Diamond Nanostructures via Silicon Ion Implantation,* Physical Review Applied **5**, 044010 (2016).

[18] C. M. Knaut *et al., Entanglement of nanophotonic quantum memory nodes in a telecom network,* Nature **629**, 573 (2024).

[19] M. E. Trusheim *et al., Transform-Limited Photons From a Coherent Tin-Vacancy Spin in Diamond,* Physical Review Letters **124**, 023602 (2020).

[20] J. Arjona Martínez *et al., Photonic Indistinguishability of the Tin-Vacancy Center in Nanostructured Diamond,* Physical Review Letters **129**, 173603 (2022).

[21] J. M. Brevoord *et al., Heralded initialization of charge state and optical-transition frequency of diamond tin-vacancy centers,* Physical Review Applied **21**, 054047 (2024).

[22] E. I. Rosenthal *et al., Single-Shot Readout and Weak Measurement of a Tin-Vacancy Qubit in Diamond,* Physical Review X **14**, 041008 (2024).

[23] E. I. Rosenthal *et al., Microwave Spin Control of a Tin-Vacancy Qubit in Diamond,* Physical Review X **13**, 031022 (2023).

[24] X. Guo *et al., Microwave-Based Quantum Control and Coherence Protection of Tin-Vacancy Spin Qubits in a Strain-Tuned Diamond-Membrane Heterostructure,* Physical Review X **13**, 041037 (2023).

[25] G. Clark *et al., Nanoelectromechanical Control of Spin–Photon Interfaces in a Hybrid Quantum System on Chip,* Nano Letters **24**, 1316 (2024).

[26] D. Lindler, T. Bauer, M. Schäfer and C. Becher, *Two-Stage Quantum Frequency Conversion for SnV-resonant Photons to the Telecom C-Band,* in *Optica Quantum 2.0 Conference and Exhibition (2023), Paper QW4A.1* (Optica Publishing Group, 2023) p. QW4A.1.

[27] J. Görlitz *et al., Spectroscopic investigations of negatively charged tin-vacancy centres in diamond,* New Journal of Physics **22**, 013048 (2020).

[28] S. W. Ding *et al., High-Q cavity interface for color centers in thin film diamond,* Nature Communications **15**, 6358 (2024).

[29] D. R. Assumpcao *et al., Deterministic creation of strained color centers in nanostructures via high-stress thin films,* Applied Physics Letters **123**, 244001 (2023).

[30] M. Haas *et al., Enabling strain tuning for cavity-coupled silicon vacancy centers in diamond,* in *APS March Meeting Abstracts*, Vol. 2023 (2023) pp. M70–004.

[31] I. B. W. Harris *et al., Hyperfine Spectroscopy of Isotopically Engineered Group-IV Color Centers in Diamond,* PRX Quantum **4**, 040301 (2023).

[32] C. T. Nguyen *et al., An integrated nanophotonic quantum register based on silicon-vacancy spins in diamond,* Physical Review B **100**, 165428 (2019).

[33] I. Karapatzakis *et al., Microwave Control of the Tin-Vacancy Spin Qubit in Diamond with a Superconducting Waveguide,* Physical Review X **14**, 031036 (2024).

[34] F. F. da Silva, G. Avis, J. A. Slater and S. Wehner, *Requirements for upgrading trusted nodes to a repeater chain over 900 km of optical fiber,* Quantum Science and Technology **9**, 045041 (2024).

[35] H. Choi, M. Pant, S. Guha and D. Englund, *Percolation-based architecture for cluster state creation using photon-mediated entanglement between atomic memories,* npj Quantum Information **5**, 1 (2019).

[36] D. D. Awschalom, R. Hanson, J. Wrachtrup and B. B. Zhou, *Quantum technologies with optically interfaced solid-state spins,* Nature Photonics **12**, 516 (2018).

[37] G. Wolfowicz *et al., Quantum guidelines for solid-state spin defects,* Nature Reviews Materials **6**, 906 (2021).

[38] A. W. Elshaari, W. Pernice, K. Srinivasan, O. Benson and V. Zwiller, *Hybrid integrated quantum photonic circuits,* Nature Photonics **14**, 285 (2020).

[39] M. Dong *et al., Piezo-optomechanical cantilever modulators for VLSI visible photonics,* APL Photonics **7**, 051304 (2022).

[40] N. H. Wan *et al., Large-scale integration of artificial atoms in hybrid photonic circuits,* Nature **583**, 226 (2020).

[41] L. Li *et al., Heterogeneous integration of spin–photon interfaces with a CMOS platform,* Nature **630**, 70 (2024).

[42] N. Kalb *et al., Entanglement distillation between solid-state quantum network nodes,* Science **356**, 928 (2017).

[43] M. K. Bhaskar *et al., Experimental demonstration of memory-enhanced quantum communication,* Nature **580**, 60 (2020).

[44] K. J. Palm *et al., Modular chip-integrated photonic control of artificial atoms in diamond waveguides,* Optica **10**, 634 (2023).

ACKNOWLEDGEMENTS

During the years of my PhD, there have been many people that made it into such a fun, educative and special period.

Ronald, the combination of a great scientist, a good manager, and a kind person makes you the perfect promotor. Your involvement is exemplified by being the first to send a card for Hannah's birth. I learned a lot from your way of thinking and reasoning and often asked myself the question, "What would Ronald ask when we would present this in a meeting?", usually this was enough to lay out the next steps. And, when challenges started to feel like problems, a meeting with you gave new directions to explore. Good luck with your upcoming scientific and commercial adventures; I'm sure they will combine fun with excellence.
Tim, thank you for being my co-promotor. I enjoyed our conversations on the intricacies of nuclear spin control with an electron spin-1/2 and your creativity in thinking of new control schemes.
Thank you, **Leo DiCarlo**, **Casper van der Wal**, **Fedor Jelezko**, **Tracy Northup**, and **Leo Kouwenhoven**, for being part of my committee. I'm looking forward to the discussions during the defense.

The two people, Christopher and Matteo, who will stand by my side during the defense, have also done so during my PhD. Whether it was solving challenges in the lab, disagreeing with my scribbles on a whiteboard, playing in the QuTech band, sailing in Friesland, or being on a tiny edge on a via ferrata in the Dolomites. Thank you for those great moments.
Matteo jr., it was nice to start an entirely new direction with you, working with tins in diamond. I think we both underestimated how hard it was to get to a basic T1 measurement and how complex a 4-dimensional Hilbert space can be, but step by step it turned into a true spin-photon interface. You are a multitalented person, a scientist, a band member, and a graphic designer. Many people refer to our tutorial paper as "the one with the pretty figures." Good luck with Project Barcelona 2024!
Christopher, I could not have hoped for a better person to join me in a new, empty lab. Your skills, enthusiasm, knowledge and gründlichkeit have been why we got this new lab up and running and the experiments to work. Collaborating on our projects has truly felt like doing it together, which is such a precious feeling. And don't forget, next time you go on a sailing or hiking trip, bring a toilet bag.
Matteo sr., after being my supervisor during my Master's project, I knew how lucky I was to work again together on the three-node network, with your wide knowledge, programming skills, and kind personality. I will never forget the nightly calls during weeks-long measurements, discussing if it was worth cycling to Delft to replug a USB connector or that the setups were doomed for the day.

Sophie, thank you for getting me back up to speed with the three-node network experiment and being the head of calibrations for many weeks in a row, getting the setups in a shape where entanglement was possible. Based on what I've seen during my Master's project and my PhD, I'm confident that starting your group will be a success, and the PhD students in your group will be lucky to have a supervisor like you.
Simon, it was nice joining you three on the three nodes, fighting statistics with long measurements. But if data looked puzzling, you were always willing to give a "guide to the eye". I enjoyed visiting you in Innsbruck and I'm happy that you could move back to this lovely place between the mountains.

It was very exciting to see the tin-team grow during my PhD. Where we started as an outlier, now the majority of the group works on all kinds of projects involving tin, from fabrication, nanophononics, cavities, strain tuning, quantum frequency conversion, and microwave control to spin-photon interfaces thanks to many very nice and talented people.
Alex, your knowledge and skills were a very welcome addition to our team! On top of that, I keep being amazed by your endurance achievements during the Bruggenloop and the off-road races. Good luck taking Pingu to a new level, and please make those metal optical boxes a reality! **Nina**, as everybody knows, you are the queen of the diamond fab. I enjoyed joining you in making the striplines on our diamonds. I'm curious to see what upcoming project is lucky to receive your full dedication. **Julia**, part of both the "full house" and "kwartet" in our office. Your enthusiasm positively impacts the group, our office, and the band alike. I also like your mentality of celebrating success to motivate people around you. **Tim**, I very much enjoy having you around! Thank you for the remote coding ideas; they have been such an improvement. Good luck with VLT2 and finding a compelling name for your fridge! **Dani**, I'm happy that you joined the tin team, and I'm sure that, with your precise simulations, the skyfish/swordfish/alligator cavities will be a success! **Niv**, joining an experimental group as a theorist takes some bravery. Your addition is valuable, and I'm curious about what will come from your projects, which are so closely tied to experiments. **Lorenzo**, we were lucky that you were stuck in Delft during the beginning of Corona, as your help was extremely valuable to get through the initial phase of the tin-vacancy project. You are a very talented and likable person. **Leo**, your enthusiasm is contagious, and combined with your skills, this will lead to a bright PhD.

What I love about our research group is the appetite to help each other, even when it's an entirely different project.
Arian, you have been one of the go-to people in the group for questions about almost anything. Besides, you keep people around you sharp with discussions about nearly anything. What I admire is that you are always open for good argumentation, however contradicting with you own views it might be. **Kian**, I appreciate your dedication to bringing the technical scientific and commercial worlds closer to each other. This has resulted in a very cool thesis, and I keep on being confused when picking it up. Good luck in Canada! **Mariagrazia**, I've been impressed by you running entanglement on the network setups on your own. Bob and Charlie are not always the easiest of setups. Your

closeness to Christopher has benefitted our experiments as you have helped with your knowledge of electron and nuclear spin control and outside perspective; thank you. I also loved Chris and your interest in Hannah's little life. Good luck with wrapping up! **Yanik** and **Julius**, Chris and I were lucky enough to share a lab with you two as we could benefit from your superior lab organization and endless stock. **Yanik**, it is impressive how you build up the lab from nothing to the complete setup it is today. **Julius**, thanks for your openness and willingness to help out. It is very nice how you organized the Diamond Cup; it has been a great success, especially with you flying over the volleyball and basketball courts. **Christian**, I was happy you rejoined the group after your master's project. Starting on an entirely new research project can be challenging, but I know you will get it to work. Furthermore, I enjoy your well-informed opinions about politics, and I'm curious how these two things will mix in the future. **Marie-Christine**, you are a great person to have around, and you positively impact the atmosphere. Enjoy the new phase in life with Josh. **Max**, now I'm at the end of my PhD myself; I'm impressed by the scope of the projects you managed to do in yours! **Matthew**, I value your well-informed and nuanced opinions. Good luck with your endeavors at QphoX; I'm looking forward to meeting you at conferences! **Alejandro**, it's fun to converse with you with such outspoken positive or critical opinions; it's great that you found such a nice place at HSBC. **Chantal**, **Esther** and **Sara**, thank you for all the help with questions, sending packages and administrative tasks.

During my PhD, I had the luck to have many talented, motivated and kind master students working on our projects.
Kamiel, you were my first master's student. We gave you a project that turned out to be impossible during the impossible Corona time, but you managed to get valuable measurements out! Thanks for being an enthusiastic member of Team Diamond. **Sarel**, you also had hurdles to overcome during your project, and you found creative ways to overcome them. I enjoyed all the nice-looking presentations and thesis! **Zarije**, thank you for helping to get Pingu up and running. I'm happy that you found a nice PhD project with Menno. **Timo**, we were fortunate to have you join the project; it soon felt like having another PhD student in the lab. Therefore, I'm very happy that you decided to come back as an actual PhD student! Just one piece of advice for your PhD; maybe don't extrapolate to liberally with a straight line. **Noé**, it was nice to have you join a physics experiment as a computer science student. I've enjoyed your motivation to learn. Good luck with finding the right niche between software and quantum. **Stijn**, *the fiber wisperer*, thank you for all the record-breaking PM splices in our setup.

The Diamond Cup requires two teams; luckily, there are the TimTams. Having a sister group is not only double the fun socially but also scientifically very valuable, especially when your project is about nuclear spin control.
Conor, it is great having you back in Delft. Thank you for the discussions about DDRF. Good luck with the company; I'm sure you're the right person to make it a success! **Hans** - finally, I don't need to clarify which Hans B. I mean - thank you for all the conversation on what might be different between controlling nuclear spins with SnV or NV centers. Solving riddles in Stockholm was fun! **Nicolas**, you would say that by now, we would

have perfected the Blues Brother handshake, but it's misleadingly difficult... The trips to Stockholm and Minnesota were highlights. Good luck finishing your PhD and getting those nasty and awesome pairs in check! **Sjoerd**, we followed a somewhat parallel path during our master's project and PhD. You are a very outspoken and likable person. I really appreciate your attitude of asking the questions or saying what everybody thinks, but is too shy to speak up about. **Guido**, thank you for our amazing three-day road trip into the north of Minnesota, including the spooky rocking horse. I enjoyed our discussions where it feels like we think the same way but end up at completely different conclusions. **Mohamed**, it was very cool to see how far you can push science using a single NV center. **Joe**, I was always impressed how you filled any vacancy in the QuTech band, regardless of the instrument and I really enjoyed playing together. **Maarten**, it was nice to share Groningen memories in Delft. **Benjamin**, how lucky we were that you were working on the paper we needed to understand what our nuclear spins were doing! Thank you for all the help and involvement in our project. **Laurens**, I like your appetite for things outside your comfort zone and making them into a success: rapping with the band, art projects about science, and starting to investigate color centers in a new material. **Gerben**, get those V2 to be bright and shiny! **Christina** and **Margriet**, joining you on strings during the Christmas party was great. **Christina**, I'm looking forward to your complex experiments on M1. **Margriet**, keep up the fanatic climbing vibes! **Jiwon**, you changed the way I look at the vending machine! Very nice explanation for cool results. Good luck with your next steps. **Kai**, it was fun spending time in Stockholm, good luck with the well-behaved ions! **Tobi**, the one to complete the "kwartet" in our office. With your enthusiasm, I'm sure you will have a fun PhD! **Dan**, **Jasper** and **Madhumati** enjoy the science and social activities of Team Diamond and QuTech.

Chuck, when planning a meeting with the US, I always think about it relative to our "usual time": 4 PM CET and 10 AM EST. The project and meetings with you were a great addition to my PhD. I learned a great deal from you. It was very nice to have you here in Delft, and visiting Boston was awesome; thank you for being so inviting! I hope I need to be on Long Island soon. **Johannes**, you are a very skilled theoretician, and your closeness to experiments is extremely valuable. I enjoyed the discussion on the tutorial paper. It's great that you found your place in Boston. **Dirk**, thank you for your insights in our tutorial paper! It was very nice to meet you and visit your lab at MIT.

One of the great things about QuTech is the vast and skilled technical support staff. Thank you, **Siebe**, **Vinod**, **Jelle** and **Roy,** for getting our lab ready and for the excellent soundproofing of our pulse tube! **Olaf**, **Jason** and **Erik** for answering every question we had about fridges and bond wires. **Hitham** and **Régis**, thank you for keeping us safe. **Nico** and **Tim**, thank you for fabricating any part we could dream of and, of course, always with some time pressure. **Yannick**, thank you for soldering the monstrous connectors to our nano positions. **Raymond**, **Raymond**, **Martijn, Berend** and **Roy**, thank you for answering our electronics questions and figuring out that we usually needed something other than what we were asking. **Henri**, **Pieter** and **Ravi**, thank you for helping us create a code base that transcends one written by experimental physicists.

Wednesday evening has been a constant highlight during my PhD due to the rehearsals of the QuTech band Q2 and our post-rehearsal dinners at Il Peperonchino. **Matteo**, **Chris**, **Will**, **Gustavo**, **Floor**, **Anne-Marije**, **Pablo**, **Maia**, **Bart**, **Julia**, **Nicolas**, **Colin**, **Christina**, **Margriet**, **Zarije**, **Laurens**, **Joe** and **Conor,** thank you for the great music and fun! **Will**, thank you for the nice jamming session with the Q2 band and at your house and the conversations about cultural differences. I really enjoyed our trip to the Dolomites, conquering untrained a five-hour via ferrate while being uncomfortable with heights is truly impressive!

Tim and **Floriaan**, I really enjoy our continued contact and I'm sure it will last; good and old friendships are few and precious!

During my PhD, the Friday mornings were a constant factor with the breakfast club at Boulangerie Michel. Thank you, **Bas**, **Eva**, **Tobias**, **Mirthe**, **Guido**, **Lauren**, **Bodil**, **Reza**, and our youngest member **Ines**! And all others that occasionally joined. These moments have been very precious to me. I hope we can all find time in any phase of life to see a group of friends so regularly, thereby sharing each other's life.
Amoz, **Bas**, **Jacob**, **Niels**, **Daan**, **Tobias**, **Guido** and **Tessa**, thanks for the verjaardagen-weekenden and the great trip down memory lane by being together back in our rowing boat.

Maarten, **Rosa** and **Floris**, thanks for the nice time we spent together and for all studying physics so that you can follow what my PhD is about. **Rosa** and **Dylan** good luck with your future steps together and congrats on a joint paper! **Maarten** and **Georgina**, I'm happy to see that a choir brings more than just music and it's great to see your sweet care of Hannah. **Floris**, I'm curious to see where your beautiful piano play will bring you.

Ike, it was nice to do my PhD in parallel with you and having you over for weekly sleepovers in Den Haag. **Eveline**, thank you for my thesis cover. I enjoyed a lot designing and making this together with you. Every time, you surprise me with your creativity and artistic skills. I'm excited about your new adventure in the UK and hope there will be many Cambridge-Zürich exchanges.

Maarten and **Pauline**, thank you for the pleasant stays in – it's almost like France – Heerlen and our sincere conversations about my PhD and life. Also, over the past year, it was dear to see you often during the biweekly visits to Den Haag to take care of Hannah.

Dear **oma Tep**, thank you for stimulating my curiousity my whole life, even when it ment that I would keep on breaking the kitchen timers. It is a privilage to spend days with four generations.

Dear **pap** and **mam**, thank you for supporting me in this endeavor that was a bit further from home than the hospital. Part of my PhD has played out in holiday homes with you when the experiment did not adhere to holiday planning. I enjoyed how Hannah brought you to Den Haag every other week. It's great that you could leave the

practice in good hands so that you have time to come over to Cambridge and Zürich.

"My" **Sophie**, we had some great adventures in the last years, from sailing with you as the *betrouwbare matroos*, spending days in our crawling space, climbing a glacier to starting a family. Thank you for supporting me all these years, especially when measurements ended up on evenings, weekends, or sometimes holidays. I'm proud of our little **Hannah**, who brightens the days when experiments are down or deadlines close, and curiously explores the world, every detail of it. I'm looking forward to our newest adventure in Switzerland and to share life together!

LIST OF PUBLICATIONS

14. Large-Range Tuning and Stabilization of the Optical Transition of Diamond Tin-Vacancy Centers by In-Situ Strain Control
J. M. Brevoord, L. G. C. Wienhoven, N. Codreanu, T. Ishiguro, E. van Leeuwen, M. Iuliano, L. De Santis, C. Waas, **H. K. C. Beukers**, T. Turan, C. Errando-Herranz, K. Kawaguchi, R. Hanson; *Appl. Phys. Lett.* 126, 174001 (2025)

13. Control of Solid-State Nuclear Spin Qubits Using an Electron Spin-1/2
H. K. C. Beukers*, C. Waas*, M. Pasini, H. B. van Ommen, Z. Ademi, M. Iuliano, N. Codreanu, J. M. Brevoord, T. Turan, T. H. Taminiau, and R. Hanson; *Physical Review X*, 15, 021011, 2025

12. Improved Electron-Nuclear Quantum Gates for Spin Sensing and Control
H. B. van Ommen*, G. L. van de Stolpe*, N. Demetriou, **H. K. C. Beukers**, J. Yun, T. R. J. Fortuin, M. Iuliano, A. R.-P. Montblanch, R. Hanson, and T. H. Taminiau; *PRX Quantum*, 6, 020309, 2025

11. Remote-Entanglement Protocols for Stationary Qubits with Photonic Interfaces
H. K. C. Beukers*, M. Pasini*, H. Choi*, D. Englund, R. Hanson, and J. Borregaard; *PRX Quantum*, 5, 010202, 2024

10. Nonlinear Quantum Photonics with a Tin-Vacancy Center Coupled to a One-Dimensional Diamond Waveguide
M. Pasini, N. Codreanu, T. Turan, A. Riera Moral, C. F. Primavera, L. De Santis, **H. K. C. Beukers**, J. M. Brevoord, C. Waas, J. Borregaard, and R. Hanson; *Physical Review Letters*, 133, 023603, 2024

9. Heralded initialization of charge state and optical-transition frequency of diamond tin-vacancy centers
J. M. Brevoord*, L. De Santis*, T. Yamamoto, M. Pasini, N. Codreanu, T. Turan, **H. K. C. Beukers**, C. Waas, and R. Hanson; *Physical Review Applied*, 21, 054047, 2024

8. Entangling remote qubits using the single-photon protocol: an in-depth theoretical and experimental study
S. L. N. Hermans, M. Pompili, L. D. S. Martins, A. R.-P. Montblanch, **H. K. C. Beukers**, S. Baier, J. Borregaard, and R. Hanson; *New Journal of Physics*, 25, 013011, 2023

7. Qubit teleportation between non-neighbouring nodes in a quantum network
S. L. N. Hermans*, M. Pompili*, **H. K. C. Beukers**, S. Baier, J. Borregaard, and R. Hanson; *Nature*, 605, 7911, 2022

*Equally contributing authors

6. Realization of a multinode quantum network of remote solid-state qubits
M. Pompili*, S. L. N. Hermans*, S. Baier*, **H. K. C. Beukers**, P. C. Humphreys, R. N. Schouten, R. F. L. Vermeulen, M. J. Tiggelman, L. dos Santos Martins, B. Dirkse, S. Wehner, and R. Hanson; *Science*, 372, 259, 2021

MEDICAL PUBLICATIONS

5. Area-weighted unipolar voltage to predict heart failure outcomes in patients with ischaemic cardiomyopathy and ventricular tachycardia
R. Rademaker, Y. Kimura, M. de Riva Silva, **H. K. C. Beukers**, S. R. D. Piers, A. P. Wijnmaalen, O. M. Dekkers, and K. Zeppenfeld; *EP Europace*, 26, euad346, 2024

4. Multisize electrode field-of-view: validation by high resolution gadolinium-enhanced cardiac magnetic resonance
S. Omara, C. A. Glashan, B. J. Tofig, L. Leenknegt, H. Dierckx, A. V. Panfilov, **H. K. C. Beukers**, M. H. van Waasbergen, Q. Tao, W. G. Stevenson, J. C. Nielsen, P. Lukac, S. B. Kristiansen, R. J. van der Geest, and K. Zeppenfeld; *JACC: Clinical Electrophysiology*, 10, 637, 2024

3. Volume-Weighted Unipolar Voltage Predicts Heart Failure Mortality in Patients With Dilated Cardiomyopathy and Ventricular Arrhythmias
Y. Kimura, **H. K. C. Beukers**, R. Rademaker, H. S. Chen, M. Ebert, T. Jensen, S. R. Piers, A. P. Wijnmaalen, M. de Riva, O. M. Dekkers, W. G. Stevenson, and K. Zeppenfeld; *JACC: Clinical Electrophysiology*, 9, 965, 2023

2. Multielectrode Unipolar Voltage Mapping and Electrogram Morphology to Identify Post-Infarct Scar Geometry: Validation by Histology
C. A. Glashan, B. J. Tofig, **H. K. C. Beukers**, Q. Tao, S. A. Blom, P. R. Villadsen, T. R. Lassen, R. M. de, S. B. Kristiansen, and K. Zeppenfeld; *JACC: Clinical Electrophysiology*, 8, 437, 2022

1. Mini-, Micro-, and Conventional Electrodes: An in Vivo Electrophysiology and Ex Vivo Histology Head-to-Head Comparison
C. A. Glashan, **H. K. C. Beukers**, B. J. Tofig, Q. Tao, S. Blom, B. Mertens, S. B. Kristiansen, and K. Zeppenfeld; *JACC: Clinical Electrophysiology*, 7, 197, 2021

*Equally contributing authors

CURRICULUM VITEA

Hans Karel Clemens BEUKERS
September 29th, 1992, Apeldoorn, The Netherlands

2020 - 2025	PhD in Physics Delft University of Technology, Delft, The Netherlands Thesis: *"Quantum Networks with Diamond Color Centers: Local Control and Multi-Node Entanglement"* Promotor: Prof. Ronald Hanson Copromotor: Dr. Tim H. Taminiau
2015 - 2019	Master of Science in Physics, *Cum Laude* University of Groningen, Groningen, The Netherlands Thesis: *"Improving coherence of quantum memory during entanglement creation between nitrogen- vacancy centers in diamond."* Supervisors: Prof. Ronald Hanson and Prof. Caspar van der Wal
2015 - 2020	Master of Science in Medicine University of Groningen, Groningen, The Netherlands Thesis: *"The etiology of epicardial double potentials and the correlation between the transmural activation delay and contrast-enhanced MRI delineated scar in non-ischemic cardiomyopathy patients with ventricular tachycardia."* Supervisor: Prof. Katja Zeppenfeld, Leiden University Medical Center
2012 - 2014	Bachelor of Science in Physics, *Cum Laude* University of Groningen, Groningen, The Netherlands Thesis: *"Design and building of an optical set-up for water droplet transport over a light-switchable surface."* Supervisor: Prof. Petra Rudolf
2010 - 2013	Bachelor of Science in Medicine University of Groningen, Groningen, The Netherlands
2004 - 2010	Secondary school Vrije School "De IJssel", Zutpthen, The Netherlands

TU Delft

ISBN: 978-94-6384-794-0